ISSN 2367-7570

Workshop
"Solar Influences on the Magnetosphere, Ionosphere and Atmosphere"

Book
of
Proceedings

Tenth Workshop
Primorsko, Bulgaria, June 4÷8, 2018

Organized by:

Space Research and Technologies Institute
Bulgarian Academy of Sciences

Scientific Organizing Committee

Editors: **Katya Georgieva, Boian Kirov, Dimitar Danov**

DOI: 10.31401/ WS.2018.proc

CONTENT

Sun and Solar Activity

Solar Wind-Magnetosphere-Ionosphere Interactions

CONTENT

CONTENT

Long-term Solar Variability and Sunspot Indices

Solar Influences on the Lower Atmosphere and Climate

Proceedings of
Tenth Workshop "Solar Influences on the Magnetosphere, Ionosphere and Atmosphere"
Primorsko, Bulgaria, June 4÷8, 2018

A series of powerful solar flares in minimum of solar activity. Proton acceleration on the solar back side.

I. M. Podgorny [1], *A. I. Podgorny* [2]

[1] Institute of Astronomy RAS, Moscow, Russia
[2] Lebedev Physical Institute RAS, Moscow, Russia
E-mail: podgorny@inasan.ru

Abstract.

A powerful series of solar flares is occurred in the minimum of solar activity 2017 September 4 – 11 over the active region AR12673. This active region produces two large and many small flares. The flare X8.2 is followed by solar cosmic rays. The active region at that time is situated on the back side of the Sun disk behind the Western limb. The front of the accelerated protons flux arrives to the Earth with the delay not exceeding the proton flight time from the Sun. Such proton propagation can occur only along the lines of the interplanetary magnetic field. There is no reason to believe that the mechanisms of cosmic ray acceleration on the Sun and other stars are of different nature. The flux of relativistic electrons does not show any connection with the solar cosmic rays. The results of SDO spacecraft are used to study the pre-flare state and flare development. The source of flare radiation in the spectral lines of the highly ionized irons FeXXIV and FeXXIII is observed in the corona. The emission of these spectral lines sharp increases during flare X-ray radiation appearing. The energy release of a flare occurs in the corona above an active region. The temperature in the flare is greater than 20 MK. The size of the hot plasma cloud is ~10^{10} cm.

Introduction

The solar constant indicates an amazing stability of the solar thermonuclear reactor. The solar constant is 1367 W/m^2. The change of the solar constant during the 11-year cycle of solar activity does not exceed ~10^{-3}. Against the backdrop of this amazing stability of the Sun's work the big solar flares are observed several times per a year. The flare energy release takes place in the corona over a complex active region with a magnetic flux greater than 10^{22} Mx. The energy of a solar flare can exceed 10^{32} erg. The flare duration is from 10 to 100 minutes. The flare is a manifestation of a number of physical processes, including X-ray radiation, the ejection of the corona substance and proton acceleration to the relativistic energy of not less than 20 GeV [Balabin *et al.,* 2005; Podgorny and Podgorny, 2016].

The Sun is the only astronomical object that generates proton pulses with the relativistic energy. The solar proton acceleration takes place along a singular line of the current sheet above an active region. The electric field $\mathbf{E} = -\mathbf{V}\times\mathbf{B}/c$ for proton acceleration is generated at magnetic lines reconnection. The accelerated proton spectra coincide with the spectra calculated for acceleration in the current sheet in the numerical MHD simulation of real solar flares [Balabin *et al.,* 2005; Podgorny and Podgorny, 2016]. The pulses of relativistic protons accompanying flares are recorded against the background of a continuous flux of galactic cosmic rays with the energy of more than 10^{15} eV. For more than 100 years the galactic cosmic ray acceleration has been studied, but the physical mechanisms of acceleration remain unclear. The most popular, but unproven hypothesis, is the proton acceleration in interstellar shock waves. It is impossible to exclude that galactic cosmic rays are accelerated by the same mechanism as the solar cosmic rays. However, the energy of galactic cosmic ray particles is several orders of magnitude higher than the maximum energy of protons accelerated on the Sun. This fact for a long time does not allow us to state unambiguously that the acceleration of galactic and solar cosmic rays occurs by the same mechanism. The modern detection of giant flares on the star dwarfs of the class G [Maehara *et al.,* 2005; Shibayama *et al.,* 2013]

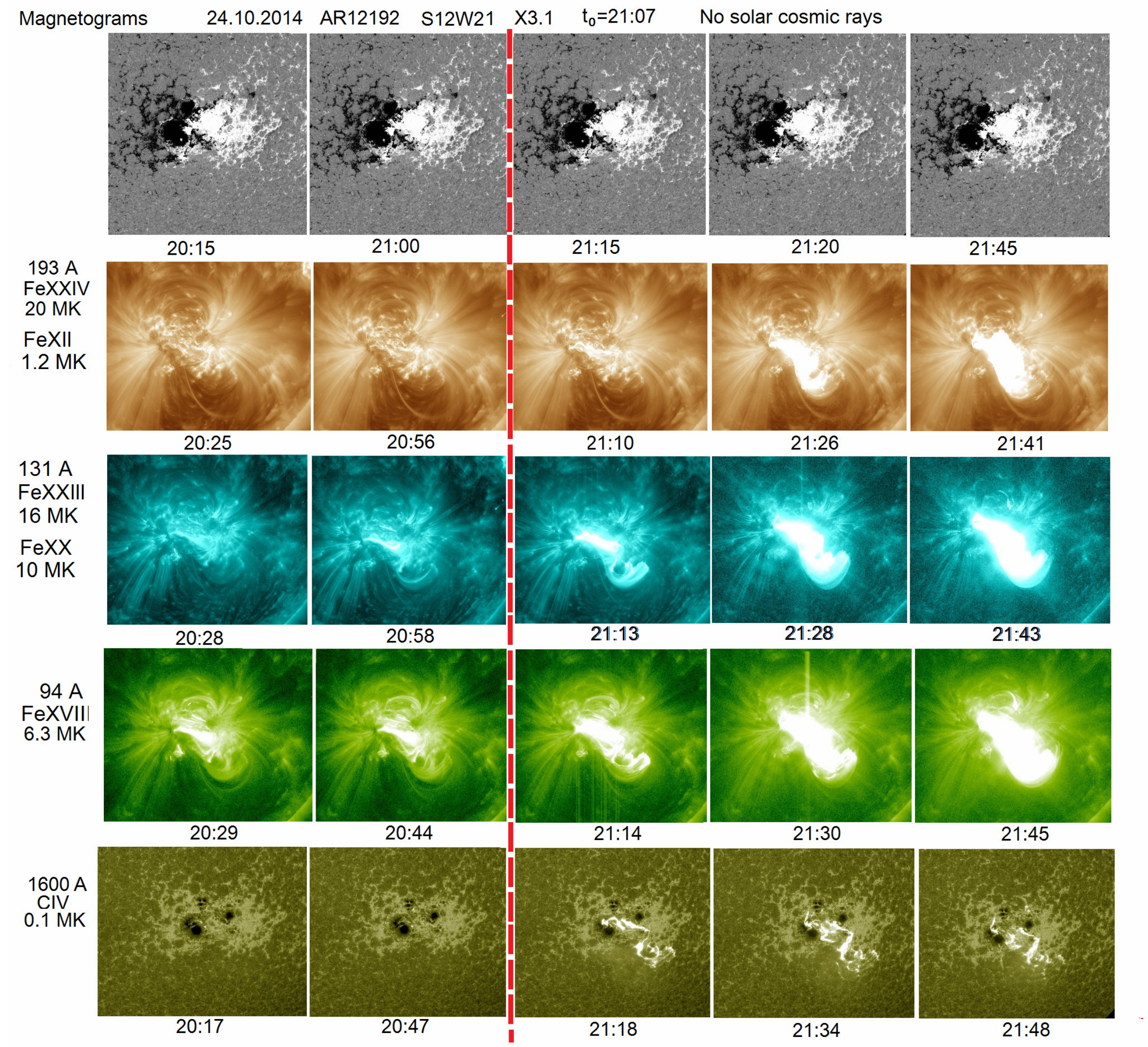

Fig. 1. Flare emissions of atoms of different degrees of ionization in the pre-flare state and during the flare occurring in the middle of the solar disk.

with the energy significantly exceeding the energy of the solar flares indicates the possibility of proton acceleration beyond the boundary of the solar system to energies significantly greater than the energy of solar cosmic rays.

The previously considered significant difference in the energy maximums of galactic and solar cosmic rays did not contribute to the idea of the same cosmic ray acceleration mechanisms on the Sun and on stars. The recent data [Shibayama *et al.*, 2013] is showed that the energy of the stellar flare can exceed 10^{36} erg. It is by 3-4 orders greater than the energy of a large solar flare, and, apparently, the energy of the protons accelerated in these stellar flares can significantly exceed the energy of the particles registered from flares on the Sun. Thus, the flare can be a universal astronomical process responsible for proton acceleration on the Sun and on the stars. The flare and dynamics of the pre-flare state of the active region that caused the flare are available for direct investigation only on the Sun.

The solar flare physics is very important branch of the modern astronomy. The solar flare is a complex physical phenomenon with the energy release above 10^{32} erg, which causes perturbation of the Earth's magnetic field and often leads to unpleasant economic consequences. Solar cosmic rays with the energy of at least 20 GeV, often accompanying a solar flare, produce a serious threat to the health of crews in planned interplanetary missions.

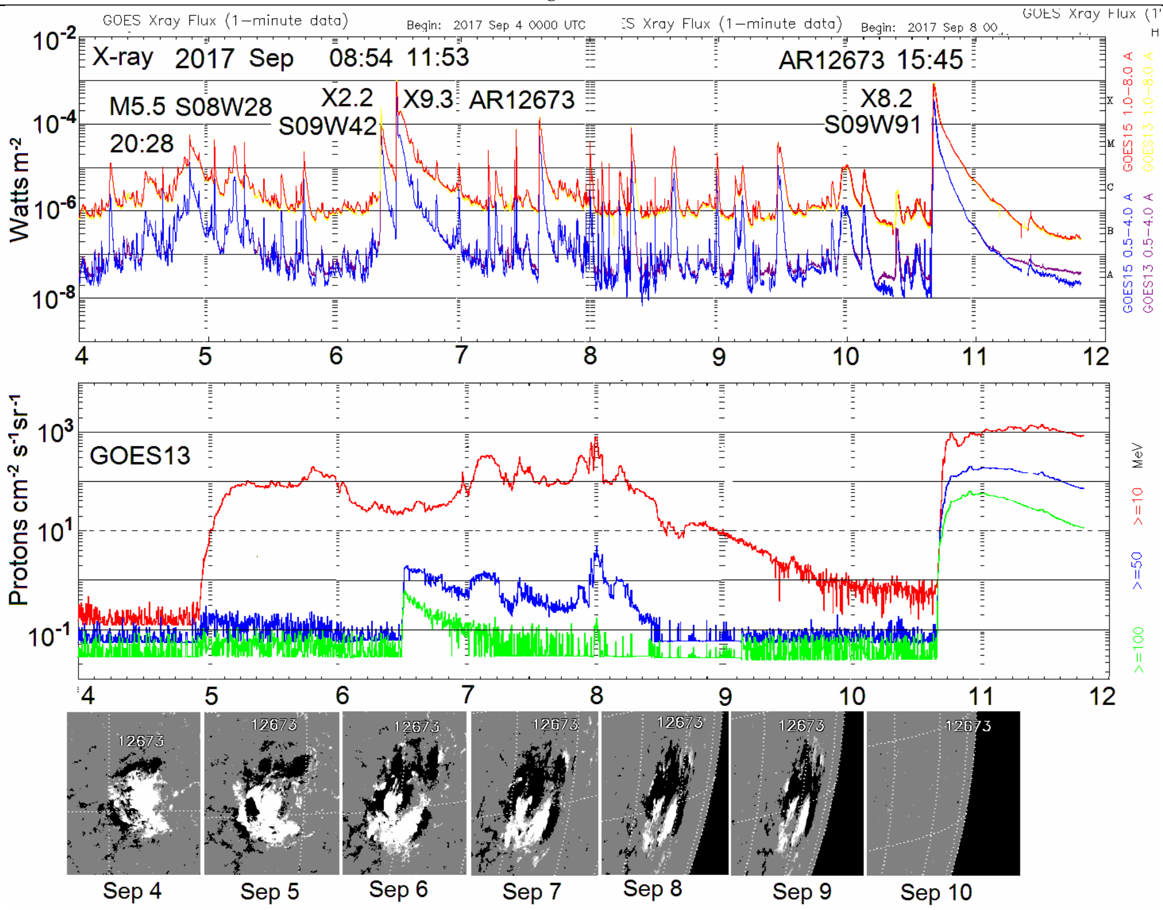

Fig. 2. The event 4 – 10 September, 2017 at the minimum of solar activity and the the magnetic field evolution in the active region AO12673.

The flare in spectral lines of highly ionized iron

The flares development is demonstrated in the spectral lines of highly ionized atoms [Podgorny and Podgorny, 2017, 2018] detected with the Solar Dynamic Observatory (https://sdo.gsfc.nasa.gov/data). A typical development of a solar flare on the solar disk is shown in Fig. 1. To the left of the vertical (red) line the frames are shown that taken before the flare. The flare X3.1 appears above an active region in the central part of the solar disk on September 24, 2014 at t_0 = 21: 07. The photos presented to the right of the vertical red line show the flare development.

The first line shows one of the most fundamental properties of a solar flare - practical constancy over one and a half hours of distribution of the magnetic field sources on the photosphere immediately before the flare and during the flare. The results of the numerical MHD simulation [Podgorny and Podgorny, 2012, 2013] shows a very slow (for several days) formation of the pre-flare configuration (current sheet) in the corona over an active region occurs. Very slow dissipation of the magnetic field of this current sheet takes place. The flare appears at t_0 = 21:07. Noticeable perturbations of the magnetic field on the photosphere during the flare are not observed. In numerical MHD simulation [Podgorny and Podgorny, 2012, 2013], the initial and boundary conditions on the photosphere are determined from measurements of the pre-flare state of the active region for several days before a real flare. The simulation results show that a current sheet in the corona is formed before the flare. The magnetic field energy that accumulated in this current sheet is realized during a flare. The second line shows a very slight increase in the emission of the hot plasma spectral line of 193 Å FeXXIV before the flare, but its emission sharp increase during the flare. The third line (131 Å FeXXIII line) also demonstrates the beginning of slight heating of the coronal plasma cloud during the current sheet formation above an active region and the rapid heating of the plasma during the flare. The fourth line photos indicates the preheating of the coronal plasma cloud during the formation of the current sheet and the development of the emission of the 94 Å FeXVIII line in the flare. The fifth line demonstrate small torn chromospheric structures - flare filaments, which for a long time have been considered as the main flare manifestation.

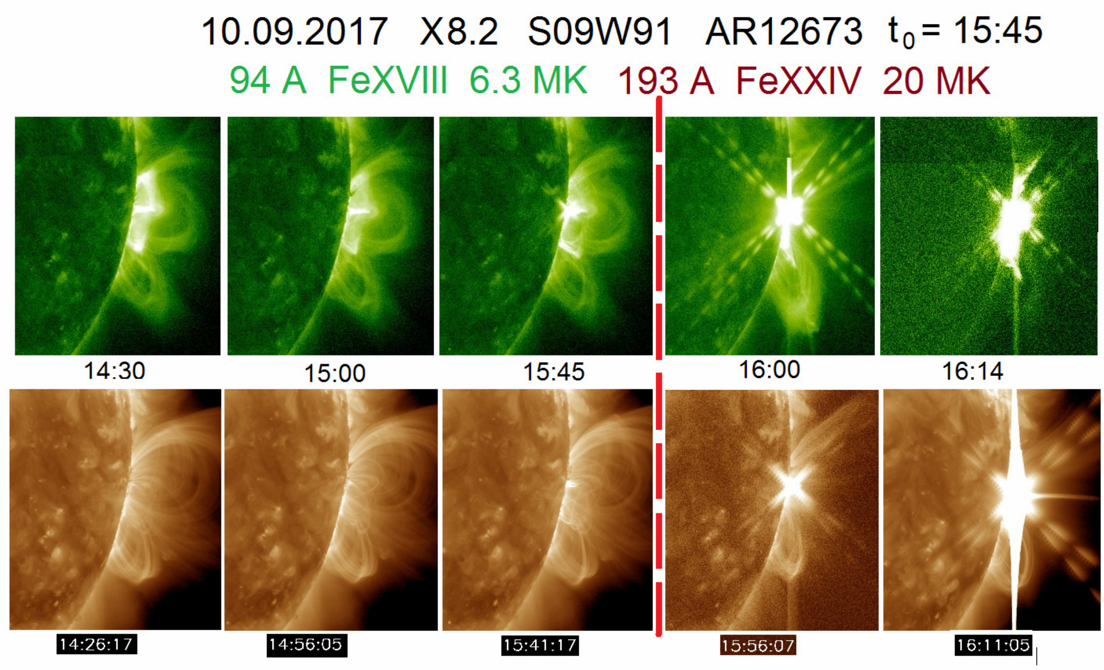

Fig. 3. The flare X8.2 in the hot spectral lines 94 Å and 193 Å. The active region is located on the back side of the Sun. The heating of the plasma during the flare occurs in the corona beyond the solar disk boundary.

Not an ordinary event is shown in Fig. 2. At the solar activity minimum the developing active region appeared on the eastern limb. When the active region is moving along the disk its development is accompanied by a series of solar flares of various sizes. The first flare of M5.5, which appeared near the eastern limb, (S08W28) develops unusual. The front of its X-ray radiation is tightened by two orders of magnitude in comparison with the normally recorded flares. The last flare X8.2 is appeared above the active region that situated on the solar disk back side. The active region is not seen on the disk (Fig. 2), but hot spectral line emission (193 Å and 131 Å) demonstrate plasma cloud heating in the corona during the flare. Fig. 3 shows that emission of the hot line 94 Å (6.3 MK) is appeared in the pre-flare state and increased sharply in the flare, but strong very hot line 193 Å (20 MK) is appeared only in the flare. These photos can be considered as a new independent evidence of the flare appearing in the corona, but not in the chromosphere. During the series of flares on September 4 - 10, 2017, a flux of relativistic electrons is recorded (Fig. 4), however, the dynamics of the proton flux clearly shows the complete independence of the detected electron fluxes of the dynamics of flare protons. There generation of relativistic electrons is associated with a solar flare.

Fig. 5 shows that the protons, which occurred near the western limb, arrive to the Earth with a sharp front ~ 30 min and with a delay which equals to the time of flight of the particle between the flare and the spacecraft. Such a process can occur when particles are moving on the front without collisions along the magnetic field line of Archimedes' spiral. The arrival of the front of the particles from flares that appeared in the center of the disk (N15E02) and near the east limb (S15E65) occurs only with a much longer delay of ~3 hours. Particles from such flares can arrive to Earth only across the lines of the magnetic field. The front of the proton flux from these flares is a rather flat with duration of 10 to 20 hours. The delay in the arrival of the proton flux front from the flares of the eastern and central parts of the disk is clearly less than the time of particle transfer by the solar wind. Apparently, their delay is determined by the diffusion of protons across the magnetic field due to scattering by field fluctuations caused at beam instability [Istomin, 2005].

Cosmic ray acceleration on the Sun and in the galactic

Solar cosmic rays generation takes place in the flare current sheet. The pulse of fast protons appears simultaneously with appearing the flare. The measured spectra of solar cosmic rays coincide with the spectra calculated for acceleration in a flare current sheet. The exact coincidence is observed at the reconnection rate 10^7 cm/s. The measured spectra of solar cosmic rays are calculated for acceleration in a real flare current sheet [Balabin *et al.,* 2005; Podgorny and Podgorny, 2016], using measured initial and boundary conditions. The Sun is the only astronomical object that generates proton pulses with the energy of at least 20 GeV, which origin is accessible to direct research. Galactic cosmic ray has been discovered 100 years ago, but still there are no information about the mechanism of their acceleration. The most popular, but unproven hypothesis is the proton acceleration in interstellar shock waves.

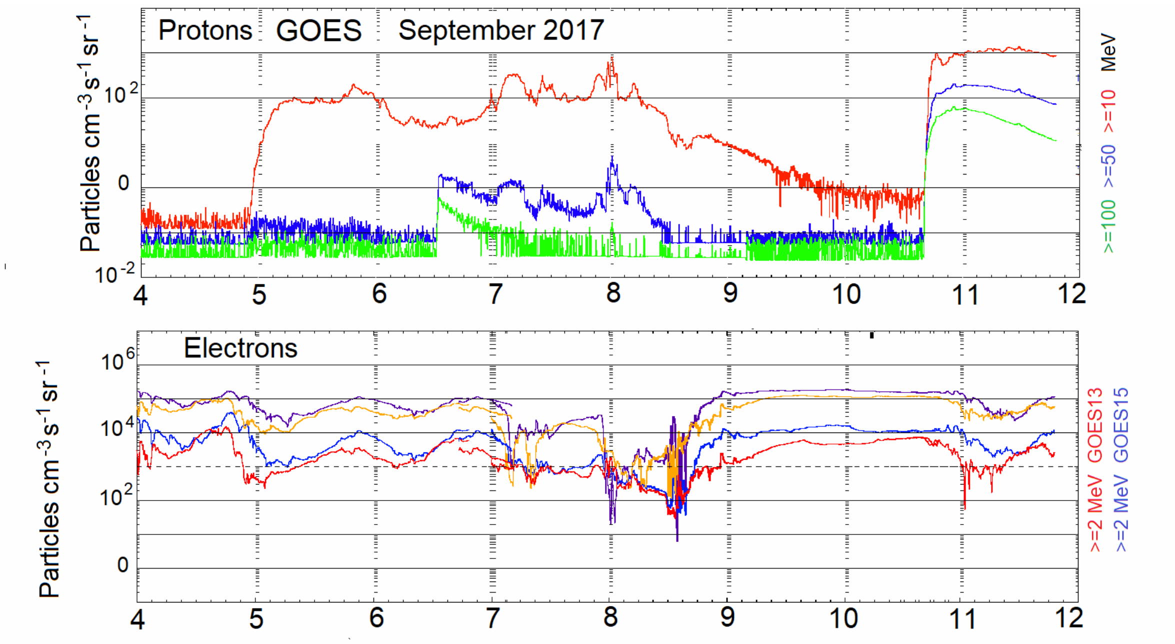

Fig. 4. The fluxes of accelerated protons near the Earth's orbit, generated by a series of flares, and fluxes of relativistic electrons.

There is every reason to assert that solar cosmic rays and galactic cosmic rays are generated by the same mechanism. However, the energy of galactic cosmic rays is several orders of magnitude higher than the maximum energy of protons accelerated on the Sun. This fact for a long time did not allow us to state unambiguously that the acceleration of stellar and solar cosmic rays occurs by the same mechanism.

The discovery of giant flares on the G dwarfs [Maehara *et al.,* 2005; Shibayama *et al.,* 2013] with the energy significantly exceeding the energy of the solar flares brings new information. It is impossible to exclude that such gigantic flares can accelerate ions up to the energy much bigger than solar cosmic rays. The results of [Maehara *et al.,* 2005; Shibayama *et al.,* 2013] can be considered as a new independent argument in favor of cosmic ray generating in the flares, but not in shock waves. The flare is the universal astronomical process that responsible for proton acceleration on the Sun and on the stars. The flare and dynamics of the pre-flare state of the active region that caused the flare are available for direct

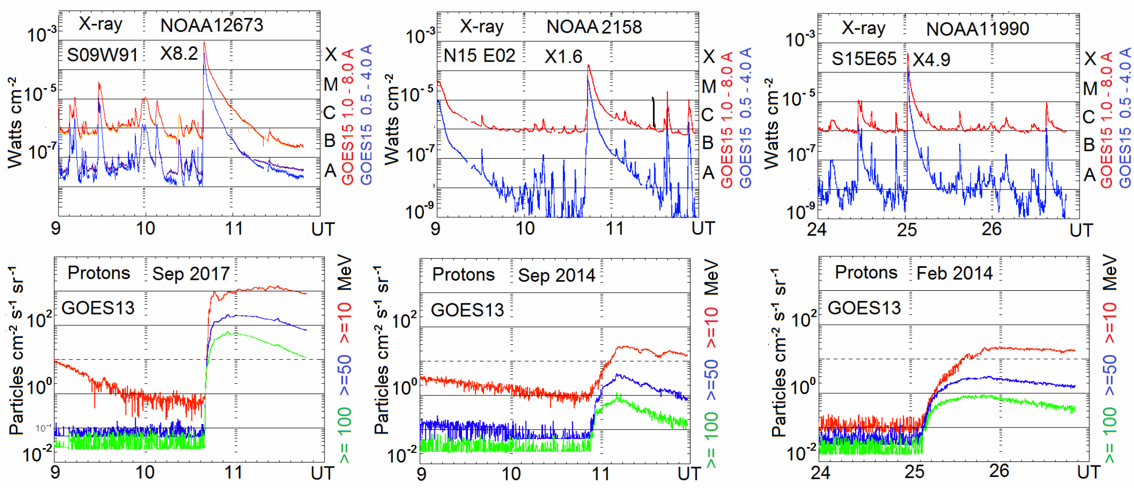

Fig. 5. Solar cosmic ray fluxes from flares occurred in various regions of the solar disk.

observation only on the Sun. The solar flare is a complex physical phenomenon with the energy release above 10^{32} erg, which causes perturbation of the Earth's magnetic field.

Conclusion

The flare is a universal astronomical process that generates cosmic rays. Flares occur on the Sun and stars. A detailed study of the flare is possible only on the Sun. The active region of AR12673 has appeared at the minimum of solar activity, when no flares are usually observed during a year. The flare energy release is occurred in the corona over the active region. The AR12673 region has produced series of large flares, including the X8.2 flare on the back side of the solar disk. The plasma cloud in the corona is heated up to the temperature at least 20 MK. The flare on the back side of the Sun produces a flux of solar cosmic rays that observed at the Earth. The protons from the flare X8.2 came with a steep front and with the delay equal to the proton transit time along the line of the interplanetary magnetic field. The recorded protons could reach the Earth, propagating without collisions along the line of the interplanetary magnetic field of the Archimedes spiral. The generation of solar cosmic rays is not revealed any correlation with the flux of relativistic electrons. The discovery of flares appeared on dwarfs of class G with release of the flare energy 3 to 4 orders of magnitude higher than by the flares on the Sun is a new argument in favor of the mechanism of galactic cosmic ray acceleration based on the current sheet rather than acceleration in shock waves.

References

Balabin Yu.V., Vashenyuk E.V., Mingalev O.V., Podgorny A.I. Podgorny I.M. (2005). The spectrum of solar cosmic rays: data of observations and numerical simulation. Astronomy Reports, 82, 940–949.

Maehara H., Shibayama T., Notsu S., et al. (2012). Superflares on solar-type stars. Nature, 485, 478–481.

Istomin, Ya. N. (2010). Relativistic jets in active galactic nuclei: time variability. Mon. Not. R. Astron. Soc., 408, 1307–1312.

Podgorny, A.I., Podgorny, I.M. (2012). Magnetohydrodynamic simulation of a solar flare: 2. Flare model and simulation using active_region magnetic maps. Geomagn.and Aeronomy, 52, 162–175.

Podgorny, A.I., Podgorny, I.M. (2013). Simulation of solar flare current sheet position and comparison with X-ray observations in active region NOAA 10365 Sun and Geosphere, 8, 71–76.

Podgorny, I.M., Podgorny, A. I. (2016). Solar cosmic ray acceleration and propagation. Sun and Geosphere, 11, 85–90.

Podgorny I.M., Podgorny A.I. (2017). On solar cosmic ray propagation in the interplanetary space and highly ionized ions emission. Proceedings of the 40th Annual Apatity Seminar (2-6 March, Apatity), pp. 78–81.

Podgorny I.M., Podgorny A.I. (2018). Solar flares dynamics investigation using UV diagnostics. Sun and Geosphere, 13, 69–76.

Shibayama T., Maehara H., Notsu S., at al. (2013). Superflares on solar-type stars observed with Kepler. I. Statistical properties of superflares. Ap. J. Suplimento Ser., 209:5 (13pp).

Proceedings of
Tenth Workshop "Solar Influences on the Magnetosphere, Ionosphere and Atmosphere"
Primorsko, Bulgaria, June 4÷8, 2018

Initiation, Interaction and Eruption of Filament Flux Ropes from the Perspective of Their Magnetic Twist and Environment

Duchlev P., Koleva K., Dechev M.

Institute of Astronomy and National Astronomical Observatory,
Bulgarian Academy of Sciences, Bulgaria
E-mail: duchlev@astro.bas.bg

Abstract.

We present two prominence/filament eruptions (FEs) that belong to the class of rarely reported eruptions of two near-by flux ropes (FRs) of the same filament. The FRs (FR1 and FR2) of the FE on 2014 May 4 with the same helicity, i.e. left- handed twist and writhe, interact during the eruption. Their kinematics indicate a slow successful eruption of FR1 associated with a slow coronal mass ejections (CME) and a failed kinked FR2 eruption with a strong non-radial propagation followed by its reformation. The second FE on 2014 March 14 is composed by both hot, bright flux rope (BFR) and cool massive flux ropes (MFR) that underwent merging followed by splitting during the eruption. This FE produced a partial-halo CME with a bi-component bright core and an impulsive flare and post-flare loop arcade, as well. The comparative analyses of two eruptive prominences (EPs) suggest that the character of FR's interaction in each of them play a crucial role for both the driver of eruption (kink or torus instability) and the type of eruption - failed, partial or successful.

Introduction

Magnetic flux rope (FR) eruptions in the solar atmosphere play a key role in eruptive activities of the Sun, such as filament eruptions, CMEs, and flares. Prominences/filaments occur frequently as major precursors of coronal mass ejections (CMEs) as indicated by the observed close association between their eruptions and CMEs [*Munro R.H. et al.*, 1979, *Webb D. F. and Hundhausen A. J.*, 1987]. Several basic mechanisms that can disrupt the FRs include both ideal processes such as helical kink instability and torus instability of twisted coronal FRs and the non-ideal (resistive) process of the fast magnetic reconnections in current sheets [*Aulanier G.*, 2013, for a review].

It is known that two adjacent filaments sometimes approach each other and interact. There are four fundamental types of interaction: bounce, merge, slingshot, and tunnel [*Jiang Y. et al.*, 2013, *Joshi, N. C. et al.*, 2016]. The interacting filaments studies can contribute for verifying different filament models and for better understanding the coronal magnetic field structures and their dynamics, as well. However, such observational reports are still rare.

There are cases, when both branches belonging to a single filament FR are separated later that results into two ropes with the same handedness. According to previous observations and simulations, such splitting often occurs during the eruption or, in some cases, just before the filament eruption (FE) [*Liu, R. et al.*, 2012, *Kliem B. et al.*, 2014, for a review]. Such cases are very rarely reported.

The aim of this work is the comparison of two eruptive prominences (EP) that belongs to afore-mentioned last class of very rarely reported eruptions. The FRs (FR1 and FR2) of the first EP on 2014 May 4 with the same helicity interact during the eruption. The FR1 presents a slow successful eruption associated with a slow CME and the FR2 underwent a failed kinked eruption with a strong non-radial propagation followed by its reformation [*Dechev M. et al.*, 2018a]. The second EP on 2014 March 14 is composed by both hot, bright flux rope (BFR) and cool massive flux ropes (MFR) that underwent merging followed by its splitting during the eruption. This EP produces a partial-halo CME with a bi-component bright core and an impulsive flare and post-flare loop arcade, as well [*Dechev M. et al.*, 2018b].

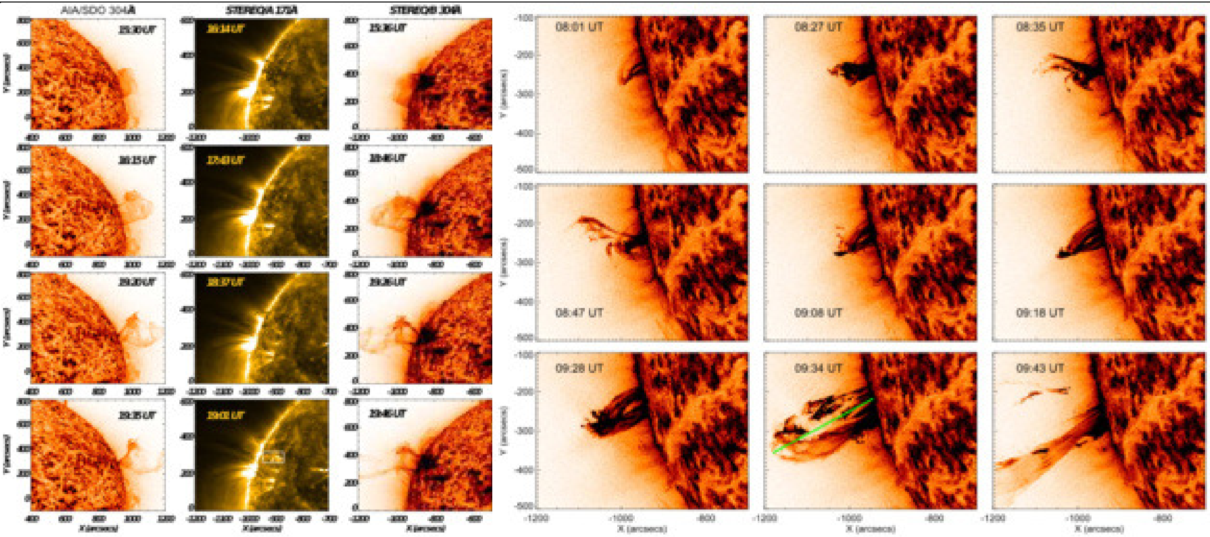

Fig. 1 Evolution of the EP on 2014 May 4 in reversed color images in the AIA/SDO and STEREO Å and B FOVs (left). Evolution of the EP on 2014 March 14 in reversed color SDO/AIA 304 Å images. The green line marks the slice position used for height determination. (right).

Data

The two EPs on 2014 March 14 and 2014 May 4 were observed from three different fields-of-view (FOV) by Solar Dynamics Observatory (SDO) and Solar Terrestrial Relations Observatory (STEREO) A and B (Fig. 1). Therefore, for the analysis of EPs we used data from the instruments Atmospheric Image Assembly/SDO (AIA) and Extreme UltraViolet Imager (EUVI) of STEREO A and B. For examination of the CMEs associated with the EPs, we used data from the coronagraphs Large Angle and Spectrometric Coronagraph (LASCO) C2 and C3 of SOHO and COR1 and COR2 of STEREO A and B, as well.

Results

a) Source regions

The EP source on 2014 May 4 was two coupled filament FRs (FR1 and FR2) located in the same polarity inversion line (PIL), i.e. in the same filament channel in a quiet solar region. The eruptive event was well observed as an EP above the limbs from SDO/AIA and EUVI B instriments, while in the EUVI A FOV, it was observed as a FE on the disk. The EP source on 2014 March 14 was a filament located along polarity inversion line in a young short-lived active region (AR) still in its emergence phase. In a large scale, the filament was situated at the bottom of a unipolar-bipolar-unipolar ambient multiple-arcade helmet streamer. The event was observed as an EP in the SDO/AIA and STEREO-A/EUVI FOVs, while in the EUVI B FOV it was observed as FE.

b) Kinematics

EP on 2014 May 4. In the AIA 304 Å FOV, the FR1 slowly rose with velocities from 5.7 km/s to 31.3 km/s at accelerations between 0.2 m/s^2 and 4.9 m/s^2 (Fig. 2c) undergoing a kink-induced successful, partial eruption, which was associated with a slow CME. As a bright core in the CME cavity, the FR1 could be traced up to 15 $R_\odot$. The kinked FR2 exhibited non-radial failed eruption and its kinematics shows two phases (Fig. 2d). The FR2 kinked loop underwent a short-time eruption in negligible height diapason of 10 Mm. Afterward it displayed a long-lasting downward motion with velocities of several tens km/s up to the original place, where it was rebuilt. The post-eruptive phase was accompanied by apparent plasma draining along the FR2 legs.

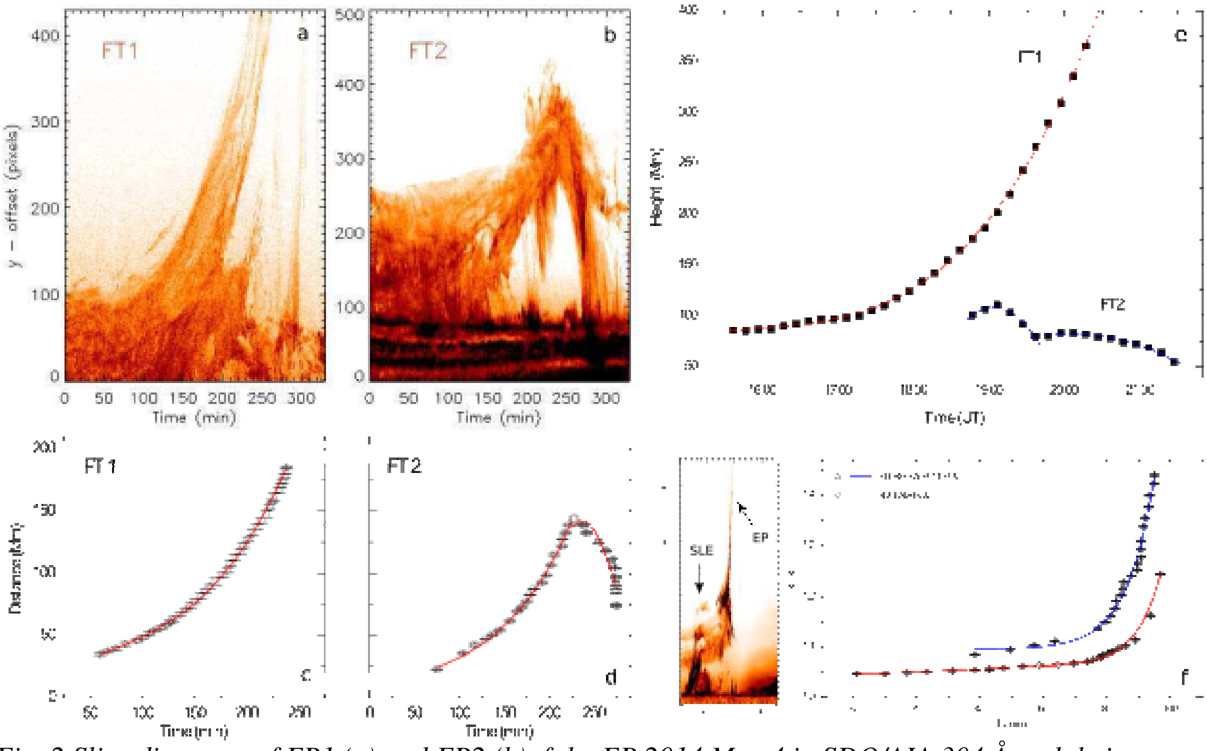

Fig. 2 Slice diagrams of FR1 (a) and FR2 (b)of the EP 2014 May 4 in SDO/AIA 304 Å and their height-time profiles (c) and (d). The zero time-point is 15:30 UT. Height-time profiles of the FR1 and FR2 in the STEREO-B FOV (e). Slice diagram of the EP on 2014 March 14 (f left) and corresponding height-time profiles as observed in AIA/SDO and STEREO FOVs (f right).

In the EUVI B 304 A FOV the FR1 showed two phases of eruption. The slow rising phase took place in the height diapason from 85 Mm to 133 Mm, where the velocity increased from 1.7 km/s to 14 km/s at acceleration between 0.13 m/s^2 and 3 m/s^2. During the fast phase the FR1 rose with velocity from 14 km/s to 50 km/s at acceleration between 3.1 m/s^2 and 6.2 m/s^2. The FR2 evolution showed two phases - eruptive and post-eruptive (Fig. 2e). During the first phase FR2 initially slowly rose in a narrow height diapason (100-110 Mm) with velocities from 170 km/s to 75 km/s at an acceleration of –15.2 m/s^2. Later, FR2 entered in the second phase, when it gradual decreased from 80 Mm to 54 Mm with velocities from 75 km/s to 21 km/s with an acceleration of –2.1 m/s^2. Finally, FR2 was rebuilt at the original position with strongly simplified structure.

EP on 2014 March 14. As one can see in Fig. 2f, the EP clearly shows two distinctive phases: a slow rise phase and a fast acceleration phase. During the slow rise phase in in AIA FOV, the EP rose with an average speed of ~3 km/s, while in the EUVI A FOV it rose with speeds from 2 km/s to 12 km/s at accelerations from 1 m/s^2 to 11 m/s^2. During the fast phase as observed in the AIA FOV, the EP exponentially accelerated with speeds from ~3.5 km/s to ~280 km/s, while in the EUVI FOV the EP speeds increased from 12 km/s to 470 km/s at accelerations in the range 23-890 m/s^2. It should be noted that in the EUVI A FOV, only last 62 minutes of EP slow raising was observed because the EP position was of ~25° behind the EUVI A western limb. However, in the EUVI FOV the eruptive phase was observed to bigger altitudes because of the bigger FOV (1.7 $R_\odot$ vs 1.3 $R_\odot$ of AIA FOV).

c) Interaction of EP flux ropes

EP on 2014 May 4. During the last stage of the slow rise phase, the upper parts of the coupled FR1 and FR2 underwent merging and interacting. The magnetic treads in the EP upper part gradually brighten up. The brightening was observed in all EUV lines and resulted in upward U-shaped structure forming. After brightening peak, U-shaped structure began to fade accompanied by FR1 and FR2 splitting and when it disappeared the FR1 and FR2 were already clearly separated. The EUV brightening could be interpreted as a signature of slow magnetic reconnection [*Su Y. et al.*, 2015]. Such brightening evolution suggests mass and flux transfer which according to *Liu et al.* (2012) must involve a transfer of current from the lower FR2 FR to the upper FR1. Moreover, accumulation of a flux under the apex of FR1 can contribute to its twist, i.e. it affords the destabilization process [*Kliem B. et al.*, 2014].

The sequence of the kink-induced FR1 partial and FR2 failed eruptions involved in this event, as well their evolution are consistent with one of simulation scenarios developed by *Kliem et al.* [2014], according which a similar flux rope configuration enable the eruption of the upper FR, followed by downward motion the lower one if it is unstable. There are two arguments for FR2 unstable state:(1) the EUV brightening covering almost whole FR2 upper part and especially the region around cross-point between its kinked legs; (2) the apparent plasma drainage in FR2 legs.

EP on 2014 March 14. The EP initially appear as a slow rising MFR and later, the tightly twisted BFR initiated by surge eruption [*Dechev M. et al.*, 2018b] began slowly to rise beneath the MFR. This process lasts up to the EP fast-rise onset, when the BFR was already visible as bright loop, merged with the MFR inner edge forming in this way a single EP FR. After FRs merging, the single FR underwent gradual brightening from the top downwards. Such brightening suggests subsequent reconnections that redistribute the magnetic flux between the FRs into single FR. There are two possible processes of merging. First one depends on the properties of the flux rope configuration and perturbation and is reliable to merging if the lower FR show the stronger instability (as in our case) [*Kliem B. et al.* 2014]. Another process based on the Taylor relaxation model [*Hussain A. S. et al.* 2017] is reliable if the FRs have different twist degrees. In our case, the BFR has sufficiently bigger twist than MFR. Therefore, the MFR and BFR can merge through reconnection into a single FR.

During the early fast eruption phase, the bright single EP underwent EUV dimming in different part of its body. Subsequently, only three regions of strong EUV emission remained in the EP: at the top, in the middle part of northern leg, and at FR footpoints. These regions contained strongly heated plasma because they were well visible in all EUV lines. In addition, during the EUV dimming process a flare started at the EP vicinity that suggests a sympathetic casual relation between the EP and the flare.

Just after of the onset of EP strong acceleration, the single FR upper part began to split laterally, which is similar to the cases of partial eruptions (*Liu R. et al.*, 2007). The splitting of MFR and BFR within the single FR could be explained by the transfer of magnetic flux from the lower to the upper rope [*Kliem B. et al.*, 2014]. Moreover, in some extent our case is in conformity with the scenarios of *Kliem B. et al.* [2014] for full eruption of the double-FR, in which the dominant instability of lower FR revealing as upward perturbation is applied to upper FR. Such full eruption is clearly driven by the stronger torus instability of the lower flux rope and is very similar to the eruption of a single torus-unstable flux rope.

c) Associated CMEs

CME associated with EP on 2014 May 4. The CME associated with the EP FR1 was well observed by the coronagraphs of SOHO/LASCO C2 and C3 and STEREO-B/COR1 and COR2, where it was a very poor event. The CME had a classical three-part structure, with a bright leading edge, dark cavity, and a bright core (Fig. 3 left). In the late EP stage, the FR1 appeared as a bright CME core and its propagation showed small deflection toward the northern CME legs. Moreover, the evolution of FR1 kinked shape is clearly displayed in the LASCO C2 FOV. The close temporal and spatial relationship between the CME and the FR1 is the best presented in Fig. 3 left and Fig. 4 left. The height-time profile of CME propagation is presented in Fig. 4 left.

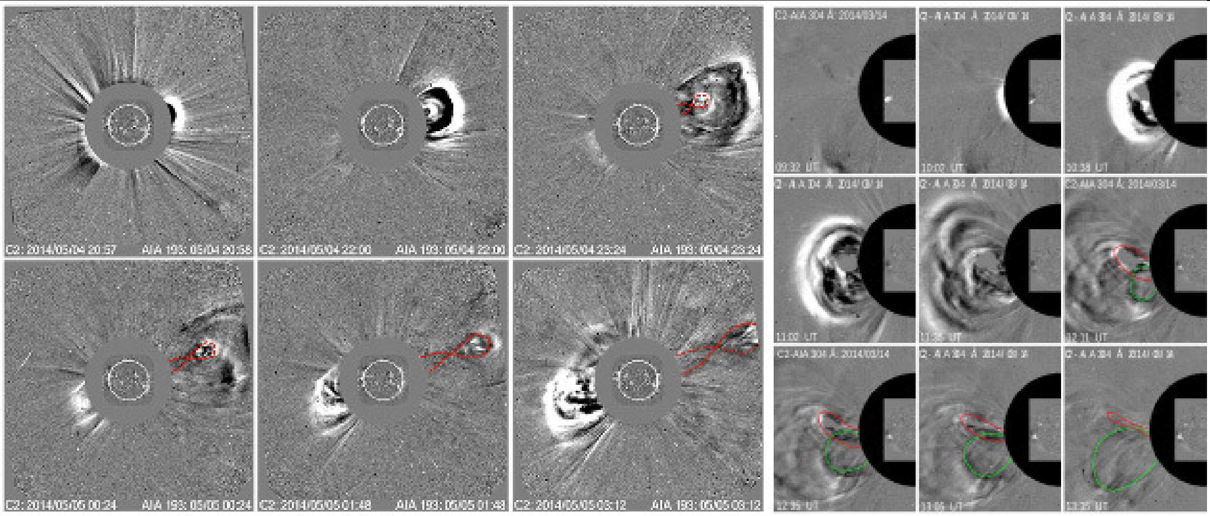

Fig. 3 CME evolution on 2014 May 4 observed by LASCO/C2 coronagraph. The red dotted line trace out the kinked structure of FR1 (left). Partial-halo CME evolution with the EP as a bright CME core on 2014 March 14 by LASCO C2 and SDO/AIA 304 Å running difference. The dashed lines in the last four frames trace the loops of EP FRs: green - MFR and red – BFR (right).

The CME propagated with linear velocity of 329 km/s or 2nd-order velocity of 342 km/s at constant acceleration of 0.8 m/s^2. The apparent CME propagation could be traced up to a distance of ~21 $R_\odot$ in LASCO C3 FOV. In the STEREO B COR2 FOV the CME core (FR1 top) propagation can be traced up to 15 $R_\odot$. In the LASCO C3 FOV, the core front gradually fades and at a distance of 18 $R_\odot$ it fully disappeared, which suggests the FR1 underwent a successful eruption.

Partial-halo CME associated with EP on 2014 March 14. The CME was surrounded by multiarcade helmet streamer and by this reason it had specific features with respect to the classical CME three-part structure (Fig. 4 right). The CME leading front loop was relatively faint followed by the secondary apparent bright loop and the cavity bellow them was inhomogeneous because of the multiarcade streamer. The CME bright core presented a bi-component structure produced by the upper parts of cool MFR and hot BFR, which had quite different asymmetrical positions in the cavity. Such bright core with hot and cool components was reported for the first time by *Li and Zhang* [2013] from on-disk observations of a filament eruption. After the bifurcation of EP single FR, the MFR began to propagate in direction close to those of the southern unipolar streamer, while the thin BFR propagated bellow the bipolar streamer. The MFR upper part gradually faded with its growth, while the BFR underwent strong brightening.

Conclusions

EPs on 2014 March 14 and 2014 May 4 occured in disparate source regions. Each of them presented two main closely located erupting FRs, which displayed disparate kinematics as well as different types of eruptions because of interactions between them.

1. The source of EP on 2014 May 4 was two coupled filament FRs (FR1 and FR2) located along the same PIL, in a quiet region. Two FRs of the EP on 2014 March 14 is located along the PIL in young AR still in the emergence phase. The AR was located in beneath multiarcade helmet streamer that is favorable for producing sympathetic events.

2. The FR1 and FR2 of EP on 2014 May 4 represented slow eruptions with velocities from several km/s to several tens km/s with a small acceleration of about several m/s^2. The FR1 eruption was successful, while the FR2 underwent failed eruption followed by its rebuilding. The FR1 eruption was associated with a slow CME and it could be traced as a CME bright core up to 20 solar radii.

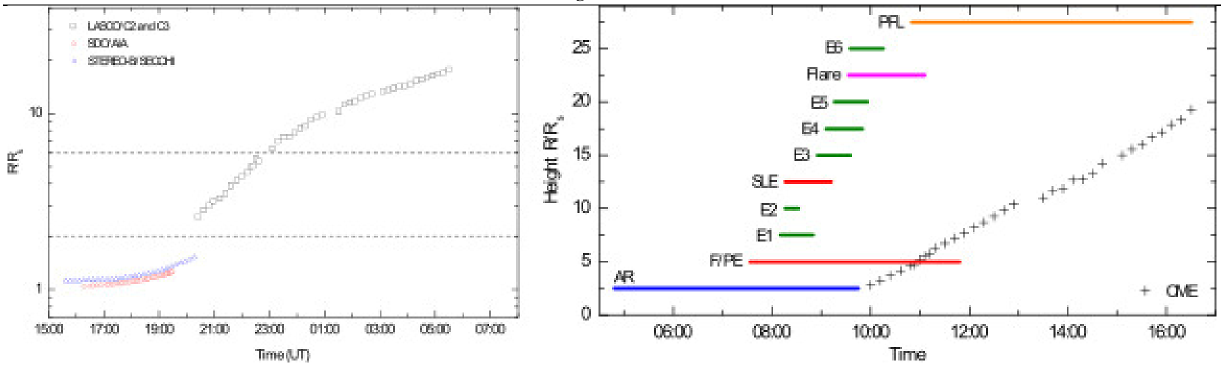

Fig. 4 Height-time profile of the CME associated with the EP on 2014 May 4, by LASCO C2 and C3 data. The horizontal dashed lines are bounds of the C2 FOV. The height of the EP observed by EUVI 304 Å and AIA 304 Å are overplotted (left). Height-time profile of the CME on 2014 March 14 with the overplotted exact duration of all associated events.

Initially the MFR and BFR of EP on 2014 March 14 slow rose with a speed from 2 km/s to 12 km/s at accelerations from 1 m/s^2 to 11 m/s2. The EP fast rising occurred with a growing speeds from 12 km/s to 470 km/s at accelerations in the range of 23-890 m/s^2. In a late stage, the EP produced a bi-component bright core of partial-halo CME.

3. The top parts of FR1 and FR2 of EP on 2014 May 4 underwent merging followed by splitting. Such interaction via slow magnetic reconnection lead to flux and current transfer from the lower FR2 F to the upper FR1 which enable the eruption of the upper FR1 followed by downward motion od FR2. Final result is a sequence of the kink-induced FR1 partial and FR2 failed eruptions. The BFR and MFR of EP on 2014 March 14 underwent merging during their slow rising folowed by splitting during their fast rising. These interaction leads to transfer of magnetic flux from the BRE to the MFR. The dominant instability of lower BFR reveals as upward perturbation that is applied to upper MFR. According to *Kliem B. et al.* [2014] such full eruption is clearly driven by the stronger torus instability of the lower flux rope and is very similar to the eruption of a single torus-unstable flux rope.

Acknowledgment

This work is co-funded by a bilateral collaborative project NTS/AUSTRIA 01/23, 28.02.17, under agreement between Bulgaria’s National Science Fund and Austria’s OeAD-GmbH. It was also funded by Bulgarian National Science Fund under Grants DH 081/13.12.2016 and DN 18/13-12.12.2017

References

Aulanier, G. (2014), in IAU Symp., 300, 184-197.
Dechev, M., Koleva, K., Duchlev, P. (2018a), NewA 59, 45-53.
Dechev, M.; Duchlev, P.; Koleva, K. (2018b) BlgAJ 28, 60-78.
Gopalswamy, N., Shimojo, M., Lu,W., Yashiro, S., Shibasaki, K., Howard, R.A. (2003), ApJ 586, 562–578.
Hussain, A. S.; Browning, P. K.; Hood, A. W. (2017), A&A 600, A5.
Jiang, Y., Hong, J., Yang, J., Bi, Y., Zheng, R., Yang, B., Li, H., & Yang, D. (2013), ApJ, 764, 68-73.
Joshi, N. C., Filippov, B., Schmieder, B., Magara, T., Moon, Yong-Jae, Uddin, W. (2016), ApJ 825, 123-138.
Kliem, B., Török, T., Titov, V. S., et al. (2014), ApJ, 792, 107-116.
Li, L. P., Zhang, J. (2013), A&A 552, L11.
Liu, R., Alexander, D., Gilbert, H. R. 2007, ApJ 661, 1260-1271.
Liu, R., Kliem, B., Török, T., et al. (2012), ApJ, 756, 59-72.
Munro, R.H., Gosling, J.T., Hildner, E., MacQueen, R.M., Poland, A.I., Ross, C.L. (1979), Sol. Phys. 61, 201-215.
Su, Y., van Ballegooijen, A., McCauley, P., Ji, H., Reeves, K. K., DeLuca, E. E. (2015), ApJ 807, 144-160.
Webb, D.F., Hundhausen, A.J. (1987), Sol. Phys. 108, 383–401.

Stealth coronal mass ejections: identification of source regions and geophysical effects

Iu.S. Zagainova [1], *V.G. Fainshtein* [2], *L.I. Gromova* [1], *S.V. Gromov* [1]

[1] Pushkov Institute of Terrestrial Magnetism, Ionosphere and Radio Wave Propagation RAS, Moscow, Russia
[2] Institute of Solar-Terrestrial Physics SB RAS, Irkutsk, Russia
E-mail: yuliazagainova@mail.ru

Abstract

By example of the 16 June 2010 event, a stealth coronal mass ejection (stealth-CME) emergence is shown to be probably accompanied by various manifestations of small-scale activity in the solar atmosphere and some features of variations in the magnetic field parameters. We also discuss the response of the geomagnetic field to the effect of this CME on the Earth magnetosphere.

Introduction

The bulk of the coronal mass ejections (CMEs) recorded with coronagraphs are related to various manifestations of low coronal signatures (LCSs): flares, filament eruptions, EUV waves, jets, etc. It appeared that there exist CMEs that are observed within the coronagraph field-of-view (FOV) and emerge (from different data) on the Sun visible surface, but they are not accompanied by LCSs, at the same time. The review by Howard and Harrison [*Howard T.A., et al,* 2013] addresses the history of observing such CMEs, discusses their unique features, and presents possible interpretations of their emergence. At present, such CMEs are referred to as stealth-CMEs [*D'Huys E., et al.,* 2014]. Stealth-CMEs, when they reach the Earth orbit, are established to possibly lead to origin of Forbush decreases [*Heber B., et al.,* 2015]. Some researchers [*Nieves-Chinchilla T., et al.,* 2013] relate the origin of the geomagnetic field noticeable disturbances to the stealth-CME effect on the Earth magnetosphere. Over the last years, by using advanced methods to process the Sun images obtained in different spectral channels with high-temporal and high-spatial resolution instruments, it became possible to detect related LCSs for many stealth-CMEs [*Alzate N., et al.,* 2017]. Nevertheless, there are grounds to believe that, except the discovered activity in the sites of probable stealth-CME sources, there are also other solar activity manifestations accompanying stealth-CME emergence. To detect those, one should develop new methods to process Sun images. Besides, one should also take into account the features and dynamics of the magnetic field in the assumed region of stealth-CME formation. In this study, by example of one event, we show that a stealth-CME emergence stealth-CME is accompanied by various manifestations of small-scale activity in the solar atmosphere. Also, we investigated the features of variations of the magnetic field parameters. Also, the response of the geomagnetic field to this CME effect on the Earth magnetosphere is discussed.

Data

We studied the solar activity accompanied by the emergence of a stealth-CME recorded within the LASCO C2 FOV onboard SOHO, on 16 June 2010 (14:54:05 UT). The main characteristics of this CME from https://cdaw.gsfc.nasa.gov/CME_list/ are: central position angle (CPA) = 61^o, angular width (AW) = 153^o (Partial Halo CME), linear projection velocity (V_{lin}) = 236 km/s, acceleration (a) = 6.5 m/s^2, mass (m) = 6.8 10^{14}, kinetic energy (E_{kin}) = 1.9 10^{29} erg.

To search for the CME formation probable site and to detect various manifestations of solar activity therein, we used Sun observations in several spectral channels (93, 304, 171, 193, 211, and 131 Å) of telescopes with high-temporal and high-spatial resolutions (SDO/AIA). To analyze the properties and dynamics of the magnetic field in the stealth-CME source region, we used vector measurements of the magnetic field with the SDO/HMI. The response of the geomagnetic field to the CME effect on the Earth magnetosphere was analyzed from https://omniweb.gsfc.nasa.gov/, and from the IMAGE magnetometer network.

Results

a) Solar activity at Stealth CME initiation

Fig. 1(a) shows the addressed CME within the LASCO C2 FOV, and Fig. 1(b) presents the GOES SXR time variation. The CME image in Fig. 1(a) has a poor quality. It is typical of most stealth-CMEs recorded within a coronagraph FOV. Fig. 1(b) illustrates the absence of a CME-related X-ray flare. The vertical line in Fig. 1(b) marks the instant of recording the CME with the C2.

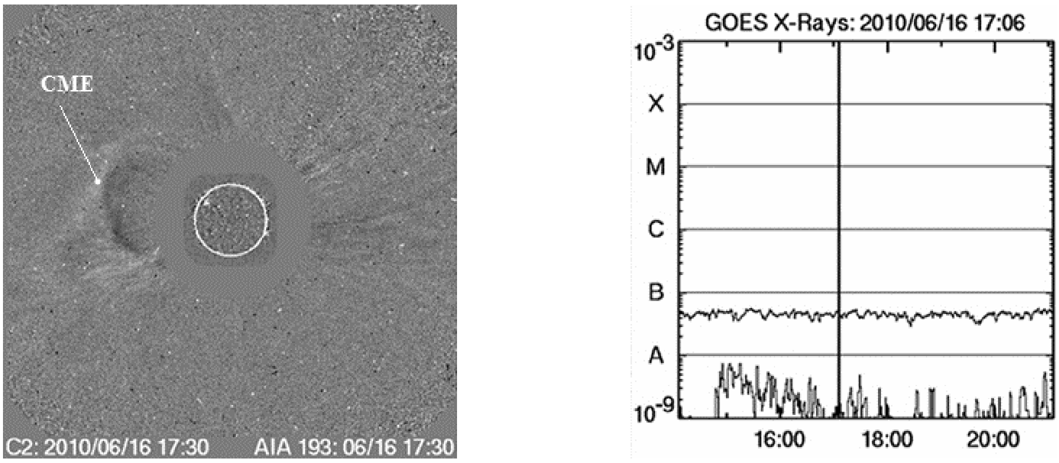

a) b)

Fig. 1. a) – Stealth CME at 16 June 2010 within the LASCO C2 FOV; b) – absence of X-ray flare.

To detect the CME source site, we split the visible surface of the Sun into 200"×200" segments, and highlighted the segment that appeared to be the source of a dramatic short-time emission increase in several EUV channels (94, 131, 171, 193, 211, 304, 335Å) over the interval close to the CME formation onset (see Fig. 2a).

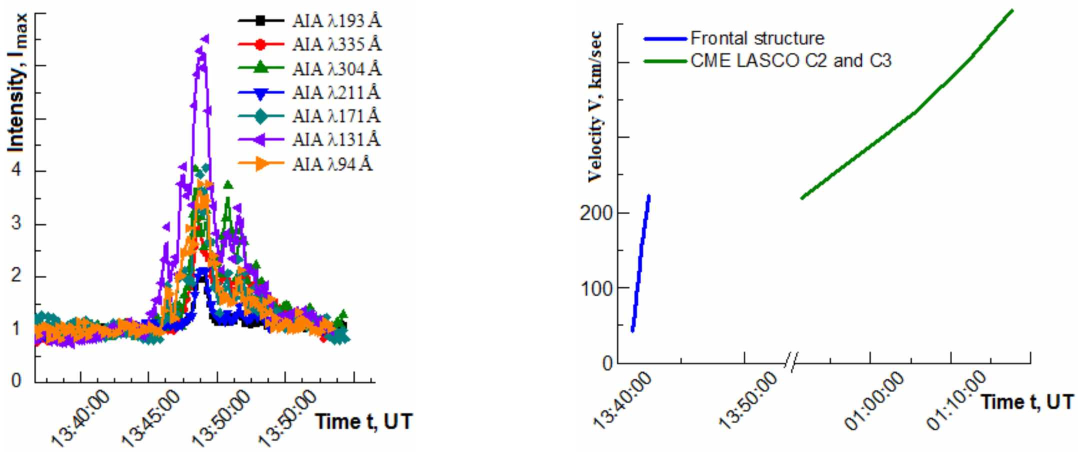

a) b)

Fig. 2. a) - time dependences of the relations of the emission intensity in the investigated region I_a to the intensity I_q in the adjacent quiet region; b) – CME FS velocity profiles.

Fig. 2a shows the time dependences $I_n=I_a/I_q$ that are the relations of the emission intensity in the investigated region I_a to the intensity I_q in the adjacent quiet region. The intensities were obtained in different spectral channels. The most powerful emission was observed in 131 Å, and the weakest emission intensity was in 211 Å. This emission sources are small-size (<20"×20") sites on the solar disk (light spots, "points").

Note that the emission intensity increase in the UV channels started after the CME frontal structure (FS) formation. Fig. 2b shows the CME FS velocity profiles from the 193 Å images (dark blue line) and within the LASCO C2 and C3 FOVs (green line). From the two time dependences of the CME velocity, one may conclude that, between ≈13:43 UT and 14:54 UT, the velocity reaches its maximum, then decreases, and increases again within the LASCO C2 and C3 FOVs.

Fig. 3 presents the 193 Å difference images of the Sun site at different instants with a spot of strong radiation left of the light arc. Presumably, the light arc is the CME forming FS.

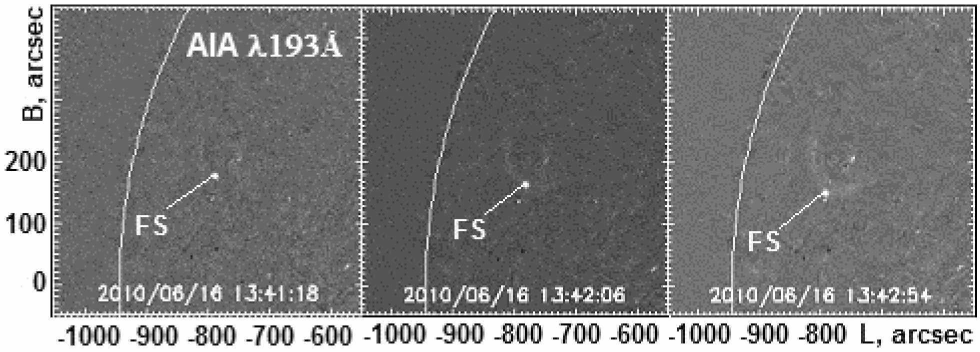

Fig. 3. AIA 193 Å difference solar images.

Except the short-time increase in the EUV emission intensity, the CME formation was accompanied by motion of small-scale loops (ropes), Fig. 4. This figure shows the solar disk site involving the CME formation region, from observations in the 193 Å channel, with a highlighted loop-like structure. In this case, the structure motion started before the CME FS formation. Most likely, this rope served as a trigger of the CME FS formation.

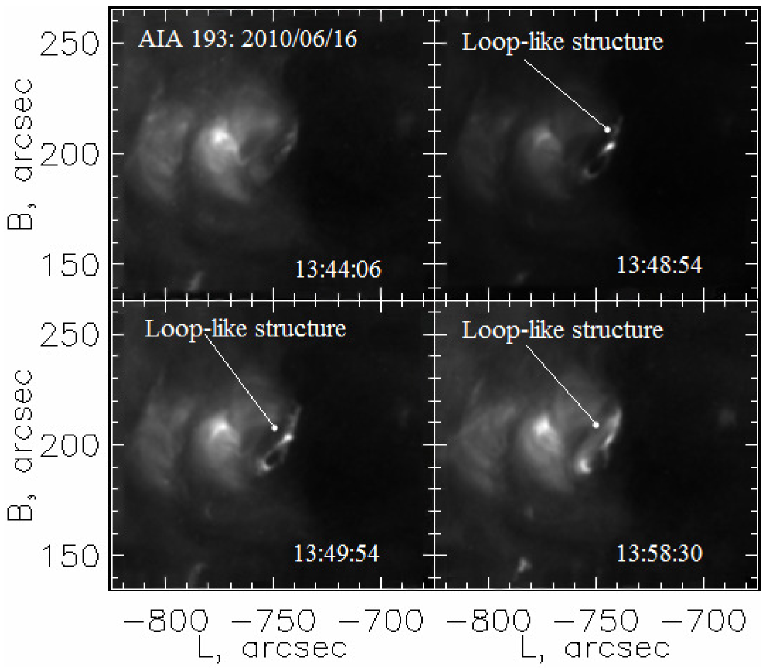

Fig. 4. Solar disk site involving the CME formation region, with a highlighted loop-like structure.

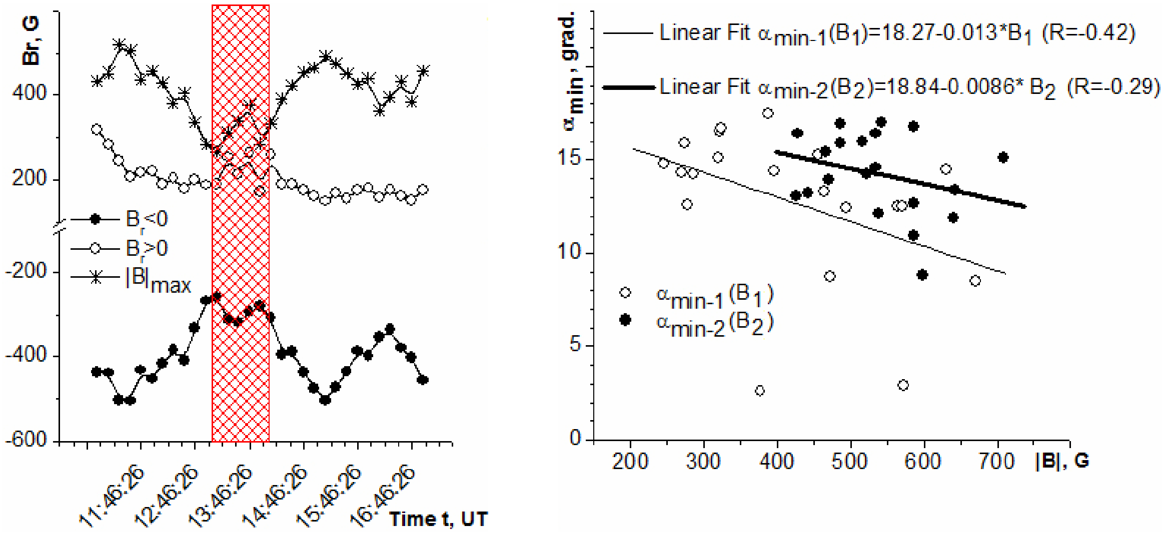

a) b)

Fig. 5. a) - time dependences of the maximal module positive and negative values for the magnetic field radial component Br; b) – correlation between α_{min} and |B| measured at several hours before and after the eruptive event onset. R is the correlation coefficient.

We also studied the magnetic field behavior in the CME FS assumed formation region. Fig. 5(a) shows the time dependences of the maximal module positive and negative values for the magnetic field radial component Br (+max(|B_r>0|) and (-max(|B_r<0|), as well as max(|B_r|) in the CME generation region (~100”×100” square). The vertical red strip highlights the time interval, when the module B_r decrease stops, and its short-time increase by several tens of G starts. This time interval includes the FS formation period and the period of intense emission in the EUV channels. Thus, the CME formation is accompanied by a noticeable variation in the character of the magnetic field behavior in the CME assumed source region.

On the magnetograms corrected for the π-uncertainty of the field transverse component, the region of the assumed eruption includes several hills of the magnetic field, a part of which coincides with small-scale sources of short-time emission pulses within the EUV range. The above hills are not sunspots or pores. In each such hill, we determined maximal values for the magnetic induction modulus |B| and the minimum angle α_{min} between the field lines and the positive normal to the Sun surface, both time-dependant. Fig. 5(b) shows (by example of two hills) a negative correlation between α_{min} and |B| measured at different instants: several hours before and after the eruptive event onset. Note that similar dependences were obtained for the same magnetic field characteristics determined in umbrae of leading and closing sunspots [*Zagainova Iu.S., et al., 2017*].

b) Geomagnetic activity as response to Stealth CME approach

Taking to account the speed of considered CME it was supposed the CME could reached the Earth’s orbit on 21-22 June. Fig. 6 shows the Interplanetary Magnetic Field (IMF) components (magnitude B and Bz component), parameters of the Solar Wind (SW) such as speed, the proton density, the proton temperature of the solar wind, and the indices of geomagnetic activity (AL and Sym/H, which is minute analog of Dst) in 21 June 2010.

Analysis of the data of the Interplanetary Magnetic Field (IMF) and the solar wind (SW) showed that the interplanetary shock (Si) attached the magnetosphere at ~03 UT on 21 June 2010 when the weak jumps of the solar wind proton density (~2 1/cm^3) and velocity (from 380 up to 420 km/s), and changing of the IMF Bz from negative value to positive one were fixed. Magnetic Cloud (MC) reached the Earth’s surface near 06 UT (http://www.srl.caltech.edu/ACE/ASC/DATA/level3/icmetable2.htm). Here one can observe the jump of the SW proton density (from 5 up to 9 1/cm^3) and the SW proton temperature drop under increasing IMF |B| and low-speed SW flow.

We can note that after Si approach, the IMF Bz weakly varied near zero. There was no a conditions for a magnetic storm development, Dst index remained very small. But short period (05-06 UT), when B_z was stale negative, caused development of the weak auroral activity, which was reflected in the AL index. The substorm (till -250 nT) was resisted in the night side of the magnetosphere at Fort Churchill station (it is not seen here). But any increasing of geomagnetic activity was not observed after 09 UT due to the fact that Bz became positive and did not change its sign during long time period.

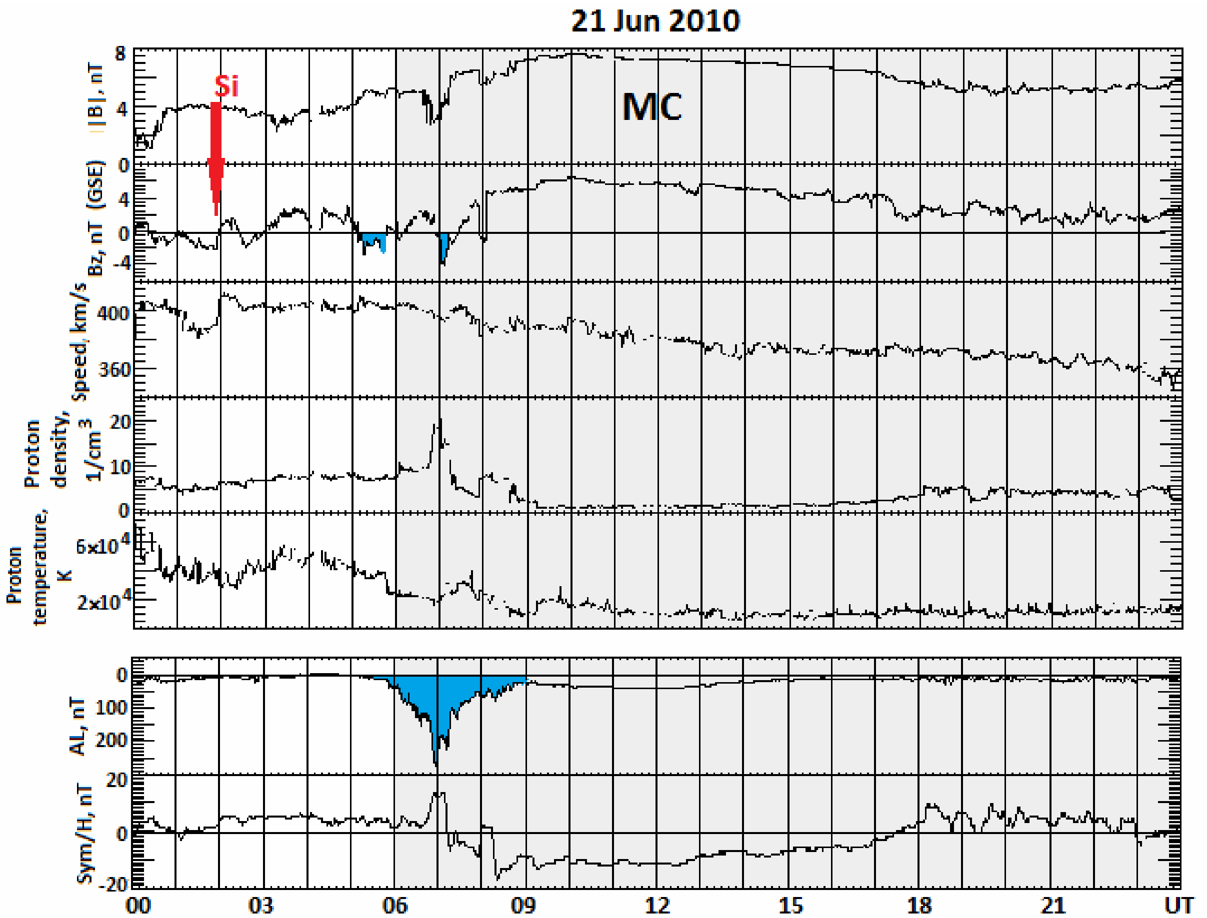

*Fig. 6. Variation of IMF B and Bz components, the velocity, proton density, and temperature of the solar wind, the geomagnetic indices of substorm activity AL and the magnetic storm intensity Sym/H (Dst) in 21 Jun 2010. Red arrow indicates the moment of Si approach. MC area is marked by grey. The data sets of the high resolution OMNI database (*http://omniweb.gsfc.nasa.gov*).*

Conclusions

1. We found that the stealth-CME recorded on 16 June 2010 within the LASCO FOV was accompanied by various manifestations of short-time small-scale activities in the site of the CME assumed formation. Those activities involved emission intensity increases in different EUV channel, motion of small-scale loops (loop-like structure), and formation of the CME frontal structure.
2. We revealed the features of the magnetic field dynamics in the CME formation site: before the eruptive event onset, the field radial component modulus of each sign decreased, and increased after the event end.
3. We showed that, in the magnetic field hills within the eruptive event region, there is an inverse correlation between αmin (angle between the magnetic field lines and the positive normal to the Sun surface) and the magnetic field maximal value (|B|max). Here, the αmin and |B|max values were measured at different instants: several hours before and after the eruptive event onset.
4. We drew a conclusion that the addressed CME forcing on the Earth magnetosphere did not lead to a noticeable geomagnetic field disturbance described by the Dst-index. At the same time, the transition of the stealth-CME front close to the Earth was accompanied by weak substorms. It is assumed that the stealth CME in the Earth orbit has an MC structure.

Acknowledgment

The authors thank the SOHO/LASCO, SDO/AIA, SDO/HMI, GOES teams for a possibility to freely use the data from those instruments. The study was done with budgetary funding of Basic Research program II.16.

References

Alzate N., H. Morgan (2017). Identification of Low Coronal Sources of “Stealth” Coronal Mass Ejections Using New Image Processing Techniques. The Astrophysical Journal, 840:103, 1–14.

D'Huys E., D.B. Seation, S. Poedts, D. Berghmans (2014). Observational characteristics of coronal mass ejections without low-coronal signatures. The Astrophysical Journal, 795:49, 1–12.

Heber B., Wallmann C., Galsdorf D., Herbst K., Kühl K., Dumbovic M., Vršnak B., Veronig A., Temmer M., Möstl, Davilla S. (2015). Forbush decreases associated to Stealth coronal mass ejections. Cent. Eur. Astrophys. Bull., 39, no. 1, 75–82.

Howard T.A., R.A. Harrison (2013). Stealth Coronal Mass Ejections: A Perspective. Solar Physics, 285, 269-280.

Nieves-Chinchilla T., A. Vourlidas, G. Stenborg, N. P. Savani, A. Koval, A. Szabo, L. K. Jian (2013). Inner hemispheric evolution of a "Stealth" CME derived multi-view imaging and multipoint in situ observations. I. Propagation to 1 AU. The Astrophysical Journal, 779:55, 1-13.

Zagainova Yu. S., V. G. Fainshtein, G. V. Rudenko, V. N. Obridko (2017). Comparison of the Magnetic Properties of Leading and Following Spots and the Overlying Ultraviolet Emission Astronomy Reports, 2017, Vol. 61, No. 6, pp. 533–549.

Proceedings of
Tenth Workshop "Solar Influences on the Magnetosphere, Ionosphere and Atmosphere"
Primorsko, Bulgaria, June 4÷8, 2018

Filament Eruptions Associated with Flares, Coronal Mass Ejections and Solar Energetic Particle Events

K. Koleva[1], *P. Duchlev*[1], *M. Dechev*[1], *R. Miteva*[2], *K. Kozarev*[1], *A. Veronig*[3], *M. Temmer*[3]

[1] Institute of Astronomy and National Astronomical Observatory, Bulgarian Academy of Sciences, Bulgaria
[2] Space Research and Technology Institute, BAS, Bulgaria
[3] Institute of Physics/IGAM of the University of Graz,Austria
E-mail: koleva@astro.bas.bg

Abstract

We present analysis of three cases of filament eruptions (FEs) that occurred on 04 Aug 2011, 09 Nov 2011 and 05 Apr 2012 and their associations with flares as sources of solar energetic particles (SEPs) and coronal mass ejections. The associated FEs and SEP-related solar flares were selected by simultaneous observations in X-ray, EUV and radio wavelengths.

Introduction

The aim of this work is to investigate the various pre- and eruptive signatures that were observed during three complex events, including filament eruptions (FEs), solar energetic particles (SEPs) related solar flares, coronal waves (CWs) and coronal mass ejections (CMEs). We focus on the filament helical morphology and kinematic evolution (heights, velocities, accelerations) in order to determine their eruption mechanisms and the rate of their connections with the associated flares, CMEs and SEPs, as well.

Data

We used data from AIA/SDO (*Lemen, et al.* 2012) in He II 304 Å channel to study the eruptions kinematics.

The analyzed events were observed in hard X-ray (HXR), extreme ultraviolet (EUV) and radio wavelengths, and had associated SEP fluxes observed at 1 AU.

We used data from RHESSI (Lin et al. 2002) to trace the flare properties in HXRs.

High-energy particles related to the studied events are analyzed in different energy channels using proton data from SoHO/ERNE instrument (Torsti et al. 1995) and electron data from ACE/EPAM DE (Gold et al. 1998).

In order to search for a possible association with CMEs, data from SoHO/LASCO CME catalog (https://cdaw.gsfc.nasa.gov/CME_list/) and STEREO (Wuelser et al. 2004) were also used.

Results

a) The event from 4 Aug 2011:

The filament eruption was observed on 4 Aug 2011 close to the AR 11261 with heliographic coordinates N16W51. The eruption started at about 03:30 UT in the AIA field-of-view (FOV) and lasted about 5h. It was an asymmetric full type eruption with well pronounced twist. Its evolution is shown in base-difference images in Figure 1 (a).

The eruption clearly showed two evolution phases: The initial phase lasted about 44 min. During this phase the velocity rose from 10.4 km/s to 49.4 km/s with a constant acceleration of 23.2 m/s2. During the second phase the filament rose with a constant velocity of about v = 65.1 km/s. The height-time profile of prominence evolution and eruption velocities and acceleration are shown in Figure 1 (b).

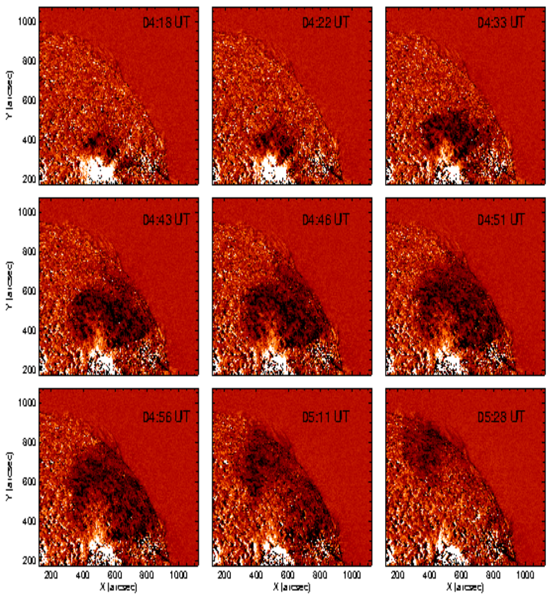

a)

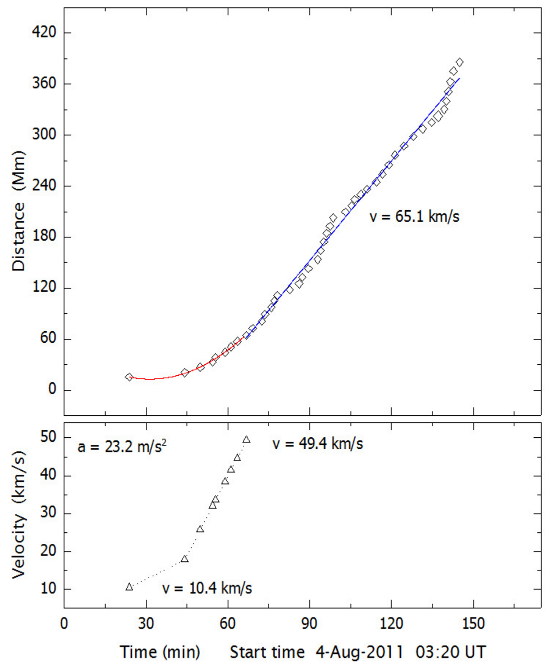

b)

Fig. 1 Base-difference images in 304 Å AIA/SDO channel, showing the evolution of FE from 2011 Aug 4 (a); Height-time profile (top) and eruption velocities and an acceleration (bottom) (b)

The eruption was followed by a M9.3 GOES class SEP-related solar flare. The flare started at 03:41 UT, about 11 min after the eruption onset. In Figure 2 (plot made using http://server.sepserver.eu/) the proton and electron intensities from SoHO/ERNE and ACE/EPAM DE are presented, respectively.

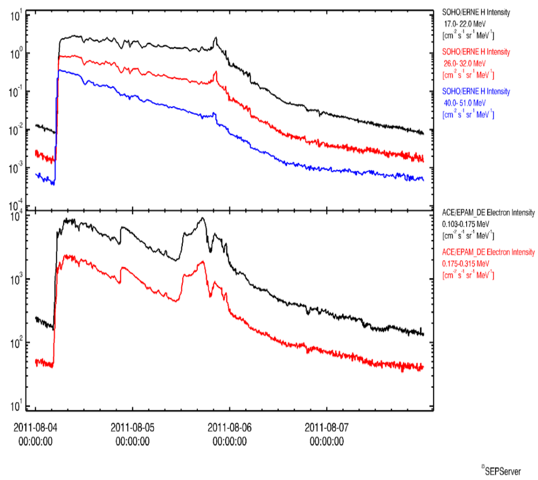

Fig. 2 Proton (top panel) and electron (bottom panel) intensities, obtained from SoHO/ERNE and ACE/EPAM DE, respectively, in different energy channels for the event on 04 Aug 2011.

In Figure 3 as an example of SEP event on 04 Aug 2011 are shown the proton intensities in three GOES energy channels (>10, >50, and >100 MeV), the CME height-time plot and the soft X-ray flare light curves in two energy channels. The flare phase is indicated with dashed lines.

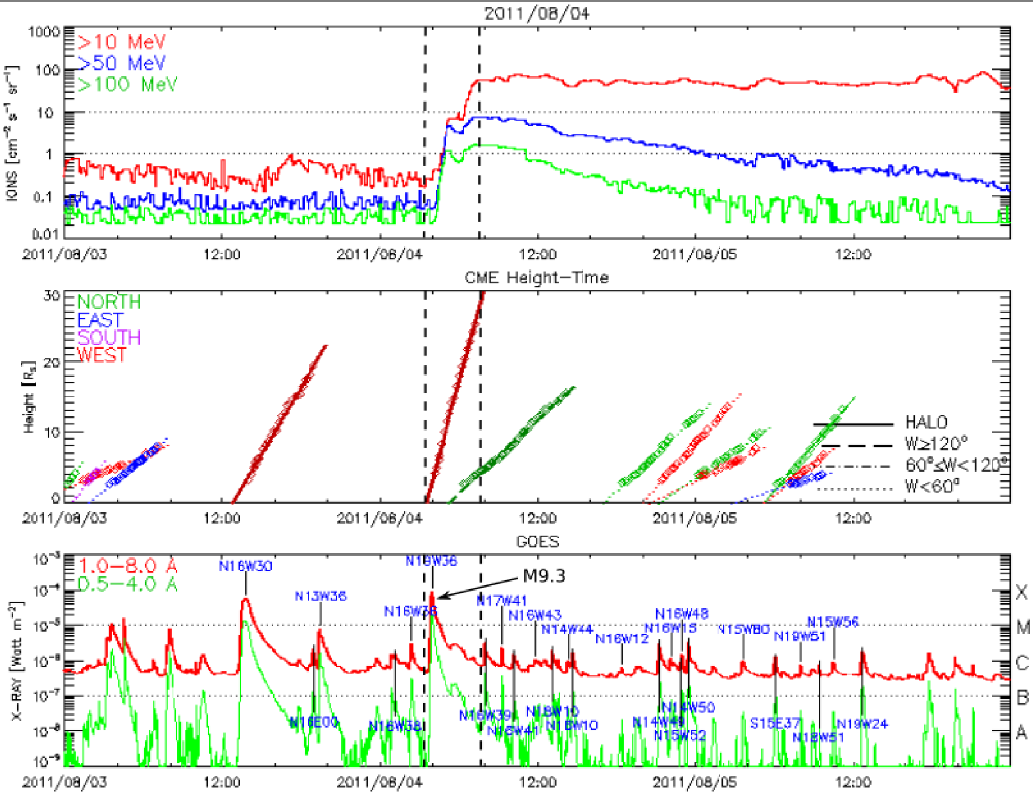

Fig. 3 The time variation of SEP intensity in three energy channels (first panel); the CME height-time plot (second panel); and the soft X-ray flare light curves in two energy channels (third panel). The vertical dashed lines outline the flare phase.

The event was associated with a fast halo CME, which first appearance in LASCO C2 was at 04:12 UT. The filament material could be traced in the corona in STEREO (A and B) coronagraph C1 FOV more than 3 hours after the eruption onset (Fig. 4).

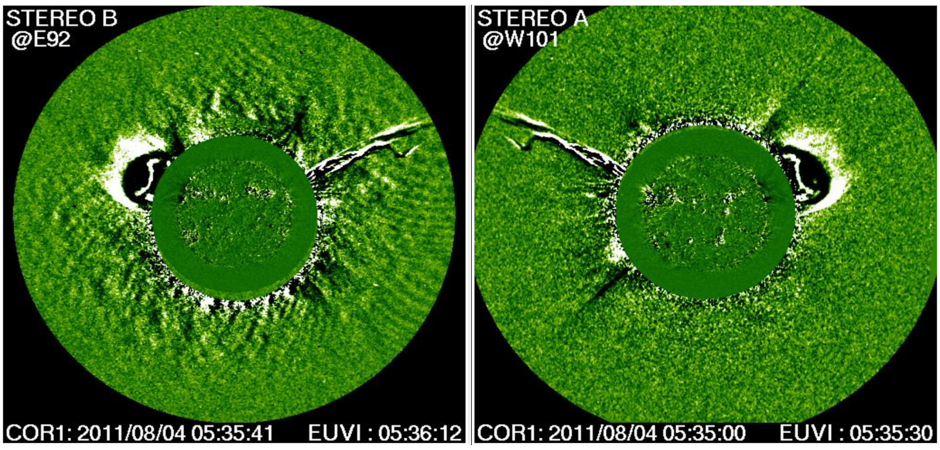

Fig. 4 The CME, associated with 04 Aug 2011 event in STEREO A and B COR1 FOVs.

b) The event from 9 Nov 2011

The filament eruption was observed on 09 Nov 2011 close to the east limb with heliographic coordinates N18E20. The filament was situated along the polarity inversion line (PIL) in AR 11342 with magnetic configuration of type βγδ/βγδ. In this event two consecutive eruptions was observed, here named FE1 and FE2. The eruptions were linked to a two ribbon solar flare of M1.1 GOES class, which start and peak time was at 13:04 UT and 13:35 UT, respectively.

The FE1 started about 30 min before the flare peak at 12:05 UT. The eruption showed two phases: initial phase with velocities from 0.4 km/s to 154 km/s at increasing acceleration from 0.5 m/s^2 to 820 m/s^2 and second phase with velocity of 166.8 km/s. The FE2 started at 14:05 UT, 30 min after the flare peak. This eruption had a linear height-time profile and velocity of 131 km/s. The height-time evolution FE1 and FE2 and corresponding velocities and acceleration are shown in Fig. 5a.

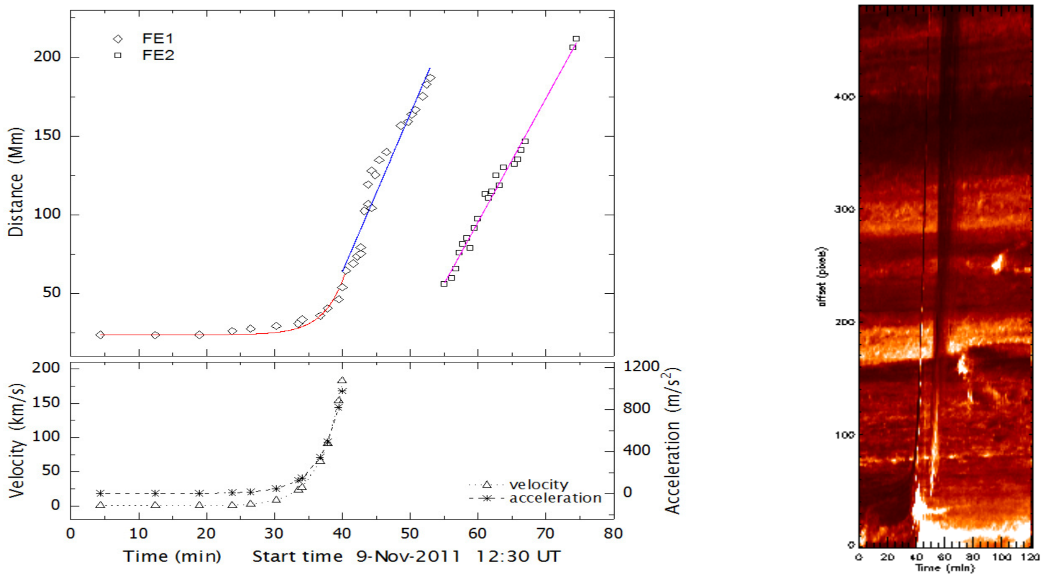

a) b)

Fig. 5. Height-time profile of FE1and FE2 evolution (top) and eruption velocities and acceleration (bottom) (a). Time-slice diagram used for height determination (b).

The event on 9 Nov 2011 was associated with a fast halo CME with a linear speed of 907 km/s, which first appearance in LASCO/C2 was at 13:36 UT (Fig.6).

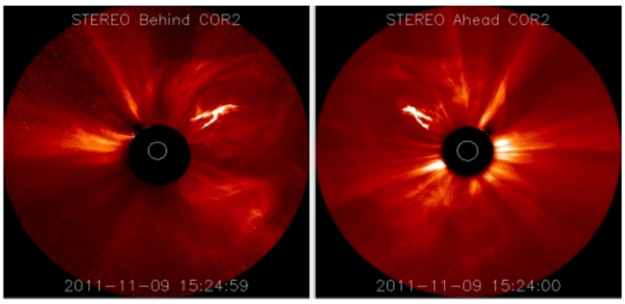

Fig. 6. The CME associated with 9 Nov 2011 event in the STEREO COR2 FOV.

c) The event from 5 Apr 2012

The filament eruption on 5 Apr 2012 was observed close to the AR 11450 (N17W33). The eruption was followed by a two ribbon solar flare of C1.5 GOES class, which started at 20:49 UT. The filament eruption began at 21:10 UT and lasted about 2h. This time coincides with the time of flare peak intensity. No apparent filament twist was observed during the eruption.

During the FE the velocity increased from 20 km/s to 224 km/s and then decreased in the final stage to 214 km/s. Acceleration changed from 330 m/s^2 to 19.6 m/s^2, then it became negative, which suggest plasma returning during the final stage.

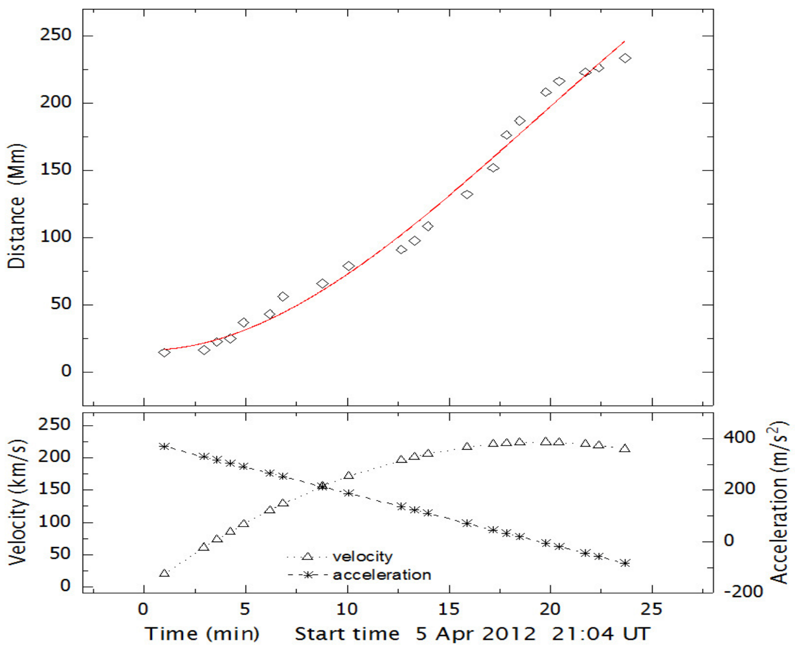

Fig. 7. Height-time profile for the event of 5 Apr 2012 (top) and relevant velocities and acceleration (bottom).

This eruption was also associated with a halo CME with linear speed of 828 km/s, whose first C2 appearance was at 21:25 UT. The prominence material was well visible as the CME bright core and could be traced in the STEREO A/COR1 FOV up to 21:55 UT.

Summary

Time lines for solar activity involved in each of the studied events are presented in Fig. 8. The duration of activities from the onset to the end are indicated by solid lines: flares - orange, filament eruption (FEs) - dark blue, coronal waves (CWs) - green, CMEs - purple (in LASCO C2 FOV), hard X-ray - violet and electron and proton intensities enhancement - light blue and cyan. The peak's times of the GOES SXR flux are also indicated with green arrows.

In the event from 4 Aug 2011 the FE preceded the flare start. In this case the reconnection process between the erupting filament and surrounding magnetic field could be regarded as a trigger of the two ribbon solar flare.

During the event from 9 Nov 2011 two consecutive FEs were observed: one before and one after the flare start. This sequence of events may be interpreted as the so-called "sympathetic events" (*Moon et al.* 2002; *Wang et al.* 2007; *Joshi et al.* 2016), i.e. successive eruptions and flares occurring within a short time interval and physically linked.

In the event on 5 Apr 2012 the flare start was followed by FE, which started at the time of flare intensity peak. In this event filament destabilization was probably due to magnetic filed reconstruction during the solar flare.

Acknowledgment

This research is co-funded by a bilateral collaborative project NTS/AUSTRIA 01/23, 28.02.17, under agreement between Bulgaria's National Science Fund and Austria's OeAD-GmbH.

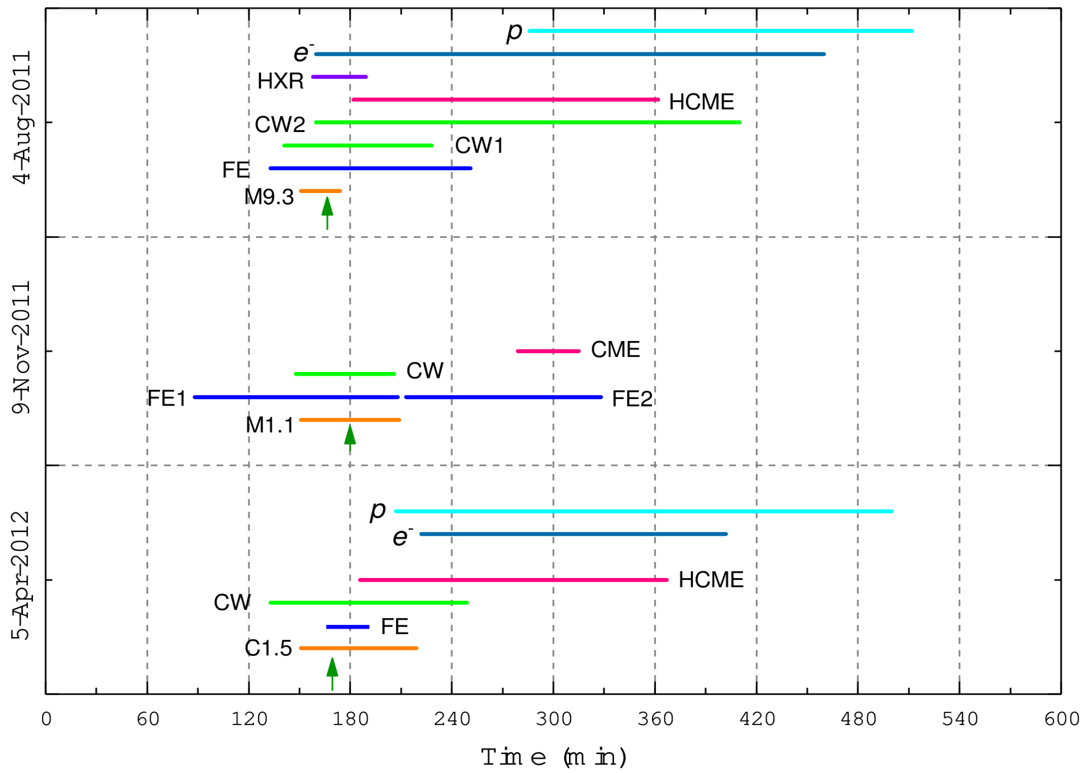

Fig. 8. Time lines for solar activities involved in each of 3 events. The time of 150 minutes before the flares onset is selected as a start point.

References

Gold, R. E.; Krimigis, S. M.; Hawkins, S. E., III; Haggerty, D. K.; Lohr, D. A.; Fiore, E.; Armstrong, T. P.; Holland, G.; Lanzerotti, L. J., (1998) Electron, Proton, and Alpha Monitor on the Advanced Composition Explorer spacecraft, Space Science Reviews, v. 86, Issue 1/4, p. 541-562

Joshi, N., Schmieder, B., Magara,T., Guo,Y.ang & Aulanier,G.2016, ApJ, 820, 126

Lemen, J. R., Title, A. M., Akin, D. J., et al. 2012, Sol. Phys., 275,17

Lin, R. P.; Dennis, B. R.; Hurford, G. J.; Smith, D. M.; Zehnder, A.; Harvey, P. R. et al. (2002) The Reuven Ramaty High-Energy Solar Spectroscopic Imager (RHESSI), Solar Physics, v. 210, Issue 1, pp. 3-32

Moon, Y.-J., Choe, G. S., Park, Y. D., Wang, H., Gallagher, P. T., Chae, J., Yun, H. S., & Goode, P. R. 2002, ApJ, 574, 434

Torsti, J., E. Valtonen, M. Lumme, P. Peltonen, T. Eronen, M. Louhola, E. Riihonen,G. Schultz, M. Teittinen, K. Ahola, C. Holmlund, V. Kelhä, K. Leppälä, P. Ruuska, E. Strömmer (1995) Energetic Particle Experiment ERNE, Solar Physics, Volume 162, Issue 1-2, pp. 505–531

Wang, H., Liu, C., Jing, J., & Yurchyshyn, V. 2007, ApJ, 671, 973

Wuelser, J., Lemen, J. R., Tarbell, T. D., et al. 2004, in SPIE Conf. 5171, ed.S. Fineschi, & M. A. Gummin, 111

Large-scale and small-scale structure of interacting solar wind streams

A.T. Lukashenko [1], *D.G. Rodkin* [2], *K.B. Kaportseva* [3], *Yu.S. Shugay* [1],
I.S. Veselovsky [1,4], *V.A. Slemzin* [2]

[1] SINP MSU, Moscow, Russia
[2] Lebedev Physical Institute of RAS, Moscow, Russia
[3] Faculty of Physics, MSU, Moscow, Russia
[4] Space Research Institute of RAS, Moscow, Russia
E-mail: a_lu@mail.ru

Abstract.

A classification of solar wind streams according to the main hydrodynamic parameters -- a combination of the velocity (fast or slow), temperature (hot or cold) and density (dense or rarefied) of protons -- is considered. According to this approach, we specify eight types of the solar wind: fast-hot-dense (FHD), fast-hot-rarefied (FHR), fast-cold-dense (FCD), etc. As an additional parameter, the proton plasma β is taken into account for description of the magnetic state of solar wind streams (high-, mid-, low-magnetized subtypes). The listed types of streams occur with different frequencies depending on the phases of solar activity cycles. This classification is compared with the classical division of solar wind streams into high-speed streams (HSSs) from coronal holes, coronal mass ejections (CMEs) and slow solar wind from the streamer belt. The comparison is carried out for the events in August 2010 and May 2011 when CME–CME and CME–HSS interactions, respectively, were observed. In both cases there was the rare FCD-type of the wind. We concluded that the classical description of the large-scale structure of solar wind (hours and days), in particular, consideration of the solar wind ion composition, makes it possible to determine the nature and source of solar wind streams, whereas consideration of the hydrodynamic parameters including β is useful for a detailed description of the small-scale structure (minutes) of complex regions appeared in the cases of interaction of several streams in the heliosphere.

Introduction

The most common classification of solar wind streams is their division into quasistationary high-speed streams (HSS), sporadic flows associated with coronal mass ejections (CMEs) and slow wind ([*Parker E.N.*, 1963], [*Richardson I.G. et al.*, 2012], [*Feldman U. et al.*, 2005]). In [*Xu F. & Borovsky J.E.*, 2015], a classification was proposed with dividing of the solar wind plasma into 4 categories, based on coronal sources: coronal-hole-origin plasma, streamer-belt-origin plasma, sector-reversal-region plasma and transient events (such as CMEs). The division was made on the basis of quantitative criteria for three parameters: entropy of protons, their Alfvén velocity, and their temperature relative to the expected from the wind speed.

These solar wind streams are large-scale structures in time and space. HSSs last from several days to several weeks and have the velocity from about 450 to 800 km/s, CMEs last from several hours to 1–2 days with a speed from 200 to 2000 km/s. Flows of slow wind have the velocity in order of or less than 400 km/s ([*Feldman U. et al.*, 2005], [*Cane H.V. & Richardson I.G.*, 2003]). The spatial scales of these streams are related to the size and shape of their sources on the Sun. HSSs originate from coronal holes, exist at all phases of the solar cycle and cause moderate, but prolonged geomagnetic disturbances. CMEs are the result of spontaneous solar activity and are associated with flare regions or eruptions of prominences. The solar wind flows associated with CMEs manifest themselves in the heliosphere as interplanetary coronal mass ejections (ICMEs). Slow wind streams originate from streamers and sets of non-localized sources in the quiet solar corona.

An important parameter characterizing the sources of solar wind is the ion composition of plasma, given by such parameters as the ratio of the O^{7+}/O^{6+} for oxygen ion densities, C^{6+}/C^{5+} for the carbon, the average iron ion charge $\langle Q_{Fe} \rangle$, and the Fe/O density ratio characterizing the balance of elements with low and high ionization potential (*FIP*-effect). The plasma ion composition of solar wind is created in the solar corona under the conditions of the collision balance between ionization and recombination processes, and it "freezes" in the low corona (R ~ 2–5 R_{sun}), where rates of collision transitions become negligibly small ([*Feldman U. et al.*, 2005], [*Hundhausen A.J. et al.*, 1968]), and remains unchanged in the heliosphere. Thus, the ion composition is directly related to processes of formation of wind streams in the sources and is an important parameter of their large-scale description. The ion composition helps to consider complex cases of interaction of different flows which in solar activity maxima can be up to 50% [*Rodkin et al.*, 2018].

Solar wind streams also show a small-scale structure with characteristic times in the intervals of few minutes in the velocity, density and temperature of protons, and also in the modulus and direction of the components of the interplanetary magnetic field. This structure is created by the turbulence in solar wind, the presence of discrete jets, and the interaction of solar wind flows from various coronal sources ([*Mullan D.J.*, 1990], [*Tu C.-Y. & Marsch E.*, 1995], [*Šafránková J. et al.*, 2013]).

The interaction of solar wind streams can change their kinetic and magnetic parameters, which leads to an increase or decrease in the forecasted geomagnetic disturbance (see, for example, [*Rouillard et al.*, 2010] and [*Liu Y.D. et al.*, 2014]).

In this paper, we compare the classical description of the large-scale structure of solar wind streams, in the intervals of hours and days, and the small-scale structure of the hydrodynamic wind types and MHD subtypes, in the intervals of a few minutes. On examples of two events of the 24th solar cycle in August 2010 and May 2011, the features of the structure of solar wind associated with the sources of flows and interaction in the heliosphere were analyzed.

Data

As initial data, we used the ACE satellite database, that available at http://www.srl.caltech.edu/ACE/ASC/, and the OMNIWeb database, at https://omniweb.gsfc.nasa.gov. We took 1-minute averaged values of proton speed, density, temperature and module of magnetic field from the OMNI database for the 23rd (May 1996–December 2008) and the current 24th (January 2009–April 2018) solar cycles. It should be noted that this OMNI database represent averaged data from the *Geotail*, *IMP-8*, *ACE*, *Wind* spacecrafts obtained with regard to time shifts due to the difference in their positions. We used 1-hour values of ion composition (O^{7+}/O^{6+} and $\langle Q_{Fe} \rangle$) from the *ACE* database for the events on 3–5 August 2010 and 27–30 May 2011.

Results

a) MHD classification of solar wind

When considering the small-scale properties of solar wind streams, a scheme was used that consisted of the following elements of the quantitative classification of solar wind near the Earth's orbit with orientation to typical values of velocity V (fast-slow), temperature T (hot-cold) and density n (dense-rarefied) of protons. Earlier in [*Dmitriev A.V. et al.*, 2009] 1-hour data from the OMNIWeb database for the 20th–23rd solar cycles were analyzed. The mean, median and most probable values for V, T, and n were obtained, as well as for the plasma parameter $\beta = (8\pi n\ k_B\ T)/B^2$ for protons, where B is the magnetic field and k_B is the Boltzmann constant (see Table 1).

Table 1. The mean, median and most probable (mode) values of V, T, n, and the plasma parameter β for 1964–2007 according to [Dmitriev A.V. et al., 2009]

Value	V, km/s	T, K	n, cm^{-3}	β
Mean	430	$8.3\cdot10^4$	5.4	0.43
Median	420	$8.5\cdot10^4$	5.3	0.48
Mode	370~390	$7.2\text{\textasciitilde}9.4\cdot10^4$	4.3~5.3	0.44~0.65

Because for the some applications it is more convenient to use a classification based on rounded and fixed numerical values, we considered that the wind is fast if $V > 450$ km/s, and slow, if $V < 400$ km/s; hot, if $T > 10^5$ K, and cold, if $T < 7.5\cdot10^4$ K; dense if $n > 6$ cm^{-3}, and rarefied, if $n < 5$ cm^{-3}. If at least one parameter is within its interval of exclusion, then the wind was considered to refer to the so-called "zero" or indeterminate type. The mean and median values from Table 1 are within these intervals of exclusion. The list of the solar wind types, their abundance and possible sources are given in Table 2.

Table 2. Hydrodynamic types of solar wind streams (May 1996–April 2018)

Type	Abbre-viation	Abun-dance, %	Possible sources of different types
fast-hot-dense	FHD	3.94	CMEs after strong flares [*Gosling*, 1996], shock waves, compressive regions in CIR
fast-hot-rarefied	FHR	19.08	High-speed streams from coronal holes [*Mursula et al.*, 2002]
fast-cold-dense	FCD	1.04	Some CMEs (maybe prominences [*Yao et al.*, 2010]), interaction streams
fast-cold-rarefied	FCR	4.58	Tails of the high-speed streams from the coronal holes [*Usmanov et al.*, 2005]
slow-hot-dense	SHD	1.53	Occasionally occurs in flows from the streamer belt
slow-hot-rarefied	SHR	0.89	Sources for this type are not yet determinate. We suppose, that this type can occur in expanding hot remnants of eruptive plasma clouds
slow-cold-dense	SCD	21.92	Flows from the streamer belt, sector reversal regions [*Sanchez-Diaz et al.*, 2016]
slow-cold-rarefied	SCR	11.88	Flows from the streamer belt
indeterminate type	--	35.13	Sources may be identified only in some cases

It should be noted that the wind parameterization used by us was obtained on the basis of typical (mean and median) parameter values for 20–23 activity cycles, known from the literature. In the future, it is proposed to determine the change in the frequency of MHD-types depending on typical values at the different levels of solar activity.

The prevalence of types defined as indicated above can vary significantly depending on the phase of the solar activity cycle (Fig. 1). With the decline of in solar activity FHR-type often dominates. In this case, the following alternation of types is typical (see Table 1): FHD (compressive regions in CIR)–FHR–FCR (tail of HSS). Then, through an indeterminate type, a transition is made to the slow wind of SCR and SCD types.

To take into account the magnetization of solar wind streams, we introduce MHD wind subtypes defined as follows:

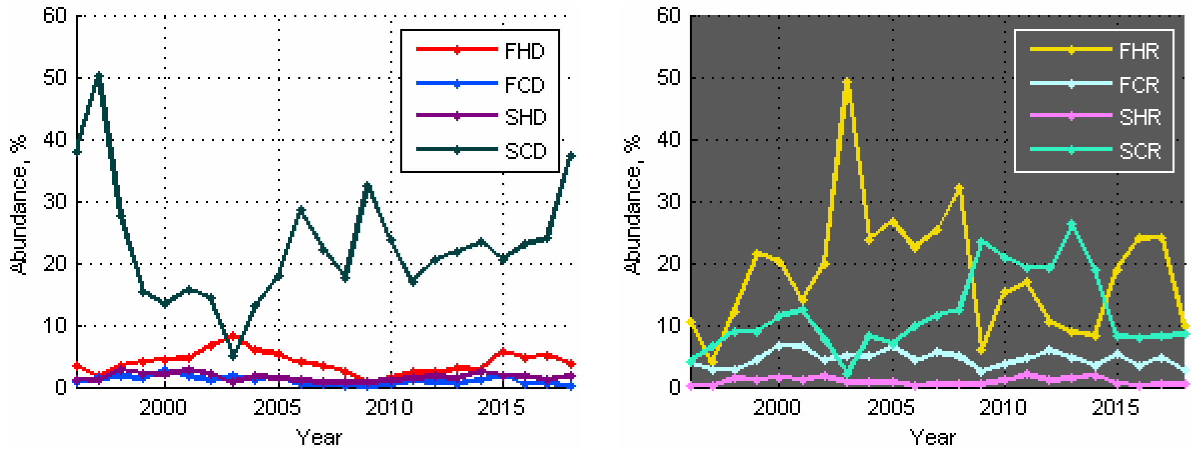

a) b)

Fig. 1. The prevalence of solar wind types during the 23rd and 24th solar cycles: a) – dense types; b) – rarefied types. Colour designations: FHD — red, FHR — yellow, FCD — blue, FCR — cyan, SHD — purple, SHR — pink, SCD — dark-green, SCR — light-green

- high-magnetized: $\beta < 0.5$ (below the rounded mean from the last column in Table 1);
- mid-magnetized: $0.5 < \beta < 1$;
- low-magnetized: $\beta > 1$.

To demonstrate the peculiarities in the solar wind structure, revealed under the “classical” and MHD approaches, there were analyzed two events with streams interaction. In both of these cases the rare FCD-type was observed.

b) Event 3–5.VIII.2010: CME–CME interaction

Event 3–5.VIII.2010 (18 h. 3.VIII.2010–8 h. 5.VIII.2010) is an example of CME–CME interaction. The most probable sources are two CMEs recorded in the coronagraph 1.VIII.2010 in 03.54/04.24 and 08.24/08.54 respectively (according to the SEEDS catalog). The 2nd CME (speed 1100/906 km/s measured by STEREO-A, -B) overtook the 1st (speed 670/528 km/s according to STEREO-A, -B).

There are four parts in the solar wind structure (see Fig. 2*a*):

1. 0–18 h. 3.VIII.2010 — tail of the stream from a coronal hole. It belongs to the indeterminate type, which corresponds in this case to the slow wind;
2. 18 h. 3.VIII.2010–4 h. 4.VIII.2010 — shock wave formed by the arrival of the 1st CME, followed by the compression region (sheath). In this part FHD-type is visible, differing in magnetization (~20, 35 and 30% for FHDh, FHDm and FHDl respectively);
3. 4 h. 4.VIII.2010–8 h. 5.VIII.2010 — region of interaction between the 1st and 2nd CMEs (in the ionic composition the peaks for O^{7+}/O^{6+} and $\langle Q_{Fe} \rangle$ can be distinguished out, the first peak corresponds to the 1st CME, the second one corresponds to the faster 2nd CME). In this part (complex ICME) there is the fast cold magnetized flow with variable density (FCDh (30%), FCRh (35%));
4. 8 h. 5.VIII.2010–0 h. 6.VIII.2010 — unidentified high-speed stream. The largest component is FHRl-wind (25%), as well as FHRm (15%) and FCRh (10%).

c) Event 27–30.V.2011: CME–HSS interaction

Event 27–30.V.2011 (9 h. 27.V.2011 09.00–0 h. 31.V.2011) is an example of the complex structure resulting from CME–HSS interaction. The most probable sources of it are CME and a coronal hole.

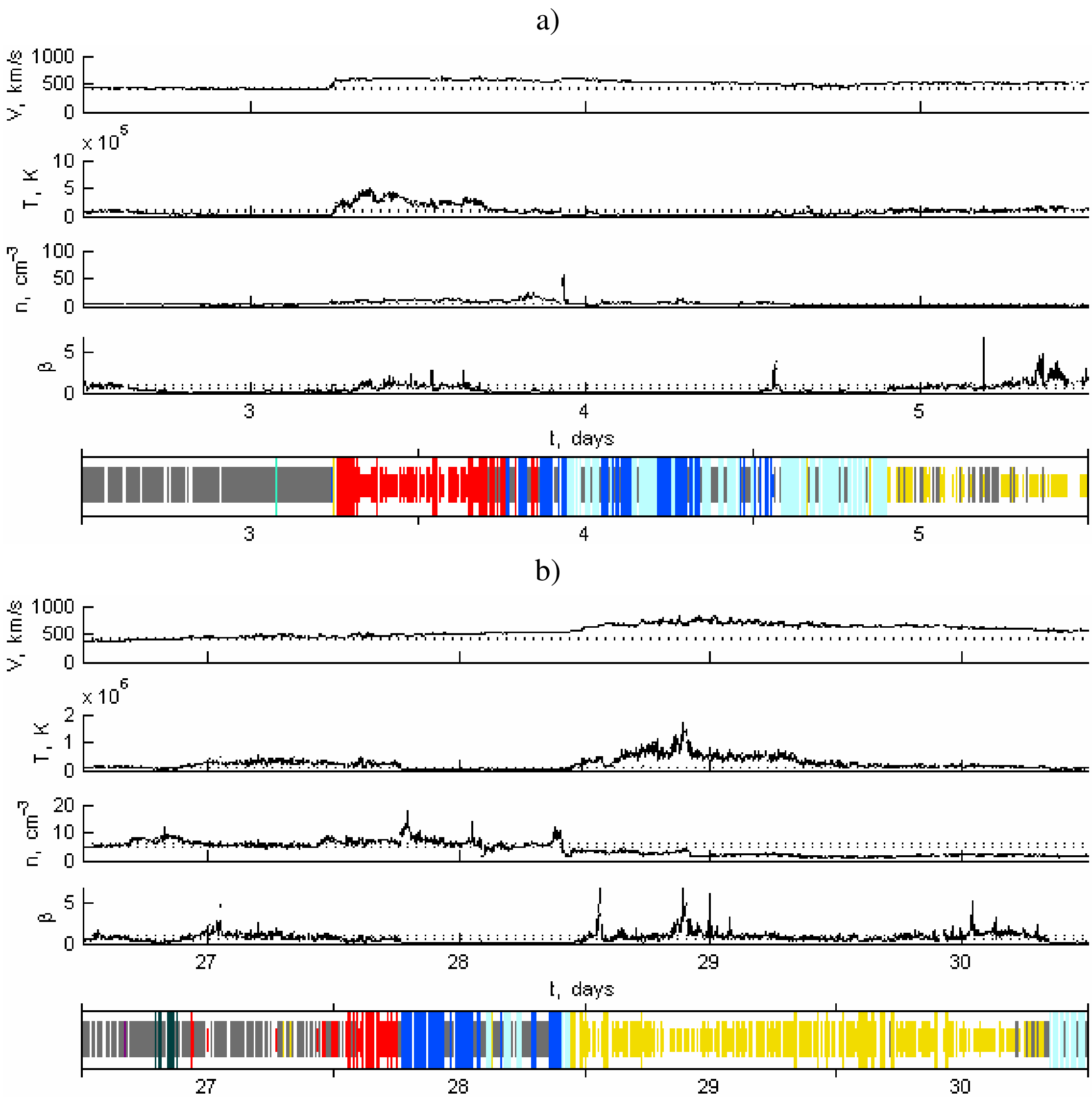

Fig. 2. The alternation of the hydrodynamic types and MHD subtypes of solar wind during the events: a)– 3–5.VIII.2010, b)– 27–30.V.2011. Color designations are the same as in Fig. 1. Wide stripes designate high-magnetized solar wind streams, medium stripes correspond to the mid-magnetized subtypes and indeterminate type, and narrow stripes point to low-magnetized wind. White areas correspond to the gaps in the data.

There are also four regions (Fig. 2*b*):

1. 0–9 h. 27.V.2011 — corresponds to the heliospheric current sheet (sectors of the magnetic field reversed on May 26 at 11 h.). Wind mainly belongs to the indeterminate and SCD types;
2. 9 h. 27.V.2011–6 h. 28.V.2011 — relates to the 1st part of the high-speed stream from the coronal hole that existed on the Sun during 23–25.V.2011. Indeterminate (~50%) and FHD (25%) types predominate;
3. 6 h. 28.V.2011–23 h. 28.V.2011 — corresponds to CME that can be seen in solar wind parameters. There is a pronounced peak for O^{7+}/O^{6+} and $\langle Q_{Fe} \rangle$. The wind is fast, cold and highly magnetized, so FCDh (45%) and FCRh (15%) subtypes are visible;
4. 23 h. 28.V.2011–0 h. 31.V.2011 — the 2nd part of the high-speed stream from the same coronal hole. The arrival of HSS can be seen from the rise in velocity and drop of in ion composition. The main contribution is made by FHR-type (75%, including 10% FHRh, 40% FHRm and 25% FHRl).

Conclusions

1. Two methods of the classification of the solar wind are considered: on the scale of hours and days by plasma-kinetic parameters and on the scale of minutes by MHD parameters. On the examples of events 3–5.VIII.2010 and 27–30.V.2011 it is shown that both concepts complement each other and allow more precise understanding of the solar wind structures that arise during the interaction of flows of the CME–CME and CME–HSS types.
2. The introduced MHD classification is evident and plausible. It visually reflects deviations from some average and typical state of the heliospheric plasma at the Earth’s orbit in both directions for each of the main hydrodynamic parameters and takes into account the plasma parameter β.

References

Cane H.V., Richardson I.G. (2003). Interplanetary coronal mass ejections in the near-Earth solar wind during 1996–2002. J. Geophys. Res.: Space Phys., 108, CiteID 1156.

Dmitriev A.V., Suvorova A.V., Veselovsky I.S. Statistical characteristics of the heliospheric plasma and magnetic field at the Earth's orbit during four solar cycles 20–23. In: Handbook on solar wind: effects, dynamics and interactions. Ed. Johannson H.E. New York: Nova Science Publishers, 2009. P. 81–144.

Gosling J.T. (1996) Corotating and transient solar wind flows in three dimensions. Annu. Rev. Astron. Astrophys, 34, 35–73.

Feldman U., Landi E., Schwadron N.A. (2005) On the sources of fast and slow solar wind. J. Geophys. Res., 110, A07109.

Hundhausen A.J., Gilbert H.E., Bame S.J. (1968). Ionization state of the interplanetary plasma. J. Geophys. Res., 73, no. 17, 5485–5493.

Liu Y.D., Yang Z., Wang R., Luhmann J.G., Richardson J.D., Lugaz N. (2014). Sun-to-Earth characteristics of two coronal mass ejections interacting near 1 AU: Formation of a complex ejecta and generation of a two-step geomagnetic storm. Astrophys. J. Lett., 793, L41.

Mullan D.J. (1990) Sources of the solar wind — What are the smallest-scale structures? Astronomy and Astrophysics, 232, no. 2, 520–535.

Mursula K., Hiltula T., Zieger B. (2002). Streamer belt north-south asymmetry and its long-term evolution. In: Solar variability: from core to outer frontiers. The 10th European Solar Physics Meeting, 9–14 September 2002, Prague, Czech Republic. Ed. Wilson A. ESA SP-506, Vol. 1. Noordwijk: ESA Publications Division.

Parker E.N. Interplanetary dynamical processes. Interscience Publishers, 1963.

Richardson I.G., Cane H.V. (2012). Near-earth solar wind flows and related geomagnetic activity during more than four solar cycles (1963–2011). J. Space Weather Space Clim., 2, A02.

Rodkin D.G., Slemzin V.A., Zhukov A.N., Goryaev F.F., Shugay Yu.S., Veselovsky I.S. (2018). Single ICMEs and complex transient structures in the solar wind in 2010–2011. Solar Phys., 293:78.

Rouillard A.P., Lavraud B., Sheeley N.R., Davies J.A., Burlaga L.F., Savani N.P., Jacquey C., Forsyth R.J. (2010). White light and in situ comparison of a forming merged interaction region. Astrophys. J., 719, 1385–1392.

Šafránková J., Němeček Z., Cagaš P., Přech L., Pavlů J., Zastenker G.N., Riazantseva M.O., Koloskova I.V. (2013). Short-scale variations of the solar wind helium abundance. Astrophys. J., 778, no. 1, article id. 25.

Sanchez-Diaz E., Rouillard A.P., Lavraud B., Segura K., Tao C., Pinto R., Sheeley Jr.N.R., Plotnikov I. The very slow solar wind: Properties, origin and variability (2016). J. Geophys. Res., 121, no. 4, 2830–2841.

Tu C.-Y., Marsch E. (1995). MHD structures, waves and turbulence in the solar wind: Observations and theories. Space Science Reviews, 73, no. 1–2, 1–210.

Usmanov A.V., Goldstein M.L., Ogilvie K.W., Farrell W.M., Lawrence G.R. (2005). Low-density anomalies and sub-Alfvénic solar wind. J. Geophys. Res., 110, A01106.

Xu F., Borovsky J.E. (2015). A new four-plasma categorization scheme for the solar wind. J. Geophys. Res.: Space Phys., 120, no. 1, 70–100.

Yao S., Marsch E., Tu C.-Y., Schwenn R. (2010). Identification of prominence ejecta by the proton distribution function and magnetic fine structure in interplanetary coronal mass ejections in the inner heliosphere. J. Geophys. Res., 115, A05103.

Proceedings of
Tenth Workshop "Solar Influences on the Magnetosphere, Ionosphere and Atmosphere"
Primorsko, Bulgaria, June 4÷8, 2018

Dynamcis and magnetic properties in coronal holes using high-resolution multi-instrument solar observations

K. Krikova [1], *D. Utz* [1,2], *A. Veronig* [1,3], *P. Gömöry* [4], *S. Hofmeister* [1,5], *M. Temmer* [1]

[1] Institute of Physics, University of Graz, Austria
[2] Instituto de Astrofisica de Andalucía, Granada, Spain
[3] Kanzelhöhe Solar Observatory for Solar Environmental Research, Treffen, Austria
[4] Astronomical Institute of the Slovak Academy of Sciences, Tatranská Lomnica, Slovakia
[5] National Space Institute, DTV Space, Denmark
E-mail: K.Krikova@uni-graz.at

Abstract.

Using high-resolution solar observations from the Hinode Instruments SOT/SP, EIS and XRT as well as IRIS from a coronal hole on the 26th of September 2017, we are investigating the dynamics within the coronal hole visible on the specified date. Further satellite data support is given by full disc images from SDO with the AIA and HMI instruments. EIS and IRIS data provide us with crucial information about the plasma and energy flow from the Sun's chromosphere into the corona using the EUV and UV spectra and images. Investigating the magnetic configuration as well as the dynamics and changes within the coronal hole by using the SOT/SP data will give us additional crucial insights about the physical processes leading to the corresponding changes in the higher atmosphere. We compare the Hinode data with AIA and HMI data to get a firm comprehensive picture about the connection from high resolved photospheric fields and its dynamics within the higher layer. Within the timeframe of the analysed EIS dataset two microflare events associated with a solar jet were captured, originating inside the coronal hole under investigation. We believe that it is totally worthwhile to study these features in full detail as not so much attention was paid to high energy processes within coronal holes and their basic relationship to the harboring coronal hole and they show surprisingly high downflows in the Fe XII iron line (up to 140 km/s). In the current proceeding we will outline the state of the art of this investigation and give an overview of the further steps necessary. The mentioned data were obtained during a recent GREGOR campaign with the joint support of IRIS and Hinode (HOP 338).

Introduction

A significant scientific effort has been made in the recent years in the direction of the investigation of the relationship between chromospheric and coronal plasma and energy flows with the magnetic configuration and dynamics seen at the solar surface. Nevertheless, there are still plenty of unanswered questions such as, how the energy is transported in addition to the connection to the dynamics of the magnetic configuration as well as related and triggered consequences for the higher corona. The dataset under investigation, covering a recurrent microflare associated with a solar jet, gives us the opportunity to study the plasma and energy flow as well as the corresponding magnetic field changes, which led to the recurring event. The goal of our work is to obtain information about the energy and plasma flow from the chromosphere and the corona within the given possibilities of our dataset. To do so, we use the different instruments of Hinode, IRIS and SDO (unfortunately we do not have co-temporal and co-spatial GREGOR data for this particular data set of the joint campaign). This proceeding shows the current progress of our work and gives some outlook for further studies.

Data

For our work we used data from three different space missions, namely Hinode, IRIS and SDO. Our data set was recorded on the 26th of September 2017 and covers a region inside a coronal hole with the identifier SPoCA26579. Three different instruments are onboard Hinode: XRT, SOT, and EIS, which were all used in our work. The XRT data were taken from 09:19 UT to 09:49 UT as well as from 11:13 UT to 13:14 UT with a cadence of 1 minute in the filters Al Mesh and Al Poly. SOT/SP data were obtained from 09:04 UT with 3 scans, at 09:52 UT with 6 scans, and at 11:14 UT with 6 scans (the scan cadence amounts to 10 min for all 3 sub-sets). The EIS data is from 09:02 UT to 10:33 UT, and 11:12 UT to 13:00 UT with a cadence of 11 minutes. Our study included 12 spectral lines as listed in Tab. 1. Our IRIS/SJI data is from 11:09 UT taken through three different SJI passbands belonging to the following ions C II, Si IV, Mg II h/k and Mg II wing.

We calibrated our dataset using the preparation routines provided by the different instrument teams. Thus we work with level-1 XRT and EIS data, and level-2 SOT/SP data already post-processed by the MERLIN inversion code. IRIS spectra and images are available as level-2 data. After calibration we co-aligned the Hinode and IRIS data to AIA (193 Å) and HMI data. XRT and EIS data were co-aligned to AIA. For EIS we can identify a bright structure which helps in aligning the data to AIA. SOT/SP and IRIS were co-aligned to HMI data. This allows us to investigate various intensity and spectral data related to magnetic structures as in the case of our microflare. The first microflare can be seen in our EIS dataset starting at 12:20 UT, while the second microflare was scanned at 12:32 UT. Around the same time AIA and HMI data were used to investigate the magnetic configuration, the time evolution of the microflare and the associated solar jet. The exact position of the microflares is outlined in Fig. 1.

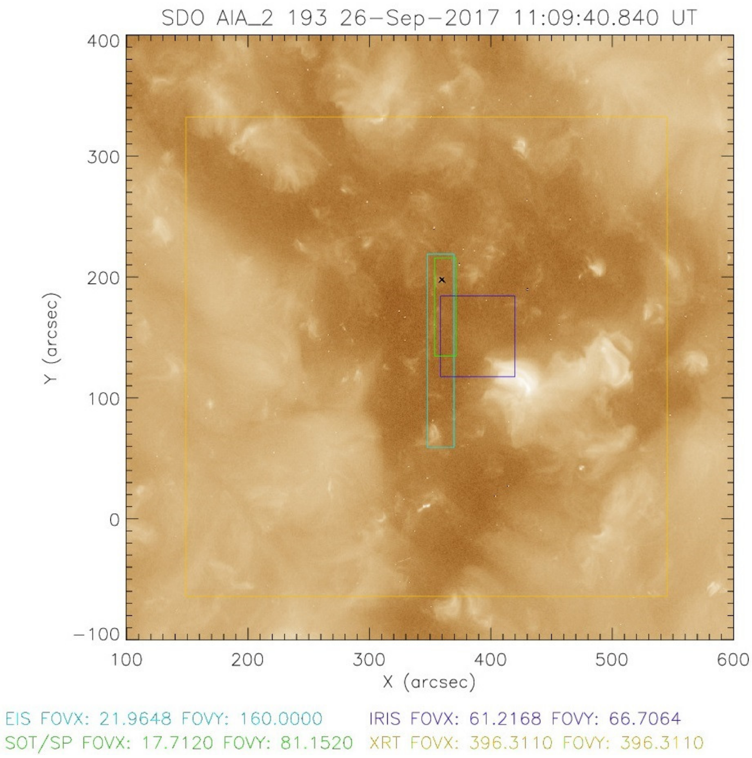

Fig. 1 AIA 193 Å image with over-plotted field of views (FOVs) from the different instruments. Bottom left we see the legend for the different FOV boxes. FOVX and FOVY give the size in x-direction and y-direction in arcsec, respectively. The position of the microflares are marked with a black cross at the top of the EIS FOV.

Results

As a next step of our analysis we used the EIS data to calculate intensities and velocities by fitting Gaussian profiles into the spectra measured by EIS. To achieve a better signal to noise ratio, the EIS data were binned at the microflare region in y-direction over 4 pixels. This procedure results in only one pixel representing the microflare. One important step was to

Table 1. Listed ions used in our study with wavelength and formation temperature

Ion	Wavelength [Å]	log(T)
Fe X	184.54	6.0
Fe XII	186.88	6.1
Fe XI	188.23	6.1
Ca XVII	192.82	6.7
Fe XII	195.12	6.1
Fe XIII	196.54	6.2
Fe XIII	202.04	6.2
Fe XIII	203.82	6.2
He XII	256.68	4.7
Fe X	257.26	6.0
Fe XIV	264.78	6.3
Fe XIV	274.20	6.3

identify the blending lines for the different ions which are close enough to contribute to the line formation (see Young, et al., 2007 and Del Zanna, 2013). To identify blending lines and their contribution we used CHIANTI (Dere, et al., 1997, Landi, et al., 2013 and Young, et al., 2016) to create synthetic spectra. Due to the weak signal in the coronal hole we can only use ion lines for which the sensitivity of the detector is very high. The Fe XII 195.12 is the strongest iron line observed by EIS and was therefore best suited to calculate the plasma velocity. We used the methods described by Young, et al., 2009 to perform the spectral line fitting. The result for the second and stronger microflare is shown in Fig. 2.

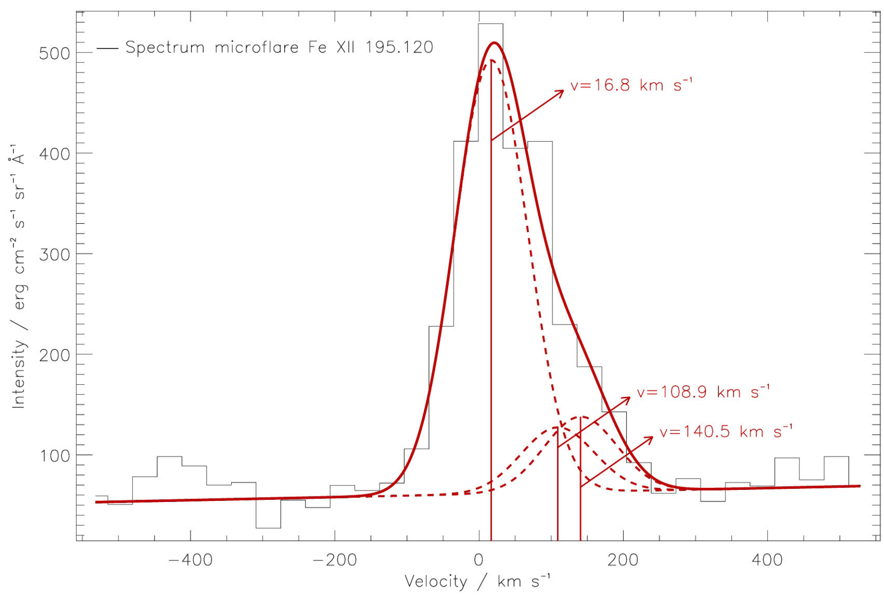

Fig. 2 Shows the spectrum of the microflare at 12:30 taken with EIS and the corresponding fits. The Doppler shifts of the line centroids are shown in the figure near the red arrows. Three single Gaussian fits are shown (red dashed lines) and the resulting combined Gaussian, which represents the spectrum (solid red line).

The absolute wavelength calibration was calculated with the method described by *Kamio*, et al., 2010 and rest-wavelengths were taken from *Brown*, et al., 2008. This is included in the methods provided by P. R. Young which were used. In addition, we used the quiet sun to calculate a rest-wavelength for comparison as shown in Fig. 3. This rest-wavelength spectrum was calculated for the averaged quiet sun region at the bottom left of the EIS field of view.

To show the evolution of the microflare associated with a solar jet we used AIA images of all wavelength channels. This is also important to show exactly where the EIS raster scan captured the microflare and at which time.

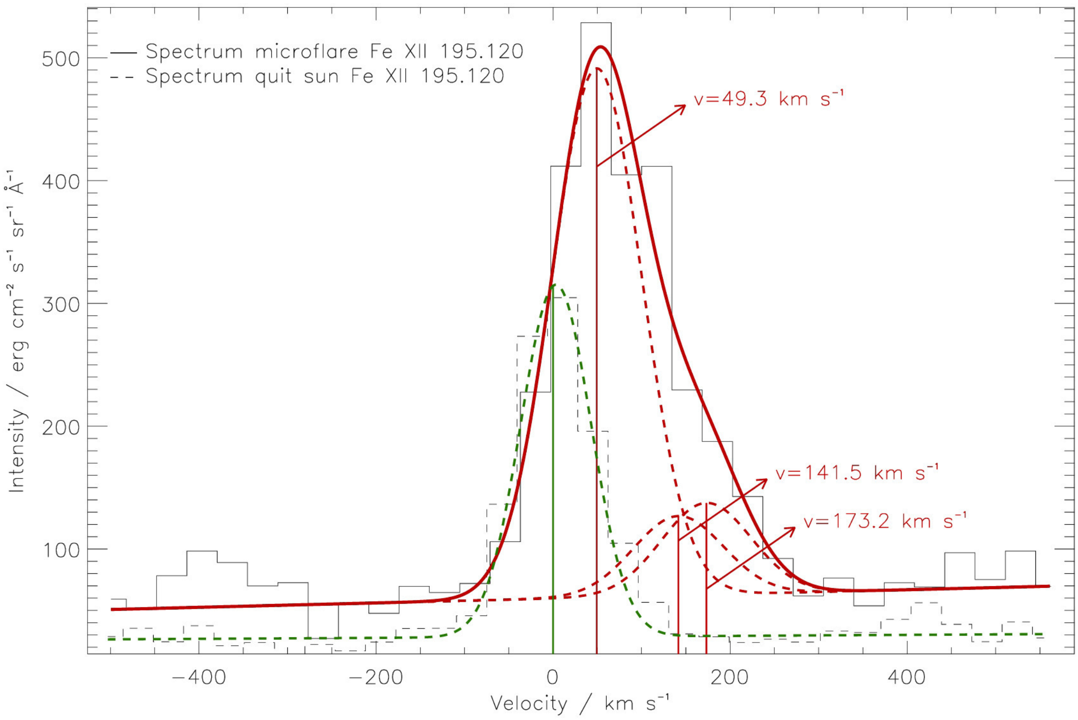

Fig. 3 Shows the spectrum of the microflare at 12:30, taken with EIS and the corresponding fits. The Doppler shifts of the line centroids are shown in the figure near the red arrows. Three single Gaussian fits are shown (red dashed lines) as well as the combined Gaussian profile, which represents the spectrum (solid red line). The used rest-wavelength fit from the quiet sun is shown as a green dashed line.

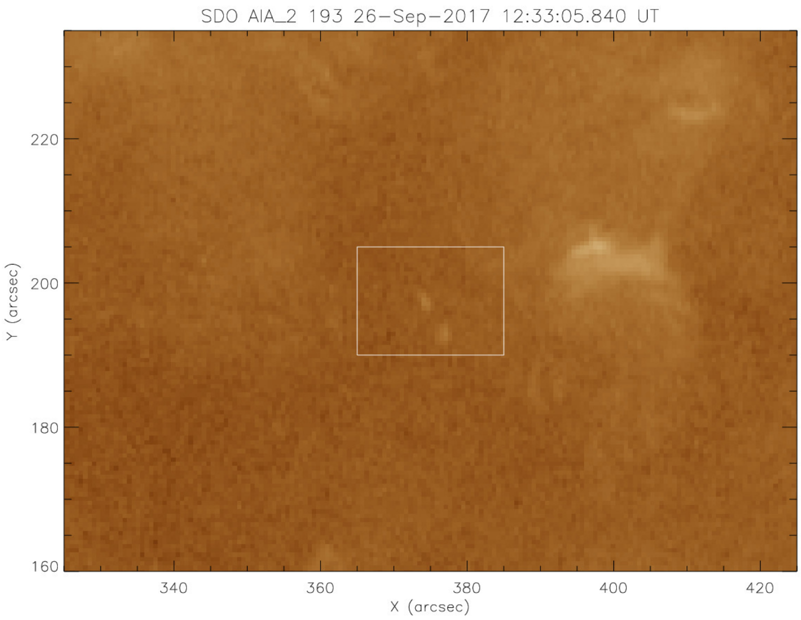

Fig. 4 AIA 193 image of the region where the microflare appeared. The white rectangular shows the area for which the light-curves were calculated.

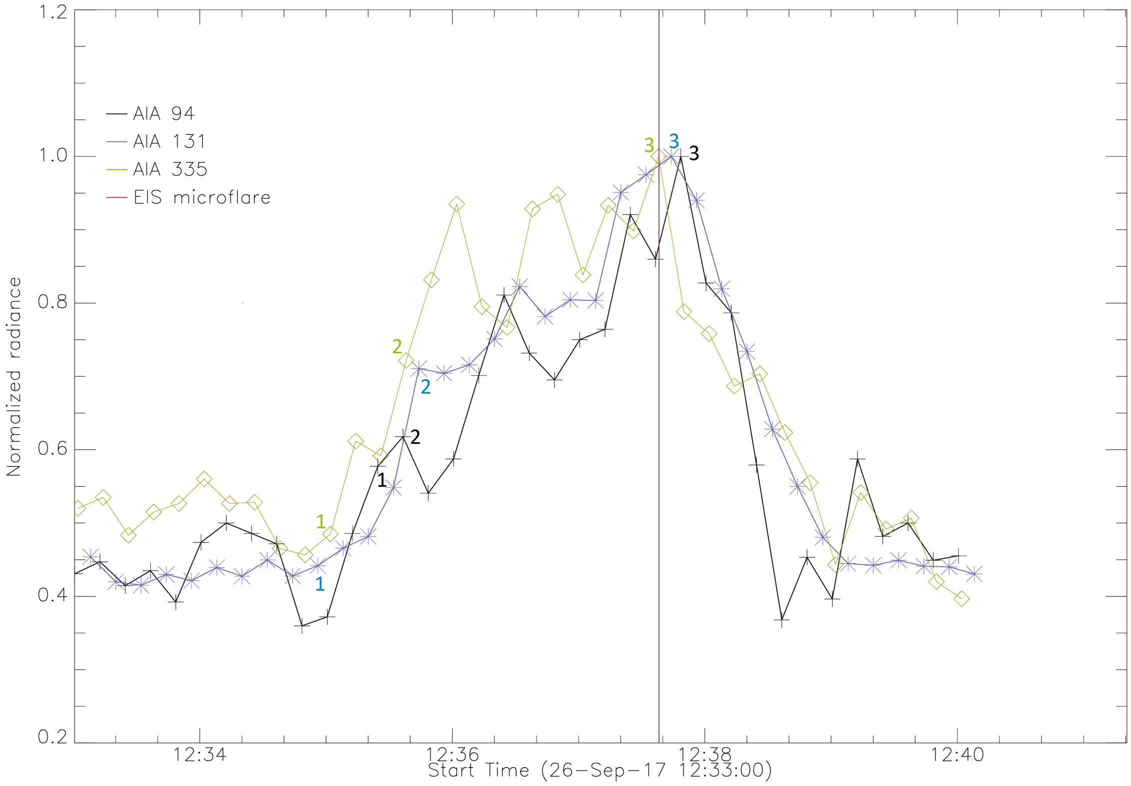

a)

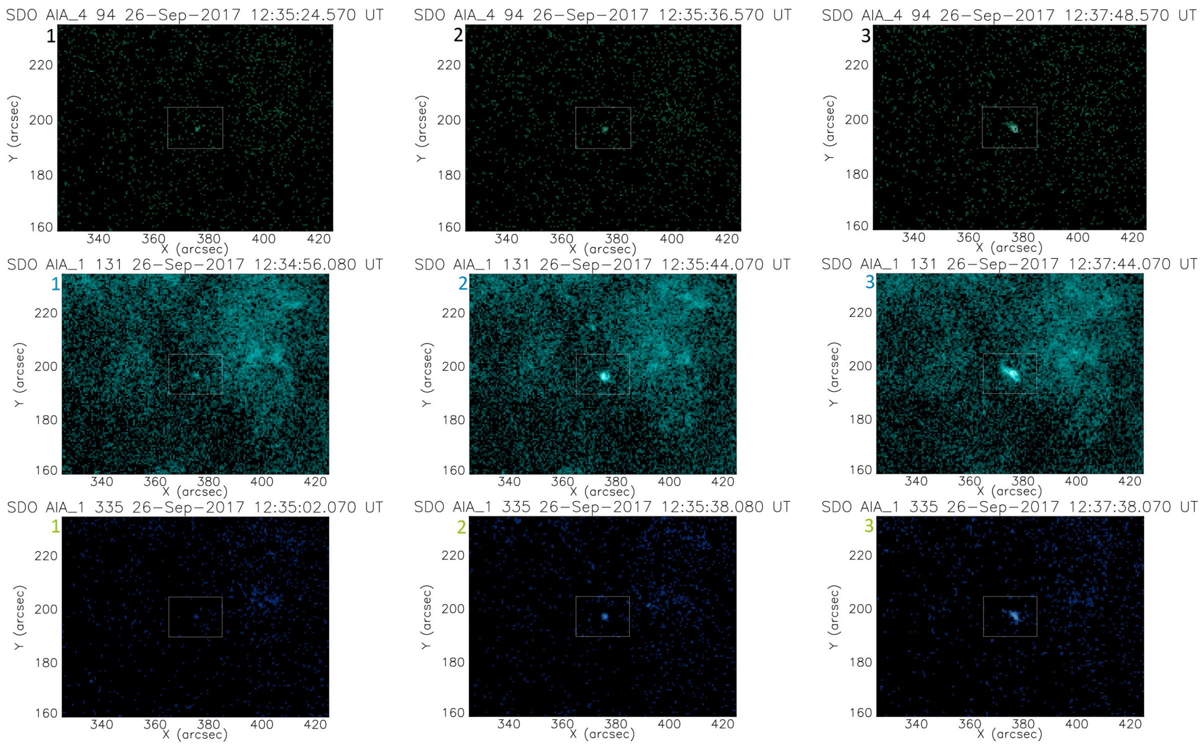

b)

Fig. 5 a) AIA 94, 131, 335 light-curves with a vertical line indicating the time of the EIS scan. Legend at the top left shows the color for the different channels. b) Shows the microflare and jet at three different stages for the AIA channels. First image (1) when the microflare begins, second (2) the microflare at its maximum and third (3) maximum of the associated jet. The numbers are also shown in panel a).

We calculated the AIA light-curves for a particular region (seen in Fig. 4) around the microflare, for all AIA channels (see Fig. 5a). The exposure time midpoint of the EIS scan capturing the microflare is indicated in the light-curves of Fig. 5a by a vertical line and occurs shortly before the jet intensity reaches its maximum.

Conclusions

All AIA channels show the microflare and solar jet which indicates that the plasma temperatures could have been above 2 MK pointing to the fact that microflare events can have as high temperatures as larger flaring regions.

The corresponding EIS spectra as seen in Fig. 2 and Fig. 3 show a redshift of the spectrum which is broadened in the right wing. The difference in velocity of the two methods is probably because the region where the quiet sun method was performed is not at rest. Applying the method by *Kamio*, et al., 2010 for the quiet sun region, used before to determine the rest-wavelength, resulted in upflows of up to 30 km/s. This would explain the high downflows in Fig. 3 and would be in agreement with the values from Fig. 2. The broadened right wing of the spectrum shows downflows up to approximately 140 km/s which could be even higher resulting from a line of sight effect. Fe XII (195.23 Å) ion is formed around 1.58 MK and the spectrum shows small downflows. Therefore, the transition region where upflows change to downflows would be even higher and lies within the typical height range of flares. This also supports the model of chromospheric evaporation (*Neupert*, 1968).

This proceeding shows the current state of the art of our investigation and gives an introduction into our ongoing work. Still the first microflare needs to be analyzed in more detail as well as the changes in the magnetic field configuration which lead to the second stronger microflare.

Acknowledgment

This work was supported by FWF grant: P27800. We are grateful to the Hinode team for the possibility to use their data. Hinode is a Japanese mission developed and launched by ISAS/JAXA, with NAOJ as domestic partner and NASA and STFC (UK) as international partners. It is operated by these agencies in co-operation with ESA and NSC (Norway). CHIANTI is a collaborative project involving George Mason University, the University of Michigan (USA) and the University of Cambridge (UK). P.G. acknowledges support from the project VEGA 2/0004/16.

References

Brown C.M., U. Feldman, J.F. Seely, C.M. Korendyke, H. Hara (2008). Wavelengths and Intensities of Spectral Lines in the 171-211 and 245-291 Å Ranges from Five Solar Regions Recorded by the Extreme-Ultraviolet Imaging Spectrometer (EIS) on Hinode. ApJS, 176, 511.

Del Zanna G. (2008). A revised radiometric calibration for the Hinode/EIS instrument. A&A, 55, A47.

Dere K.P., E. Landi, H.E. Mason, B.C. Monsignori Fossi, P.R. Young (1997). CHIANTI - an atomic database for emission lines. A&A, 125, 149.

Kamio S., H. Hara, T. Watanabe, T. Fredvik, V.H. Hansteen (2010). Modeling of EIS Spectrum Drift from Instrumental Temperatures. Solar Physics, 266, 209.

Landi E., P.R Young, K.P. Dere, G. Del Zanna, H.E. Mason (2013). CHIANTI—An Atomic Database for Emission Lines. XIII. Soft X-Ray Improvements and Other Changes. ApJ, 763, 86.

Neupert W.M. (1968). Comparison of Solar X-Ray Line Emission with Microwave Emission during Flares. ApJ, 153, L59.

Young P.R., et al. (2008). EUV Emission Lines and Diagnostics Observed with Hinode/EIS. PASJ, 59, 857.

Young P.R., T. Watanabe, H. Hara, J.T. Mariska (2009). High-precision density measurements in the solar corona. I. Analysis methods and results for Fe XII and Fe XIII. A&A, 495, 587.

Young P.R., K.P. Dere, E. Landi, G. Del Zanna, H.E. Mason (2016). The CHIANTI atomic database. Journal of Physics B, 49, 7.

Proceedings of
Tenth Workshop "Solar Influences on the Magnetosphere, Ionosphere and Atmosphere"
Primorsko, Bulgaria, June 4÷8, 2018

Modelling the solar photospheric plasma and magnetic field dynamics in the quiet Sun and comparison of these results with the flow fields in an evolving active region

Jose Iván Campos Rozo [1,2], *Dominik Utz* [1,3], *Astrid Veronig* [1], *and Santiago Vargas Domínguez* [2]

[1] Institute of Physics/IGAM University of Graz, Austria
[2] Observatorio Astonómico Nacional - Universidad Nacional de Colombia, Colombia
[3] Instituto de Astrofísica de Andalucía IAA-CSIC, Granada, Spain
E-mail: jose.campos-rozo@uni-graz.at

Abstract.

In the present work a detailed study of the flow velocities of a quiet solar region is made and then compared with the flow fields during the emergence and prior to the evolution of AR-11190 on 11-April-2010. The velocity fields are computed from intensity as well as LOS magnetograms by using Local Correlation Tracking (LCT) techniques. The magnitudes of the obtained velocity vectors can be modelled by a single and simple Rayleigh distribution in the case of the quiet Sun and by a combination of two different statistical distributions in the case of the active region. Primarily this combination consists of a Rayleigh distribution that models the background velocity magnitudes as well as the general behavior of the combined velocity distribution, plus a weaker additional component that recreates the fast changes within the field of view. We propose two different distributions (implying different physical interpretations) for this second component of our combined fitting model. Generally, we can say that all the distributions show a strong correlation between the plasma motions and the movements of magnetic elements except during time instances when strong and fast magnetic flux elements start to appear within the region of interest.

Introduction

The emergence of convective flows defines the dynamics on the solar surface, transporting plasma, energy as well as magnetic field from the solar interior and across the surface. These emergences display flow convective patterns so-called granulation, mesogranulation, and supergranulation on different spatial and temporal scales depending on how they are organized. On the photosphere it is also possible to observe the arrangement of magnetic fields at different scales (see *Zwaan* 1987), from small-scales, like Magnetic Bright Points (MBP; *Utz* et al. 2013), to large-scale magnetic concentrations such as sunspots or Active Regions (AR). It is well-known that there is a strong interaction of the solar magnetic fields with the photospheric plasma dynamics, such as convective flow emergences (*Parker* 1970; *Bushby* 2008; *Danilovic* et al. 2010).

Besides the plasma vertical intrinsic emergences, the photospheric evolution is strongly influenced by the expansion and fragmentation of the granules. The meso and supergranules have been associated to fast emergence flows (*Palacios* et al. 2012), as well as to explosive granules, which occur with higher frequency in mesogranule regions (e.g. *Title et al.* 1989), or during the emergence of magnetic field, and its ensuing accumulation in intergranular zones (*Domínguez Cerdeña* 2003; *Ishikawa & Tsuneta* 2011).

Different Local Correlation Tracking (LCT) techniques have been used for the analysis of those features. The general LCT algorithm is based on Eq. 1 and was applied for the first time in solar photograms by *November and Simon* (1988). The algorithm follows the simple but powerful idea to find the best cross-correlation between the intensities of two consecutive images.

$$C_{t,t+\tau}(\delta,\mathbf{x}) = \int J_t\left(\zeta - \frac{\delta}{2}\right) J_{t+\tau}\left(\zeta + \frac{\delta}{2}\right) W(\mathbf{x}-\zeta)\partial\zeta \qquad \text{Eq. 1}$$

where $C_{t,t+\tau}$ is a four-dimensional function that depends on the position and the displacement. The function $W(x)$ represents an apodization Gaussian window, whereas J_t, and $J_{t+\tau}$ represent two consecutive images taken in t, and $t+\tau$ time instances. In this work we aim on applying such a LCT algorithm on the flow fields created in a quiet region on the solar surface and compare the characteristics of this flow field then with the one prior to, as well as during the evolution of AR 11190 to investigate if the flow field characteristics are changed due to the magnetic field emergence and if so, in which way.

Data

The used data covers a quiet Sun region as well as a snapshot of the evolving AR 11190 (see Fig. 1) of April 11, 2011. The left side of the figure shows in the top left the continuum image data of the quiet region and below the Line Of Sight (LOS) magnetogram. The right panels show AR 11190, a very complex and highly evolving active region. Again, we can see the intensity photoheliogram in the top position followed below by the magnetogram. All the used and analyzed magnetogram and intensity photoheliogram data were recorded by HMI/SDO (Helioseismic and Magnetic Imager, *Hoeksema* et al. 2014, onboard of the Solar Dynamics Observatory, see *Pesnell* et al. 2012) with a cadence of 45 seconds, a pixel size of 0.504 arcsec, and finally obtained by us from the data center with the preparation level 1.5. This means that the data is given in physical units, and pre-processing steps are not necessary. Nevertheless, the data still needed to be prepared for the correct analysis (e.g. de-rotation, co-aligment, subsonic filtering). All the preparation of the data and analysis have been done using Python programming language, and the specialized library for the solar data analysis SunPy (*SunPy Community et al.* 2015).

Analysis and Results

a) Flow fields

We focused on the detailed study of the formation, evolution, and behavior of the horizontal (see Eq. 1), and vertical velocity fields obtained from intensity as well as magnetic field maps from a quiet Sun region in comparison to the evolution of similar flow fields within the evolving AR 11190. The vertical velocities can be calculated by

$v_z(v_x, v_y) = h_m \nabla \cdot v_h(v_x, v_y)$	Eq. 2

where h_m represents the mass flux scale height (see *November* et. al 1987; *November* 1989). Due to the fact that emergence flows are associated to meso and supergranules (*Palacios et al.* 2012), the size of the correlation window FWHM was chosen to be 12.5 arcsec (~ 9 Mm; *November et al.,* 1981) with a temporal average of 2 hours (Life-time average for mesogranules; ver *Hill et al.*1984; *Rast* 2003).

Figure 2 shows the horizontal and vertical velocity fields calculated using the LCT algotihm for both the quiet Sun region and the evolving AR 11190. The top row is dedicated to the quiet Sun whereas the bottom row shows AR 11190. The first column shows the horizontal velocities calculated from the continuum data. Here various contour levels represent vertical positive velocities overplotted on the vertical velocity maps which form the background. In this kind of plot the yellow arrows represent the horizontal velocities averaged over the previous mentioned 2 hours averaging time period.

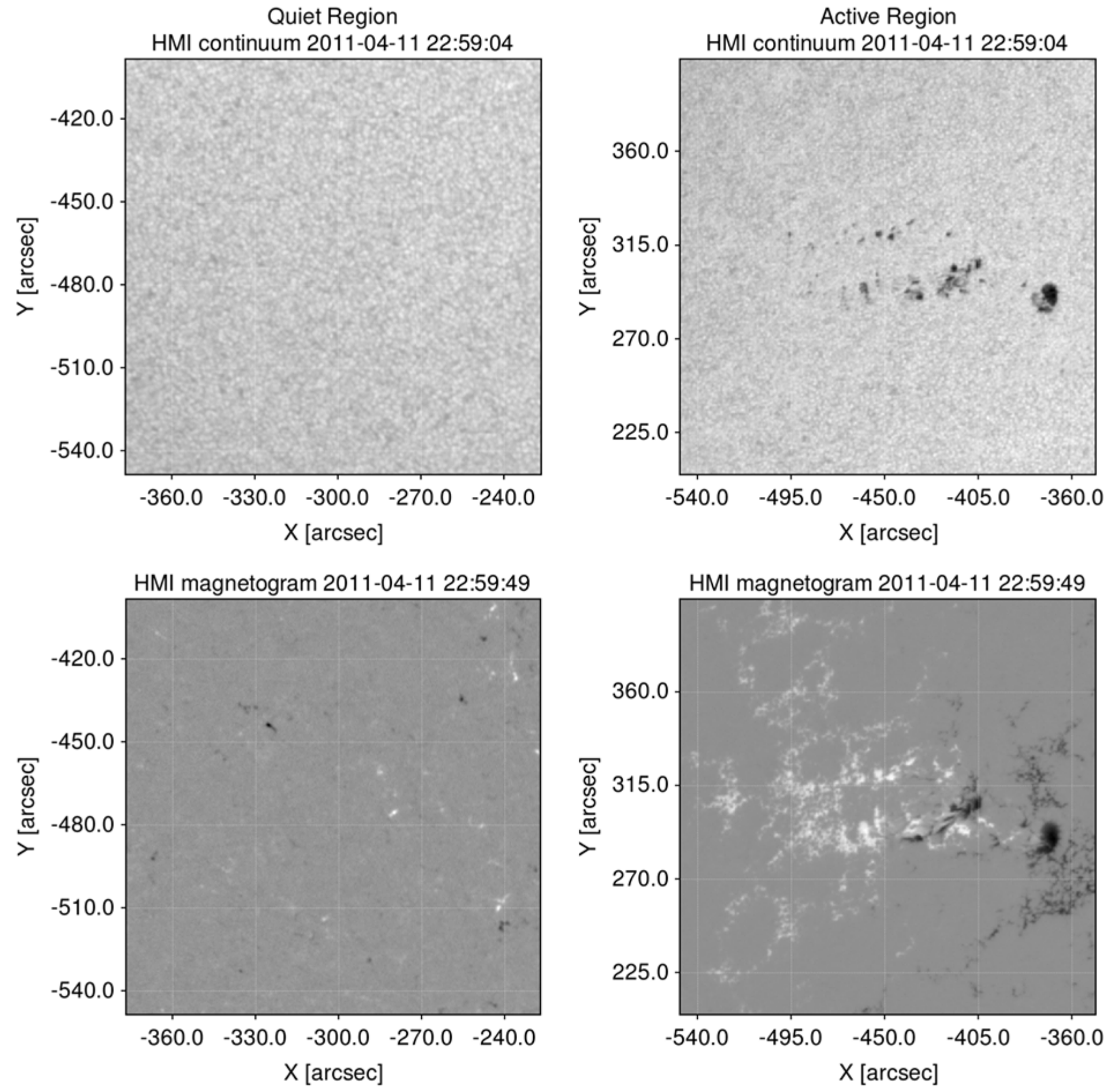

Fig. 1 Shows the comparison of the two regions of interest. On the left side from top to bottom: intensity photoheliogram of a quiet Sun region as observed by the whitelight channel of HMI. Below the corresponding magnetogram is shown. On the right-side top: AR 11190 observed on April 11, 2011 shows a complex configuration, with small sunspots with partial penumbrae and several pores in intensity while the bottom illustrates the complex bipolar magnetic field configuration.

The second column displays the horizontal velocities obtained from LOS magnetograms, as well as the vertical velocities represented by contours plotted over the maps at the respective times. The red and blue arrows represent strong positive and negative magnetic elements motions, whereas the green and yellow arrows indicate the motions linked to weak magnetic element (< 50 G) movements. The third column shows the correlation between the vertical velocities obtained from the continuum images, as well as the vertical velocities calculated from the magnetograms.

From these plots it is apparent that the flow fields in the quiet Sun are more homogenous and in a way more orientated, while the active region shows more irregular flows as well as strong magnetic elements appearing and being displaced. To discuss this behaviour in more detail we now wish to have a look on the distribution of the magnitudes of the velocity vectors.

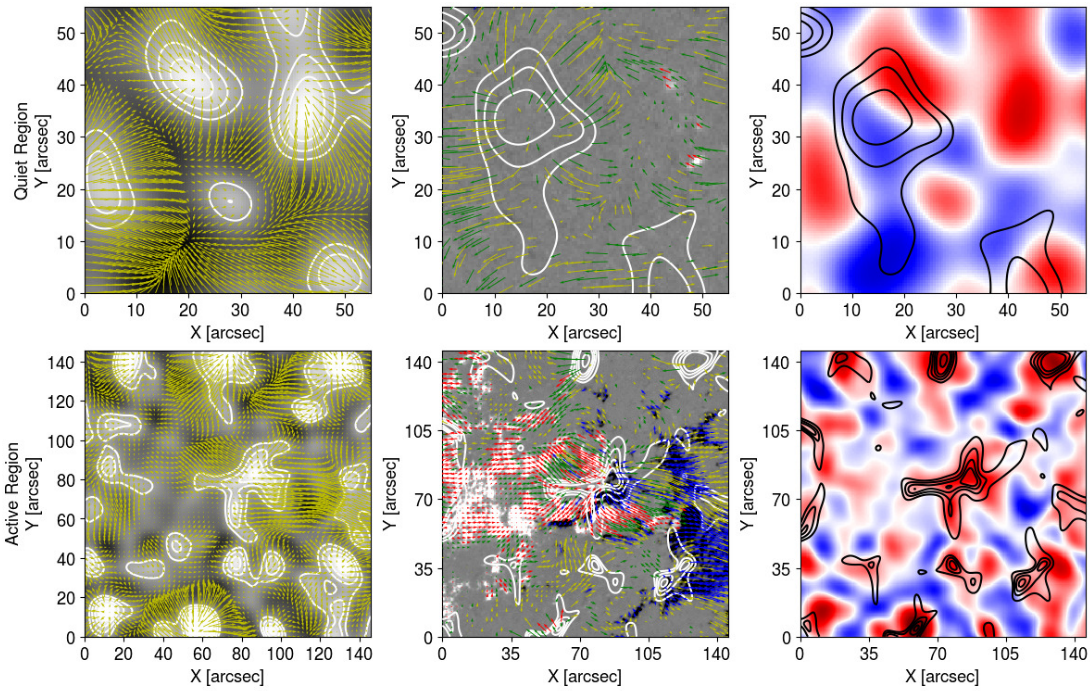

Fig. 2 Single snapshot maps of the horizontal and vertical velocity fields for the quiet Sun region in comparison with the active region (be aware of the different sized field of view). [Left] Plasma horizontal velocities with the vertical velocities being shown in the background images. [Middle] Horizontal and vertical velocities of the magnetic elements. The background maps illustrate the corresponding LOS magnetogram for the given time instance. [Right] Vertical velocity correlations between the vertical velocities calculated from the continuum images (in the background) as well as the LOS magnetograms (contour lines). The contour lines represent velocity values of [0.5, 1., 1.5, 2., 3] km s^{-1}.

b) Fitting the magnitude of the velocity fields.

An exemplary plot of the magnitudes distribution for the flow field veloctiy vectors for the quiet Sun as well as the active region under consideration can be found in Fig. 3.

In this histogram plots we show the velocity magnitudes overplotted in solid line by two component curve fit models. The left column shows the case where we tried to model the flow field magnitudes with a system consisting of a two Rayleigh fit components distribution. The right side on the other hand illustrates the case where we introduced a combined model of one Rayleigh (background component) with one Gaussian component. The mathematical equations born out by the combination of the two statistical distributions are outlined in Eq. 3, and Eq. 4, which can be found below for the velocity fields calculated from LOS magnetograms as well as continuum maps.

The first component in both equations is given by a Rayleigh distribution, whereas the second component will be represented by a secondary Rayleigh distribution, or a Gaussian distribution. We would interpret the combined fitting model in the following way, namely that the first component represents the proper motions of the quiet, and uneffected background, whereas the second component will represent the caused perturbations due to strong changes such as fast and violent emergences. Besides, the separate movements from positive and negative magnetic elements will have a stronger influence in the active region changing quite dramatically the flow fields and the corresponding magnitude distributions. Such violent magnetic field emergences as well as seperate magnetic field polarity movements can appear regularly in active regions and are generally not seen within the quiet Sun.

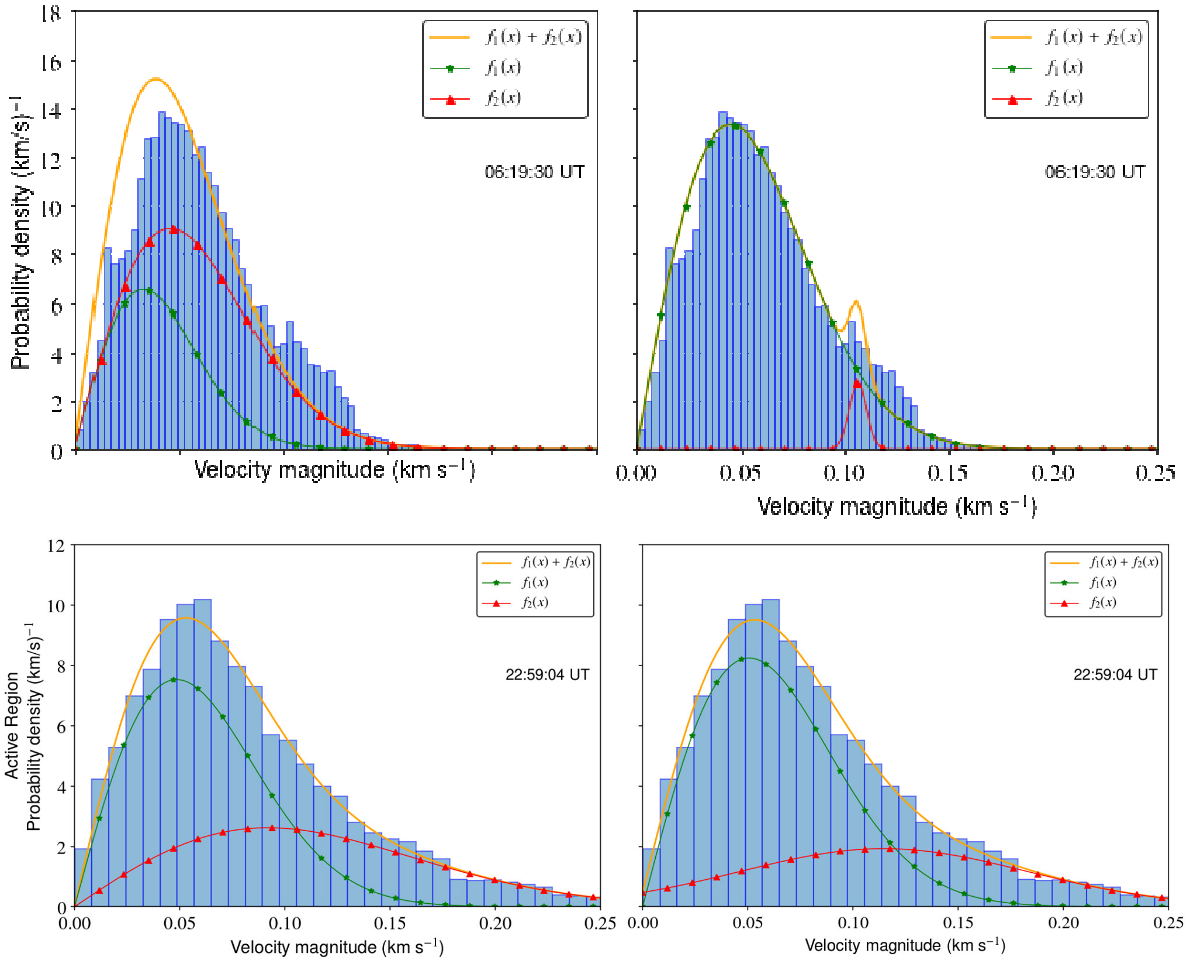

Fig. 3 Giving the histograms of the velocity vector magnitudes for single maps of the flow fields of the two regions of interest. The top row shows the quiet Sun region while the lower row gives the active region. Overplotted on the histograms are line fits. The red (triangle symbol) and green (dotted symbol) solid lines show two fit components applied to the histograms while the orange line shows the combination of both components to form the total of the fit. The left column uses a two Rayleigh component fitting while the right column uses a one component Rayleigh plus one component Gaussian fitting.

$f(v,\sigma_{R_1}) + f(v,\sigma_{R_2}) = A_1 \frac{v}{\sigma_{R_1}^2}\exp\left(\frac{-v^2}{2\sigma_{R_1}^2}\right) + B_1 \frac{v}{\sigma_{R_2}^2}\exp\left(\frac{-v^2}{2\sigma_{R_2}^2}\right),$	Eq. 3
$f(v,\sigma_{R_1}) + f(v,\mu_G,\sigma_G) = A_2 \frac{v}{\sigma_{R_1}^2}\exp\left(\frac{-v^2}{2\sigma_{R_1}^2}\right) + \frac{B_2}{\sqrt{2\pi}\,\sigma_G}\exp\left(\frac{-(v-\mu_G)^2}{2\sigma_G^2}\right);$	Eq. 4

where σ_{R_1} , σ_{R_2} represent the Rayleigh parameter, which are related to the mean velocity of the proper motions, whereas μ_G and σ_G are the mean and standard deviation from the Gaussian distribution.

Conclusions and Outlook

Active Sun regions, especially during their early stage evolution, are quite distinctive from quiet Sun regions in the way that they show a prolonged velocity magnitude tail reaching to far higher velocities than the ones which can be seen in the quiet Sun. Generally, the flow fields comprise, in the case of active regions, of stronger magnetic elements, which are often also of bipolar nature showing a way more turbulent behavior than their corresponding counterparts in the quiet Sun. Nevertheless, in a first approximation a Rayleigh distribution fits quite well the magnitudes of the velocities within the FOV. However, inspecting the velocity field vectors in an active region in more detail shows that the high velocity tail should be fitted by a more complex two component model. At this moment we would propose to try either a combination of a two-components Rayleigh fit or a one component Rayleigh fit combined with one Gaussian modelling the high velocity tail of the distribution. An interesting point of our study would be the finding of precursor changes in the velocity magnitude distribution prior to the flux emergence event. However, so far in our investigation we cannot report of such a finding. Another interesting future aspect lies then in inspecting the evolution and strength of the two components of the fit models as these can tell us more details about the violent flux emergence events. A fully detailed study is currently under preparation and refinement and more details on this modelling efforts will be given in the immediate future in the work, Campos Rozo et al. 2018, currently under preparation.

Acknowledgment

This research received support by the Austrian Science Fund (FWF) project: P27800-N16: The Interaction of the Solar Granulation with small-scale Solar Magnetic Fields. Jose Iván Campos Rozo and Santiago Vargas Domínguez acknowledge funding from Universidad Nacional de Colombia research Project code 36127: Magnetic field in the solar atmosphere. HMI/SDO data are courtesy of NASA/SDO and the AIA, EVE, and HMI science teams, and they were obtained from the Joint Science Operation Center (JSOC). Part of this research has been created by using SunPy libraries, an open-source and free community-developed solar data analysis package written in Python.

References

Bushby, P. J., (2008). Philosophical Transactions of the Royal Society of London Series A, 366,4465-4476.

Campos Rozo, J. I., D. Utz, S. Vargas-Domínguez, A. Veronig, T. Van Doorsselaere 2018, A&A Photospheric plasma and magnetic field dynamics during the formation of solar AR 11190, under review

Danilovic, S. e. a. (2010). Transverse Component of the Magnetic Field in the Solar Photosphere Observed by SUNRISE. Astrophysical Journal Lectures, 723, L149-L153.

Domínguez Cerdeña, I. 2003, A&A, 412, L65.

Hill, F., Gough, D., & Toomre, J. 1984, Mem. Soc. Astron. Italiana, 55, 153.

Hoeksema J. T., Y. Liu, K. Hayashi et al. (2014). The Helioseismic and Magnetic Image (HMI) Vector Magnetic Field Pipeline: SHARPs – Space- Weather HMI Active Region Patches, Sol. Phys. 289, 3549

Ishikawa, R. & Tsuneta, S. 2011, ApJ, 735, 74.

November, L. J. e. a. (1981). The detection of mesogranulation on the sun. Astrophysical Journal Lectures, 245,L123-L126.

November,L. J. and Simon,G.W., 1988, Astrophys. J.333, 427.

Palacios, J., Blanco Rodríguez, J., Vargas Domínguez, S., et al. 2012, A&A, 537, A21.

Pesnell, W. D., B. J. Thompson, P.C. Chamberlin (2012). The Solar Dynamics Observatory (SDO), Sol. Phys. 275, 3

Parker, E. N. (1970). The Origin of Solar Magnetic Fields. Annual Review of Astronomy and Astrophysics, 8:1.

Rast, M. P. 2003, ApJ, 597, 1200

Title, A. M., Tarbell, T. D., Topka, K. P., Ferguson, S. H., Shine, R. A., and SOUP Team (1989). Statistical properties of solar granulation derived from the SOUP instrument on Spacelab 2. ApJ, 336:475-494.

The SunPy Community, et al. 2015, Sunpy-Python for Solar Physics, APJ - Computational Science and Discovery, 8.

Utz D., J. Jurčák, A. Hanslmeier, R. Muller, A. Veronig, O. Kühner (2013), Magnetic field strength distribution of magnetic bright points inferred from filtergrams and spectro-polarimetric data. A&A, 554, 65.

Zwaan C. (1987), Elements and patterns in the solar magnetic field. Annual review of astronomy and astrophysics, 25, 83

Proceedings of
Tenth Workshop "Solar Influences on the Magnetosphere, Ionosphere and Atmosphere"
Primorsko, Bulgaria, June 4÷8, 2018

Advection and Inter-Component Connections in the Quasar

Krasimira Yankova

Space Research and Technology Institute – Bulgarian Academy of Sciences, Sofia
e-mail: f7@space.bas.bg

Abstract.

In this paper is analyzes the impact of the restructuring in the accretion flow, over self-induction of the advection and exchange of energy in the stream. Emergence and action of non-deforming advection builds connections between the elements in quasar; and for that allows researching the evolution of the mechanism in some of them.

MHD models of non-stationary accretion disc showed appear and rapidly developing corona. Advective warming into the pad maintains vitality the corona.

Extension on advective hypothesis in the general relativity allows tracing the continuation of the advective spiral inner the event horizon.

1. Introduction

We constructed geometrically thin, optically thick, one-temperature Keplerian disc in a normal magnetic field, around a black hole. Model which was built in the Galilean transformations Iankova (2007, 2009); Yankova (2012-2015) with pseudo-Newtonian correction Abramowicz et al. (1988); Igumenshchev &Abramovich (2000). And in contrast to the other models, we suggest the advection in the form of the complete advective term (Yankova 2015a), which is naturally produced in the equations describing the flow dynamics. Advection of this type is in self-induction mode, which is due to *contribution of the electro-magnetic field. MF in the disk:* Determine the direction of the middle flow displacement in the disc uniquely; it provides additional dissipative mechanism, и Prevents transition to the dominant mode *as controlled the sign of the entropy.*

Sign of the entropy and in particular Negative gradient $\partial_t S$ determined the basic criterion for development and the self-induction on the advection and represents the active feedback.

Results of researches and particular solution on the model have shown that magnetized accretion disks are forming three types of spirals: Tidal spiral that is logarithmic Iankova (2007a), Iankova (2009). MHD spirals (Matsuda et al.2000), Kaburaki (1999) and Advective rings Iankova (2007a, 2009), Yankova (2012-2015).

Advective rings are formed as a result of self-control of avection through entropy. They are sections the advective spiral, which Elliptic instability in the disk fragments into parts. To them there are no forbidden regions of the disk, because advective spirals are Keplerian, and they are obeying the specific properties of the gravitational field of the black hole. Their behaviour suggests the fundamental nature of deformationless advection as a mechanism for which the other types of advection will represent specific boundaries.

Although we ignore the self-gravity in the the quasi-classical flow model and advective rings, it directly affects the MF and the current in it. So although we do not take this interaction into account in the nonrelativistic case, it is reflected in the behavior of the EMF and the following him plasma and therefore on the advective mechanism.

2. Relativistic advection

Relativistic advection is determined by two factors: the topology of the magnetic field and the self-gravity of the formations in which advection occurs. (Reality is composed of multiple stitched and nested manifolds – formations).

Self-gravity (of these metrics-formations) and background potentials determined by space-time metrics are directly interrelated to the evolving advection, because as a full differential, it must follow the metrics of manifold Giuseppe Frè (2013), The Galactic Black

Hole (2003). Topology the magnetic fields include and determine the feedbacks the mechanism of fundamental advection.

$$\frac{D}{D_T}\begin{pmatrix} \nu \\ B \\ S \end{pmatrix} \sim T_{IJ} = \begin{pmatrix} T_{00} & T_{0i} \\ T_{i0} & T_{ij} \end{pmatrix} \qquad (1)$$

where $I = (0, i)$, $i = (1,2,3)$, $J = (0, j)$ and $j = (1,2,3)$.

This means that, for example, if manifold is stratified by some feature (by number of dimensions - primary cleavage (ADM formalism) - branches; quantum cloning - laying on alternatives→ sheets; spatial density; ...) the left sides of the equations (1) will be the same, but the response as a result of the reverse image of the factorization plating (not only one-froms the tangent bundle but also spectrum of higher derivatives), the right sides (1) in the layers and sub-layers of manifold will be different.

M(n, m)

The full form of relativistic advection in mixed dimensions is obtained when consider the advection operator through the characteristic parameter χ (trajectory element - the world line), then there is no difference of temporal and spatial components for the mechanism, and shifting along time is nothing less than part by the advective operator

$$\left(\partial_{t_i} + \nu_{ij}\partial_{x_j}\right)\nu_{ji} = \beta_{ji}\partial_{t_i} + \delta_{ij}\partial_{t_j} \qquad (2)$$

Advection is a specific, directed differential that includes a particular spatial direction along with the assigned direction of time τ (Yankova 2017, 2018), defined by the sign of entropy in the layer of manifold. i.e Advection is a full differential, but in a direction determined by the source, therefore it does not correspond to the full metric, but is one of the one-forms E^a of the metric.

$$g_{\mu\nu} = E^a_\mu E^b_\nu \eta_{ab}, \quad \text{[Giuseppe Frè (2013)]} \qquad (3)$$

– that means it is only a fraction of the tangential bundle oriented to or by the formation that generates it.

3. Action of the relativistic advection

Action of relativistic advection, builds connections between the elements in quasar: indirectly, such as on the corona - disk boundary; and directly – Advective screw as a continuation of the advective spiral after the last stable disk orbit from the inner edge to and into the compact object.

3.1 Behaviors on the border corona - disk.

In the disk sound and the magneto-sonic speeds are the most sensitive to the energy exchange from interaction between the parameters and the influence of the non-linear effects over them. They create multiple contours of increasing, which combined with fast growing magnetic field ensure the emergence of compacted regions genetically unrelated to the helices (Yankova 2015b). These are precisely the advective rings that provide heating of the pad at the base of the corona. Periastron Advance (Schwarzschild precession) allows spiraling of the advective stream without disturbing its Keplerian nature. Advective rings create a sufficient metric deviation to close the potential of the EMF and this way provides self-induction on advection in the disk and on the border. Their self-gravity also contributes to the acceleration of the process of unloading the magnetic lines Yankova (2007b), Yankova (2009) (catalyzing the action of Parker's instabilities) and the decrease of mass density in the corona.

(1) The disk corona develops on a background metric, asymptotic to Ker-Newman without modification: Beyond the horizon there are no flat orbits parallel to the equatorial plane;
(2) Boundary corona-disk also is important, because there manifest themselves the effects of the warming into the pad: it causes sharply increases optical transparency in the corona; thence it cannot sustain self-inducing advection. This does not mean that can not to have the secondary excitement of a borderline mode, a sub-type of the advection mechanism.

In the corona the azimuthal rotation is weak $\Omega \rightarrow 0$. Slower and relatively cold plasma component to the hot ones immersed in it magnetic lines is a good prerequisite for the development of a two-temperature sub-Edington advection.

In the jets, advection originates as combination from that in the corona's flow and this one which is missed from an advective spiral, but here mechanism is reinforced through extra excitation by the interaction with the central dynamo and is super- Edington.

3.2 Advective screw

In the last stable orbit, the advective spiral opens completely and passes into an advective screw. Advective Screw develops in as own manifold of the universe. Unlike most authors of theoretical physics instead of a compact fourth spatial dimension, we assume a second global time dimension orthogonal to time with a generated direction in our universe.

Flow that is stored in the screw belong the mainstream passed through the equatorial window. As a consequence advective screw is located entirely in the equatorial plane and in terms of spatial coordinates is limited in the vertical direction Z. Mainstream is adjacent along manifold wall. This screw form is a direct consequence of the above conclusion (3).

4. Conclusions

In conclude will note that the advection in all elements of the quasar is a product of the central dynamo and different degrees of its interaction with gravity

Concrete consideration of each of these variants of the mechanism in the quasar components is precisely the subject of our future research

References

Abramowicz M. A., Czerny, B., Lasota, J. P., Szuszkiewicz, E., 1988 Slim accretion disks, ApJ, 332 646-658.

Giuseppe Frè P, 2013, Gravity, a Geometrical Course I

Iankova Kr.D., 2007a, Accretion disk with advection and magnetic field , BG-Ursi School and Workshop on Waves and Turbulence Phenomena in Space Plasmas, 1–9 July, 2006, Kiten, Bulgaria, BSSPP Proceedings, Series No. 1, pp 143-146, 2007, http://sp.phys.uni-sofia.bg/Kiten06/Pres/Iankova.pdf ,.

Iankova Krasimira 2007b, " Evinces of interaction of flow in disk with magnetic field'", Sofia, Bulgaria, Heron Press Ltd.Science series, pp 326-29, 2007.

Iankova Kr.D., 2009, Stability and evolution of magnetic accretion disk, Publ. Astron. Soc. "Rudjer Bošković", No. 9, pp 327-333, Belgrade (2009). http://aquila.skyarchive.org/6_SBAC/pdfs/31.pdf;

Igumenshchev, I.V., Abramovich, M.A.: 2000, Two-dimensional Models of Hydrodynamical Accretion Flows into Black Holes, ApJ 130, 463-484.

Kaburaki Os., 1999, Analytic Model for Advection-Dominated Accretion Flows in a Global Magnetic Field, arXiv: astro-ph/9910252.

Matsuda T, Makita M, Fujiwara H, Nagae T, Haraguchi K, Hayashi E, H.M.J. Boffin: 2000, Numerical simulation of accretion discs in close binary systems and discovery of spiral shocks,Astrophysics and Space Science 274: 259–273, 2000.

THE GALACTIC BLACK HOLE (2003) Lectures on General Relativity and Astrophysics, Institute of Physics, Publishing Bristol and Philadelphia

Yankova Krasimira, 2012, Structure of accretion disk in the presence of magnetic field, Publications of the Astronomical Society "Rudjer Boskovic", vol. 11, pp. 375-383. http://adsabs.harvard.edu/abs/2012PASRB..11..375Y

Yankova Kr.D.: 2013, Generation and development of the disk corona, Proceedings of the VIII Serbian-Bulgarian Astronomical Conference (VIII SBAC), Publ. Astron. Soc. "Rudjer Bošković" vol. 12, 375-381. http://wfpdb.org/ftp/8_SBAC_D1/pdfs/34.pdf

Yankova Kr., 2014, Theoretical analysis on the development in relationships of the system disk – corona, Proceedings SES 2014, ISSN 1313-3888 , 35-40, 2015.

Yankova Kr.: 2015a, MHD of accretion-disk flows, BlgAJ, Vol. 22, p. 83. http://adsabs.harvard.edu/abs/2015BlgAJ..22...83Y

Yankova Kr.: 2015b, Behaviour of the flow on the boundary in the system disk-corona, Proceedings of the IX Bulgarian-Serbian Astronomical Conference: Astroinformatics (IX BSACA), Publ. Astron. Soc. "Rudjer Bošković" No 15, 2015, 107-115.

Yankova Kr.: 2017, Inter-component connections in Quasar, SSTRI-BAN, Sofia, Proceedings SES 2017, ISSN 1313-3888, 85-88, 2017.

Yankova Kr.: 2018, Deformationless advection, Proceedings of the XI Bulgarian-Serbian Astronomical Conference: Astroinformatics (IX BSACA), Publ. Astron. Soc. "Rudjer Bošković" No, in press.

Proceedings of
Tenth Workshop "Solar Influences on the Magnetosphere, Ionosphere and Atmosphere"
Primorsko, Bulgaria, June 4÷8, 2018

Morphology and Geomagnetic Effects of Corotating Interaction Regions in 2008 - 2014

DarijeMaričić [1], *Dragan Roša* [1], *Filip Šterc* [1], *Mile Karlica* [2]

[1] Astronomical Observatory Zagreb, Croatia.
[2] Sapienza University of Rome, Italy.
E-mail: dmaricic@zvjezdarnica.hr

Abstract

We presented an analysis of the geoeffectiveness of corotating interaction regions (CIRs) employing the data recorded from January 2008 to December 2014. For this purpose we made a list of 283 solar wind (SW) disturbances incorporated into an online catalog for general use. After we separated solar wind signatures on: CIRs, interplanetary coronal mass ejections (ICMEs), interactions and complex signatures; we focused our attention on 173 CIRs (61% of all SW signatures) where the stream interface (SI) was clearly recognizable. Furthermore, we analyzed in detail the correlation of solar wind parameters in different parts of CIRs, particularly in front and behind of SI, with changes in geoeffectiveness. In this analysis, in most events (95% of the analyzed CIRs) weak increase of Dst index occurs between forward shock and SI, while the main decreases of Dst index occurs between SI and reverse shock of CIR. The correlation coefficients between Dst index and the magnetic field B, proton density Np, flow speed v and proton thermal speed v_{th}, in the region behind the SI are: cc = 0.72, 0.62, 0.45 and 0.64, respectively. Correlations for region between forward shock and SI are significantly lower.

Keywords: Sun, coronal mass ejection, solar wind disturbance, stream interface, corotating interaction regions

Introduction

Corotating interaction regions (CIRs) are formed by interaction of the high speed solar wind streams (HSSs), with velocity up to 900 kms^{-1} and slow solar wind stream with typically velocity of ~ 400 kms^{-1} (e.g., *Tsuratani et al.,* 2006, and references therein). Since CIRs originates from a coronal hole, they cause recurrent activity in the interplanetary space (e.g. *Gosling,* 1996). CIRs at heliocentric distance of around 1 AU are usually bounded by magnetohydrodinamic forward and reverse waves, who develop into forward and reverse shocks at a larger distance, occasionally in some events already at 1 AU (*Smith and Wolfe,* 1976). CIRs causes periodic geomagnetic storms of weak to medium strenghts (e.g. *Vennerstorm,* 2001; *Verbanec et al.,* 2011a,b; *Hajra et al.,* 2013, *Vršnak et al.,* 2017). Although this phenomena is much stronger when it is caused by a single ICME or with interaction of ICMEs, the importance of CIRs is that they occur more common throughout the solar cycle and their cumulative effect is larger than those of ICMEs (*Tsuratani et al.,* 2006). From the measurements of the solar wind at 1 AU, CIR structure is characterized by compression region associated with stream interface (SI). Inside the compression region the magnetic field, the temperature and the plasma density are increased (*Dumbović et al.*, 2012, and references therein). Compression region usually lasts typically one day. The whole region contains strong fluctuation and the increase of the southward-directed magnetic field is always present. Fast HSS from coronal holes lasts typically several days and attain flow speeds that can reach values above 800 kms^{-1}. For the evolution and structure of CIRs see articles *Baloghet al.,* 1999 as well as *Gosling and Pizzo,* 1999. The main objective of the analysis presented in this article is a comparison of geoeffectiveness caused by different parts of the CIR, measured by the change of the Dst index. In following section we analyse geomagnetic effect of CIRs that were recorded by *in situ* measurements at the Langrangian point L1, focusing on the period from January 2008 to December 2014. In particular, we focus on the Dst index as geomagnetic parameters to analyze in detail the relationship of four basic CIR related solar wind parameters: the magnetic field, B; the flow speed, v; the thermal proton speed, v_{th}; and proton density, Np, in different parts of CIRs, in front and behind the SI. In Section 2 we describe the data set used in this analyze. The data analysis is presented in Section 3, displaying the results for both analyzed parts of CIR. The main results and conclusions of the research are summarized and discussed in Section 4.

The data set

For measuring of solar wind disturbances at L1 point we used the data recorded by the Wind Magnetic Field Investigation (MFI) and Solar Wind Experiment (SWE) with 1 minute resolution data in GSE coordinates (http://wind.nasa.gov/mfi_swe_plot.php). For some SW disturbances we used aditional hourly-averaged level-2 data from ACE satellite (*Stone et al.,* 1998). Data is given at http://www.srl.caltech.edu/ACE/ASC/level2/. The CIR events were separated by detailed analysis of plasma and the magnetic field structure, as described in *Dumbović et al.* 2012. First we identified the increase of the plasma speed above the current background wind speed level, which corresponds to high-speed streams and were related to coronal holes (for details see *Vršnak, Temmer, and Veronig,*2007a). Then, we found the compression region or SI at the rising phase of the HSS from the data of plasma temperature, density and magnetic field (a sharp peak of the density and field strength, as well as sharp increase of temperature). With that data we were able to identify CIRs. For the analyzed period, from 283 solar wind disturbances, 216 have been recognized as a CIRs (76% of all SW samples). From the whole CIRs sample, 61% of CIRs show this typical field and plasma structure and SI inside the CIR can be clearly recognized. Between 216 CIR events, 43 events (15% of whole CIR sample) have complex signatures. Complex signatures are consequences of CIRs or ICME-CIR interactions. These events are are excluded in our analysis. List of CIRs are cataloged for general on the web page of Zagreb Observatory

To exclude CIRs from ICMEs we also checked and compared with our own made database of ICMEs which can be found on the following link at (https://zvjezdarnica.hr/en/programs/science-and-scientific-work/exploring-of-the-icme/list-of-the-icmes/). For recognizing of the accompanied ICMEs we used data from STEREO satellites - SECCHI-COR2 Outer Coronagraph and SECCHI Heliospheric Imager (http://stereo-ssc.nascom.nasa.gov/browse/) SOHO satellite - LASCO C2 Coronagraph (http://lasco-www.nrl.navy.mil/daily_mpg/) and SDO Atmospheric Imaging Assembly (AIA) and Helioseismic Magnetic Imager (HMI) (http://sdo.gsfc.nasa.gov/data/). For the analyzed period we identified 1524 ICMEs. By simultaneously measuring the position angle (PA) in three coronagraphs, two COR2 from STEREO A & B and LASCO C2 chronograph from SOHO, we made a list of Earth directed ICMEs which have high probability to cause solar wind disturbance visible in solar wind data at 1 AU.

Furthermore, for every ICME we made elongation-time measurement, using HM approximation (developed by *Lugaz* 2010; for the application of the HM method see, *e.g*., *Möstl et al.* 2011, *Harrison et al.* 2012, *Rlloett et al.* 2012, and *Temmer et al.* 2012) we calculated the direction and arrival time of ICME at Earth distance. Using this simple method we correlated 105 ICMEs with 67 corresponding solar wind disturbances (24% of all SW disturbances). With this method it was possible to confirm is the CIR connected or affected with the arrival of the ICME. Solar wind signatures connected with the arrival of the ICME were excluded form our analysis.

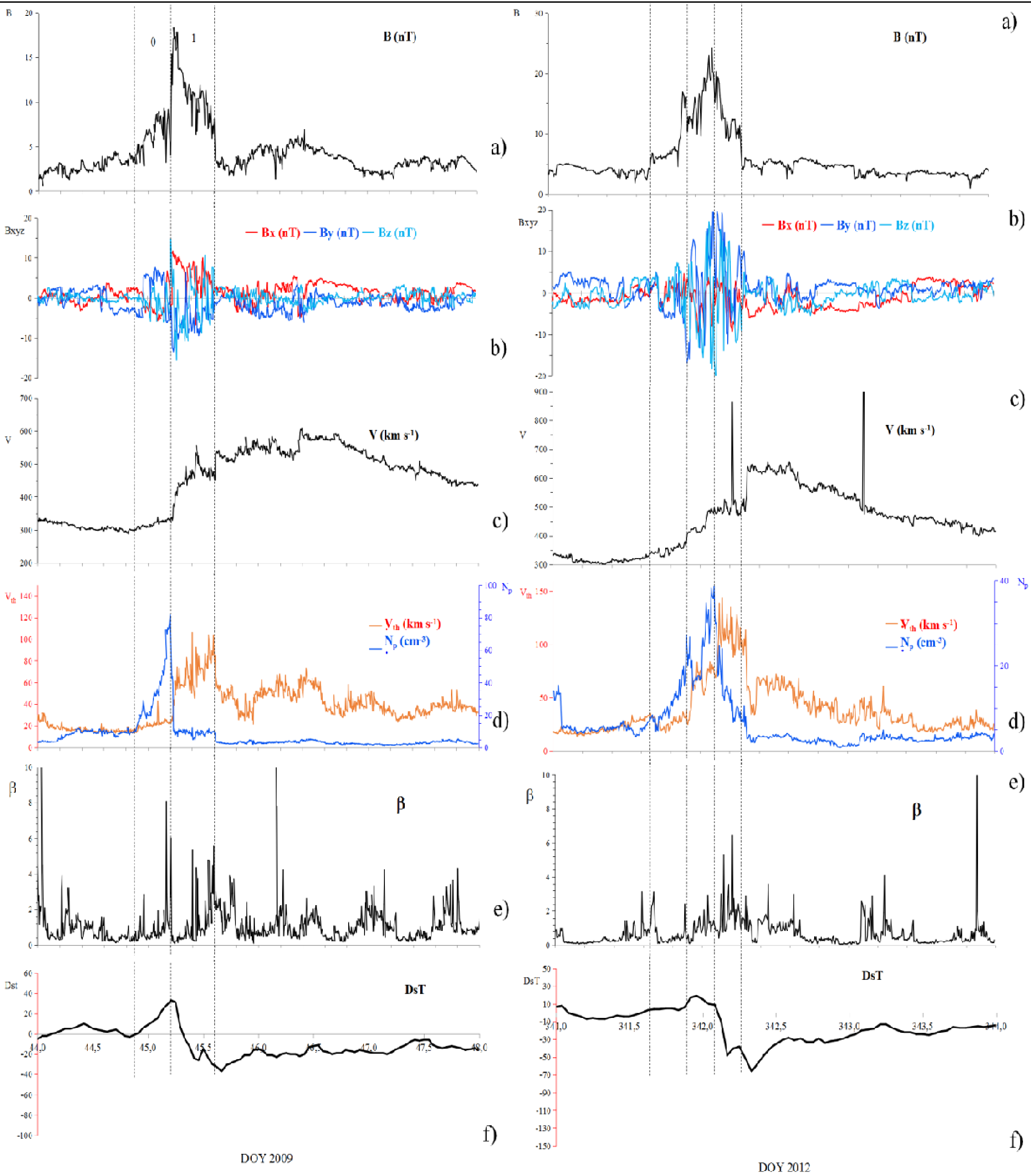

Figure 1. On both sides of presented figures the following labels are: a) the magnetic field strength, b) GSE magnetic field components, c) Theta and Phi magnetic field components d) solar-wind speed, e) proton density and thermal velocity f) plasma-to-magnetic pressure ratio and g) Dst index. Left form a) to g):Example of the CIR in situ WIND measurements at L1 (DOY (day of year) = 44 is 13 February 2009). This CIR, measured by WIND satellite occurred on 13 February 2009, represents events with clearly distinctive features of SI (middle dashed vertical line). The morphology of such CIR can be divided into two different parts: part of the CIR between the front wave and SI (which is marked with number 1) and part of the CIR between SI and reverse wave (which is marked with number 2). Right from a) to g): In situ Wind measurements at L1 (DOY = 341 is 6 December 2012). This CIR, measured by the WIND satellite 13 February 2009, shows events for which is not possible to clearly recognize the features of the SI. First and last vertical dashed line represent forward and reverse waves, while the two middle dashed lines represent two possible stream interfaces or interaction region.

(https://zvjezdarnica.hr/en/programs/science-and-scientific-work/exploring-of-the-icme/list-of-the-sirs-and-cirs/).

We used the Dst index as teh indicator of the geomagnetic activity (see *Rostoker,* 1972). The plasma and magnetic field data for the CIR were compared with Dst values we obtained from Kyoto University given at http://wdc.kugi.kyoto-u.ac.jp/dstdir/index.html. The geomagnetic disturbance index Dst (*Sugiura and Wilson,* 1964) represents the axially symmetric surface disturbance at the dipole equator of Earth, based on the hourly-averaged measurements of the horizontal magnetic field performed by four low latitude observatories. A decrease in Dst index is mainly caused by the ring current perturbation, while an weak increase in Dst is related to the compression of the magnetosphere caused by the increase in the solar wind dynamic pressure (frontal compression in the CIR).

Analysis

Correlation between Dst data with the solar wind *in situ* data, measured by WIND at L1, are shown in Figure 1. In Figure 1; in every plot the date is expressed as DOY. The *in situ* data in Figure 1 (left graphs) reveal the structure of the CIR, consists of two different parts (separated by vertical dashed lines). Middle vertical dashed line represents stream interface. In both parts we measured magnetic field strength, change in GSE magnetic field components, flow speed, maximum and minimum values of the flow speed components, temperature, proton density, plasma-to-magnetic field pressure (β) and change of Dst index. First region, which we have marked with number 1 (part of the CIR between front wave and SI) is characterized by a gradual increase of magnetic field strength, decreased temperature, strong increase of proton density and increase of Dst index. Second region, which we have marked with number 2 (part of the CIR between SI and reverse wave) is characterized by a sharp drop of proton density, increased magnetic field strength, flow speed and temperature.

In Figure 1 (right graphs) the *in situ* - Dst data for the CIR signatures are recognized as events with complex signatures. As an example we take a CIR which arrives at L1 distance on 6 December 2012. For such CIRs it was not possible to clearly recognize the SI, but it was possible to recognize two or more SI, which can be casued by CIRs or ICME-CIR interaction. Those CIRs (43 events out of 216 CIRs for analyzed period, or 15% of whole CIRs semple) were excluded from further analysis. From Figure 1 (left), we concluded that in all CIRs with the "two part" structure, a weak positive increase of the Dst index occurs in the transition period for part 0 (between front wave and SI). The maximum Dst index is synchronized with SI, while the Dst index decrease occurs during the transition period of the part 1 (between SI and reverse wave). The results concerning the analyzed period (from January 2008 to December 2014) are presented in graphical form in Figures 2 - 4.

In Figures 2 we presented the scatter plots relating the change of Dst index (maximum minus minimum values) to the measured solar wind magnetic field strength, proton density, flow speed and temperature over the analyzed period. In Figures 2a-d we ploted solar wind data measured for part 0, while in Figure 2e-h we show measured values for region 1. The correlations for region 0 are very weak (cc = 0.57, 0.43, 0.18 and 0.56, respectively) and for region 1 are significantly higher (cc = 0.72, 0.62, 0.45 and 0.64, respectively).

Also, correlation for magnetic field strength and temperature are in both parts higher than correlations for proton density and flow speed. The graphs reveal a quite well defined lower and upper limits to Dst (B), Dst (Np), Dst (v) and Dst (v_{th}), indicated by the dotted line. There is no Dst activity for B in region 0 below 3 nT and in region 1 below 5 nT. Furthermore, there is no Dst activity for B in region 0 above 20 nT and in region 1 above 25 nT. In every graph we displayed the linear last-squares fit for Dst - solar wind parameter related data.

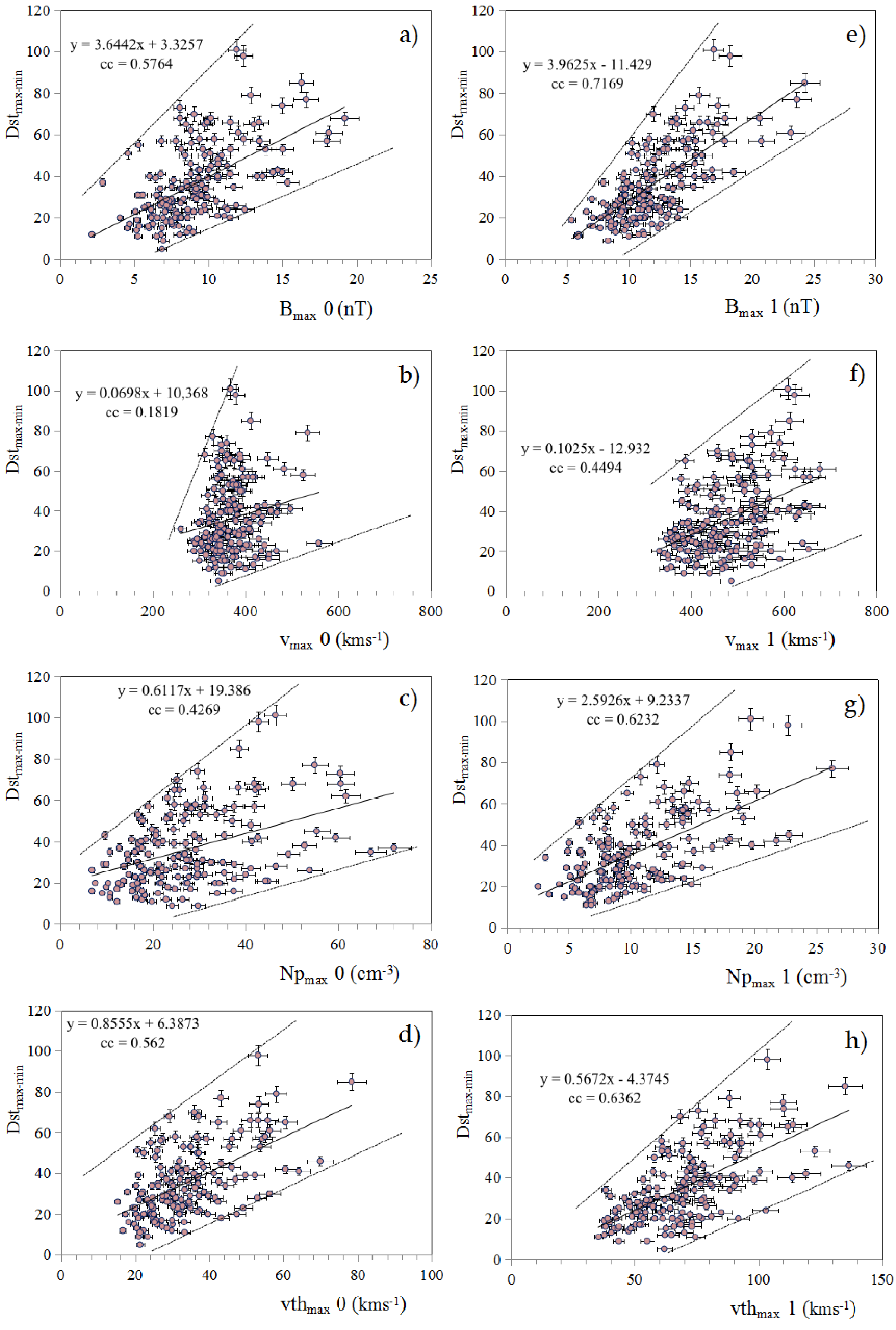

Figure 2. On both sides of presented figures the following labels are: a) the magnetic field strength, b) solar-wind speed, c) proton density and d) thermal velocity. Dashed line represents provisional drawn possible lower and heights values for the specific solar wind parameter. Variation of the Dst geomagnetic activity parameter (maximum - minimum values) versus four solar wind parameters measured in left for part 0 and right for part 1 (before SI, marked by 0).

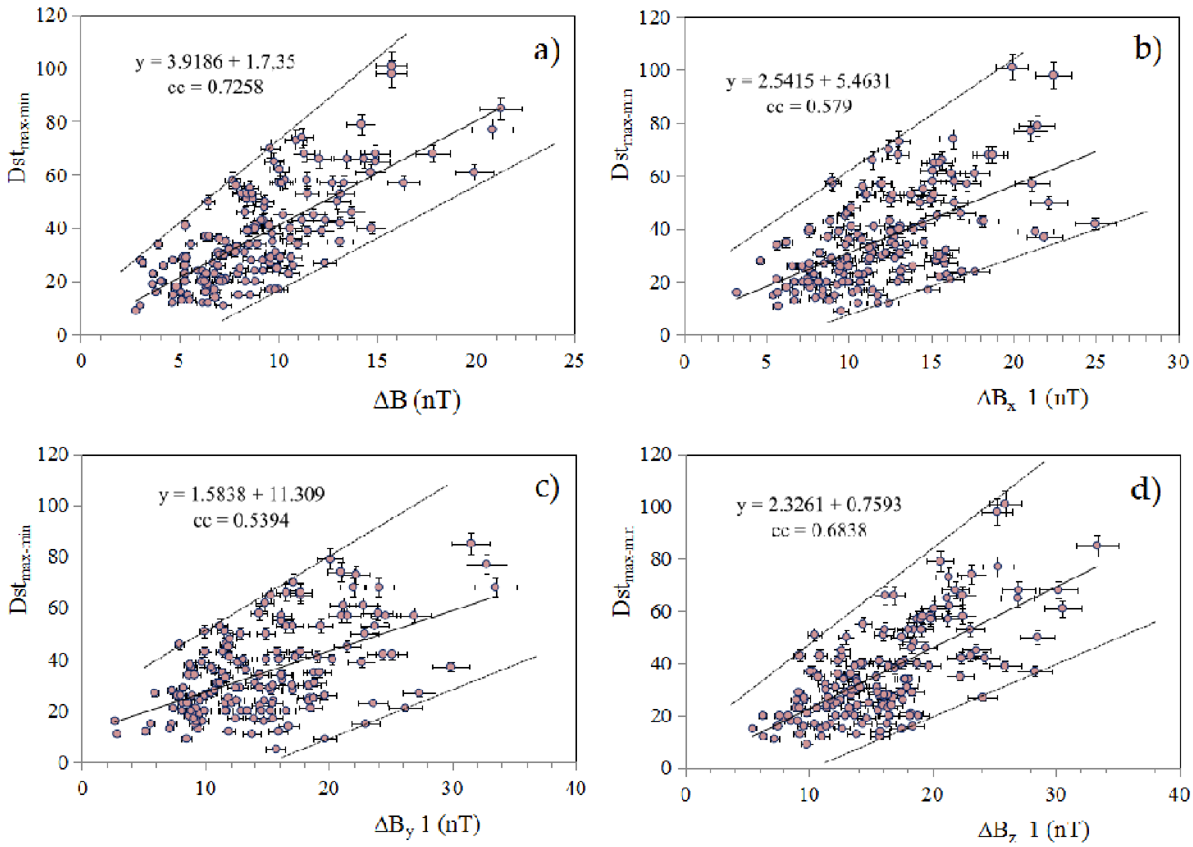

Figure 3. Variation of the Dst geomagnetic activity parameter versus ΔB - difference between maximum of magnetic field strength in region 1 and 0 (a), versus B_x (b), versus B_y (c) and versus B_z (d). Dashed line represents a provisional lower and heigher values for the specific solar wind parameter.

Furthermore, because solar wind parameters show stronger correlations with Dst index in region 1, we made additional analysis of the GSE magnetic field and flow speed components for that region. In Figure 3a we presented the scatter plots of Dst index versus ΔB (difference between maximum of magnetic field strength in region 1 and 0). Also, in Figure 3b, c and d the scatter plots are given of Dst index versus variation of the CIR magnetic field components, B_x, B_y and B_z, in region 1. There are significant correlations for ΔB, B_x and B_z components, with correction coefficient of cc = 0.73, 0.58 and 0.68, respectively. A weak but significant correlation cc ~ 0.54 , was also found for B_y component.

In Figure 4 we presented the dependence of the Dst versus Δv (difference between measured maximum of the flow speed in region 1 and 0), as well as variation (difference between measured maximum and minimum values) of the CIR flow speed components, v_x, v_y and v_z in region 1. The Figure 4 shows higher correlation between Δv and all flow speed components, but lower correlation between Δv and flow speed in both measured regions (Figure 2b and f). The correlation cc = 0.6 for Δv, is the highest correlation coefficient for Dst(v) of the CIR in both regions. Very weak correlation (cc = 0.46) was found for v_z component of the flow speed in region 1, while for v_x and v_y the correlations are higher cc = 0.59 and 0.56, respectively.

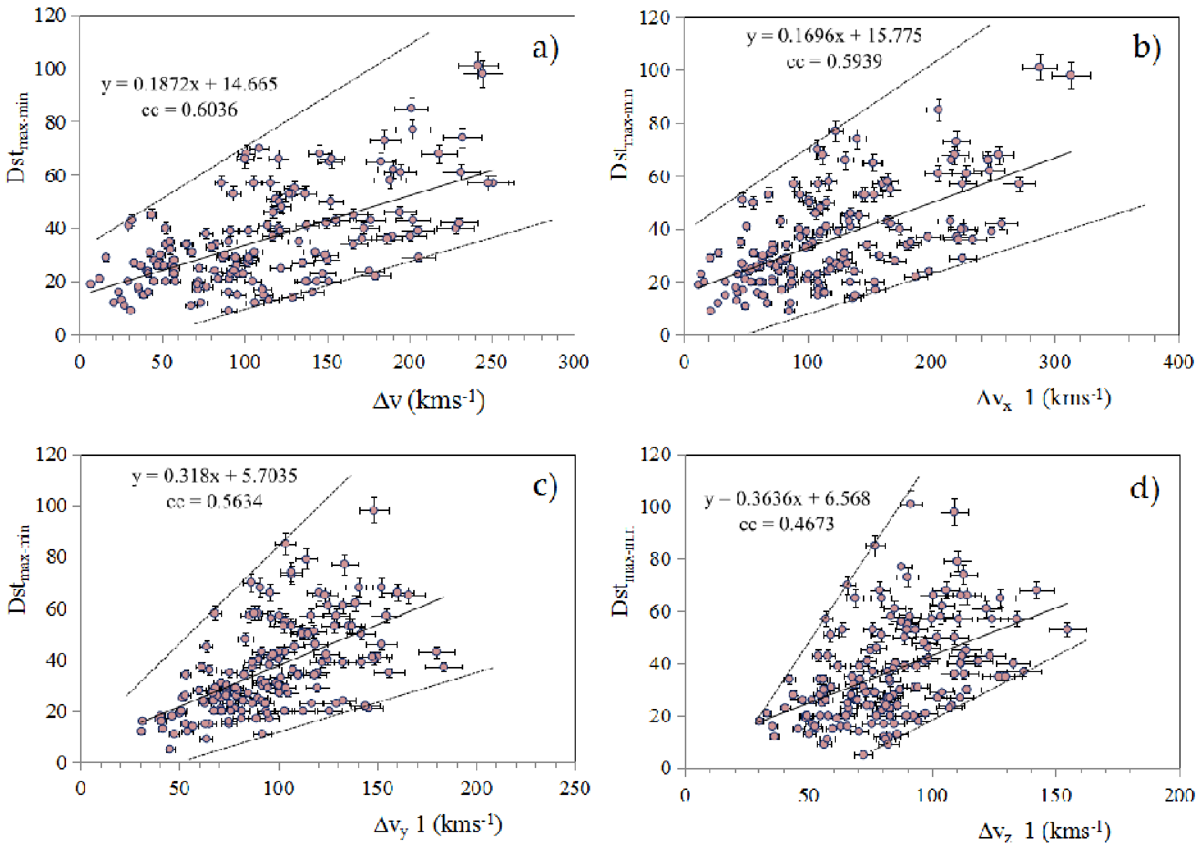

Figure 4. Variation of the Dst geomagnetic activity parameter versus Δv - difference between maximum of measured flow speed in region 1 and (a) 0, versus v_x (b), versus v_y (c) and versus vz (d) flow speed components. Dashed line represents a provisional lower and heigher values for the specific solar wind parameter.

Discussion and Conclusion

We summaries the main results of our analysis of the geoeffectiveness of two CIRs regions (before and after SI) as follows :

a) For 95% CIRs we analyzed, an increase of Dst index occurs between forward shock and SI (part marked as region 0), while the main decreases of Dst index occurs between SI and reverse shock of CIR (part marked as a region 1).
b) The correlation coefficients between the Dst index and the magnetic field *B*, proton density *N*p, flow speed *v* and proton thermal speed v_{th}, in the region behind the SI are: cc = 0.72, 0.62, 0.45 and 0.64, respectively.
c) Correlations for regions between forward shock and SI are significantly lower.
d) The correlation for magnetic field strength and temperature are in both regions higher than correlations for proton density and flow speed.

We would like to thank the WIND, ACE, SOHO, STEREO, SDO and Kyoto university teams for developing and operating the instruments and we are grateful for their open data policy.

References

Balogh, A., Gosling, J.T., Jokipii, J.R., Kallenbach, R., Kunow, H.: 1999, Corotating interaction regions.Space Sci. Rev. 89, 1.

Dumbovicć, M., Vršnak, B., Čalogović, J., Župan, R.: 2012, Cosmic ray modulation by different types of solarwind disturbances. Astron. Astrophys. 538, A28.

Gosling, J.T.: 1996, Corotating and transient solar wind flows in three dimensions. Annu. Rev. Astron. Astrophys.34, 35.

Gosling, J.T., Pizzo, V.J.: 1999, Formation and evolution of corotating interaction regions and their threedimensional structure. Space Sci. Rev. 89, 21.

Hajra, R., Echer, E., Tsurutani, B.T., Gonzalez, W.D.: 2013, Solar cycle dependence of high-intensity longdurationcontinuous AE activity (HILDCAA) events, relativistic electron predictors? J. Geophys. Res.118, 5626.

Harrison, R. A., Davies, J. A., Möstl, C., Liu, Y., Temmer, M., Bisi, M. M., et al.: 2012, Astrophys. J. 750, 45.

Lugaz, N.: 2010, Solar Phys. 267, 411-429.

Möstl, C., Rollett, T., Lugaz, N., Farrugia, C.J., Davies, J. A., Temmer, M., et al.: 2011, Astrophys. J. 741,34.

Rotter, T., Veronig, A.M., Temmer, M., Vršnak, B.: 2012, Relation between coronal hole areas on the sunand the solar wind parameters at 1 AU. Solar Phys. 281, 793.

Rostoker, G.: 1972, Geomagnetic indices. Rev. Geophys. Space Phys. 10, 935.

Smith, E.J., Wolfe, J.H.: 1976, Observations of interaction regions and corotating shocksbetween one andfive AU – Pioneers 10 and 11. Geophys. Res. Lett. 3, 137.

Stone, E.C., Frandsen, A.M., Mewaldt, R.A., Christian, E.R.,Margolies, D., Ormes, J.F., Snow, F.: 1998, Theadvanced composition explorer. Space Sci. Rev. 86, 1.

Sugiura, M., Wilson, C.R.: 1964, Oscillation of the geomagnetic field lines and associated magnetic perturbationsat conjugate points. J. Geophys. Res. 69, 1211.

Temmer, M., Vršnak, B., Veronig, A.M.: 2007, Periodic appearance of coronal holes and the related variationof solar wind parameters. Solar Phys. 241, 371.

Tsurutani, B.T., McPherron, R.L., Gonzalez, W.D., Lu, G., Sobral, J.H.A., Gopalswamy, N.: 2006, Introductionto special section on corotating solar wind streams and recurrent geomagnetic activity. J. Geophys.Res. 111, 1.

Vennerstroem, S.: 2001, Interplanetary sources of magnetic storms: a statistical study. J. Geophys. Res. 106,29175.

Verbanac, G., Vršnak, B., Veronig, A., Temmer, M.: 2011a, Equatorial coronal holes, solar wind high-speedstreams, and their geoeffectiveness. Astron. Astrophys. 526, A20.

Verbanac, G., Vršnak, B., Živković, S., Hojsak, T., Veronig, A.M., Temmer, M.: 2011b, Solar wind high-speedstreams and related geomagnetic activity in the declining phase of solar cycle 23. Astron. Astrophys. 533,A49.

Vršnak, B., Dumbović, M., Čalogović, J., Verbanec, G., Poljanić-Beljan, I.: 2017, Geomagnetic Effects of Corotating Interaction Region. Solar Phys. 292, 140.

Vršnak, B., Temmer, M., Veronig, A.M.: 2007a, Coronal holes and solar wind high-speed streams: I. Forecastingthe solar wind parameters. Solar Phys. 240, 315.

Ground-based geomagnetic signature of the 7-8 September 2017 magnetic storm as a farewell gift from solar cycle 24

Kleimenova N.G. [1], *Gromova L.I.* [2], *Gromov S.V.* [2], *Malysheva L.M.* [1]

[1] Institute Physics of the Earth RAS, Moscow, Russia
[2] IZMIRAN, Moscow, Troitsk, Russia
E-mail: kleimen@ifz.ru, gromova@izmiran.ru

Abstract

In the first half of September 2017, i.e. at the end of the 24-th cycle of the solar activity declining, there was suddenly occurring one of the most flare-productive periods. The coronal mass ejection associated with the 06 September X-9 flare produced severe (Kp = 8) geomagnetic storms on 07 and 08 September. Here we study the high-latitude ground-based geomagnetic variations in conjunction with the solar wind and Interplanetary Magnetic Field changes. Our analysis was based on the observations at the closely spaced Scandinavian IMAGE magnetometer chain. It was shown that in the first storm recovery phase, the main geomagnetic disturbances were concentrated at dayside polar latitudes. The specific behavior of geomagnetic pulsations was found in association with the variating space weather conditions.

Introduction

The solar activity in the solar cycle 24 was about twice weaker than in the solar cycle 23 and the average sunspot number is known to have declined by ~40%. [e.g., *Gopolswami et al.*, 2015, *Lepping et al.*, 2015]. It is clearly seen in Fig.1. Comparing to the cycle 23, the maximum and beginning of the declining phase of the solar cycles 24 had no geoeffective CMEs at all. In the other hand, there were many geoeffective magnetic clouds in the cycle 23.

An extreme event had happened in the end of the declining phase of the cycle 24 (September 2017). The distribution of the planetary magnetic activity (Kp-index) during 2017 is shown in Fig. 2 demonstrating that there was only one interval of really strong activity – in the beginning of September. Probably, it was the last strong magnetic disturbances in the solar cycle 24.

The interval of 04-10 September 2017 was one of the most flare-productive periods of now-waning solar cycle 24. Two solar active regions produced more than a dozen M-class flares. The arrival of the coronal mass ejection associated with the 6 September X-9 flare resulted severe geomagnetic storming on 7 - 8 September with the lowest Dst about -150 nT. Comparing with the solar cycle 23, during the cycle 24, there were not many strong magnetic storms, due to that, the September 2017 magnetic storm attracts attention special attention.

The main aim of this study is to analyze the high-latitude geomagnetic variations associated with this geoeffective period of the solar cycle 24.

Strong magnetic storm on 07-08 September 2017

The progression of Kp and Dst indices during the considered geomagnetic interval is shown in Fig. 3. This magnetic disturbance could be classified as a two-steps magnetic storm or as two separated magnetic storms because they had different drivers in the solar wind..

The first event was caused by the arrival of a magnetic cloud (MC) with the sheath, i.e. with the plasma compression region before MC, but the second one – by a sudden change of IMF Bz polarity from positive to strong negative under the high (~800 km/s) and relative constant solar wind velocity and very enhanced (~8 nPa) solar wind dynamic pressure (Psw).

On the ground, the strongest magnetic disturbances were observed on 8 September. To study their peculiarities, we analyzed the data obtained from the Scandinavian IMAGE

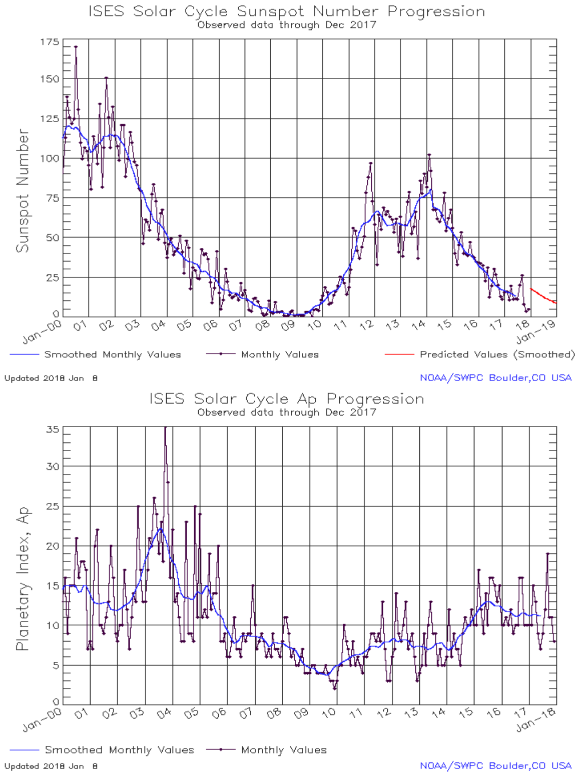

Fig. 1. Solar (upper) and geomagnetic (bottom) activity in the solar cycles 23 and 24

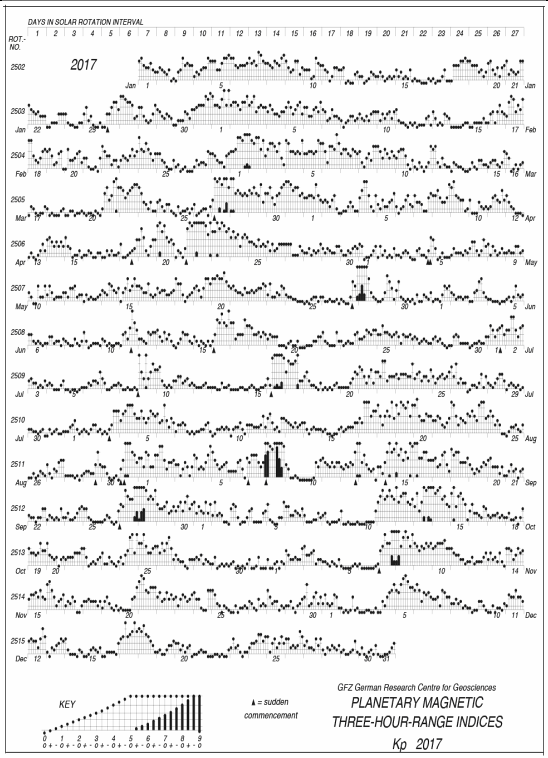

Fig. 2. The variations of the Kp-index in 2017

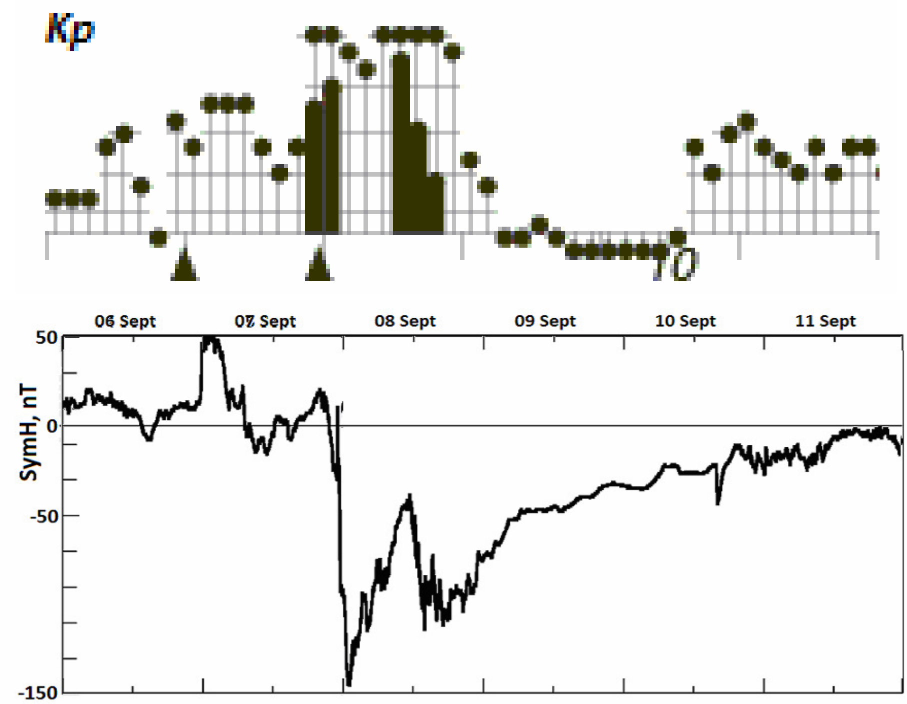

Fig. 3. The Kp and SymH (Dst) progression on 06-11 September 2017

network of magnetometers [*Viljanen and Häkkinen*, 1997]. The solar wind speed (V), its dynamic pressure (Psw) and Interplanetary Magnetic Field (IMF) variations according to the OMNI data as well as the correspondent geomagnetic indices of the auroral substorm activity

(AL-index) and the ring current intensity (Dst-index) are given in Fig.4a for the considered time interval (from 20 UT on 07 September to 20 UT on 08 September). The simultaneous IMAGE ground geomagnetic observations are shown in Fig 4b.

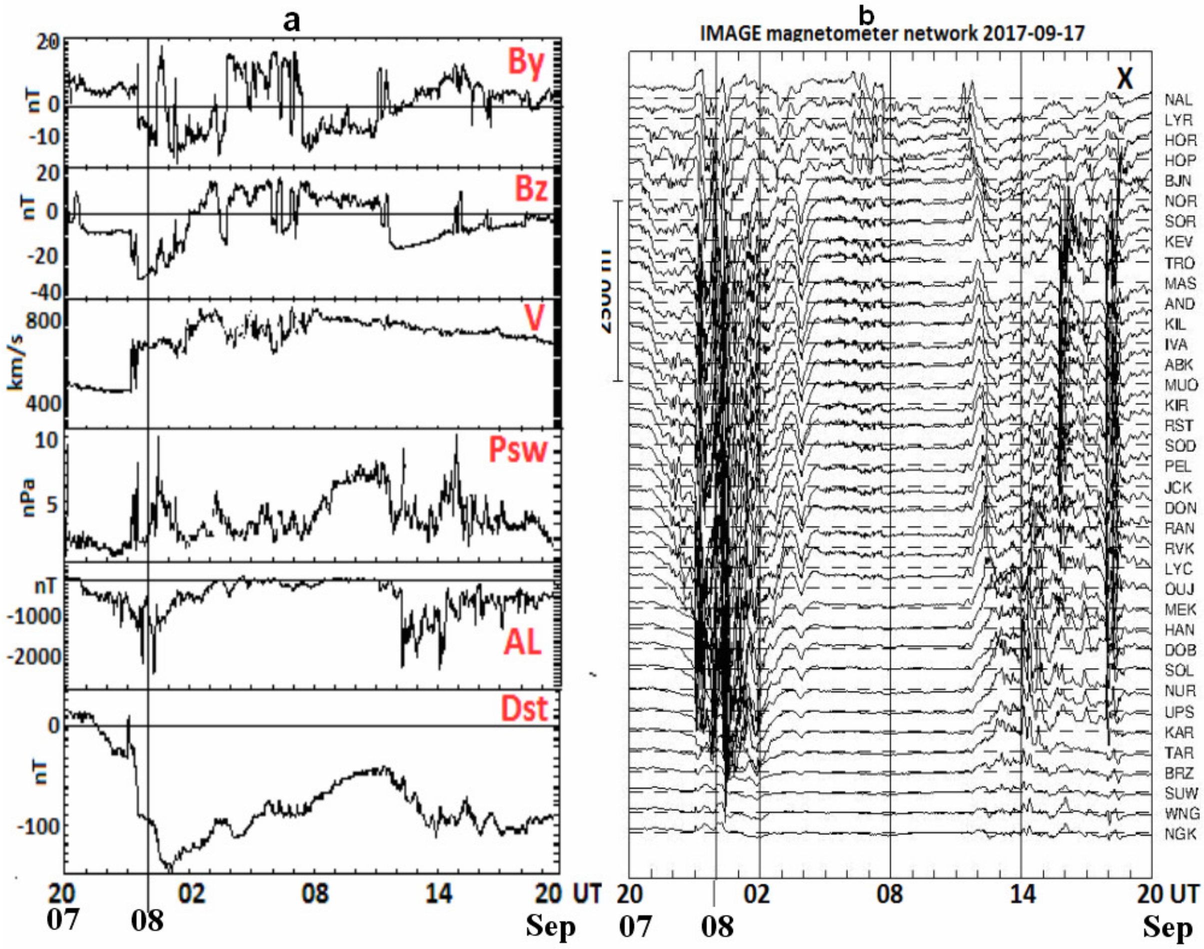

Fig. 4. a) The variations of the IMF Bz and By, solar wind speed (V) and the dynamic pressure (Psw) as well as AL and Dst; b) the magnetograms from Scandinavian IMAGE chain.

The main phase of first magnetic storm was started on 07 September at 23.15 UT after the Storm Sudden Commencement (SSC) caused by the strong Psw jump associated with the sheath arrival under the negative IMF Bz. The night-side substorm activity became very strong, and AL-index reached the values up to ~2500 nT.

At ~02 UT, the sign of IMF Bz changed to the positive values, so, the input of the solar wind energy ceased, substorm activity decreased, and the storm recovery phase started accompanying by the typical geomagnetic Pc5 pulsations generation in the morning sector of the magnetosphere.

Near 11.40 UT the IMF Bz suddenly changed the sign from positive to negative, and the new magnetic storm (or the second step of the first storm) began to develop (see Fig. 4a). Simultaneously, the night-side substorm activity enhanced. Contrary to the onset of the first magnetic storm on 07 September, the second magnetic storm (or the second step) started under the decreasing solar wind dynamic pressure and practically non-changing solar wind speed. There was no SSC before this storm.

The untypical IMF feature was observed in the early recovery phase of the first magnetic storm. At 06-08 UT, there was recorded the unusual IMF structure, namely, very strong fluctuations in IMF Bz and By occurred with the quasi-periods about 20 min and magnitudes about 20-25 nT. The variations in the IMF Bz and By were strongly in the antiphase. These variations suddenly stopped at about 08 UT, and the IMF Bz became steadily positive, and the

IMF By – steadily negative. At that time, the solar wind dynamic pressure (Psw) began increase more than twice.

Unfortunately, in this time, there were no satellite data near dayside magnetosphere: both geostationary GOES (spacecraft GOES 13 and 15) were located in the night sector of the Earth, and the THEMIS probes were located too close to the Earth surface.

During these strong IMF Bz and By fluctuations, there were no night-side magnetic substorms on the ground. However, the very strong magnetic disturbances were observed at the day-side sector of the Earth at the polar geomagnetic latitudes.

The ground-based IMAGE magnetometer data demonstrate the similar fluctuations at high-latitude stations BJN-NAL, i.e. at geomagnetic latitudes of 71-75^0 (Fig. 4b), with very strong amplitudes, up to 300-400 nT. Simultaneously, at the lower latitudes, the quasi-monochromatic Pc5 range geomagnetic pulsations at the frequency 2.5-3.0 mHz have been recorded.

The more detailed interplanetary and selected ground-based data are presented in Fig. 5

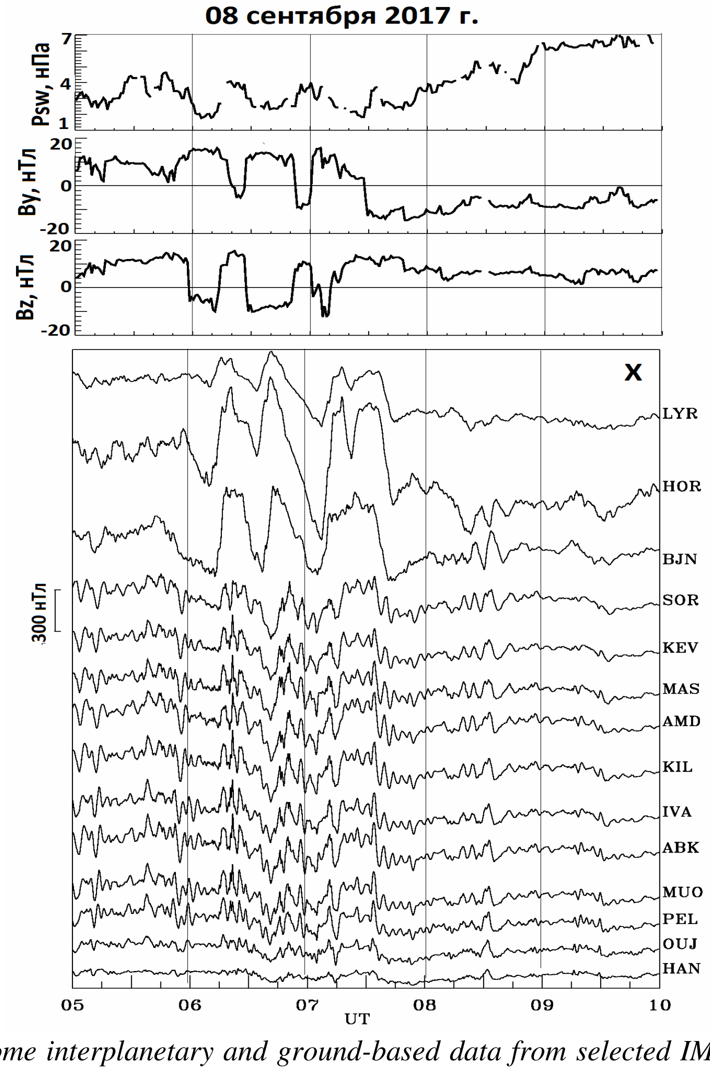

Fig.5. Some interplanetary and ground-based data from selected IMAGE stations in the interval of 05-10 UT on 08 September 2017

for 10 hours interval of 05-10 UT on 08 September. The good agreement between the occurrence of the IMF Bz and By fluctuations and the high-latitude geomagnetic variations are clearly seen. Each positive burst of IMF Bz was accompanied by the burst of Pc5 geomagnetic pulsations at OUJ-SOR IMAGE stations, i.e. at geomagnetic latitudes of 61-67^0 (Fig. 5).

The pulsation frequency was the same at all these latitudes. The occurrence of the negative IMF Bz burst resulted the Pc5 pulsation disappearance.

The 1D Ionospheric Equivalent Currents, assumed at 100 km altitude according to MIRACLE data (www. space.fmi/MIRACLE) are presented in Fig.6. The strong time-enhancements of these currents are seen in the polar latitudes. Long vertical yellow bands which continued separated polar bursts are represent the Pc5 geomagnetic pulsations generated simultaneously at large lower-latitude area. Such strange complicated ionospheric current structure was observed at the IMAGE stations for the first time.

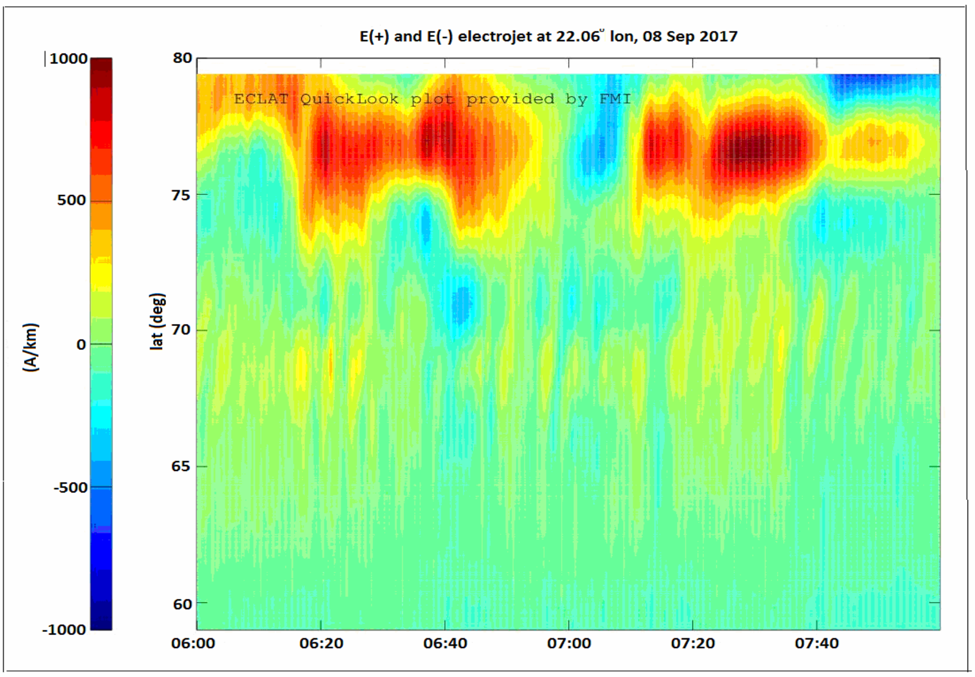

Fig.6. The 1D Ionospheric Equivalent Currents according to MIRACLE data

Discussion

We did not find the detail coincidence between the IMF Bz and By fluctuations and the ground dayside polar magnetic disturbances at 06-08 UT. However, the onset and end of both phenomena were observed simultaneously. Thus, we may suppose that these ground-based long-period polar geomagnetic variations were caused by the IMF fluctuations by some non-linear interaction processes in the turbulent bounder layer of the dayside magnetopause or near the dayside polar cusp.

The considered strong polar geomagnetic variations look like the discussed in the paper [*Kleimenova et al*., 1985] the long-period geomagnetic pulsations which were observed at the polar latitude Greenland stations and were called VLP-pulsations (*Very Long Period*).The similar geomagnetic pulsations have been reported by *Clauer* et al [1995] in association with quasi-periodic changes of IMF By. They were called "*Poleward progressing ionospheric convection disturbances*". The similar geomagnetic pulsations were published by *Pilipenko et* al. [2000] and were termed $P_{DPY}6$. However, in our case, the variations were observed not only in the IMF By, but in the IMF Bz as well. Moreover, all mention above long-period geomagnetic pulsations were observed under the negative IMF Bz. But in our case, such pulsations were observed under the positive IMF Bz.

Another plausible driver of these polar-latitude geomagnetic pulsations generation could be quasi-periodic changes of the magnetopause position as it was discussed in some papers, e.g. [*Dmitriev et al*., 2005]. Really, in the considered time interval, the long-period variations in the solar wind dynamic pressure are seen at 06-08 UT (the upper part of Fig. 5). Such pressure variations could cause the quasi-periodic motions of the magnetopause location leading to the large scale high-latitude ionospheric vortices in the dayside sector of the Earth which are looked at the ground-based polar latitude stations as the long-period geomagnetic pulsations.

Summary

- The abrupt increase of the solar activity in September 2017 produced severe geomagnetic storming.
- The 07-08 September 2017 magnetic storm represents the two-step storm or two different successive storms. The sudden jump of the solar wind dynamic pressure (Psw) under negative values of the IMF Bz formed the Storm Sudden Commencement (SC) and resulted the rapid development of the first storm main phase.
- The second storm was caused by the change of the IMF direction (from positive to negative) under strong Psw level which significantly decreased with IMF change.
- The IMF irregularity was observed in the first storm recovery phase as the 3 hours spike of the strong IMF By and Bz "dancing" values (up to 20 nT) which caused the very intense (up to 500 nT) magnetic variations at the polar latitudes both at day and night sides.
- Simultaneously with these polar variations, a long series of the Pc5 resonant geomagnetic pulsations have been generated in the inner magnetosphere. The sequence of Pc5 pulsation bursts were controlled by the IMF By and Bz variations.
- There were no Pc5 pulsations in the recovery phase of the second storm.

Acknowledgements

This work was supported by the State tasks of IPE RAS and IZMIRAN.

References

Clauer, C.R., P. Stauning, T.J. Rosenberg, E. Friis-Christensen, P.M. Miller, and R.J. Sitar (1995), Observations of solar-wind-driven modulation of dayside ionospheric DPY current, J. Geophys. Res., 100, 7607-7713.

Dmitriev, A., J.-K. Chao, M. Thomsen, and A. Suvorova (2005), Geosynchronous magnetopause crossings on 29-31 October 2003, J. Geophys. Res., 110, A08209, doi:10.1029/2004JA010582.

Gopalswamy, N., S. Yashiro, H. Xie, S. Akiyama, and P. Mäkelä (2015), Properties and geoeffectiveness of magnetic clouds during solar cycles 23 and 24, J. Geophys. Res. Space Physics, 120, 9221–9245, doi:10.1002/2015JA021446.

Kleimenova, N.G., O.V. Bol'shakova, V.A. Troitskaya, and E. Friis_Kristensen (1985), Two types of long_period geomagnetic pulsations near the equatorial boundary of the daytime polar cusp, Geomagn. Aeron., 25 (1), 163–164.

Lepping, R.P., C.-C. Wu, and D.B. Berdichevsky (2015), Yearly comparison of magnetic cloud parameters, sunspot number, and interplanetary quantities for the first 18 years of the wind mission, Sol. Phys., 290, 553–578.

Pilipenko, V.A., E.N. Fedorov, M.J. Engebretson, V.O. Papitashvili, and J. Watermann (2000), Poleward progressing quasi-periodic disturbances at cusp latitudes: The role of wave processes, J. Geophys. Res., 105, A12, 27, 569-27,588.

Viljanen, A., and L. Häkkinen (1997), IMAGE magnetometer network, Satellite-ground based coordination sourcebook, ed. Lockwood, M., Wild, M. N., and Opgenoorth, H. J., ESA publications SP-1198. 111–117.

Interplanetary conditions leading to dayside magnetic bays during the initial phase of magnetic storms

Gromova L.I. [1], *Kleimenova N.G.* [2], *Gromov S.V.* [1]

[1] IZMIRAN, Moscow, Troitsk, Russia
[2] Institute Physics of the Earth (IPE) RAS, Moscow, Russia
E-mail: gromova@izmiran.ru

Abstract

We present a study of magnetic bay-like disturbances occurred in the dayside sector of the high geomagnetic latitudes under different conditions in the Interplanetary Magnetic Field (IMF) and the solar wind (SW). As a rule, such disturbances are recorded under the positive Bz component of IMF. This situation is often observed during a long-lasting initial phase of a magnetic storm. We compared the geomagnetic effects, such as dayside magnetic bay generation, caused by interplanetary shocks (Si) that attacked the magnetosphere during the initial phase of the storms on 07-08 September 2017 and 21-23 June 2015. We showed that the appearance of the dayside high-latitude bays was collocated with the enhanced Field-Aligned Currents (FAC) obtained by the AMPERE products from the Iridium satellite constellation. We found that the rapid fluctuations in IMF components could block the development of dayside polar bays associated with Si. The ground-based magnetograms demonstrate repeatable features in the conjunction with the Bz and By IMF components.

Introduction

The solar wind and Interplanetary Magnetic Field (IMF) variations cause different disturbances in the geomagnetic field measured on the Earth’s surface. It was shown that dayside high-latitude magnetic bays are frequently observed under the positive Bz component of IMF [e.g., *Levitin et al.*, 2015; *Kleimenova et al.*, 2015; *Gromova et al.* 2016]. Such IMF conditions are often observed during the initial phase of magnetic storms characterized by variable positive or weakly negative IMF Bz

The storm initial phase is frequently caused by an interplanetary shock impact. But whether or not an interplanetary shock can ‘‘induce’’ a dayside polar magnetic bay depends on the concurrent SW and IMF conditions. Generally, under a positive IMF Bz, there is no energy input into the magnetosphere, however, in the high latitudes, dayside bay-like magnetic disturbances were observed. They could be associated with the dayside high-latitude ionospheric electric current enhancements [e.g., *Iwasak*i, 1971; *Friis-Christensen and Wilhjem*, 1975; *Feldstein*, 1976, *Feldstein et al.*, 2006]. It is known that the jumps of the solar wind dynamic pressure (Psw) enhance the daytime high-latitudes Field-Aligned Currents (FAC) and the corresponding ionospheric currents [e.g., *Lukianova*, 2004].

The aim of our investigation is to study IMF and SW conditions leading to dayside polar magnetic bays during the initial phase of the storms on 21-23 June 2015 and 07-08 September 2017.

Data

Our study is based on: (i) IMF data sets of the high resolution OMNI database (http://omniweb.gsfc.nasa.gov), (ii) the ground-based IMAGE magnetometer chain data (http://www.ava.fmi/MIRACLE), (iii) data set of INTERMAGNET global network of observatories (http://www.intermagnet.org), (iiii) the AMPERE data, based on the magnetic measurements on 66 low-altitude globally distributed Iridium communication satellites (http://ampere.jhuapl.edu/products/plots).

The solar wind and IMF variations during the initial phases of the magnetic storms on 21-23 June 2015 and 07-08 September 2017

The magnetic storms of 21-23 June 2015 and 07-08 September 2017 were the most intensive storms of the 24-the solar cycle. They have long-lasting initial phase (about 28 and 24 hours correspondingly) characterized by variable positive or weakly negative IMF Bz (Fig. 1).

The initial phases of the both storms started when the interplanetary shock (Si), i.e., the jump of the solar wind proton density (Np) and velocity (V) forming the SW dynamic pressure (Psw), impact the Earth's magnetosphere and compressed it.

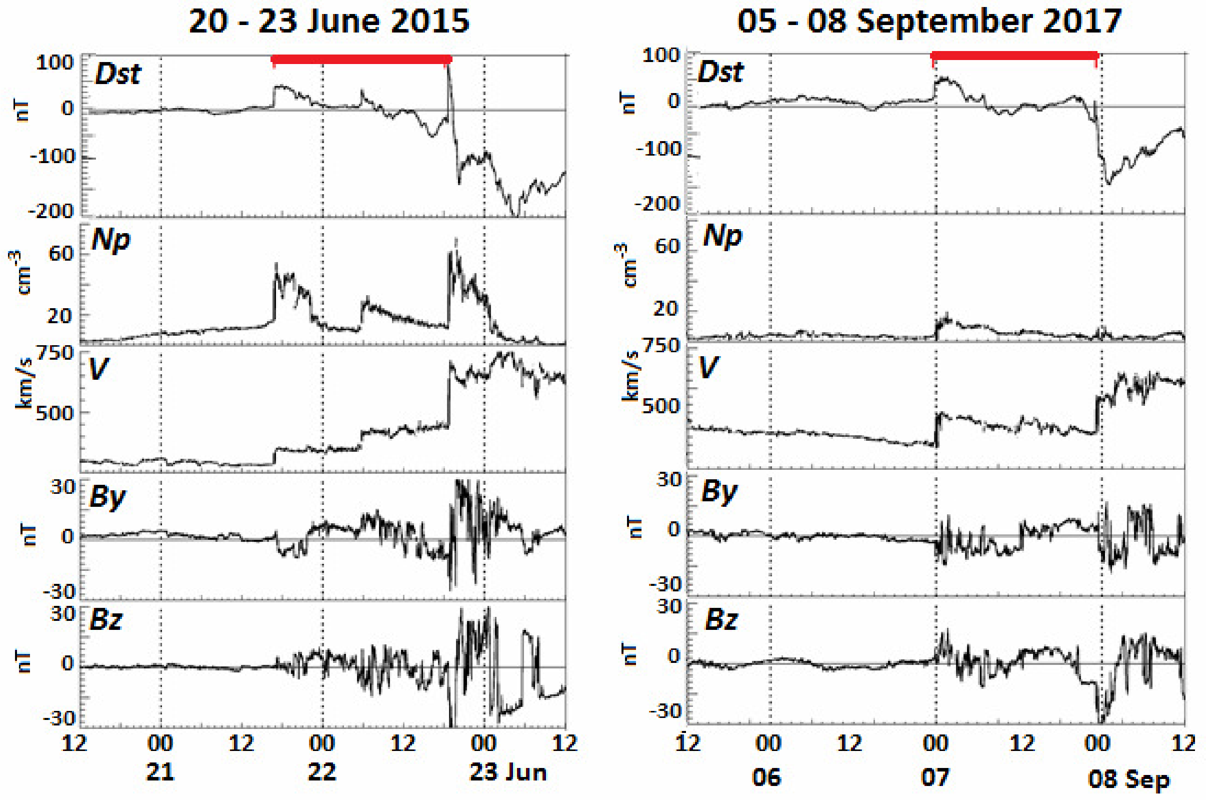

Fig. 1. Variations of the Dst index of the magnetic storm intensity, SW and IMF parameters on 20 - 23 June 2015 and 05 - 08 September 2017. The initial phase of each storm is marked by red.

Magnetic storm on 21-22 June 2015

This storm was caused by a double solar flare of class M with the following three coronal mass ejections (www.izmiran.ru/services/saf/archive/) accompanied by three sharp jumps of the solar wind dynamic pressure (Fig.1).

The first two Si impulses did not lead to the development of a magnetic storm (i.e. ring current enhancement), since the IMF Bz remained positive for a long time after the shocks, but they caused dayside high-latitude magnetic bays.

Figure 2 shows that at 16.45 UT on 21 June 2015, the Si caused the negative dayside polar bay immediately after *Si* in the near-noon sector (e.g., RES and THL stations). Thus, the westward polar electrojet (PE) was developed due to the increased ratio (|IMF By|/|IMF Bz| >1) under the negative IMF By and positive IMF Bz.

At the same way, immediately after the second Si, at 05.44 UT on 22 June 2015, under the intensive positive IMF By (|By|/|Bz| >1), the positive dayside bay was observed near local noon at the polar latitudes (NAL-HOR stations). The fluctuations of the X component at the ground-based stations could be caused by the sharply changes of the IMF Bz sign.

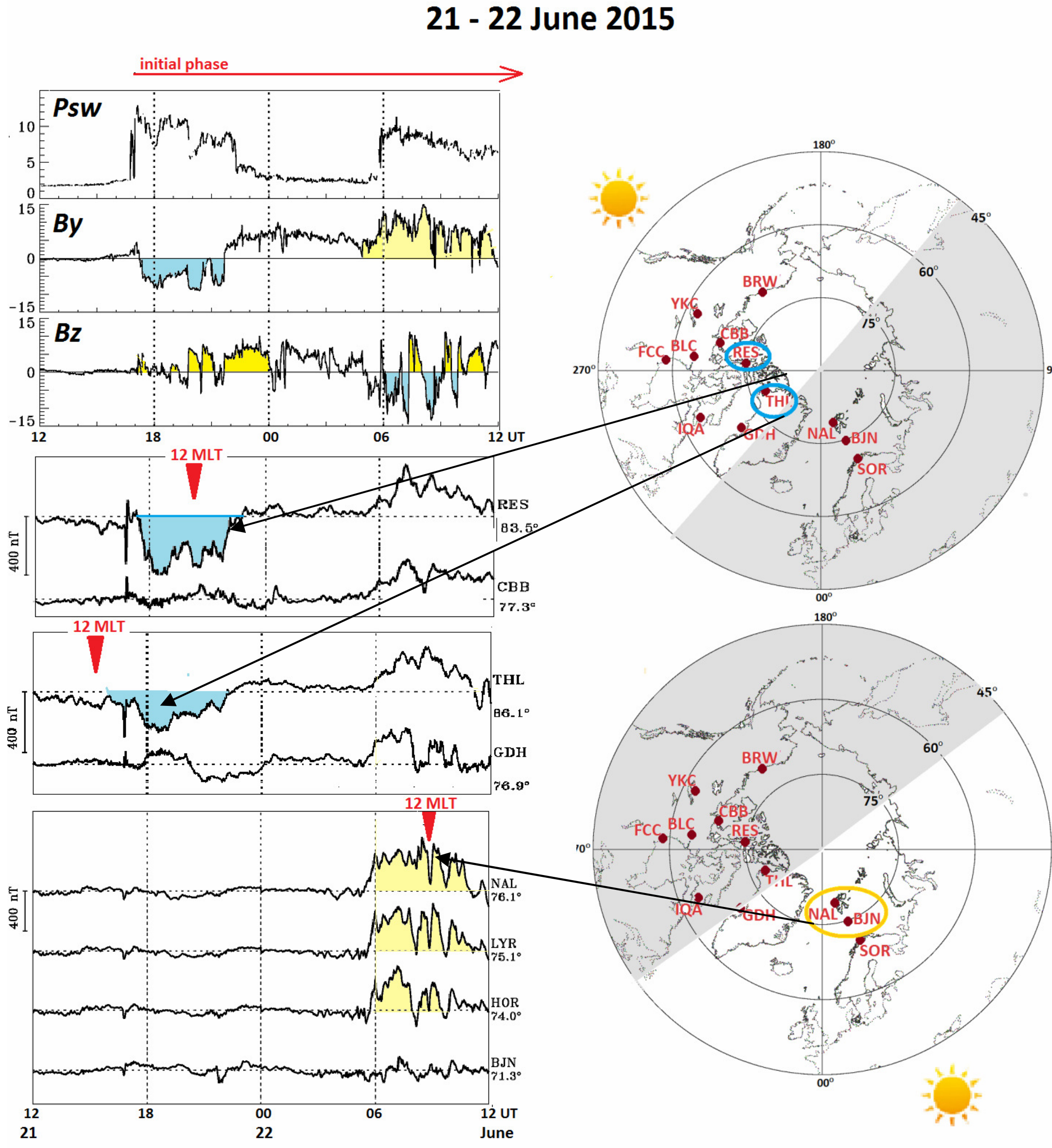

Fig.2. Variations of the Psw and IMF By and Bz, and the magnetograms from the polar stations demonstrating the dayside bays on 21-22 June 2015. The maps show the station location.

The appearance of the dayside high-latitude bays was collocated with the Field-Aligned Currents (FACs) enhancement which caused the ionospheric currents increase (see Fig.4).

On 21 June, the auroral activity was weak due to IMF Bz >0. The FACs map shows increasing of the FACs in the North American sector only (Fig. 4a) where the dayside high-latitude negative bay was observed at polar RES station (see Fig. 2).

On 22 June, the IMF Bz sharply changed from positive to negative values, that increased the night-side substorm activity (YKC and BLC stations, Fig. 3) simultaneously with the positive polar magnetic bay observed at the high-latitude NAL–HOR stations. At that time, the FACs enhancement was observed both in the dayside and night side as well (Fig. 4b).

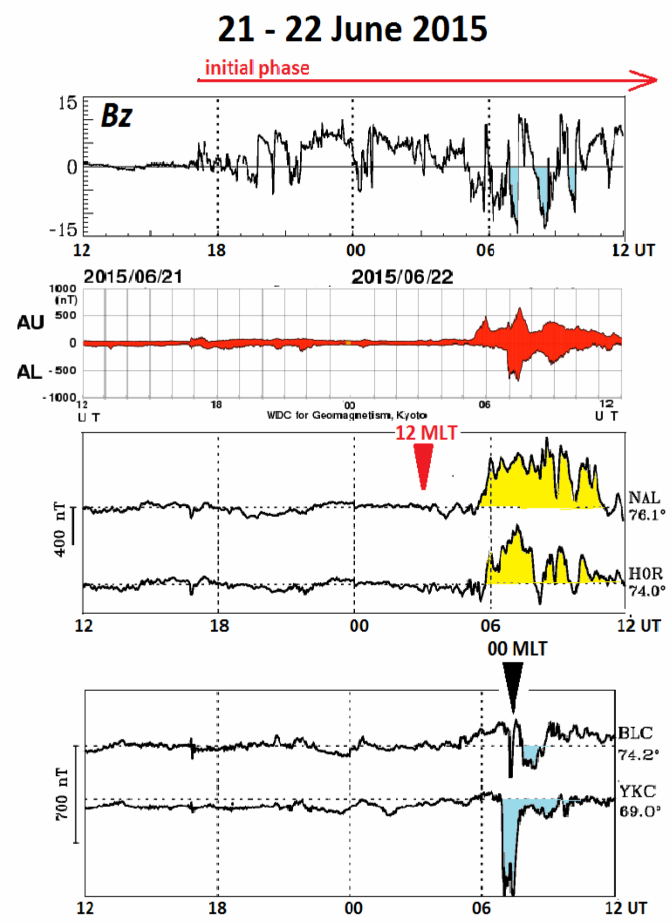

Fig. 3. The IMF Bz variation, AL-index of the auroral activity, magnetograms of the polar IMAGE stations in the dayside sector and North American ones in the night side sector.

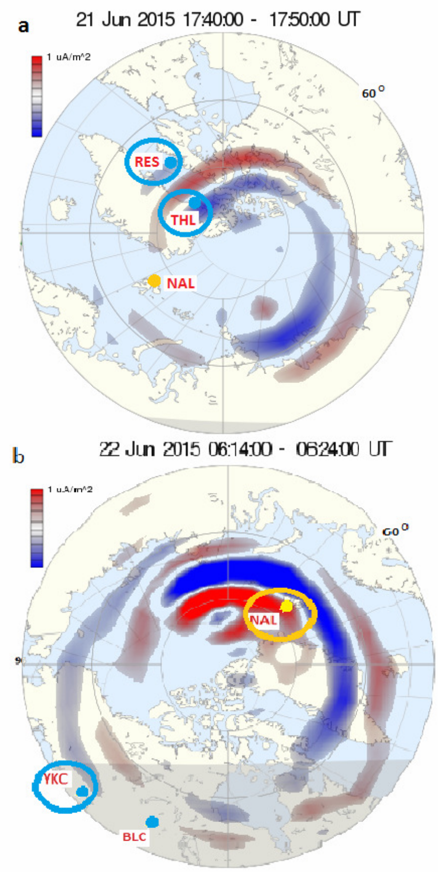

Fig. 4. FAC distribution according to AMPERE data. Circles show the location of the high latitude stations.

Magnetic storm on 07-08 September 2017

The coronal mass ejection associated with the 06 September 2B/X9.3 flare produced the severe geomagnetic storm on 07-08 September (www.izmiran.ru/services/saf/archive/).

On 07 September, the dayside high-latitude magnetic bays were also observed in the initial phase of the storm but after the end of the rapid fluctuations in the IMF components (Fig. 5). The negative high-latitude magnetic bays were developed near local noon (polar stations NAL–HOR) when the IMF By was negative. The IMF Bz showed a sequence of irregular alternating fluctuations during 06-12 UT and after that remained positive during a long period (12 - 19 UT). It is seen that when the IMF Bz became stable positive, the positive dayside magnetic bay occurred at RES station (Fig. 5).

Between 06 and 12 UT, when the dayside magnetic bays were observed at polar IMAGE stations (NAL-HOR), the night substorm activity enhanced (BRW and CMO stations, Fig. 6) due to several periods of the negative IMF Bz. At the same time, the FAC map shows FACs increasing at the high latitudes (Fig. 7a) both over the IMAGE stations and in the North American sector.

Dayside positive bay was observed at RES station (Fig. 5) in the absence of simultaneous auroral activity, probably, due to stable positive IMF *Bz*. At the same time, one can see FAC increasing only over the North American stations (Fig. 7b).

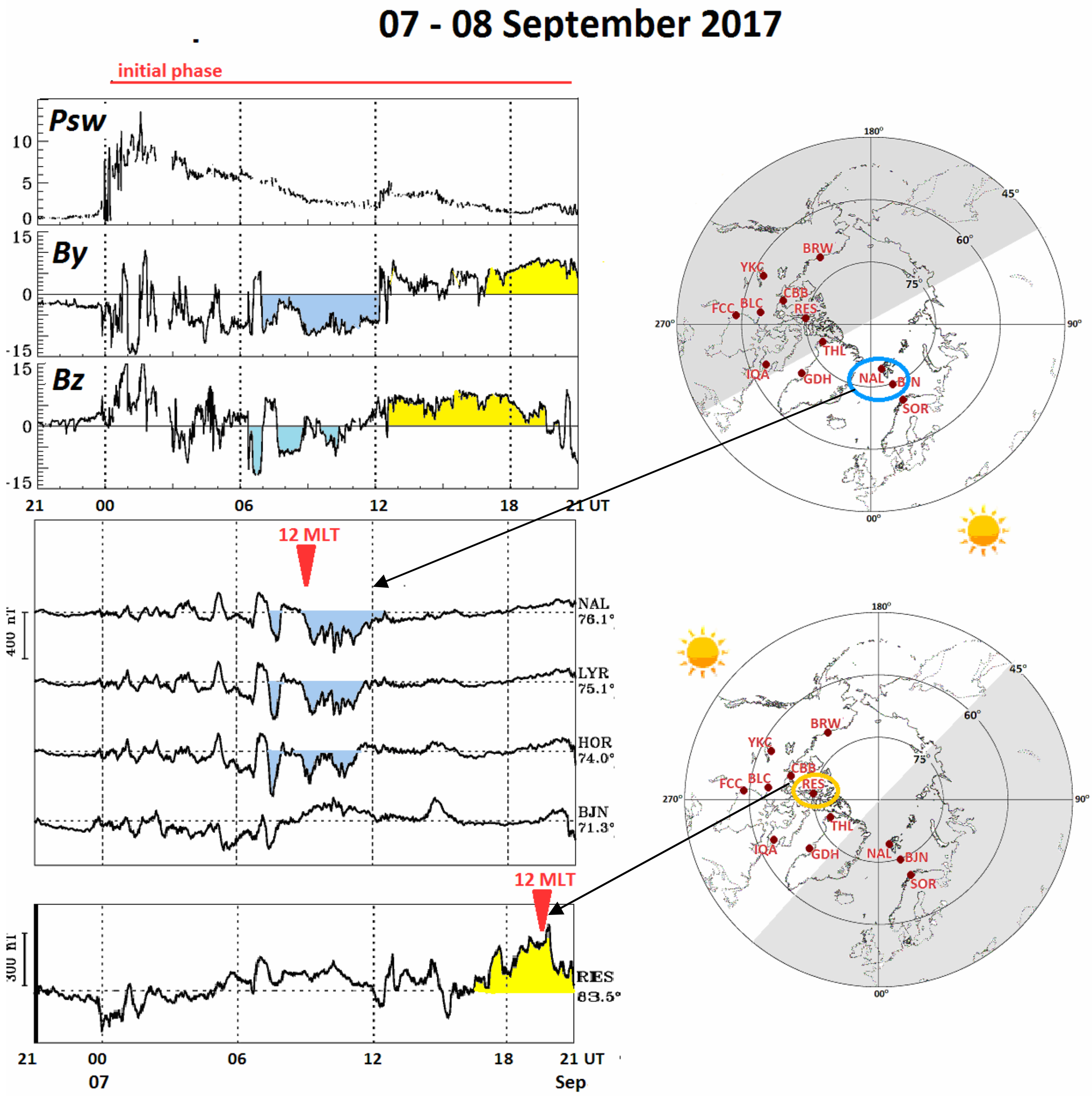

Fig.5. The same as in Fig. 2 but for 07-08 September 2017.

Summary

- In the initial phase of the strong magnetic storm on 21-22 June 2015, the solar wind dynamic pressure jumps caused the occurrence of the dayside high-latitude magnetic bays. The bay sign (i.e., the direction of the ionospheric current) was controlled by the sign of the IMF By component due to |IMF By|/|IMF Bz| >1.
- The dayside high-latitude magnetic bays were also observed in the initial phase of the strong magnetic storm on 07-08 September 2017 but only after the end of the rapid fluctuations in the IMF components which, probably, do not allow to the dayside bays develop.
- If the dayside magnetic bays were observed under negative IMF Bz, they could be accompanied by the simultaneous enhancement of the night-side substorm activity.
- Both, the dayside high-latitude and night-side auroral latitude substorms were accompanied by the Field Aligned Currents (FACs) increasing.

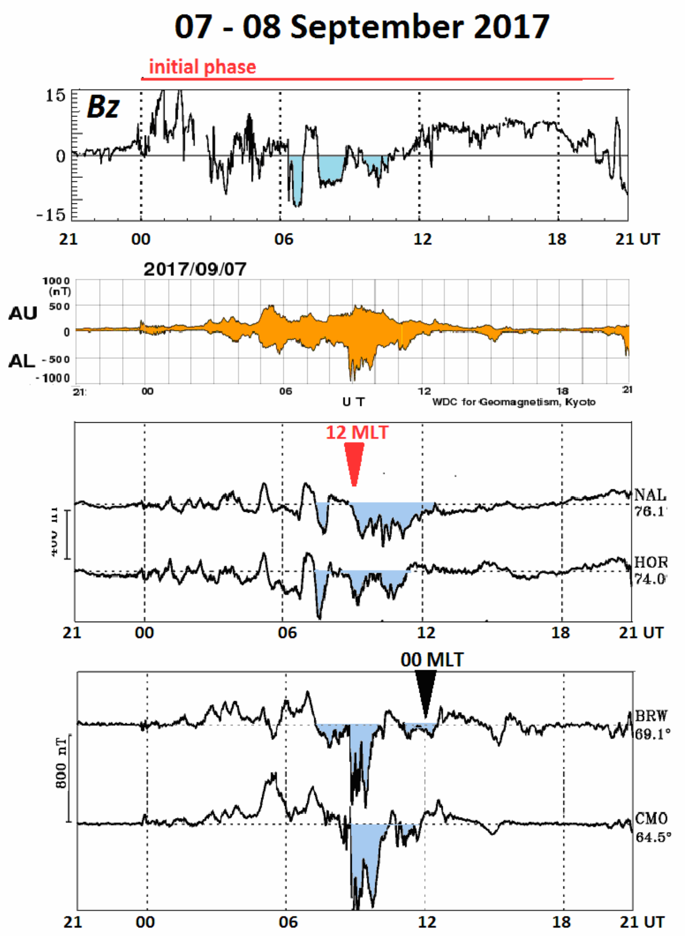

Fig. 6. The IMF Bz and AL-index, magnetograms of the polar IMAGE stations near noon and the night side North American stations on 07-08 September 2017.

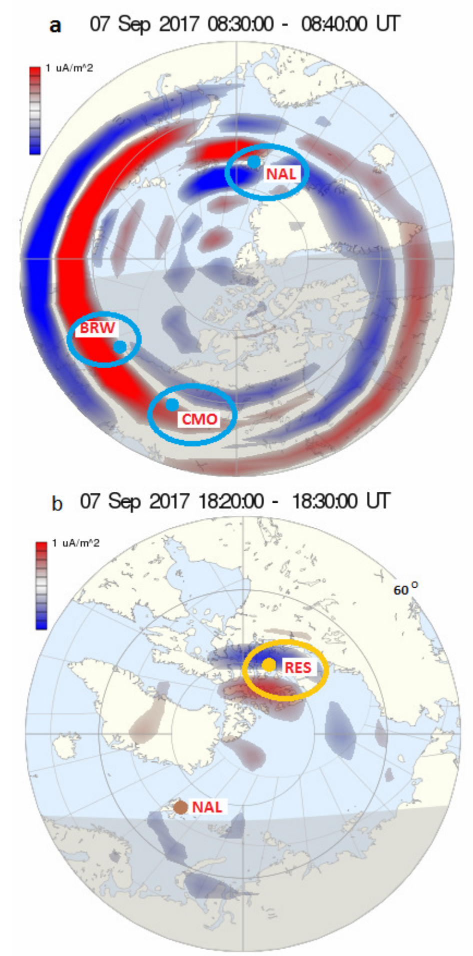

Fig. 7. FAC distribution according to AMPERE data.

Acknowledgements

This work was partly supported by the Program No 28 of the Russian Academy of Sciences (RAS) and the State tasks of IPE RAS and IZMIRAN.

References

Gromova, L.I., Kleimenova, N.G., Levitin, A.E., Gromov, S.V., Dremukhina, L.A., and Zelinsky, N.R. (2016), Daytime geomagnetic disturbances at high latitudes during a strong magnetic storm of June 21–23, 2015: The storm initial phase, Geomagn. Aeron. (Engl. Transl.), 56(3), 281–292, doi 10.1134/S0016793216030051

Feldstein, Y.I. (1976), Magnetic field variations in the polar region during magnetically quiet periods and interplanetary magnetic fields, Space Sci. Rev., 18, 5/6, 777-861.

Feldstein, Y.I., V.A Popov,. J.A Cumnock., A.. Prigancova, L.G Blomberg, J.U. Kozyra, B.T. Tsurutani, L.I. Gromova, and A.E. Levitin (2006), Auroral electrojets and boundaries of plasma domains in the magnetosphere during magnetically disturbed intervals, Ann. Geophys., 24, 2243-2276.

Friis-Christensen, E., and, J. Wilhjelm (1975), Polar cap currents for different directions of the interplanetary magnetic field in the Y-Z plane, J. Geophys. Res., 80(10), 1248 – 1256.

Iwasaki, N. (1971), Localized abnormal geomagnetic disturbance near the geomagnetic pole and simultaneous ionospheric variation, Rep. Ionos. Space Res. Japan., 25, 163-286

Levitin A.E., Kleimenova N.G., Gromova L.I., Antonova E.E., Dremukhina L.A.,. Zelinsky N.R, Gromov S.V., and Malysheva L.M. (2015), Geomagnetic disturbances and pulsations as a high_latitude response to considerable alternating IMF variations during the magnetic storm recovery phase (Case Study: May 30, 2003), Geomagn. Aeron. (Engl. Transl), 55(6), 755–768.

Lukianova R. (2004). Effect of abrupt changes in the solar wind dynamic pressure on the polar cap convection. Geomag. Aeron. (Engl.Transl.), 44(6), 691-702.

Proceedings of
Tenth Workshop "Solar Influences on the Magnetosphere, Ionosphere and Atmosphere"
Primorsko, Bulgaria, June 4÷8, 2018

Auroral hiss events observed during the declining phase of the 24th solar cycle at two stations separated by 400 km in longitude

J. Manninen [1], N. G. Kleimenova [2], Yu.V. Fedorenko [3], L. I. Gromova. [4], A. Nikitenko [3], T. Turunen [1]

[1] Sodankylä Geophysical Observatory, Sodankylä, Finland
[2] Institute of the Earth Physics of RAS, Moscow, Russia
[3] Polar Geophysical Institute of RAS, Apatity, Russia
[4] IZMIRAN, Moscow, Troitsk, Russia
E-mail: jyrki.manninen@gmail.com, kleimen@ifz.ru

Abstract

Auroral hiss is the whistler mode emission with frequency maximum at 7-10 kHz [Helliwell, 1965]. These emissions are typically observed in the evening-night sector of the auroral zone and attributed to the Cerenkov instability developing by soft electron precipitation. Here we consider the simultaneous observations of auroral hiss at two ground stations at L~ 5.5 with longitudinal separation of ~400 km: Kannuslehto (Finland, KAN) and Lovozero (Russia, LOZ), during several winter campaigns in the declining phase of the solar cycle 24. It was revealed that the most favorable conditions for the auroral hiss generation exist during the magnetic storm recovery phase mainly prior a substorm onset. Simultaneous VLF observations at KAN and LOZ showed that the probability of the auroral hiss occurrence at the given ground-based station depends on the location of the ionospheric exit area of the VLF waves generating at the altitudes of about 500-2000 km above the ionosphere, and, may be, even higher. The several examples of auroral hiss are presented in details.

Introduction

Auroral hiss is one of the noise-like types of the VLF whistler mode emissions observed both on the ground and on spacecraft in the auroral zone in the evening-night sector with the maximal intensity at the frequencies of 7-10 kHz. We consider the simultaneous observations of auroral hiss at two stations both located at L~ 5.5 with the longitudinal separation of ~400 km (Fig. 1): Kannuslehto (Finland, KAN) and Lovozero (Russia, LOZ).

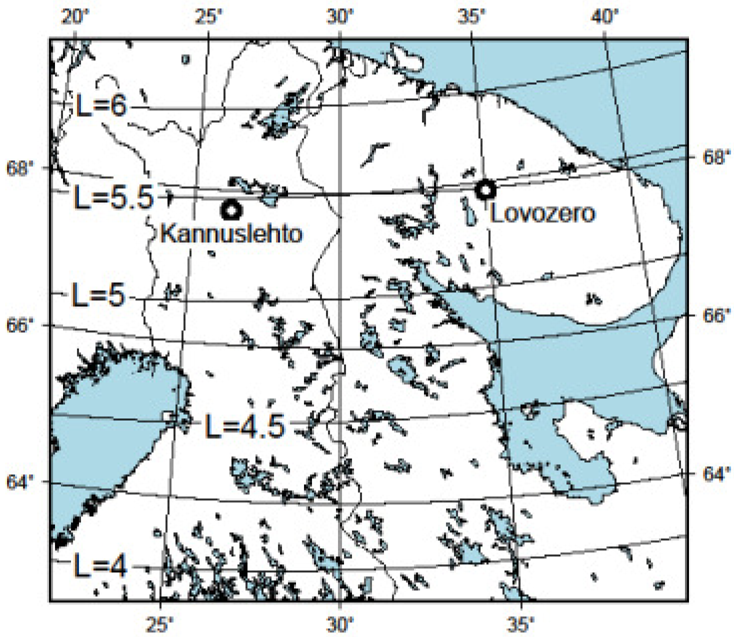

Fig. 1. The map of the stations

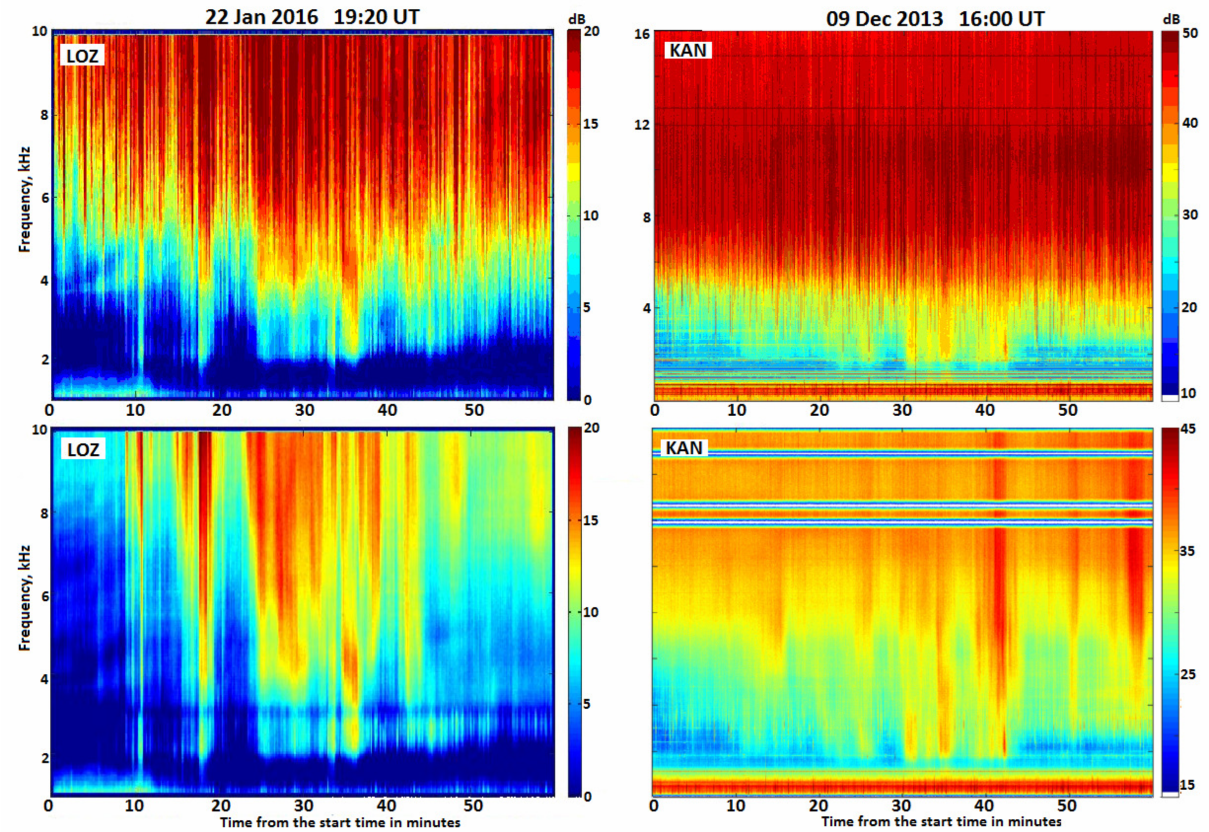

Fig. 2. Raw (upper panel) and filtered (bottom panel) VLF data at LOZ (left) up to 10 kHz and KAN (right) up to 16 kHz. The horizontal lines between 10 and 16 kHz are the transmitter signals, which have been filtered, too.

For a long time, the properties of the high-frequency auroral hiss remain unknown because many very strong atmospherics (called sferics) hide, like a curtain, all signals at frequencies above ~5 kHz. To study auroral hiss, we have to apply special programs filtering out strong impulsive sferics. The filtered VLF spectrograms (1 h duration) from LOZ and KAN are shown in Fig. 2. One can see that after filtering, the bursts of the auroral hiss became visible. The emission represents the series of the individual noise-like bursts with several minutes duration.

Previously it was established [e.g., Harang and Larsen, 1965; Gurnet and Frank, 1972; Sazhin et al., 1993; LaBelle and Treumann, 2002] that auroral hiss emissions are usually observed at high latitudes during the local evening-night time in association with visible auroras. However, nobody has studied how its generation is related to magnetic storms.

The aim of our paper is to study a relationship of the auroral hiss occurrence with magnetic storm development and to compare some longitude properties of auroral hiss bursts recorded simultaneously at KAN and LOZ, i.e., in different longitudes.

Observation and discussion

We analyzed the occurrence of auroral hiss bursts during different phases of 14 magnetic storms documented during the Finnish VLF winter campaigns 2013-2017. It was revealed that the most favorable conditions for the auroral hiss generation are created during the magnetic storm recovery phase. We found that these emissions were not observed at the ground stations in the storm main phase when strong geomagnetic disturbances were recorded.

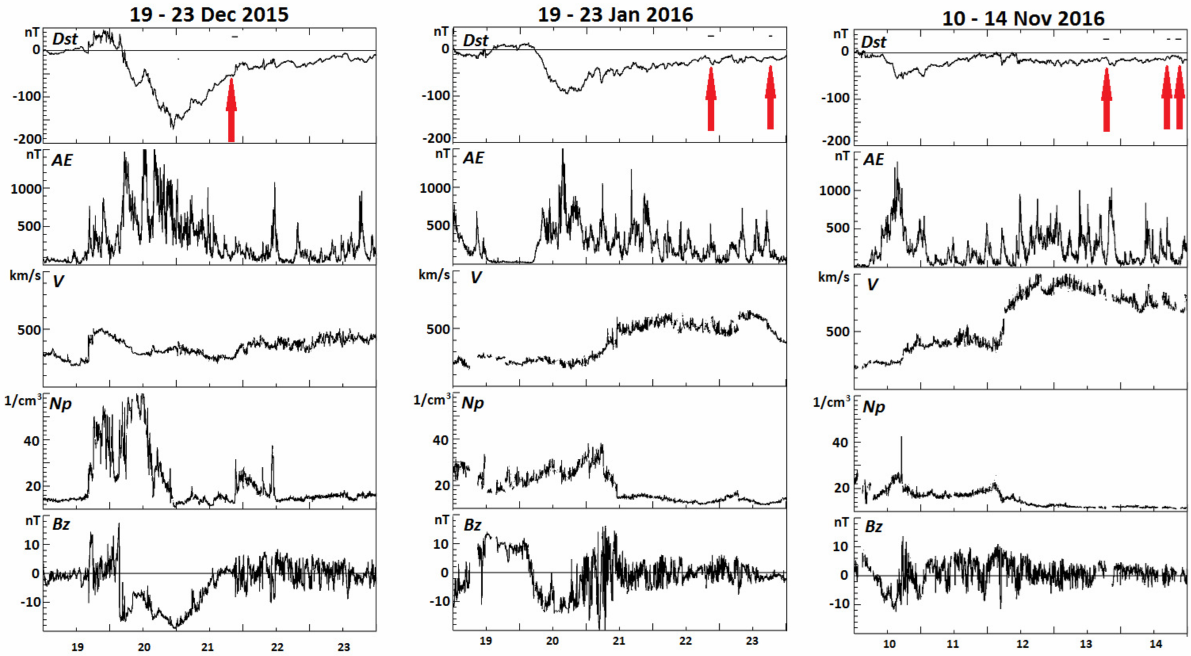

Fig. 3. The geomagnetic indices of the magnetic storm intensity (Dst) and substorm activity (AE), the solar wind velocity (V) and density (Np) , and the IMF Bz component variations during three magnetic storms. The auroral hiss events are shown by the arrows.

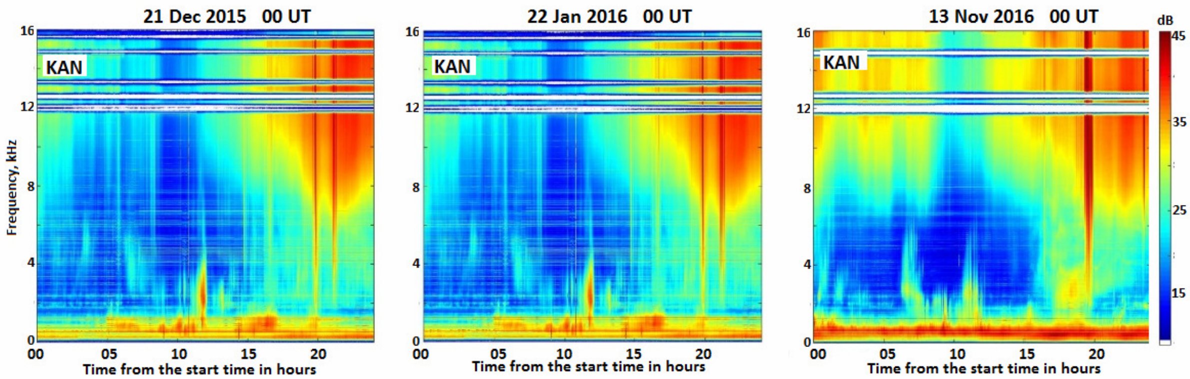

Fig.4. Examples of the 24-hour spectrograms of auroral hiss during the magnetic storms shown in Fig.3.

The examples of three magnetic storms of different intensity as well as their interplanetary and geophysical conditions are shown in Fig. 3. During all these storms, independent of their intensity, the auroral hiss was observed only in the late recovery phase under small values of AE-index, i.e., under the absence of strong auroral substorms. In this time, the IMF Bz values usually demonstrated moderate variations around zero.

The 24-hour VLF spectrograms of each storm periods shown in Fig. 3 are depicted in Fig. 4. One can see that auroral hiss bursts are observed up to 16 kHz and even higher (see narrow vertical red bands). The broad orange areas in the evening hours are the remnants of strong sferics, which have mostly been filtered out.

We found also that the auroral hiss was typically recorded in the growth phase of auroral substorms, wherein the sharp substorm onset and visible aurora break-up switch-off the auroral hiss at the ground-based station. Probably, it happened due to sharp increase of the VLF wave absorption in the ionosphere caused by the energetic electron precipitation related to the substorm.

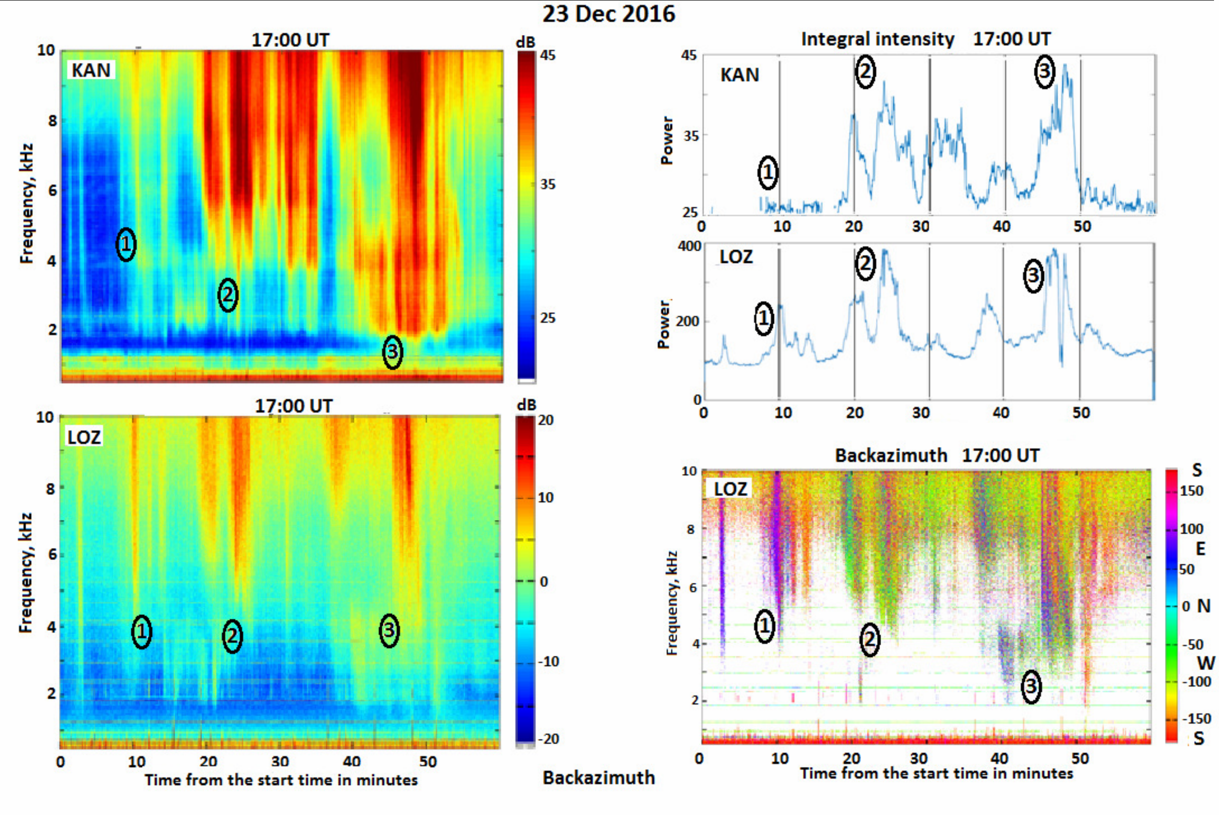

Fig. 5. The total hiss intensity variations at KAN and LOZ and the wave arriving direction at LOZ

We compared the auroral hiss bursts recorded at KAN and LOZ in the recovery phase of storm on 23 December 2016 (Fig. 5). It occurred in the declining phase of the solar cycle #24. The left panels in Fig. 5 show the 1-hour spectrograms (17-18 UT) at the frequency band of 0.5-10 kHz. The upper panels on the right part of Fig. 5 present the integrated total wave intensity variations at both stations (relative units) calculated for the frequencies higher 5 kHz. Generally, one can see that the auroral hiss bursts occurred simultaneously at both stations, but the hiss intensity was much stronger at KAN than at LOZ. However, the first hiss burst (~17:10-17:14 UT) was recorded only at LOZ and practically absent at KAN, but at 17:28-17:36 UT, the strong auroral hiss bursts were observed only at KAN and were absent at LOZ.

The 3-component VLF receiver in LOZ completes the direction-finding system allows to determine the arriving angles of the VLF emissions by the Poynting vector calculation. The obtained arriving angles are shown in the right bottom plot of Fig. 5 by different colors. It is seen that different auroral hiss bursts have different colors indicating their arriving from different directions. It means that the ionospheric wave exit points of different hiss bursts were located at different places.

We have to note that the propagation of auroral hiss from its source region to the ground is poorly understood. The standard whistler mode propagation in a smooth magnetosphere predicts that auroral hiss generated at large wave-normal angles along the auroral field lines by Cerenkov resonance cannot penetrate to the ground. But in the paper by Sonwalkar and Harikumar [2000] it was shown that the presence of density depletions along the field lines in the auroral zone and meter-scale density irregularities at altitudes < 5000 km at high latitude permits the auroral hiss propagation to the ground.

Due to the random nature of auroral hiss emissions, the direction and magnitude of the Poynting vector of the ground observations demonstrates the random variations associated with the shape and location of the Cherenkov resonance area in the magnetosphere.

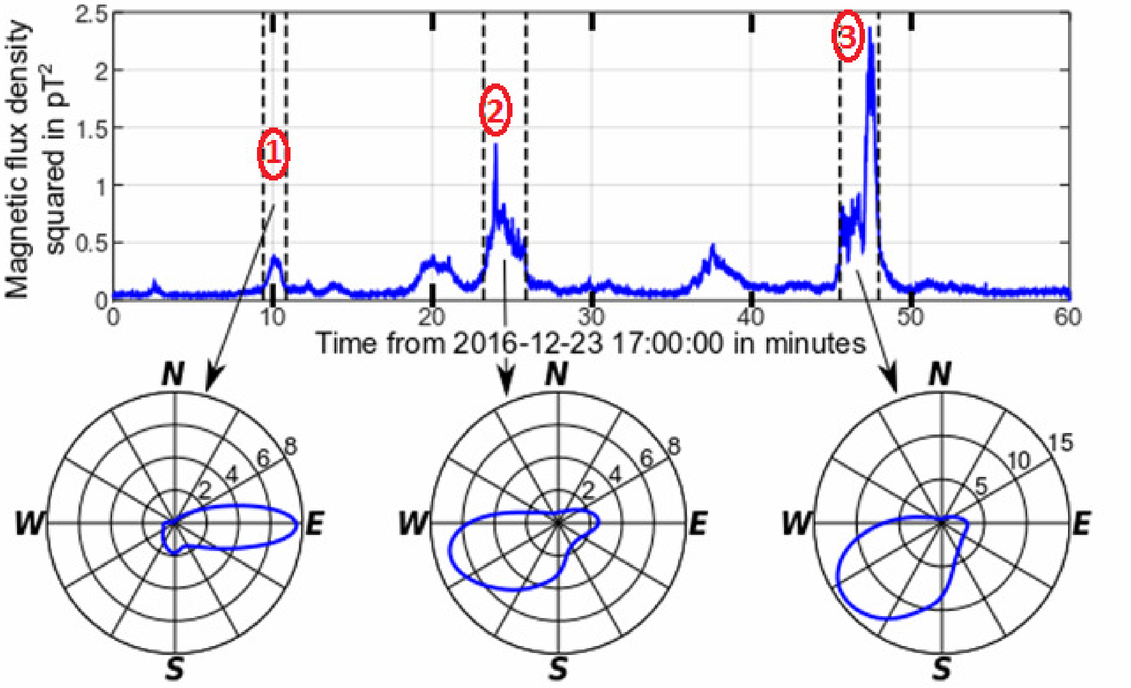

Fig. 6. Horizontal magnetic induction squared (top) and azimuthal distribution of magnitude of the Poynting vector in pWm^{-2}.

We calculated the plausible location of the ionospheric exit area of auroral hiss in the case of these waves are generated at altitudes ~500÷2000 km along the magnetic field line. The calculated polar diagram of its ground distribution is given in the bottom part of Fig. 6. Here we considered three main clusters (No 1, 2, 3) of the auroral hiss bursts on 23 December 2016 which are presented in Fig. 5. For convenience, the direction of Poynting vector is inverted thus the maximum of distribution matches the path to the exit point.

The first burst of auroral hiss near 17:10 UT showed the rather narrow angular distribution of the Pointing vector direction that may be due to remote location of the wave exit area eastward from LOZ. Due to that the hiss intensity was larger at LOZ as a station located eastward from KAN. Other two bursts (near 17:25 UT and near 17:47 UT) arrived from its west-south-west (№ 2) and south-west (№ 3) location. Due to that the auroral hiss was more intensive at KAN than at LOZ located at ~400 km to the East.

Thus, the location of the hiss ionospheric exit point could be significant variable. Probably, it depends on the peculiarities of some meter-scale density irregularities.

We have to note that these results are very preliminary and they need more seriously investigations both theoretically and experimentally with considering the influence of the different mode wave propagation in the Earth-ionosphere wave guide.

Conclusion

1. It was revealed that at L ~ 5.5, the strong auroral hiss was not observed in the main phase of a magnetic storm, but, however, it was typical for the recovery phase of storm. That was common for all 14 magnetic storms documented during the winter campaigns in 2013-2017. The auroral hiss is usually observed in time of small or moderate geomagnetic disturbances at higher latitudes.
2. It was shown that auroral hiss bursts are rather localized phenomena and could not be coherent at KAN and LOZ stations, which are located at the same geomagnetic latitude, but separated by ~400 km in longitude.
3. We found that the probability of the auroral hiss occurrence at KAN or at LOZ depends on the location of the wave exit area. The hiss, which was observed at LOZ but was absent at KAN, could be associated with its exit point location eastward from LOZ. Accordingly, the auroral hiss will be stronger at KAN if the wave exit point is located westward from KAN.
4. Simultaneous VLF observations at KAN and LOZ showed that the probability of the auroral hiss occurrence at the given ground-based station depends on the location of the ionospheric exit area of the VLF waves generated at the altitudes of about 2000-3000 km above the ionosphere and, may be, even higher.

Acknowledgements

The research was supported by the Academy of Finland (grant no. 287988 for N.K. and L.G.). The work of N.K. was partly supported by the Program No 28 of the Russian Academy of Sciences (RAS).

References

Helliwell, R. A. (1965) Whistler and related ionospheric phenomena. Stanford. Stanford Univ. Press. 349 p. 1965

Gurnett, D.A. and Frank, L.A. (1972) VLF hiss and related plasma observations in the polar magnetosphere. J. Geophys. Res., 77, 172–190. doi:10.1029/JA077i001p00172.

Harang, L. and Larsen R. (1965) Radio wave emissions in the VLF-band observed near the auroral zone—I. Occurrence of emissions during disturbances. J. Atmos. Terr. Phys., 27, 481–497, doi:10.1016/0021-9169(65)90013-9.

LaBelle, J. and Treumann, R. (2002) Auroral Radio Emissions, 1. Hisses, Roars, and Bursts. Space Science Reviews, 101(3), 295–440.

Sazhin, S. S., Bullough, K., and Hayakawa, M. (1993) Auroral hiss: a review // Planet. Space Sci., 41, 153–166.

Sonwalkar, V.S, and Harikumar, J. (2000) An explanation of ground observations of auroral hiss: Role of density depletions and meter-scale irregularities. J. Geophys. Res., 105, 18,867–18,884, doi:10.1029/1999JA000302.

Unusual *Pc1* geomagnetic pulsations observed on the ground in the end of 24-th solar activity cycle

Kleimenova N.G., Feygin F.Z., Khabazin Yu.G., Malysheva L.M.

Schmidt Institute of the Earth Physics RAS, Moscow, Russia
E-mail: kleimen@ifz.ru, feygin@ifz.ru

Abstract.

The results of analysis of structure and dynamics of unusual Pc1 geomagnetic pulsations observed on the ground in the end of 24-th solar activity cycle are presented. This event was observed on 11 September 2017 in the late recovery phase of a strong magnetic storm that occurred on 07–08.09.2017, i.e. on the 4th day after the main phase of the magnetic storm. The ground-based records at IMAGE chain demonstrated the similar spectral shape of pulsation, spaced from 67 to 57^0 geomagnetic latitude. In course of this storm only one Pc1 event was recorded at Scandinavian induction magnetometer chain demonstrating as a unusual event of Pc1 geomagnetic pulsations with very similar dynamic spectrum at all 5 stations and with the amplitude maximum at the lowest latitude station (Nur, L = 3.3). The theoretical interpretation of the behavior of the unusual of Pc1 pulsations on the ground is presented.

Introduction

Interest in the study Pc1 pulsations is associated with the important role they play in the system of solar-terrestrial relations [*Guglielmi, Kangas,* 2007]. Pc1 pulsations are generated via the cyclotron instability of radiation belt protons with anisotropic velocity distribution [*Cornwall*, 1966; *Kennel and Petchek*, 1966; *Feygin and Yakimenko*, 1971; and many others]. These pulsations are sensitive to changes in the dynamics and structure of the magnetosphere. We show that the behavior of the unusual of Pc 1 pulsations on the ground 11 September 2017 is associated with the dynamics of plasmapause in course and at the end of the recovery phase of the magnetic storm.

The aim of this work is the study of the new phenomenon and to propose a reasonable interpretation scenario related to the associated geophysical phenomena in the magnetosphere and the solar wind pressure.

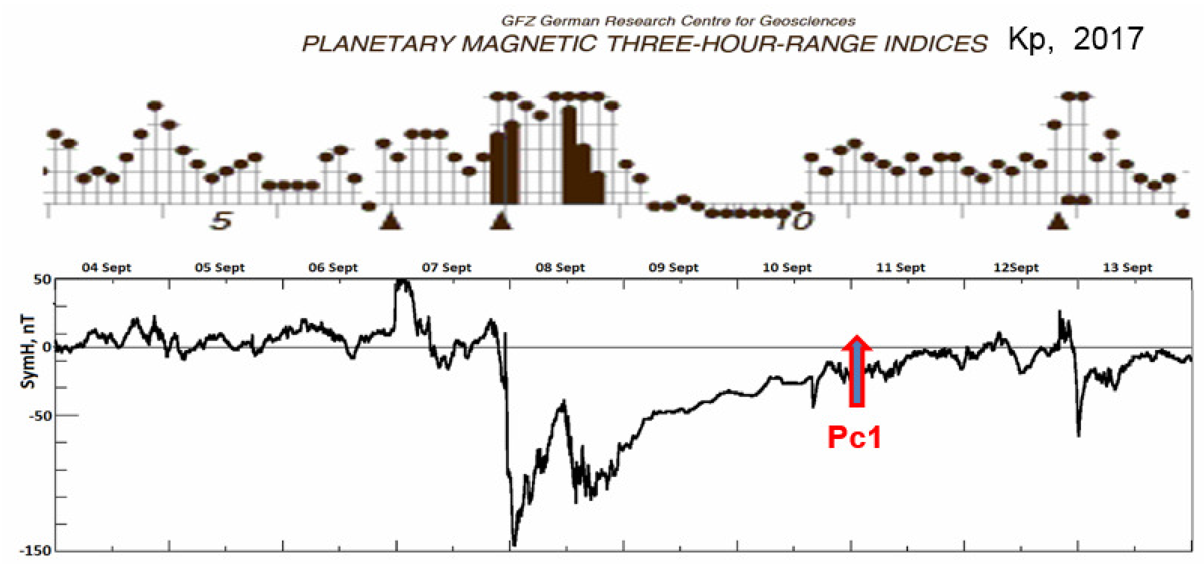

Fig. 1. Kp and SymH variations.

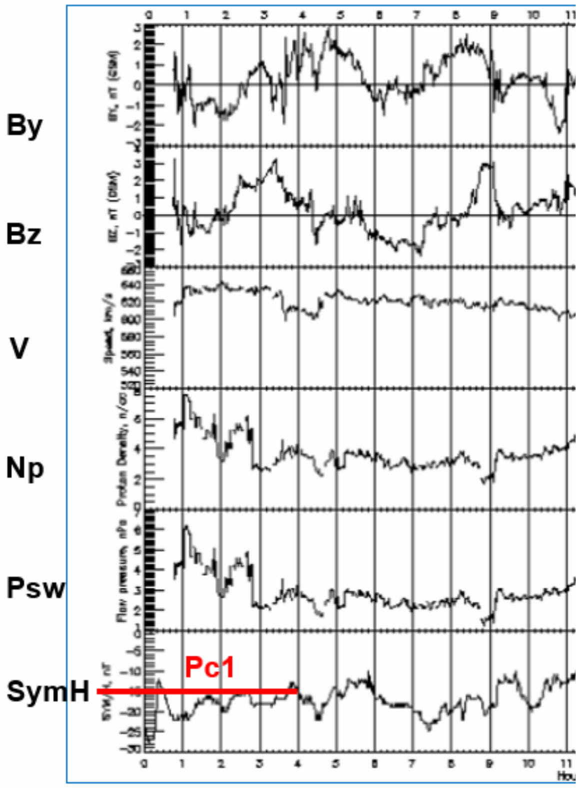

Fig. 2. IMF and solar wind data

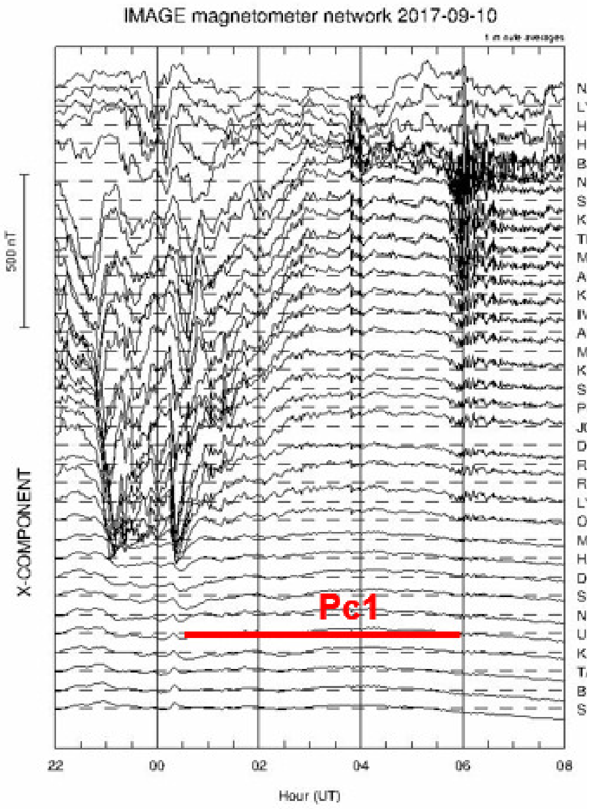

Fig. 3. IMAGE magnetogram

Data: Magnetic storm on 7-8 September 2017

At the end of the 24-th cycle of the solar activity declining, there was the strong magnetic storm with Kp = 8 was recorded on 7–8 September 2017 (Fig. 1, 2).

Before this storm, the magnetic activity was enhanced (*Kp* ~ 2–4). However after 8 September 2017, the *Kp*-index dropped up to *Kp* = 0 for about two days. In course of this storm, only one Pc1 event was recorded at Scandinavian induction magnetometer chain demonstrating a complicates spectrum (Fig.3, 4)

Discussion

Geomagnetic activity had a complex structure in the form of superposition of two different emission generated simultaneously at two different source location.

The first emission resembled the classical Pc1 pulsations lasting 4 hours at slightly increasing central frequency (from ~1.4 to ~1.7 Hz) but with unusually large bandwidth (~0.6 Hz). Such Pc1 emissions usually are generated in vicinity of the plasmapause. We suppose that these wave generation associates with so called 'old' plasmapause corresponded to that which was formed during quiet period (Kp=0).

The second Pc1 emission event presents a series of bursts (frequency range 2–3 Hz) with a follow-up period of 7 to 15 minutes. These series of the bursts is a rare event. Each burst lasts about 20–25 minutes, in which the central frequency is practically unchanged. But every next burst starts at a lower frequency. All the bursts have a wide frequency spectrum $f/f_0 \sim 0.4$ compared to the classical "pearls" ($f/f_0 \sim 0.1$). The overall frequency trend is from 2.5 Hz to 1.5 Hz and continues from 01 UT to 02.30 UT.

The empirical models [Carpenter et al., 1992; *Moldwin et a*l., 2002], show that on 11 September, the plasmapause was located at *L* ~ 4.2, and on 10 September – at *L* ~ 5.5 (The "old" plasmapause). The substorm observed prior to considered Pc1 event, provided the injec-

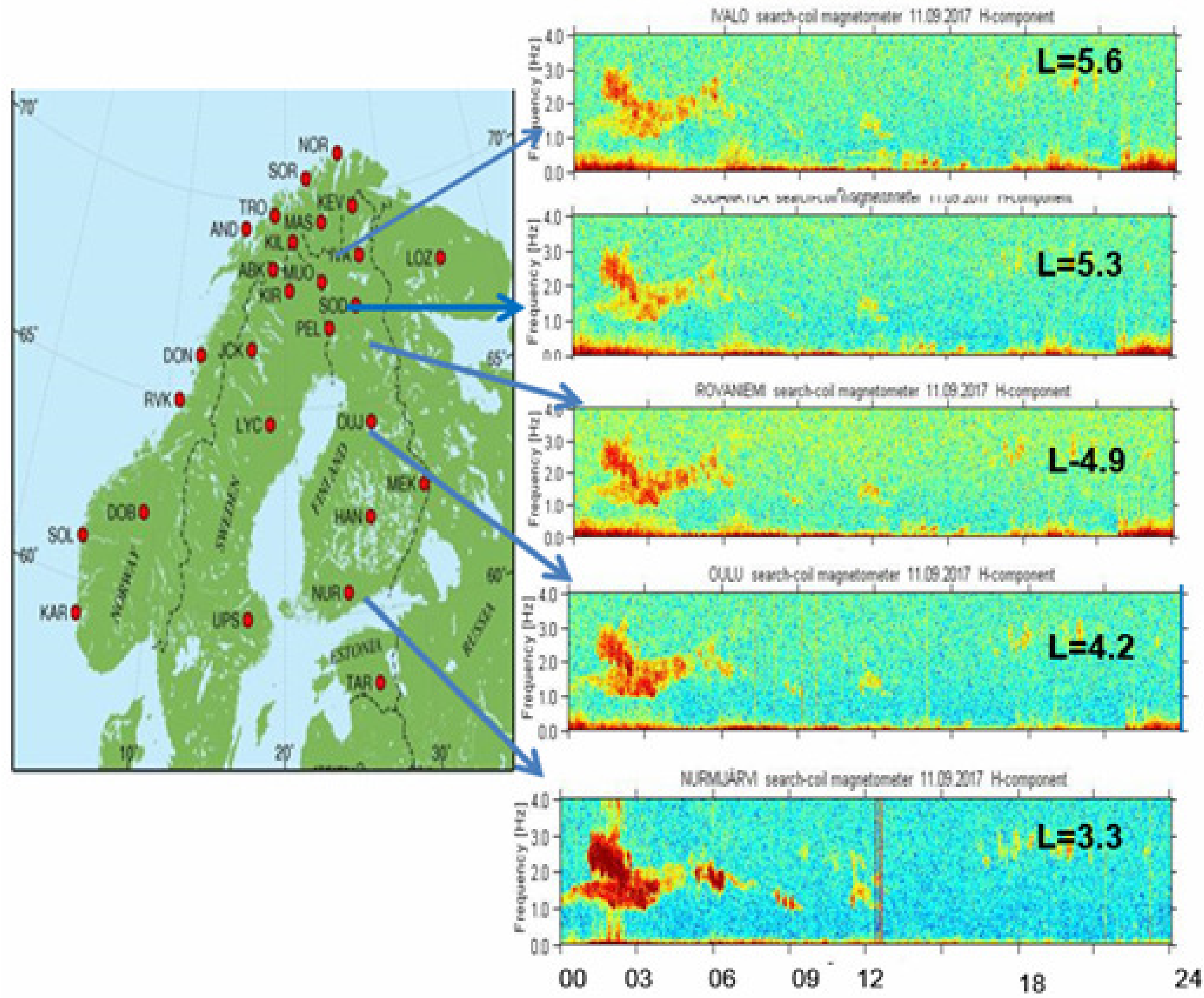

Fig. 4. Pc1 spectrograms at Scandinavian stations

tion of additional charged particles from the tail being then trapped. The strong impulsive geomagnetic disturbances (Fig. 3) stopped the Pc1 emission generation near 06 UT.

The scenario of the development of the process leading to the generation of the observed emission associated with the dynamics of the plasmapause during the recovery phase of a strong magnetic storm and nonlinear processes is proposed.

The nature of the second Pc1 event could be explained by applying the generally accepted model of the resonant interaction of the electromagnetic ion cyclotron (EMIC) waves with hot anisotropic protons in the Earth's magnetosphere [see, for example, *Kangas et al*., 1998; *Demekhov*, 2007]. The maximum amplification of the EMIC waves occurs at the frequency [*Feygin and Yakimenko*, 1971, *Gendrin et al*., 1971]:

$$\omega_0 = \frac{e_i}{4\pi m_i c} \frac{B^2}{(4\pi m_i N_i)^{1/2} U_{\parallel}} \tag{1}$$

where $U_{\parallel}$ – thermal longitudinal velocity of the hot protons, B – geomagnetic field in the generation area, and N_i – the effective concentration of ions.

It is known that the most favourable area of Pc1 generation locates in the vicinity of the plasmapause. During the considered time interval, due to strong decrease of the solar wind pressure (Psw) from 6 nPa to 2 nPa (Fig.5b), the plasmasphere expanded and the plasmapause shifted to the higher *L*-shells.

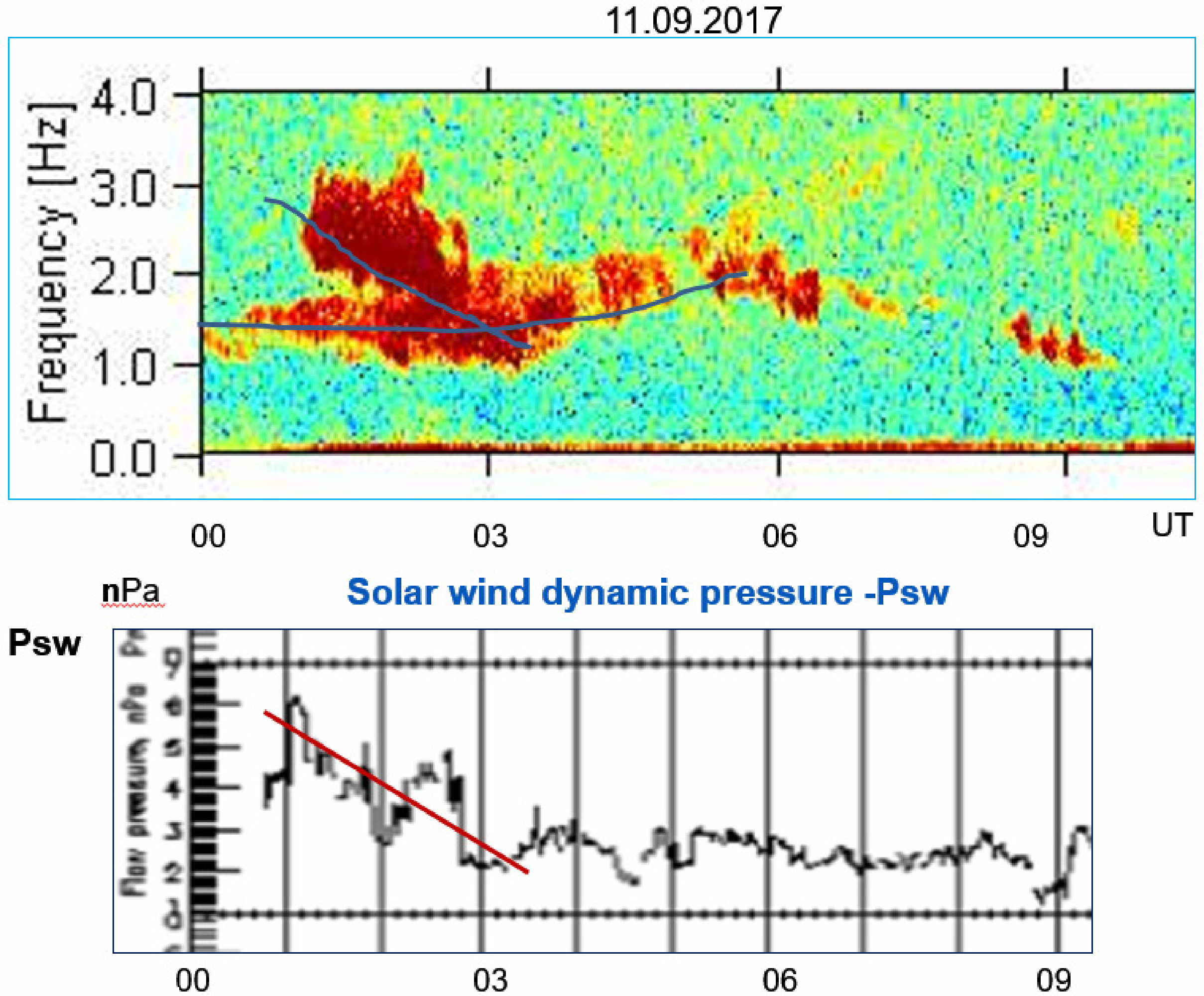

Fig. 5. (a)- Pc1 spectrogram at NUR, (b)- Psw variations

According to that, we suppose that the source of Pc1 pulsation in the recovery phase of the magnetic storm is shifted to higher *L*-shells as well, i.e. to the regions with a reduced magnetic field, which enters into Eq. (1) as B^2, and density of the background plasma. Both these parameters control the Pc1 frequency (see Eq.1). However, the influence of the magnetic field is more significant than the change in the plasma density. Such motion of the source could lead to decrease of the frequency of Pc1, as it is seen at all considered stations at 01–03 UT (Fig.4).

Another feature of the events under consideration is rather broad dynamic spectra of the emissions (Fig. 5a), which could be result of the spectral broadening in the process of the quasilinear interaction EMIC wave with energetic anisotropic protons. Feygin and Kurchashov (1975) have done a numerical experiment allowing permanent control of the quasilinear stage of the Pc1 development. They have shown that in the quasilinear stage, the broadening of the spectrum can take place. This effect could be seen in the considered event.

There is an opportunity simply to explain the different shapes of the dynamic spectrum, basing only on the assumption of Pc1 generation by cyclotron instability [*Gendrin et al.,* 1971]. Qualitatively, we will show the influence of the nonlinear processes on the macrostructure of Pc1 pulsations. Besides, we will not specify whether this process can be treated in the framework of a quasilinear theory or any other nonlinear approach. The only fact important here is that the effective growth rate of EMIC waves is decreasing with time, due to interaction with the resonant protons. According to the results obtained by [*Gendrin et al.,* 1971], the frequency width of the Pc1 spectrum is controlled by the magnetic field and density of the background plasma at the top of the geomagnetic field line, and we could roughly estimate that as:

$$\Delta\omega \propto B^{1/2} N_i^{3/2} \tag{2}$$

Around 01.00 UT, the plasmasphere was compressed and the plasmapause was located in a region with the increased magnetic field and density of the background plasma, the Pc1 spectral width was enhanced too. Later on (in our event at ~ 02.30 UT), when the plasmapause was shifted to higher *L*, i.e. to a region of the lower magnetic field and lower density of the background plasma, the Pc1 spectrum width became reduced.

The proposed interpretation of "unusual Pc1 geomagnetic pulsations" is possible, but not the only one. We did not take into account, for example, that simultaneous precipitation of protons into the ionosphere can change the quantitative parameters of the ionosphere, which can lead to a change in the frequency of transmission of the frequency range through the ionospheric Alven resonator over time [*Mursula at al.,* 2000*; Yahnin at al.,* 2007].

Conclusions

1. During the last strong magnetic storm on 7–8 September 2017, the unusual Pc1 event was found which was generated in the end of the late recovery phase of this magnetic storm.
2. The Pc1 pulsation event was observed at all ground-based Scandinavian stations, spaced from L = 3.3 to L = 5.6, with similar complicated dynamic spectra and with the amplitude maximum at the lowest latitude station (Nur, L = 3.3).
3. We showed that the behavior of the unusual of Pc1 pulsations on the ground 11 September 2017 is controlled by the pressure of the solar wind, the dynamics of plasmapause and nonlinear processes.

References

Carpenter D.L., Anderson R.R. (1992). An ISEE/whistler model of equatorial electron density in the magnetosphere, J. Geophys. Res. 97, 1097–1108. DOI: 10.1029/91JA01548.

Cornwall J.M. (1966). Micropulsations and the outer radiation zone, J. Geophys. Res., 71, 2185–2199.

Demekhov, A.G. (2007). Recent progress in understanding Pc1 pearl formation, J. Atm. Solar-Terr. Phys., 69, 1609–1622.

Feygin F.Z., Yakimenko V.L. (1971). Appearance and development of geomagnetic Pc1 type micropulsations ("pearls") due to cyclotron instability of proton belt, Ann. Geophys., 27, 49–55.

Feygin F.Z., Kurchashov Yu.P. (1975). A quasilinear dynamics of Pc1 geomagnetic pulsations (Pearls), J. Geomag. Geoelectr., 26, 539–548.

Gendrin R., Lacourly S., Roux A., Solomon J., Feygin F.Z., Gokhberg M.B., Troitskaya V.A., Yakimenko V.L. (1971). Wave packet propagation in an amplifying medium and its application to the dispersion characteristics and to the generation mechanism of Pc1 events, Planet. Space Sci., 19, 165–194.

Guglielmi A., Kangas J. (. 2007). Pc1 waves in the system of solar terrestrial relations: New reflections // J. Atmosph. Solar-Terrestrial Phys., 69, 1635–1643.

Kangas J., Guglielmi A., Pokhotelov O. (1998). Morphology and physics of short-period magnetic pulsations, Space Sci. Rev., 83. , 435–512.

Kennel C.F., Petschek H.E. (1966). Limit on stably trapped particle fluxes, J. Geophys. Res. 71, 1–28.

Moldwin M.B., Downward L., Rassoul H.K., Amin R., Anderson R.R. (2002). A new model of the location of the plasmapause: CRRES results, J. Geophys. Res., 107, no. A11, pp. 1339. DOI: 10.1029/2001JA009211.

Mursula K., Prikner K., Feygin F.Z., Braysy T., Kangas J., Kerttula R., Pollari P., Pikkarainen R., Pokhotelov O.A. (2000). Non-stationary Alfven resonator: New results on Pc1 pearls and IPDP events. J. Atmosph. Solar-Terrestrial Phys., 62, 299–309.

Yahnin A.G., Yahnina T.A. (2007). Energetic proton precipitation related to ion– cyclotron waves, J. Atmos. Sol.-Terr. Phys., 69, 1690–1706.

Yahnin A.G., Yahnina T.A., Semenova N.V., Popova T.A., Demekhov A.G. (2017). Proton aurora to the equator from the oval as a manifestation of the ion-cyclotron instability in the Earth' magnetosphere (brief review), Physics of Auroral Phenomena, 40, 66–73.

Features of mid-latitude substorms during large magnetic storms

Guineva V.H. [1], *Despirak I.V.* [2], *Kleimenova N.G.* [3]

[1] Space Research and Technology Institute (SRTI) BAS, Stara Zagora, Bulgaria
[2] Polar Geophysical Institute RAS, Apatity, Russia
[3] Schmidt Institute of the Earth Physics RAS, Moscow, Russia
E-mail: v_guineva@yahoo.com

Abstract.

We considered some peculiar properties of mid-latitude substorms during different solar wind and geomagnetic conditions. The data of the INTERMAGNET and IMAGE magnetometer networks and OMNI data base have been combined. Large magnetic storms (SYM/H<-100 nT) during the 24[th] solar cycle have been analyzed. Two severe storms, on 17 March 2015 (SYM/H_{min}=-235 nT) and on 22 June 2015 (SYM/H_{min}=-208 nT) have been chosen. The substorms registered at middle and low latitudes in the main phases of the selected magnetic storms have been considered. We have also studied the solar wind and Interplanetary Magnetic Field (IMF) conditions which could be favorable for the occurrence of a possible relationship of the low-latitude substorms with the so called "expanded" substorms developing at high latitudes.

Introduction

Substorms are a characteristic event at auroral latitudes. It is well known that during the progress of the substorm expansion phase, the westward electrojet shifts poleward, and depending on the magnetic activity could reach latitudes well above the typical location of the night side auroral oval [e.g., *Akasofu S.-I.*, 1964; *Feldstein Y. L. and Starkov G.V.*, 1967; *Kisabeth J.L. et al.*, 1974; *Wang H. et al.*, 2005; *Despirak I.V. et al.*, 2008; *Tanskanen E.I. et al.*, 2009; *Clausen et al.*, 2013; *Despirak I. V. et al.*, 2014], i.e., it forms so called an "expanded oval". However, it is generally accepted that under strong disturbed conditions, for example, at increased magnitude of the IMF negative B_Z component, the equatorward boundary of the oval shifts as well down to about 50° geomagnetic latitude. So, in such conditions, magnetic substorms can be observed at middle and even low latitudes as positive magnetic bays [e.g., *McPherron et al.*, 1973]. *Akasofu et al.*, [1965] thought that the positive bay was created by the low-latitude return currents from the westward electrojet. The mid-latitude positive bays usually accompany the substorm expansion phase and are caused by the substorm current wedge [*McPherron et al.*, 2017, 2018].

The goal of our paper is to study the interplanetary and geomagnetic conditions favorable for the substorms activity at middle and low latitudes and their possible relationship with the high-latitude "expanded" substorms basing on the analysis of the magnetic disturbances observed during two large magnetic storms: on 17 March 2015 and 22 June 2015.

Data

We used magnetic data from the IMAGE and INTERMAGNET data sets, namely data from the IMAGE meridional chain Suwalki (SUW) - Ny Ålesund (NAL), from 50º to 75º CGM lat., and data from chosen INTERMAGNET stations in the longitudinal range 92°-104° CGMlon., from 35° to 64° CGMlat. The westward electrojet development was estimated by the equivalent ionospheric currents distribution and progress, computed by the Finish Meteorological Institute (FMI) on-line tool. The Active Magnetosphere and Planetary Electrodynamics Response Experiment (AMPERE) summary plots provided the distribution of the field aligned currents. The solar wind and Interplanetary Magnetic Field (IMF) parameters were taken from OMNI database.

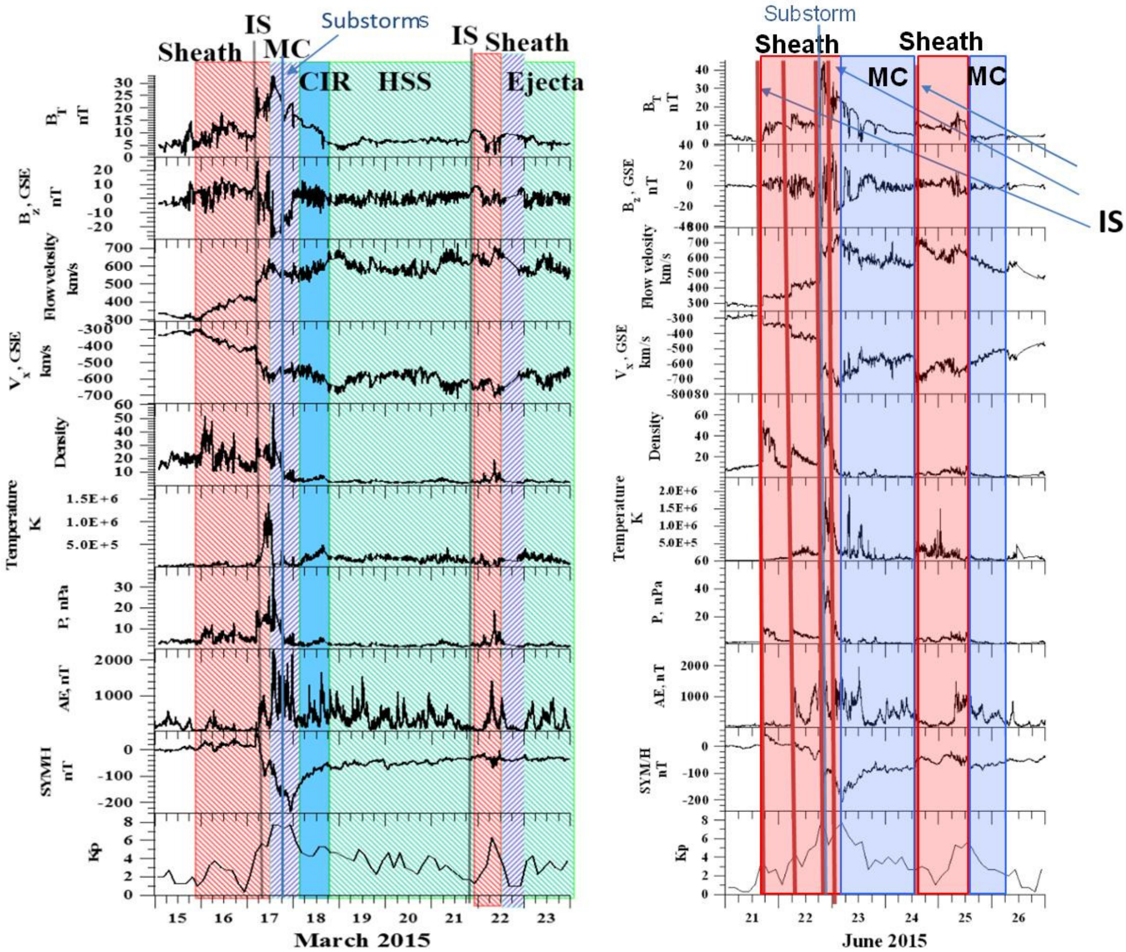

Fig.1 Interplanetary and geomagnetic conditions during the storms on 15 March 2015 and 22 June 2015.The structures in the solar wind are marked by rectangles in different colours and inscribed in the upper part of the figure. The moments of interplanetary shocks (IS) arrivals are indicated by straight vertical lines. The time of the substorms during the main storm phases are marked by blue vertical lines.

Results

Selection of geomagnetic storms

Substorms during intense geomagnetic storms (SYM/H<-100nT) in the 24th solar sycle have been examined. It was found out, that noticeable perturbations in the magnetic field at midlatitudes were observed only in relation with the substorms generated during the main phase of severe storms, in which the minimal value of SYM/H was less than -200 nT. Two severe magnetic storms during the early descending phase of the Solar Cycle 24 (SC24) have been selected: on 17 March 2015 (St. Patrick storm) and on 22 June 2015. They are the most intensive storms in the SC24 (SYM/H_{min} reached -235 nT and -208 nT, correspondently).

The interplanetary conditions in the time of these storms are presented in Fig.1. From up to down, the following quantities are shown: the magnitude of the interplanetary magnetic field (IMF) B_T, the IMF Bz, the flow velocity Vx, the plasma density, temperature, pressure (P), and the AE, SYM/H and Kp geomagnetic indices. Both storms were very similar: they were provoked by interplanetary shocks in the Sheath region in front of magnetic clouds, they had clearly expressed storm sudden commencements (SYM/H jumped from 16 to 66 nT in the first storm and from -20 to 88 nT in the second one), two-step main phases and long lasting recovery phases (see Fig.1). During both storms Kp index reached 8.

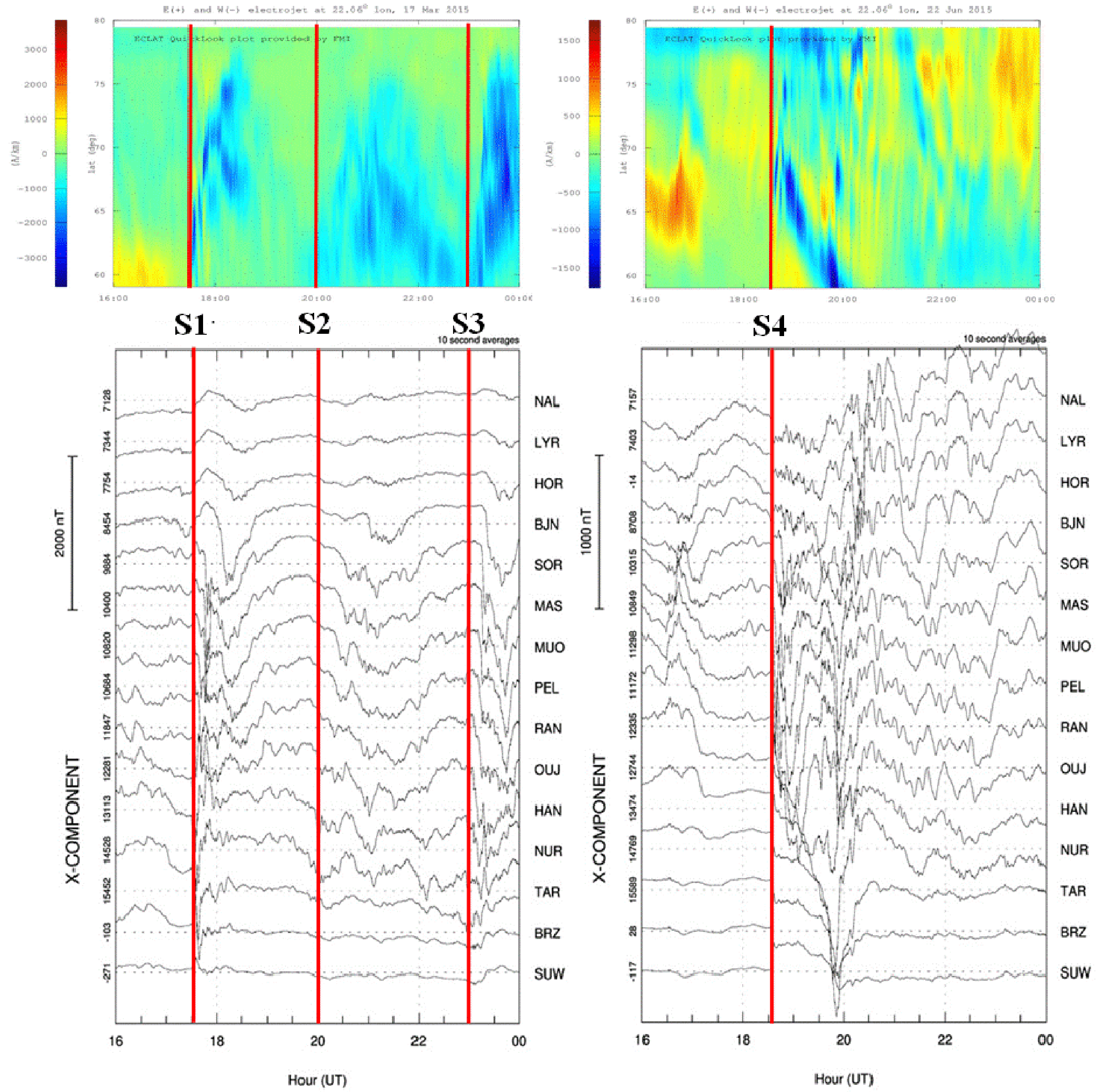

Fig.2 Equivalent ionospheric currents (upper panel) and Bx component of the magnetic field (bottom panel) during the substorms on 17 March 2015 (to the left) and during the storm on 22 June 2015 (to the right). The onset times are marked by red vertical lines. The west electrojet development is done depending on the geographic coordinates.

Interplanetary and geomagnetic conditions during the substorms

Three substorms have been registered during the main phase of the first storm (with their onsets at 17:29 UT, 19:59 UT and 22:55 UT on 17 March 2015), and one substorm generated during the main phase of the second storm at 18:33 UT on 22 June 2015. These substorms are marked further in the text and in the figures by S1, S2, S3 and S4, respectively. In Fig.2, the equivalent ionospheric currents and the Bx component of the magnetic field at the IMAGE latitudinal chain SUW-NAL during the considered substorms are presented, and in Fig.3 – the Bx component at the selected INTERMAGNET stations. The substorm onsets are indicated by the red vertical lines. The values of the IMF B_T, IMF Bz and solar wind parameters were averaged for 1.5 hours before the substorm onsets.

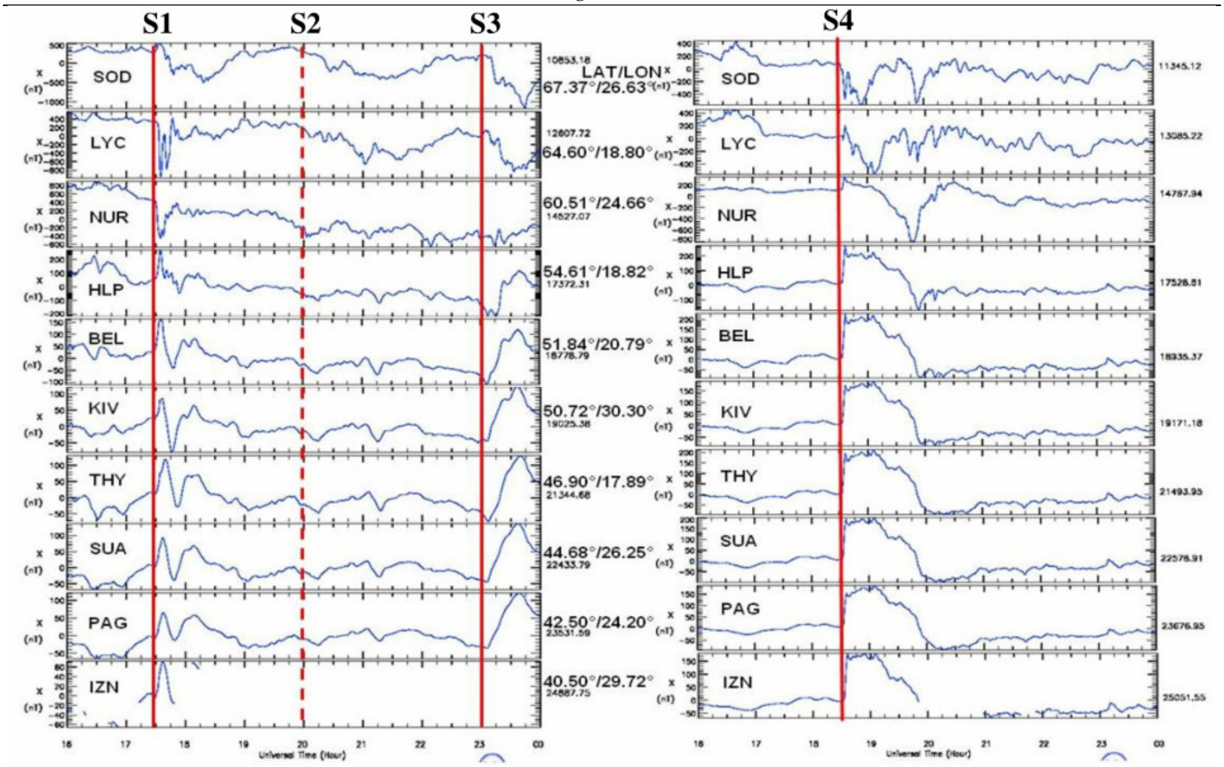

Fig.3 B_x component of the magnetic field during the substorms on 17 March 2015 (to the left) and during the storm on 22 June 2015 (to the right) by the chosen INTERMAGNET stations. The name abbreviations are written on each graphic, and their geographic coordinates - between the panels. The onset times are marked by red vertical lines.

Substorm at 17:29 UT on 15 March 2015 (S1)

This substorm occurred during the magnetic cloud (MC) caused the main storm phase. The averaged parameters values were: B_T = 23 nT, By = 2.0 nT, Bz = -19 nT, Vx = -570 km/s. At the substorm onset, SYM/H was -176 nT. The westward electrojet moved to Nord from ~56°-62° to ~74° CGMlat. A slower movement to South was observed as well (Fig.2, upper panel). The disturbances in Bx begun at NUR (56.89 CGM lat.), and moved to the North reaching NAL (75.25°CGMlat.). Simuntaneously they were moved as well to the South to BRZ (52.30°CGMlat.) (Fig.2, bottom left panel). At lower latitudes the positive bay in Bx was observed at all midlatitude stations from HLP (50.70°CGMlat.),(Fig.3, left panel). It lasted about 20 min. This positive bay could be seen even at equatorial latitudes, at the station Adis Abeba (AAE), at 5.22°CGM lat. (not shown in Fig.3).

Substorm at 19:59 UT on 15 March 2015 (S2)

The S2 substorm originated during the MC, in the main storm phase. The averaged IMF and solar wind parameters were follows: the IMF B_T = 19 nT, IMF By = 3.2 nT, IMF Bz =-16 nT, Vx = -550 km/s. The SYM/H index was -161 nT. The westward electrojet shifted to the North from ~57°-59° to 67° CGMlat. (Fig.2, upper left panel). The Bx perturbations begun at TAR (54.47° CGMlat.), and were clearly observed up to BJN (71.45° CGMlat.), no disturbances were registered to the South from TAR (54.47° CGMlat.) (Fig.2, bottom left panel). The positive magnetic bay at midlatitudes was not clearly expressed (Fig.3, left panel).

Substorm at 22:55 UT on 15 March 2015 (S3)

The third substorm on 17 March 2015 (S3) developed also during the MC, at the boundary between the main storm phase and its recovery phase, close to the SYM/H_{min}. The following average values were obtained: IMF B_T = 20.45 nT, IMF By = -10 nT, IMF Bz = -15 nT, Vx = -550 km/s. At the substorn onset, SYM/H = -161 nT. The westward electrojet moved to the North, from ~54° to ~74° CGMlat. (Fig.2, upper left panel). The disturbances in

Bx begun at TAR (54.47°CGMlat.), reached NAL (75.25° CGMlat.) and were observed to the South up to BRZ (52.30° CGMlat.) (Fig.2, bottom left panel). A positive Bx bay was registered first at HLP (50.70 CGMlat.) as well as in all midlatitude stations to the South from it (Fig.3, left panel), and also at equatorial latitudes (AAE, not presented here). It lasted about 1 hour.

Substorm at 18:33 UT on 22 June 2015 (S4)

The S4 substorm originated during Sheath in the solar wind (compressed plasma in front of a magnetic cloud). Its onset coincided with the time when a shock wave (IS), third in this disturbed period, reached the magnetosphere (Fig.1, right panel). Its arrival was characterized by a sharp increase of the solar wind parameters: the dynamic pressure jump was from 5 to about 60 nPa, the velocity increased from 450 km/s to 700 km/s, the proton density – from 15 to 60 n/cc, and the temperature – from $2*10^5$ to $1.4*10^6$ K. The magnitude of the IMF B_T rose from 10 to 45 nT, and IMF Bz turned southward in 18:39 UT and reached -40 nT in 19:22 UT. The average IMF and solar wind parameters values prior to the onset were: IMF B_T = 9.57 nT, IMF By = -6 nT, IMF Bz = -1.1 nT, Vx = -435 km/s. The fast decrease of Bz and the change of its direction provoked the storm sudden commencement (SSC) in 18:33 UT. SYM/H increased sharply from -20 nT to 88 nT, after that decreased and at 19:18 UT became negative. Then the main storm phase began. The substorm onset coincided with the SSC and its development continued through the main phase.

The westward electrojet moved to the South from 62°-67° CGMlat. at 18:33 UT to CGM latitudes less than 57° at 19:40-20:00 UT (the upper right panel of Fig.2). At the same time a jerk of the electrojet to the North was observed, reaching the strong values at CGM latitudes above 75°. The perturbations in Bx began at PEL (63.55° CGMlat.), reached NAL (75.25° CGMlat.) to the North and BRZ (52.30° CGMlat.) to the South at the IMAGE latitudinal chain. A positive Bx bay was seen at the midlatitude (Fig.3, right panel) and equatorial stations (AAE, not presented here).The positive bay lasted about 1.5 hours and was distinguished by a sharp increase, followed by a gradual decrease.

Discussion

The considered substorms generated during the similar severe geomagnetic storms. But their onsets and further development were in different interplanetary and geomagnetic conditions, which lead to different development of the westward electrojet, differences in the substorms extent and in the appearance of the positive magnetic bays.

The substorms S1, S2, S3 (the storm on 17 March 2015) occurred during MC, during the main storm phase, in already disturbed conditions. The S4 onset was during Sheath, and coincided with the interplanetary shock, provoked the storm, and with the storm sudden commencement. Further it developed in the main storm phase.

The west electrojet in the first 3 cases developed from ~54°-57° CGMlat. and its motion to the North could be observed (left upper panel of Fig.2). The Bx perturbations reached 72°-75° CGMlat. (left lower panel of Fig.2). In S4, the westward electrojet activated at higher latitudes, 62°-67° CGMlat., and its motion to the South and North was observed. The considerable travel of the substorm to the South was due to the change of the IMF Bz sign from positive to negative up to -40 nT. The electrojet progress to the North surpassed 75° CGMlat., after a second jump to the North. The electrojet center reached CGMlat. higher than 70° (between BJN (71.45° CGMlat.) and LYR (75.12° CGMlat.). This characteristic allows ranking this substorm among the "expanded" substorms.

The positive Bx bay at middle latitudes during S1 and S3 was nearly symmetric, and the duration of the perturbation was about 20 min and 1 hour, correspondingly. The positive bay during S4 was characterized by a sharp increase, owing to the coincidence with the IS and SSC, and by a gradual decrease. By the same reason it was about 2.5 times more intensive and longer (duration about 1.5 hours).

The boundary between the Bx perturbations expressed as negative and positive bays was observed in the range 50°-56° CGMlat. (between the stations HLP and NUR). According to the McPherron R.L. et al. (1973) scheme, this could be the boundary between the electrojet and the field alligned currents for the examined substorms.

Conclusions

1. The middle and low latitudes substorms were registered during the main phase of large magnetic storms, with SYM/H<-200 nT;
2. The middle and low latitudes substorms demonstrate the positive sign of the Bx component. The change of the bay sign from negative to positive was observed between 50° and 56° CGMlat. (between HLP and NUR stations);
3. It is seen that certain interplanetary conditions (Sheath + IS) during the storm on 22.06.2015 lead to a substorm that manifested itself at low latitudes (positive bays), and also at high latitudes (so called “expanded” substorms);
4. On 17.03.15 storm substorms were observed also at low and auroral latitudes, but without high-latitude expansion, perhaps, this is connected with the development of these substorms during magnetic cloud (MC);
5. The clear effect of the magnetic storm Sudden Commencement (SC) was expressed by the rapid substorm shift from auroral to low latitudes and the sharp increase of the substorm intensity on 22.06.2015. Its larger amplitude and longer duration are maybe due to the development in Sheath versus the development in MC of the other substorms.

References

Akasofu S.-I. (1964). The development of the auroral substorm. Planetary and Space Science, 12(4), 273–282. https://doi.org/10.1016/0032-0633(64)90151-5

Akasofu S.-I., S.Chapman, C.-I. Meng (1965). The polar electrojet. Journal of Atmospheric and Terrestrial Physics, 27(11-12), 1275–1305. https://doi.org/10.1016/0021-9169(65)90087-5

Clausen L. B. N., S.E. Milan, J. B. H. Baker, J. M. Ruohoniemi, K.-H. Glassmeier, J. C. Coxon, B. J. Anderson (2013). On the influence of open magnetic flux on substorm intensity: Ground- and space-based observations. Journal of Geophysical Research. 118, 2958- 2969, doi:10.1002/jgra.50308.

Despirak I. V., A. A. Lyubchich, H. K. Biernat, A.G. Yakhnin (2008). Poleward expansion of the westward electrojet depending on the solar wind and IMF parameters. Geomagnetism and Aeronomy. 48(3), 284–292.

Despirak I. V., A. A. Lyubchich, N. G. Kleimenova (2014). Polar and High Latitude Substorms and Solar Wind Conditions. Geomagnetism and Aeronomy. 54(5), 619-626.

Feldstein Y. L., G.V. Starkov (1967). Dynamics of auroral belt and geomagnetic disturbances. Planetary and Space Science. 15(2), 209–229.

Kisabeth J. L., G. Rostoker (1974). The expansive phase of magnetospheric substorms: 1. Development of the auroral electrojets and auroral arcs configuration during substorm. Journal of Geophysical Research. 79(7), 972–984.

McPherron R.L., C.T. Russell, M.P. Aubry, (1973). Satellite studies of magnetospheric substorms on August 15, 1968. 9. Phenomenological model for substorms. J. Geophys. Res. 78, 3131

McPherron, R. L., X. Chu (2017). The mid-latitude positive bay and the MPB index of substorm activity. Space Science Reviews, 206(1–4), 91–122. https://doi.org/10.1007/s11214-016-0316-6

McPherron, R. L., X. Chu (2018). The midlatitude positive bay index and the statistics of substorm occurrences. Jurnal of Geophysical Research: Space Physics, 123, 2831-2850. https://doi.org/10.1002/2017JA024766

Tanskanen E. I., T. I. Pulkkinen, A. Viljanen, K. Mursula, N. Partamies, J. A. Slavin (2011). From space weather toward space climate time scales: Substorm analysis from 1993 to 2008. Journal of Geophysical Research. 116, A00I34, doi:10.1029/2010JA015788.

Wang H., H. Lühr, S. Y. Ma, P. Ritter (2005). Statistical study of the substorm onset: its dependence on solar wind parameters and solar illumination. Annales Geophysicae. 23, 2069-2079. doi:10.5194/angeo-23-2069-2005.

Proceedings of
Tenth Workshop "Solar Influences on the Magnetosphere, Ionosphere and Atmosphere"
Primorsko, Bulgaria, June 4÷8, 2018

TEC perturbations of the South American ionosphere before and after the main shock of the powerful Chilean eathquake of 2014

LM. Ishkova, Yu.Ya Ruzin, I.N. Bershadskay

Pushkov Institute of Terrestrial Magnetism, Ionosphere and
Radio Wave Propagation of Russian Academy of Sciences, Moscow, Russia
E-mail: iskova@izmiran.ru

Abstract

The analysis results of the large-scale space-time variations of the total electron content (TEC) of the South American ionosphere before and after the powerful Chilean earthquake on April 1, 2014 (M=8.2), according to GPS network station data, are presented.

It was studied the development in the quiet geomagnetic conditions of the anomalous in the daily TEC values during for the periods 25.03-01.04.2014 and 02-09.04.2014, characterized by high foreshock and aftershock activity, with respect to the eight-day medians (δTEC, %, local time interval is 2 hours) in the longitudes 45°÷105°W ($\Delta\lambda=15°$) and in the latitudes $0^0 \div 60^0$S ($\Delta\varphi=5°$). It is shown that the anomalous perturbations of TEC in extended regions of the ionosphere took place both before the main shock of the Chilean earthquake and after it. Estimates of the characteristics of TEC perturbations (δTEC, %, spatial dimensions of ionosphere regions with anomalous TEC perturbations, duration of perturbations in daily course of TEC) are presented for the periods considered.

Introduction

The results of experimental studies show that there is coupling between the Earth's lithosphere processes and electromagnetic and plasma disturbances in the ionosphere. The prediction of earthquakes (EQs) is a challenging problem, even with state of the art technology and high-resolution data of today. It is of course important to note that, with the growth of good-quality data, our knowledge on 'EQ preparatory activities' as well as the role of complex EQ dynamics have advanced significantly.

The result is that scientists are now looking for EQ precursor signatures over the planet and its surroundings from the lithosphere to the upper atmosphere. One such approach that has gained importance in recent times is the use of electromagnetic (EM) signals and space plasma anomalies.

The analysis of GPS observations showed that variations of the ionosphere total electron content (TEC) are very sensitive to changes in the F2-layer electron concentration and can be effectively used to detect ionospheric earthquake precursors. Since the electron concentration at the F2-layer maximum is one of the ionospheric parameters most sensitive to seismic activity, we can use TEC data to estimate spatial scales and temporal dynamics of seismoionospheric effects practically in any seismic active region of the world [*Ruzhin Yu.Ya.*, et al., 2000; *Ishkova L.M.,* et al., 2017].

The present paper deals with this area of research. The analysis results of the large-scale space-time variations of the total electron content of the South American ionosphere before and after the main shock of the powerful Chilean earthquake on April 1, 2014 (M=8.2) are presented.

Data

As indicated above, the work investigates the response of the ionosphere of the South American region to seismic processes before and after the main shock of the powerful Chilean earthquake of 2014 during for the periods 25.03-01.04.2014 and 02-09.04.2014.

Earlier, in work [*Ishkova L.M.,* et al., 2017] the analysis results of the character of TEC daily variations in the South American region with respect to ten-day median levels during periods February 17-27, 2010 and March 25-April 03, 2014 were reported. The conclusion was made about a similar pronounced character of the South American ionosphere reaction to seismic processes before these powerful Chilean earthquakes. The characteristic features of anomalous TEC perturbations before the Chilean events were the development of strong positive perturbations relative to the median level (from 30 to 50-60% and higher) at distances up to several thousand kilometers a few days before the main shocks and in change of positive phase by negative phase for 3 - 4 days before the main shocks.

Note that the radiuses of the earthquake preparation zone with magnitude 8.2, according to the Dobrovolsky formula [*Oraevsky V.N.*, et al., 1994; *Ruzhin. Yu.Ya.*, et al., 1996] could reach 3600 km.

It was interesting to investigate the character of TEC variations in the South American region after the energy realization of the powerful main shock, under conditions of intense aftershock activity.

Table 1 provides the information on the parameters of some seismic events with magnitudes M>5 in the considered periods before and after the Chilean earthquake main shock to illustrate the results presented below in Tables 2-7.

Table 1. Parameters of the Andes seismic activity on March-April, 2014

Date	Time, UTC	φ,°	λ,°	M	Date	Time, UTC	φ,°	λ,°	M
22.03.14	12:59	-19.7	-70.8	**6.2**	02.04.14	00:03	-19.7	-70.7	**5.7**
22.03.14	13:29	-18.7	-70.9	**5.6**	03.04.14	01:58	-20.3	-70.5	**6.3**
23.03.14	18:20	-19.6	-70.8	**6.3**	03.04.14	02:44	-20.5	-70.4	**7.7**
24.03.14	11:26	-19.8	-70.7	**5.7**	03.04.14	05:26	-20.7	-70.5	**6.4**
24.03.14	11:40	-19.8	-70.8	**5.6**	04.04.14	01:37	-20.6	-70.6	**6.3**
24.03.14	15:45	-19.5	-70.8	**5.7**	04.04.14	09:52	-31.5	-70.3	**5.4**
27.03.14	23:50	-29.1	-68.7	**5.7**	05.04.14	02:22	-32.8	-71.5	**5.6**
31.03.14	12:35	-19.5	-69.1	**5.6**	07.04.14	13:43	-20.1	-70.8	**5.7**
01.04.14	**23:46**	**-19.5**	**-70.7**	**8.2**	11.04.14	00:01	-20.6	-70.6	**6.2**

Results

The study's results showed that the space- time scales of anomalous TEC perturbations were different on different days, at different latitudes and longitudes at both periods. In most cases, anomalous TEC disturbances were noted at night and in the morning.

The maximum characteristics of positive perturbations (δTEC values, their duration in daily course and spatial scales) are higher than similar characteristics of negative TEC perturbations.

In Tables 2-4 and 5-7 the spatial distributions of the maximum daily δTEC values for 3 days on Mach, 2014 and 3 days on April, 2014 are presented. The Tables also show data on the perturbation durations in TEC diurnal courses exceeding or equal to 2 hours.

Data for March 26-27 and April 4-5 characterize the positive phases of TEC perturbations before and after the Chilean earthquake main shock respectively.

The δTEC values on March 30 and April 7 were close to background negative values in the prevalent number of cases.

On March 26, a large area of the South American ionosphere was captured by positive TEC perturbations. Positive δTEC values were for the most part within the range of 31 ÷ 49%. The durations of the perturbations in the diurnal TEC course generally did not exceed one hour.

Table 2. Maximum daily δTEC, % on March 26, 2014

φ / λ	The sesmic events	March 26, 2014				
		-105°	-90°	-75°	-60°	-45°
0°		**47.2**	29.9	28.9	-24.8	-15.3
-5°		**53.5**	24.2	16.7	-26.4	**-47.8**
-10°		**56.2 *2h***	**37.8**	-28.9	**-39.9**	**-45.2**
-15°		**48.8**	**43.7 *2h***	**30.5/-30.3**	-22.2	-20.7
-20°	01.04 -19.6 -70.7 **8.2**	**39.0**	**40.0 *2h***	**34.3**	28.9	23.2
-25°		**34.4**	**36.3 *2h***	**40.5**	**43.5**	**31.9**
-30°	27.03 -29.1 -68.7 **5.7**	**34.6**	**32.6**	**40.1**	**35.6**	**40.4**
-35°		**40.9**	26.7	**34.8**	**36.5**	**46.3 2h**
-40°		**48.5**	**35.8**	**31.2**	**40.8**	**45.8 2h**
-45°		**52.4**	**42.2**	**32.5**	**36.1**	27.0
-50°		**49.0**	**35.3**	**33.5**	20.2	20.0
-55°		**35.0**	**32.5**	**38.2**	**34.2**	**33.0**
-60°		19.3	28.1	**31.7**	28.3	24.3

Table 3. Maximum daily δTEC, % on March 27, 2014

φ / λ	The sesmic events	March 27, 2014				
		-105°	-90°	-75°	-60°	-45°
0°		11.6	-15.1	**37.3 *2h***	**38.7**	**46.6**
-5°		9.4	14.1	**30.7**	**37.9 *2h***	**45.7/-41.4**
-10°		25.0	15.7	24.0	**40.6**	**35.8/-30.8**
-15°		**45.7 *3h***	**37.0 *2h***	**47.5**	**52.4**	**30.0**
-20°	01.04 -19.6 -70.7 **8.2**	**60.9 *4h***	**69.5 *6h***	**73.2 *3h***	**74.1 *2h***	**39.5**
-25°		**60.8 *3h***	**89.2 *6h***	**68.3 *6h***	**70.5 *2h***	**45.4 2h**
-30°	27.03 -29.1 -68.7 **5.7**	**52.4 *3h***	**69.2 *3h***	**77.1 *3h***	**55.1 *2h***	**49.3**
-35°		**52.7 *3h***	**43.6 *3h***	**66.9**	**50.7 *2h***	**40.0**
-40°		**57.4 *2h***	**46.4 *4h***	**46.8**	**60.8**	26.2
-45°		**52.4 *2h***	**52.0 *3h***	**55.5 *2h***	**53.0**	22.7
-50°		**39.5 *2h***	**38.4**	**37.0**	25.4	15.6
-55°		19.8	26.0	18.2	-13.8	18.5
-60°		16.5	13.0	8.1	-15.8	-25.0

Table 4. Maximum daily δTEC, % on March 30, 2014

φ / λ	The sesmic events	March 30, 2014				
		-105°	-90°	-75°	-60°	-45°
0°		-10.3	-10.2	-21.1	-12.9	20.6
-5°		-6.7	9.5	-14.2	-10.1	19.0
-10°		-14.1	-22.0	-13.4	-18.4	-26.1
-15°		-16.0	-18.3	-22.9	**-34.0**	-29.2
-20°	31.03 -19.5 -69.1 **5.6** 01.04 -19.6 -70.7 **8.2**	-21.8	-27.4	**-33.8**	**-36.3**	-19.3
-25°		-19.4	-25.7	**-34.6**	**-38.5 *2h***	**-40.2**
-30°		-11.4	-15.9	-23.5	**-30.3**	**-32.5**
-35°		-7.7	9.5	-14.8	-24.8	-22.3
-40°		-11.8	-11.3	-12.6	-18.3	-24.5
-45°		-21.2	**-30.9**	-29.2	-28.2	-24.0
-50°		-24.0	**-33.0**	-28.0	-24.7	-15.2
-55°		-21.3	**-32.5**	**-30.0**	-28.5	-21.2
-60°		-15.2	-21.8	-21.8	-15.8	8.9

Table 5. Maximum daily δTEC, % on April 4, 2014

φ / λ	The sesmic events	April 4, 2014				
		-105°	-90°	-75°	-60°	-45°
0°		24.3	23.4	16.6	17.0	-23.0
-5°		22.1	17.6	19.4	-15.1	-24.0
-10°		25.7	17.5	16.4	13.3	19.3
-15°		22.1	20.6	21.7	22.0	25.3
-20°	04.04 -20.6 -70.6 **6.3**	16.5	**30.1**	**34.7**	**32.8**	23.6
-25°		10.8	**30.3**	**31.4**	**36.0**	17.3
-30°	04.04 -31.5 -70.3 **5.4**	9.0	8.6	23.6	19.8	17.6
-35°	05.04 -32.8 -71.5 **5.6**	13.3	6.4	-12.1	13.6	-9.9
-40°		15.9	12.3	-13.1	11.1	24.2
-45°		13.7	6.5	-8.7	17.5	**36.7**
-50°		-13.7	-11.6	10.3	22.0	**34.1**
-55°		-27.0	-29.5	-27.9	-35.7	**36.3**
-60°		-19.2	-24.6	-23.2	-27.0	**31.8**

Table 6. Maximum daily δTEC, % on April 5, 2014

φ / λ	The sesmic events	April 5, 2014				
		-105°	-90°	-75°	-60°	-45°
0°		11.0	14.5	15.0	20.8	**41.6**
-5°		26.2	18.8	19.7	14.7	-29.0
-10°		16.6	11.7	19.3	-13.4	**-34.0**
-15°		13.8	-16.8	26.8	-17.3	-21.0
-20°	07.04 -20.1 -70.8 **5.7**	11.1	-22.8	-22.0	-18.4	-15.0
-25°		11.5	-20.6	-17.6	20.0	24.9
-30°	04.04 -31.5 -70.3 **5.4**	8.1	17.7	20.0	**42.7**	21.5
-35°	05.04 -32.8 -71.5 **5.6**	20.6	23.1	**31.4**	**67.4 *2h***	29.4
-40°		**32.7**	**35.7**	**37.5**	**53.6 *2h***	**41.7**
-45°		29.6	**30.1**	29.0	26.3	**52.2**
-50°		**44.3 *2h***	**39.3 *2h***	**37.9 *2h***	**38.1**	**39.4 *2h***
-55°		**44.6 *2h***	**54.1 *4h*/-41.2**	**55.7 *4h*/-47.8**	**59.1 *4h*/-40.4**	**54.8 *2h***
-60°		**41.2 *2h***	**64.3 *4h*/-34.5**	**67.3 *5h*/-45.0**	**72.4 *4h*/-34.5**	**61.2 *3h***

Table 7. Maximum daily δTEC, % on April 7, 2014

φ / λ	The sesmic events	April 7, 2014				
		-105°	-90°	-75°	-60°	-45°
0°		-9.2	-15.1	-18.8	-17.6	-16.1
-5°		22.7	-14.0	-19.9	-24.0	19.5
-10°		10.0	-14.2	26.4	29.2	23.3
-15°		9.0	-16.0	19.7	-20.4	23.5
-20°	07.04 -20.1 -70.8 **5.7**	16.3	-14.7	-20.5	-24.0	-24.9
-25°		23.5	18.5	-22.8	-22.9	-28.0
-30°		29.7	23.0	19.8	-9/7	-18.2
-35°		26.1	-26.5	22.7	10.3	14.9
-40°		21.2	19.6	11.7	-14.9	-22.5
-45°		20.0	11.9	14.8	-21.8	-28.0
-50°		15.7	12.8	14.7	-17.2	-26.7
-55°		-11.6	-15.6	-16.7	-19.3	-18.1
-60°		-14.6	-15.4	-24.6	**-30.1**	-21.3

The ionosphere extents with positive TEC perturbations on March 26 were 6000 km at the latitude -25° and 6000 km along the meridian -105°. These estimates are consistent with the Dobrovolsky formula [*Oraevsky V.N.*, et al., 1994; *Ruzhin. Yu.Ya.*, et al., 1996].

On March 27, the positive TEC perturbations were noted in the extended ionosphere regions in the latitude range from -15° to -50°. The maximum characteristics of positive TEC perturbations (their values, duration in daily course and spatial scales of ionosphere region with positive perturbations) on March 27 were noted at the latitudes -20° ÷ -40°. The region extents with positive TEC perturbations were 6000 km at the latitude -25° and 6000 km along the meridian -60°.

The δTEC values and their duration on March 27 as a whole significantly exceeded the similar characteristics of perturbations on March 26.

As can be seen from Table 5, on April 4 there were positive TEC perturbations with δTEC values from +30 to + 36% in the ionosphere near the Chilean earthquake epicenter region. The region length at latitude -20° was 3100 km, in the meridional direction - 550 km.

On April 5, positive TEC perturbations of the ionosphere are observed at latitudes -30° ÷ -60°. The length of the ionosphere region with positive TEC perturbations reached 5100 km along the latitude -40°, along the meridian -60° - 3300 km.

In several cases, both positive and negative maximums in the diurnal course of δTEC were observed. Note that this type of diurnal variation of δTEC is not an exception and in some cases has occurred in other conditions.

It should be noted that the character of the TEC variations on April 5 could be affected by the activation of seismic processes in the Andean zone to the south of the Chilean earthquake of 2014. The parameters of these seismic events are (see Table 1): 04.04.2014, 09:52, -31.5°, -70.3°, M=5.4; 05.04.2014, 02:22, -32.8°, -71.5°, M=5.6. Epicenters of these events were near the epicenter area of the powerful Chilean earthquake of 2010 (27.02.2010, 06:34, -36.1°, -72.9°, M=8.8).

Conclusions

1. The use of GPS data with sufficient space-time resolution made it possible to investigate the space-time dynamics of the development of TEC anomalous perturbations (from 30 to 50-60% and higher relative to the median level) in extended regions (up to several thousand kilometers) of the South American ionosphere.
2. TEC anomalous perturbations took place both before the main shock of the powerful Chilean earthquake of 2014 and after it.
3. The space-time scales of TEC anomalous perturbations are different on different days, at different latitudes and longitudes at both periods. In general, the maximum characteristics of positive perturbations (δTEC values, their durations in daily course and spatial scales) are higher than similar characteristics of negative TEC perturbations.

References

Buchachenko A.L., V.N. Oraevskii, O.A. Pokhotelov, V.M Sorokin, V.N. Strakhov, V.M. Chmyrev. (1996). Ionospheric precursors to earthquakes. Phys. Usp., 166, 959–967.

Hayakawa M., Y. Fujinawa (eds). (1994). Electromagnetic phenomena related to earthquake prediction. Terra Scientific Publishing Co, Tokyo.

Hayakawa M., Y. Hobara. (2010). Current status of seismo-electromagnetic for short-term earthquake prediction. Geomat. Nat. Hazards Risk, 1, 115–155.

Ishkova L.M, Yu.Ya. Ruzhin, I.N. Bershadskaya. (2017). The Large-Scale Ionosphere TEC Disturbances before Two Power Chilean Earthquakes. Proc. 9th Workshop «Solar Influences on the Magnetosphere, Ionosphere and Atmosphere», Sunny Beach, Bulgaria, 97-102.

Liperovskii V.A., O.A. Pokhotelov, S.L. Shalimov. (1992). Ionosfernye predvestniki zemletryasenii (Ionospheric Precursors of Earthquakes), Moscow: Nauka.

Oraevsky V.N., Y.Y. Ruzhin, A.K. Depueva. (1994). Seismoionospheric precursors and atmospheric electricity. Turk. J. Phys., 18, 1229–1234.

Parrot M., M.M. Mogilevsky. (1989). VLF emissions associated with earthquakes and observed in the ionosphere and magnetosphere. Phys. Earth Planet Inter., 57, 86–99.

Ruzhin Yu.Ya., Oraevsky V.N., Shagimuratov I.I. (2000). Anomalies of Ionospheric TEC above the Turkey before two strong Earthquakes at 1999. Proc. 15th Wroclaw EMC Symposium, 508−512.

Ruzhin Yu., C. Nomicos. (2007). Radio VHF precursors of earthquakes. Nat. Hazards, 40, 573–583.

Ruzhin. Yu.Ya., A.K. Depueva. (1996). Seismoprecursors in space as plasma and wave anomalies. J. Atm. Electr., 16, 271–288.

Investigating and Cataloguing High Speed Streams in the Solar Wind During Solar Cycle 24 (2009 – 2016)

G. Maris Muntean [1], *D. Besliu Ionescu* [1,2], *V. Dobrica* [1]

[1] Institute of Geodynamics of the Romanian Academy, Bucharest, Romania
[2] Astronomical Institute of the Romanian Academy, Bucharest, Romania
E-mail: gmaris@geodin.ro

Abstract.

The High Speed Streams (HSSs) in the solar wind are travelling through the heliosphere towards the orbit of Earth and beyond. They induce a lot of interplanetary disturbances that could cause geomagnetic storms (GSs), polar auroras and malfunctions in spatial and even terrestrial technological systems. We present our method of investigating and cataloguing HSSs used for events of the 24th solar cycle. A complex catalogue of HSSs and their effects in the terrestrial magnetosphere as geomagnetic storm was compiled (from 2009 up to 2016) and has been made available at www.geodin.ro/varsiti. An analysis of some specific HSS-GS event pairs is also presented, focusing on how the HSS features could influence the GS characteristics (the storm magnitude, its main phase structure and the energy transferred from solar wind to magnetosphere during the storm).

1. Introduction

The solar wind is propagating throughout interplanetary space (heliosphere) and interacting with all bodies and structures met in its way; it establishes a complex link between the solar atmosphere and the Earth system. Solar wind structure and properties are changing during the 11-yr solar cycle once their solar sources are also changing. A lot of new knowledge about its structure was brought about after the Skylab era (1973−1974) when coronal holes (CHs) were discovered as the sources of high speed, long-lived streams. The HSSs produced by coronal holes are recurrent, co-rotating streams, with an apparent tendency to occur at a 27 days interval. It is worth noticing that CHs are also the source of slow wind, which could be emerging from the bordering divergent regions of the holes. There are also different types of high speed streams in minimum and maximum solar activity. In addition, high speed plasma expelled in coronal mass ejections or other eruptive phenomena complicates solar wind structures.

The most precise data regarding the components and the parameters of the solar wind (speed, density, temperature) are recorded on board space missions from outside the terrestrial magnetosphere. The very precise and complete recordings obtained during the last solar cycle have brought detailed, high-resolution information which have completed the knowledge about the solar wind and its complex structure. Closely related to the improvement in the observational data, the analysis and modelling methods undergo a continuous improvement, as well as those used for studying the induced variabilities in the terrestrial magnetosphere and solar, heliospheric and magnetospheric phenomena forecasts.

In parallel with the solar wind data gathered by the SOHO, ACE, WIND and Ulysses missions, a series of satellites have collected data regarding the particles present in the magnetosphere and their dynamics under the influence of the solar wind. More and more studies regarding the two populations of particles – solar wind ones, and magnetosphere ones – have been published, as well as some regarding pairs of "cause and effect" events, like, for example, 'fast solar wind streams – geomagnetic disturbances'. In addition to the academic interest in how magnetized plasmas behave, it is important to study the solar wind interaction with the magnetosphere because this interaction controls space weather phenomena in the

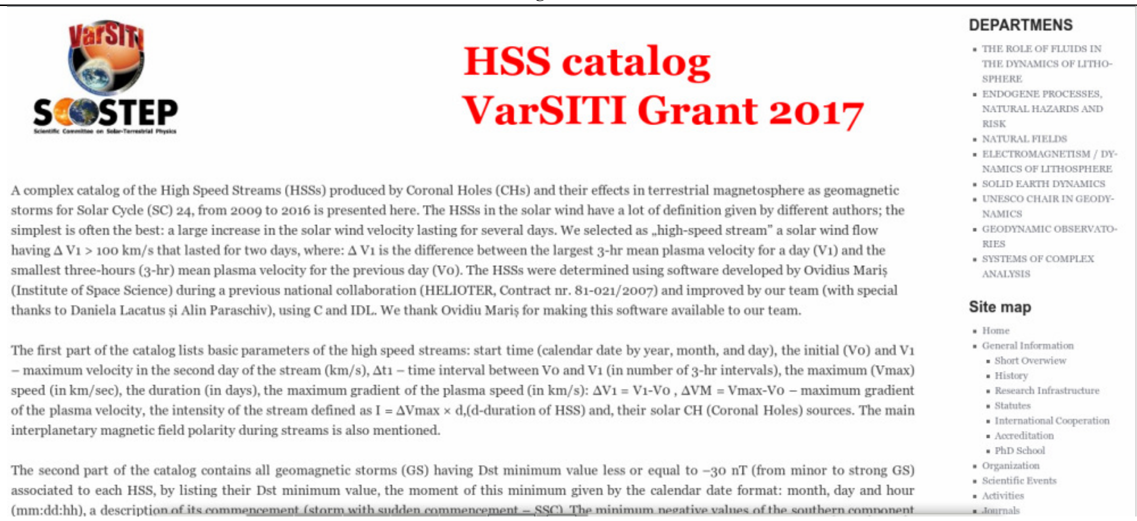

Figure 1. Screenshot of the main page of the complex catalogue of HSSs and GSs for SC 24.

terrestrial environment. The ability to develop accurate space weather forecasts depends very much on a good understanding of how solar and heliospheric disturbances interact and how the magnetosphere works.

2. HSSs Catalogue for Solar Cycle 24

A series of previous works identified and analysed the HSSs during the solar cycles (SCs) nos. 20–23. Thus, the works of the Swedish team (1, 2, 3) or the Greek team (4, 5) catalogued these currents in the solar wind for the period of three SCs, 1964–1996. HSSs during SC 23 were determined and published by other three co-authors teams (6, 7, 8).

It is known that geomagnetic activity and other associated phenomena are more influenced by the variation of the solar wind stream speed *dV/dt* rather than by the absolute value of the solar wind particles speed (1). For this reason in the attempts to define HSSs the criterion of speed variation rather than its absolute value has been used. We chose the same selection procedure of the streams as Swedish team because this one allows a more precise method to determine the HSS beginning and end. So, we selected as HSS a solar wind flow having $\Delta V1 \geq 100$ km/s that lasted for at least two days, where: $\Delta V1$ was the difference between the smallest three-hours (3-hr) mean plasma velocity for a given day *(V0)* and the largest 3-hr mean plasma velocity for the following day (*V1*). A complex catalogue for SC 24 (2009– 2016) that includes HSSs produced by solar coronal holes (CHs) and their associated GSs is presented here. Two screenshots of this catalogue (http://www.geodin.ro/varsiti/) are shown in Fig. 1 (part of the main page) and Fig. 2 (HSSs during 2010).

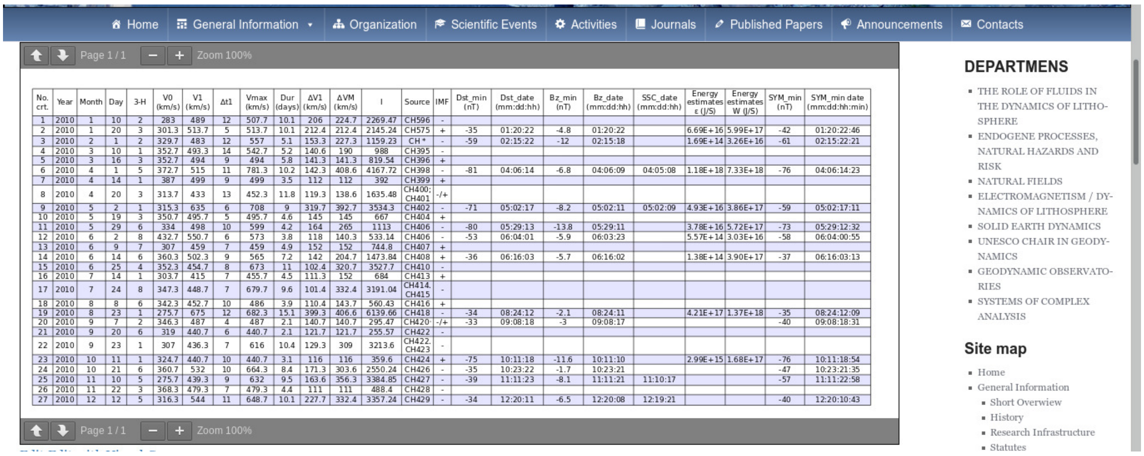

No. crt.	Year	Month	Day	3-H	V0 (km/s)	V1 (km/s)	Δt1	Vmax (km/s)	Dur (days)	ΔV1 (km/s)	ΔVM (km/s)	I	Source	IMF	Dst_min (nT)	Dst_date (mm:dd:hh)	Bz_min (nT)	Bz_date (mm:dd:hh)	SSC_date (mm:dd:hh)	Energy estimates ε (J/S)	Energy estimates W (J/S)	SYM_min (nT)	SYM_min date (mm:dd:hh:min)
1	2010	1	10	2	283	489	12	507.7	10.1	206	224.7	2269.47	CH596	-									
2	2010	1	20	3	301.3	513.7	5	513.7	10.1	212.4	212.4	2145.24	CH575	+	-35	01:20:22	-4.8	01:20:22		6.69E+16	5.99E+17	-42	01:20:22:46
3	2010	2	1	2	329.7	483	12	557	5.1	153.3	227.3	1159.23	CH *	-	-59	02:15:22	-12	02:15:18		1.69E+14	3.26E+16	-61	02:15:22:21
4	2010	3	10	1	352.7	493.3	14	542.7	5.2	140.6	190	988	CH395	-									
5	2010	3	16	3	352.7	494	9	494	5.8	141.3	141.3	819.54	CH396	+									
6	2010	4	1	5	372.7	515	11	781.3	10.2	142.3	408.6	4167.72	CH398	-	-81	04:06:14	-6.8	04:06:09	04:05:08	1.18E+18	7.33E+18	-76	04:06:14:23
7	2010	4	14	1	387	499	9	499	3.5	112	112	392	CH399	+									
8	2010	4	20	3	313.7	433	13	452.3	11.8	119.3	138.6	1635.48	CH400; CH401	-/+									
9	2010	5	2	1	315.3	635	6	708	9	319.7	392.7	3534.3	CH402	-	-71	05:02:17	-8.2	05:02:11	05:02:09	4.93E+16	3.86E+17	-59	05:02:17:11
10	2010	5	19	3	350.7	495.7	5	495.7	4.6	145	145	667	CH404	+									
11	2010	5	29	6	334	498	10	599	4.2	164	265	1113	CH406	-	-80	05:29:13	-13.8	05:29:11		3.78E+16	5.72E+17	-73	05:29:12:32
12	2010	6	2	8	432.7	550.7	6	573	3.8	118	140.3	533.14	CH406	-	-53	06:04:01	-5.9	06:03:23		5.57E+14	3.03E+16	-58	06:04:00:55
13	2010	6	9	7	307	459	7	459	4.9	152	152	744.8	CH407	+									
14	2010	6	14	6	360.3	502.3	9	565	7.2	142	204.7	1473.84	CH408	+	-36	06:16:03	-5.7	06:16:02		1.38E+14	3.90E+17	-37	06:16:03:13
15	2010	6	25	4	352.3	454.7	8	673	11	102.4	320.7	3527.7	CH410	-									
16	2010	7	14	1	303.7	415	7	455.7	4.5	111.3	152	684	CH413	+									
17	2010	7	24	8	347.3	448.7	7	679.7	9.6	101.4	332.4	3191.04	CH414. CH415	-									
18	2010	8	8	6	342.3	452.7	10	486	3.9	110.4	143.7	560.43	CH416	+									
19	2010	8	23	1	275.7	675	12	682.3	15.1	399.3	406.6	6139.66	CH418	-	-34	08:24:12	-2.1	08:24:11		4.21E+17	1.37E+18	-35	08:24:12:09
20	2010	9	7	2	346.3	487	4	487	2.1	140.7	140.7	295.47	CH420·	-/+	-33	09:08:18	-3	09:08:17				-40	09:08:18:31
21	2010	9	20	6	319	440.7	6	440.7	2.1	121.7	121.7	255.57	CH422	-									
22	2010	9	23	1	307	436.3	7	616	10.4	129.3	309	3213.6	CH422. CH423	-									
23	2010	10	11	1	324.7	440.7	10	440.7	3.1	116	116	359.6	CH424	+	-75	10:11:18	-11.6	10:11:10		2.99E+15	1.68E+17	-76	10:11:18:54
24	2010	10	21	6	360.7	532	10	664.3	8.4	171.3	303.6	2550.24	CH426	-	-35	10:23:22	-1.7	10:23:21				-47	10:23:21:35
25	2010	11	10	5	275.7	439.3	9	632	9.5	163.6	356.3	3384.85	CH427	-	-39	11:11:23	-8.1	11:11:21	11:10:17			-57	11:11:22:58
26	2010	11	22	3	368.3	479.3	7	479.3	4.4	111	111	488.4	CH428	-									
27	2010	12	12	5	316.3	544	11	648.7	10.1	227.7	332.4	3357.24	CH429	-	-34	12:20:11	-6.5	12:20:08	12:19:21			-40	12:20:10:43

Figure 2. Screenshot of the HSSs and GSs during 2010

The first part of the catalogue lists basic parameters of the HSSs :

- The start data of the streams by: Year; Month; Day (calendar data); 3-H–3-hr interval of the start day;
- *V0*–minimum (pre-stream) velocity;
- *V1*–maximum velocity in the second day of the stream;
- Δ*t1*–time interval between *V0* and *V1* (in number of 3-hr intervals);
- *Vmax*–maximum velocity of the stream;
- *Dur* – duration of the stream, in days;
- Δ*V1= V1-V0*–gradient of the velocity;
- Δ*VM = Vmax-V0*–maximum gradient of the plasma velocity;
- HSS importance (or intensity) – $I = \Delta V_{max} \times d;$
- Source – solar source of the stream: CH – coronal hole; CME – coronal mass ejection;
- IMF – the dominant polarity of the Interplanetary Magnetic Field for the duration of stream (+/– or –/+ means a magnetic sectorial border).

The second part of the catalogue contains all GSs having *Dst min ≤ –30 nT* (from minor to strong GS) associated to each HSS, by listing their main parameters:

- Dst minimum value, in nT;
- Time of minimum Dst given by the calendar date format: month, day and hour (mm:dd:hh);
- Bz minimum negative value registered just before the minimum Dst value, in nT;
- Time of minimum Bz given by the calendar date format: month, day and hour (mm:dd:hh);
- Time of SSC (Sudden Storm Commencement);
- ε – energy coupling function (9);
- W – energy coupling function (10);
- SYM minimum value;
- Time of minimum SYM.

In order to give more information on the GS evolution and characteristics, our catalogue also includes estimated values for the energy deposited in the magnetosphere from solar wind (for GSs with Dst≤–50 nT), computed using the Akasofu parameter (9), ε, integrated over the main phase of the geomagnetic storms and an improved version of this formula given by Wang et al. (10). Generally, one single GS is induced by a HSS. However, there are some cases when, during a complex HSS, two or even more (minor) GSs are registered; in such cases, the parameters of the successive geomagnetic storms will appear on successive rows in the catalogue. Recently many scientists have begun to use the SYM-H geomagnetic index instead of classic index Dst. The last two columns of the monthly tables give the SYM-H value and its time (month, day, hour, minute). The main advantage is that SYM-H has 1-min time resolution compared to the 1-hour time resolution of Dst.

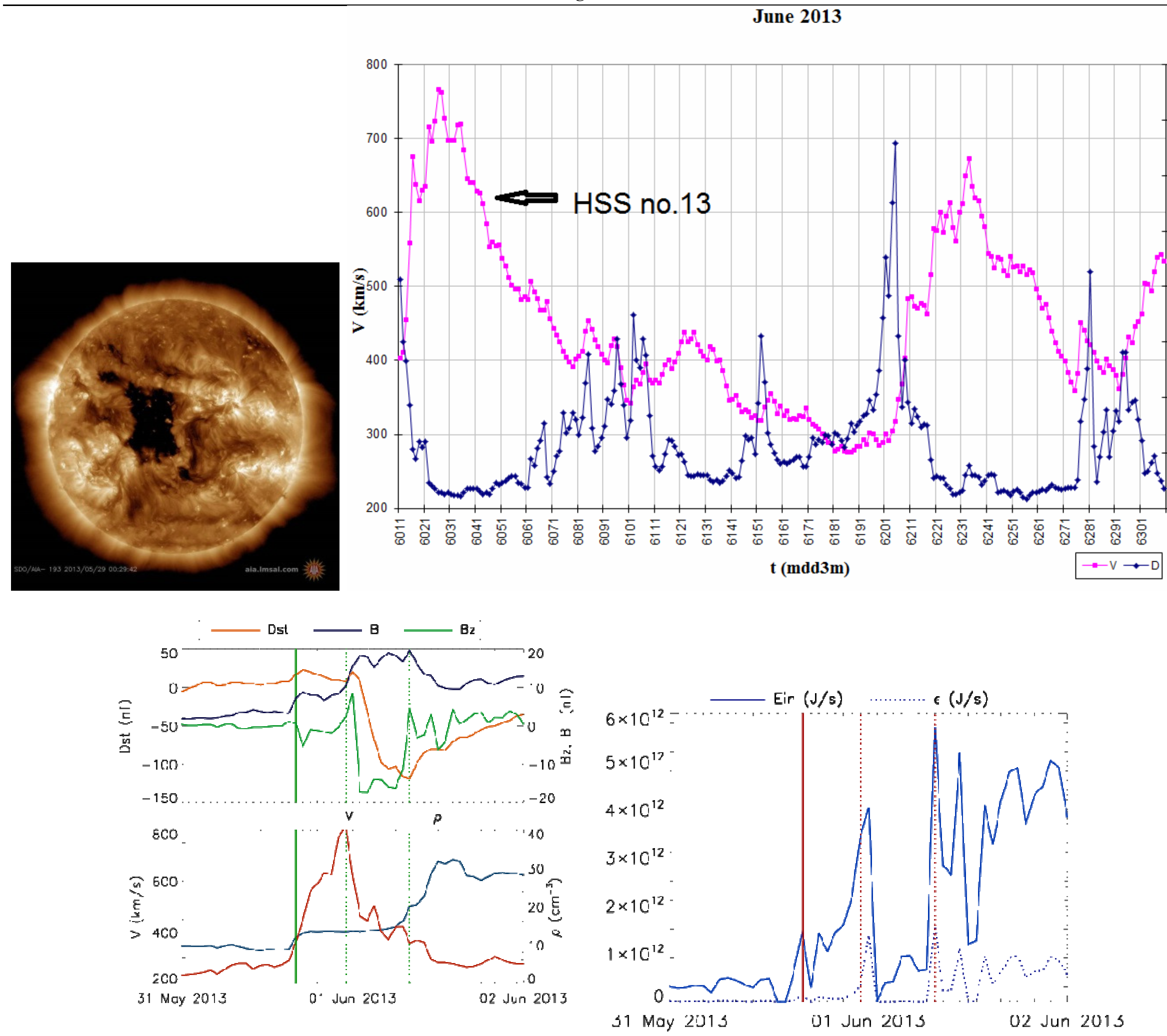

Figure 3. HSS no. 13 of 2013 and their induced geomagnetic storm.

3. Examples of Complex Events, HSS – GS

We shortly present a complex event: HSS – GS, no. 13 in the HSSs 2013 table. The figures present CH images, the analysed corresponding HSS (the entire June 2013 month), hourly variation of solar wind velocity and density as well as of Dst, B and Bz and, finally the energy deposited in the magnetosphere using the two formulas.

The values of the significant parameters for two phenomena are: V_{max} = 766 km/s; Dst=–19nT; Bz<0 during 12 h (2 values near 0); $T_{Dst} - T_{Bz}$=2 h. This current has the CH571 (seen in Fig. 3, upper left frame) as source. The CH is a rather typical CH, almost centred at the heliographic centre point, with an area of 5700 Mm^2 such as was observed on May 29. The associated HSS began two days later, in the second half of the day. The evolution of the 3-h averaged speed and density is also shown in Fig. 3(upper right frame). It is easily observed that the peak of the density is ahead of the peak in speed by almost two days. The lower left frame in Fig. 3 shows the temporal evolution of the hourly averaged B, B_z, Dst, ρ and V, while the lower right frame shows the ε and E_{IN} hourly values. The first vertical line shows the disturbance time, while the next two dotted lines show the GS main phase start and end times.

4. Summary

The "magnitude" of the HSS impact on the magnetosphere depends on solar events contributing to HSSs (heliographic position, structure). Although we do not have a complete understanding of all the processes in the magnetosphere during a geomagnetic storm, it is clear that the majority of them ultimately *derive their energy from the solar wind through reconnection processes*. The reconnection at the magnetopause and its consequences strongly depend *on the interplanetary magnetic field orientation (Bz negative).*

We hope that this catalogue will be useful to stimulate and carry out further studies in space weather field. It will be completed with HSSs during the end of the 24th solar cycle.

Acknowledgements:

This work was supported by the VarSITI/SCOSTEP grant 2007.

The data used for compiling this catalog was taken from:

- GSFC/SPDF OMNIWeb interface at https://omniweb.gsfc.nasa.gov
- http://wdc.kugi.kyoto-u.ac.jp/aeasy/index.html
- http://www.solen.info/solar/coronal_holes.html The report has been prepared by Jan Alvestad. It is based on the analysis of data from whatever sources are available at time the report was prepared.

We acknowledge all of the above for making the data available.

The HSSs were determined using software developed by dr. Ovidiu Maris (Institute for Space Sciences, Bucharest) in the frame of a national project PN2 HELIOTER (Contract no. 81-021/2007) and improved by our team (with special thanks to Daniela Lacatus and Alin Paraschiv). We thank dr Ovidiu Maris for making this software available to our team.

References

[1] Lindblad, B.A., and Lundstedt, H., 1981, A catalogue of high-speed plasma streams in the solar wind, Sol. Phys. 74, 197-206.

[2] Lindblad, B.A., and Lundstedt, H., 1983, A catalogue of high-speed plasma streams in the solar wind 1975-78, *Sol. Phys*. **88**, 377-382.

[3] Lindblad, B.A. and Lundstedt, H., 1989, A third catalogue of high-speed plasma streams in the solar wind - Data for 1978-1982 *Sol. Phys.* **120**, 145-152.

[4] Mavromichalaki, H., Vassilaki, A., and Marmatsouri, A., 1988, A catalogue of high-speed solar-wind streams - Further evidence of their relationship to Ap-index, *Sol. Phys*. **115**, 345-365.

[5] Mavromichalaki, H., and Vassilaki, A., 1998, Fast Plasma Streams Recorded Near the Earth During 1985-1996, *Sol. Phys.* **183**, 181-200

[6]Gupta, V., and Badruddin, 2010, High-Speed Solar Wind Streams during 1996 - 2007: Sources, Statistical Distribution, and Plasma/Field Properties, *Solar Phys.* **264**, 165-188.

[7] Maris, O., Maris G., 2012, Cap. 7, "High speed streams in the solar wind during the 23rd solar cycle", pp. 97-134 in: Advances in Solar and Solar-Terrestrial Physics, Research Signpost, India, (Editors: G. Maris and C. Demetrescu), ISBN: 978-81-308-0483-5.

[8] Xystouris, G.,Sigala, E., Mavromichalaki, H., 2014, A Complete Catalogue of High-Speed Solar Wind Streams during Solar Cycle 23, *Sol. Phys*. **289**, 995-1012.

[9] Akasofu, S.I.: 1981, Energy coupling between the solar wind and the magnetosphere. *Space Sci. Rev*. **28**, 121-190.

[10] Wang, C., Han, J.P., Li, H., Peng, Z., Richardson, J.D.: 2014, Solar wind-magnetosphere energy coupling function fitting: Results from a global MHD simulation. *Journal of Geophysical Research (Space Physics)* **119**, 6199-6212.

Coronal holes and high speed solar wind streams during 24th solar cycle

S. Asenovski

Space Research and Technology Institute, Bulgarian Academy of Sciences, Sofia, Bulgaria
E-mail: asenovski@gmail.com

Abstract.

In this work the high speed solar wind streams (HSS) over the 24^{th} solar cycle are examined. 312 HSS events have been determined for the 24^{th} solar cycle and their maximum speed was estimated. The results show that there is no well-defined picks for the maximum solar wind speed, and two picks of HSS count number exists – one during the ascending and the second during the descending phase of the solar cycle.

Key words: High speed solar wind, 24^{th} solar cycle

Introduction

In light of scientific terminology and mostly because of the historical reasons the term "Solar cycle" (SC) is associated with the 11 year sunspot cycle. Since its establishment by Schwabe [*Schwabe*, 1843], sunspot cycle is one of the most usable "tools" for various studies related to the sun and solar-terrestrial physics. Many other processes and phenomena identified on the Sun by humanity have such a long-term cyclicality - sunspot areas, 10.7 cm solar flux, total irradiance, magnetic field, number of coronal mass ejections and flares [*Hathaway*, 2015], coronal holes [*Luhmann, et al.,* 2002], solar wind [*Kojima and Kakinuma,1990; Rickett and Coles,* 1991]. Some of these cause cyclic behavior on different heliospheric and planetary physical processes as geomagnetic activity [*Feynman*, 1982; *Lockwood et al.*, 1999], modulation of cosmic rays [*Parker*, 1965], the structure of the interplanetary magnetic field and heliospheric current sheet [*Svalgaard and Wilcox,1976; Hoeksema,* 1995], the shape of the heliosphere [*Tanaka and Washimi,*1999]. All this listed solar or heliospheric processes have been always compared with the sunspot number.

In the current study, the focus will be on the coronal holes and high speed solar wind streams (HSS) using recent data within 24^{th} solar cycle.

Before its real detection when the existence of the solar wind is a theory, Parker made a suggestion that the properties of the solar wind and in particular solar wind flow depend on the solar activity cycle [*Parker*, 1958]. Several years later series of space probe experiments, as Lunik and Venera and their first detection of flow in the heliosphere [*Gringauz et al.*, 1960], Explorer 10 with the measurements of the solar wind properties close to the Earth's magnetopause [*Bonetti et al.,*1963] and Venus Mariner 2 which detected the variable nature of the solar wind [*Neugebauer and Snyder,*1962] confirmed the Parker's theory and gave a broad field of examination. Up to now our understanding of the solar wind and how it is modulated by solar activity cycle has been rapidly growing.

HSS and recurrent geomagnetic disturbances induced by them are essentially associated with mid latitude coronal holes and thus with solar activity cycle [*Bame et al.,*1976].

Data

312 HSS events have been identified using the hourly values of the plasma parameters gathered in OMNI data base (http://omniweb.gsfc.nasa.gov/) and the criteria for a HSS - an increase of the solar wind velocity by at least 100 km/s in no more than one day to at least 450 km/s for at least five hours along with high proton temperature and low plasma density. Coronal holes data from http://www.solen.info/solar/, provided by SDO/AIA are used as well.

Results

The profile of the maximum speed of HSS within the 24th solar cycle is characterized with lack of well-defined picks, while the HSS count number on the other hand have two picks – one during the ascending and second during the descending phase of solar cycle (Fig. 1) .

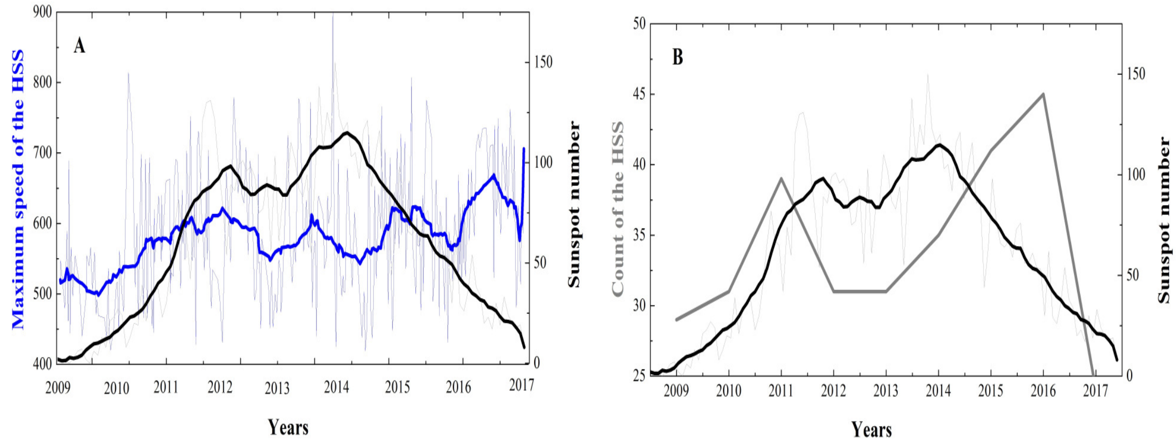

Fig. 1 Properties of the HSS during the 24th solar cycle: A - Maximum speed of the HSS; B – count

Fig. 2 Image of the Coronal hole CH820 on the visible side of solar disk in August 19, 2017 provided by SDO/AIA (left panel) and near-Earth solar wind speed variation (km/s) several days around the day of the image. The red line represent the day of the coronal hole's image.

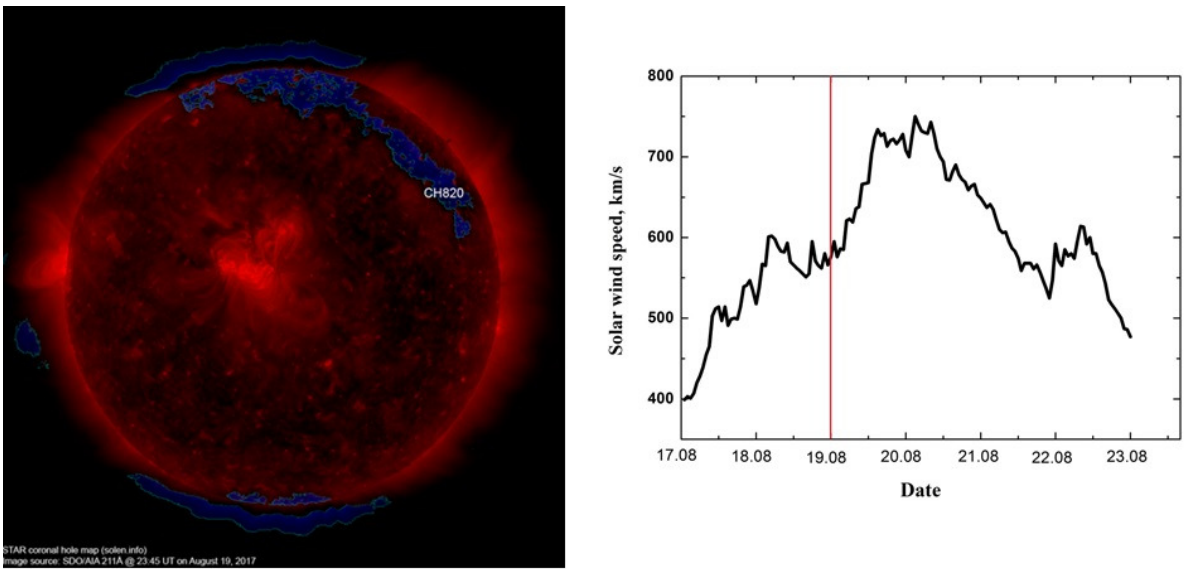

I

Fig. 2 – 5 are shown different moment (days) of the descending phase of 24th solar cycle (2017) and the influence of the Earth facing coronal holes to the near Earth solar wind speed and possible detection of the HSS. During this period which is close to the solar minimum two persistent coronal holes occupied the solar poles. Several mid-latitudes coronal holes have been detected which are source of HSS.

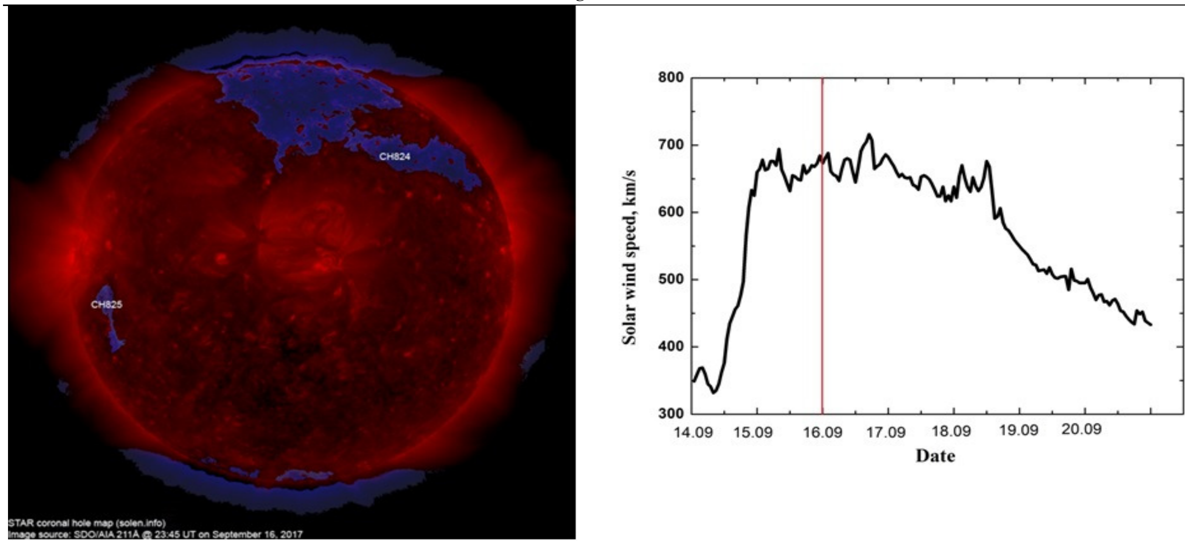

Fig. 3 Image of the Coronal holes CH824 and CH825 on the visible side of solar disk in September 16, 2017 provided by SDO/AIA (left panel) and near-Earth solar wind speed variation (km/s) several days around the day of the image. The red line represent the day of the coronal hole's image.

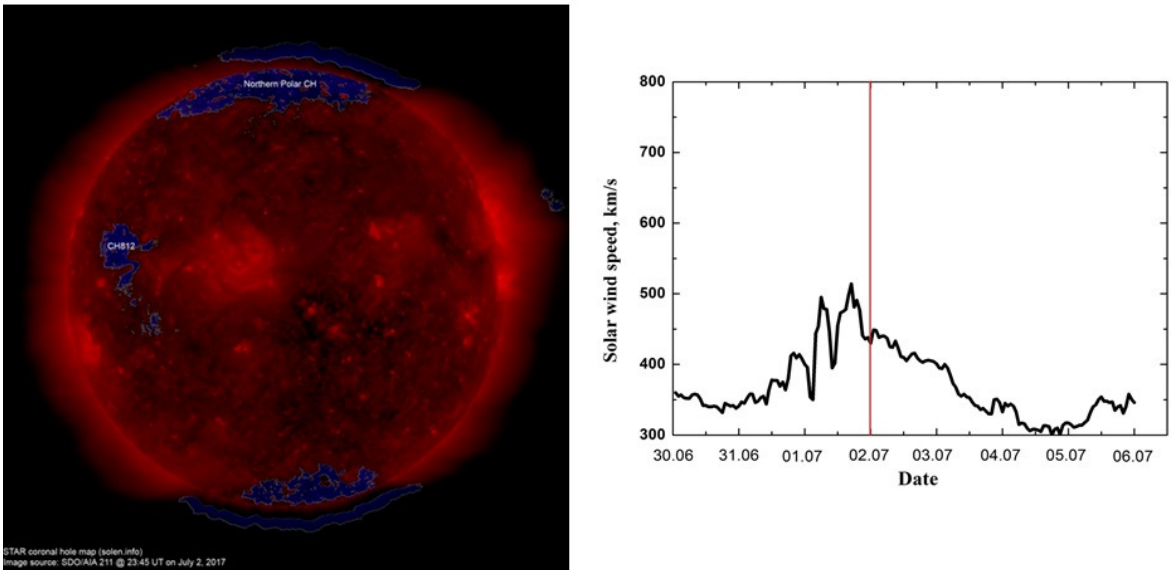

Fig. 4 Image of the Coronal hole CH812 on the visible side of solar disk in July 2, 2017 provided by SDO/AIA (left panel) and near-Earth solar wind speed variation (km/s) several days around the day of the image. The red line represent the day of the coronal hole's image.

Conclusions

The results of the presented work can be summarized in the following statements:

1. 312 HSS events have been determined for the 24th solar cycle and their maximum speed was estimated.
2. Lack of well-defined picks for the maximum solar wind speed, and two picks of HSS count number – one during the ascending and second during the descending phase of solar cycle
3. The count of the HSS is the greatest during the descending phase of 24^{th} solar cycle.
4. Several coronal holes have been observed during the descending solar cycle phase and their influence on the solar wind speed was examined.

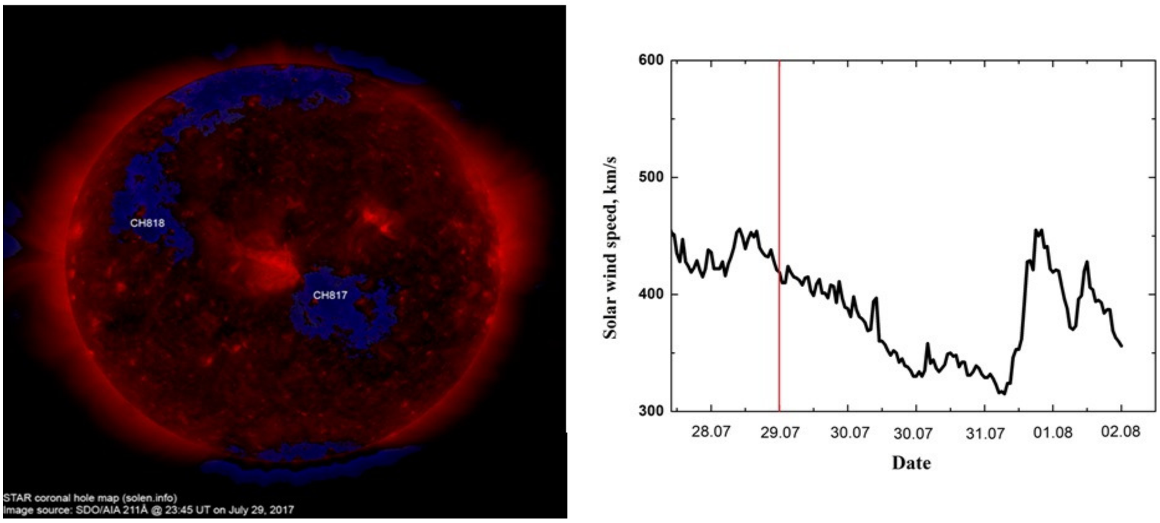

Fig. 5 Image of the Coronal holes CH817 and CH818 on the visible side of solar disk in July 29, 2017 provided by SDO/AIA (left panel) and near-Earth solar wind speed variation (km/s) several days around the day of the image. The red line represent the day of the coronal hole's image

Acknowledgment

This work was supported by the "Competition for financial support for projects of junior researchers – 2016" under grant DM 04/4 "Investigation of the impulsive solar activity agents throughout the 11-year solar cycle".

References

Bame S.J., Asbridge J.R., Feldman W.C., Gosling J.T. (1976), Solar cycle evolution of high-speed solar wind streams. Astrophysical Journal, 207, 977–980.

Bonetti A., Bridge H.S., Lazarus A.J., Rossi B., Scherb F. (1963), Explorer 10 Plasma Measurements, Journal of Geophysical Research, 68, 4017.

Feynman J. (1982), Geomagnetic and solar wind cycles, 1900-1975, Journal of Geophysical Research, 87, 6153–6162.

Gringauz K.I., Kurt V.G., Moroz V.I., Shklovskii I.S. (1960), Results of Observations of Charged Particles Observed Out to R = 100, 000 km, with the Aid of Charged-Particle Traps on Soviet Space Rockets, Astronomicheskii Zhurnal, 37, 716.

Hathaway D.H. (2015), The Solar Cycle, Living Reviews in Solar Physics, 12, 4.

Hoeksema J.T. (1995), The Large-Scale Structure of the Heliospheric Current Sheet During the ULYSSES Epoch, Space Science Reviews, 72, 137–148.

Kojima M., Kakinuma T. (1990), Solar cycle dependence of global distribution of solar wind speed, Space Science Reviews, 53, 173–222.

Lockwood M., Stamper R., Wild M.N., A doubling of the Sun's coronal magnetic field during the past 100 years, Nature, 399, 437–439.

Luhmann J. G., Li Y., Arge C. N., Gazis P. R., Ulrich R. (2002), Solar cycle changes in coronal holes and space weather cycles, Journal of Geophysical Research (Space Physics), 107, 1154.

Neugebauer M. Snyder C.W. (1962), Solar Plasma Experiment, Science, 138, 1095–1097.

Parker E.N. (1958), Interaction of the Solar Wind with the Geomagnetic Field, Physics of Fluids, 1, 171–187.

Parker E.N. (1965), The passage of energetic charged particles through interplanetary space, Planetary and Space Science, 13, 9–49.

Rickett B.J. Coles W.A. (1991), Evolution of the solar wind structure over a solar cycle - Interplanetary scintillation velocity measurements compared with coronal observations, Journal of Geophysical Research, 96:1717–1736, February 1991.

Schwabe T. (1843), Sonnen-beobachtungen im jahre 1843. Astronomische Nachrichten, 21, 233–236.

Svalgaard L., Wilcox J.M. (1976), Structure of the extended solar magnetic field and the sunspot cycle variation in cosmic ray intensity, Nature, 262, 766–768.

Tanaka T., Washimi H. (1999), Solar cycle dependence of the heliospheric shape deduced from a global MHD simulation of the interaction process between a nonuniform time-dependent solar wind and the local interstellar medium, Journal of Geophysical Research, 104, 12605–12616.

Proceedings of
Tenth Workshop "Solar Influences on the Magnetosphere, Ionosphere and Atmosphere"
Primorsko, Bulgaria, June 4÷8, 2018

SOHO/ERNE proton event catalog: Progress results under the SEP origin project

R. Miteva and D. Danov

Space Research and Technology Institute, Bulgarian Academy of Sciences, Sofia, Bulgaria
E-mail: rmiteva@space.bas.bg

Abstract.

The focus of this report is to outline the current status of the multi-energy cataloging of solar energetic protons from the SOHO/ERNE instrument in solar cycles 23 and 24. Half of the energy channels provided by the high energy detector (HED) have been analyzed and the first results are presented here. The finalized event list (1996-2018) is planned to appear on-line as a freely accessible catalog supported by the Space Climate group at the Space Research and Technology Institute – Bulgarian Academy of Sciences (SRTI-BAS).

Introduction

Various proton catalogs already exist, either as freely available event lists or as part of publications. Without the ambition for completeness, we present some known to us proton catalogs.

Freely available proton event lists:

- NOAA preliminary listing (1976-present): https://umbra.nascom.nasa.gov/SEP/
- SEPEM reference event list (1973-2013): http://dev.sepem.oma.be/help/event_ref.html
- ERNE major proton events (1996-1999): https://srl.utu.fi/erne_data/events/proton/HED/eventlist.html
- SOHO/ERNE particle events (1996-2007): https://srl.utu.fi/SEPCatalog/index.php
- SEPserver event catalogs (several, 1997-2012/2015): http://server.sepserver.eu/
- Solar proton events (1970-2008): http://www.wdcb.ru/stp/online_data.en.html#ref113

Proton catalogs provided in recent publications, the primary instrument(s) and time coverage:

- Cane et al. (2010): IMP-8 (1996-2006)
- Miteva et al. (2013): GOES, Wind/EPACT, ACE/EPAM (1996-2006)
- Papaioanou et al. (2016): GOES (1984-2013)
- Kühl et al. (2017): SOHO/EPHIN (1997-2014)
- Paasilta et al. (2017): SOHO/ERNE (1997-2016)
- Miteva et al. (2018): Wind/EPACT (1996-2016)

For the purpose of the present catalog, proton data from SOHO/ERNE (Torsti et al. 1995) instrument is used, due to wide energy coverage provided (1.6 to 131 MeV). The instrument consists of two detectors:

- low energy detector (LED): (1) 1.6-1.8, (2) 1.8-2.2, (3) 2.2-2.7, (4) 2.7-3.3, (5) 3.3-4.1, (6) 4.1-5.1, (7) 5.1-6.4, (8) 6.4-8.1, (9) 8.1-10, (10) 10-13 MeV and

- high energy detector (HED): (1) 14-17, (2) 17-22, (3) 21-28, (4) 26-32, (5) 32-40, (6) 40-51, (7) 51-67, (8) 64-80, (9) 80-101, (10) 101-131 MeV.

As a reference channel is selected the second HED channel 17-22 (19.5) MeV, namely the visual identification of the proton enhancements is performed at this energy and all other events are in fact the high (or/and low) energy signatures of the ~20 MeV protons.

Despite that proton lists based on SOHO/ERNE data already exist, the aim of the current catalog is to provide information on proton peak intensity in all 10 HED energy channels individually (and in future also in selected LED channels) as well as additional information such as: calculation of the proton (onset-to-peak) fluences, completion of the solar origin association (solar flares and coronal mass ejections, CMEs), identification of related solar eruption phenomena (prominences, radio bursts, waves, etc.).

The need for a multi-energy catalog from the same instrument has been shown by Dierckxsens et al. (2015) and their energy dependent statistics. The results on correlation studies between proton intensity and flare class (increasing trend) or/and with CME speed (decreasing trend) as a function of the proton energy have not been challenged to date.

The first version of the on-line platform of the catalog was shown in Miteva and Danov (2017a). The first results in the ~20 MeV channel were reported by Miteva (2017b), where the main guidelines for the proton identification were already presented.

At present, we report on the preliminary statistical results in five out of the ten HED energy channels of SOHO/ERNE.

Current status of the on-line SOHO/ERNE catalog

The access point to the SOHO/ERNE catalog is through a web-based interface: http://newserver.stil.bas.bg/SEPcatalog as shown in Fig. 1. After selecting the relevant button, a new overview page is opened (Fig. 2) providing a concise description of the SOHO/ERNE catalog contents, the different abbreviation used, relevant links, contact information, etc.

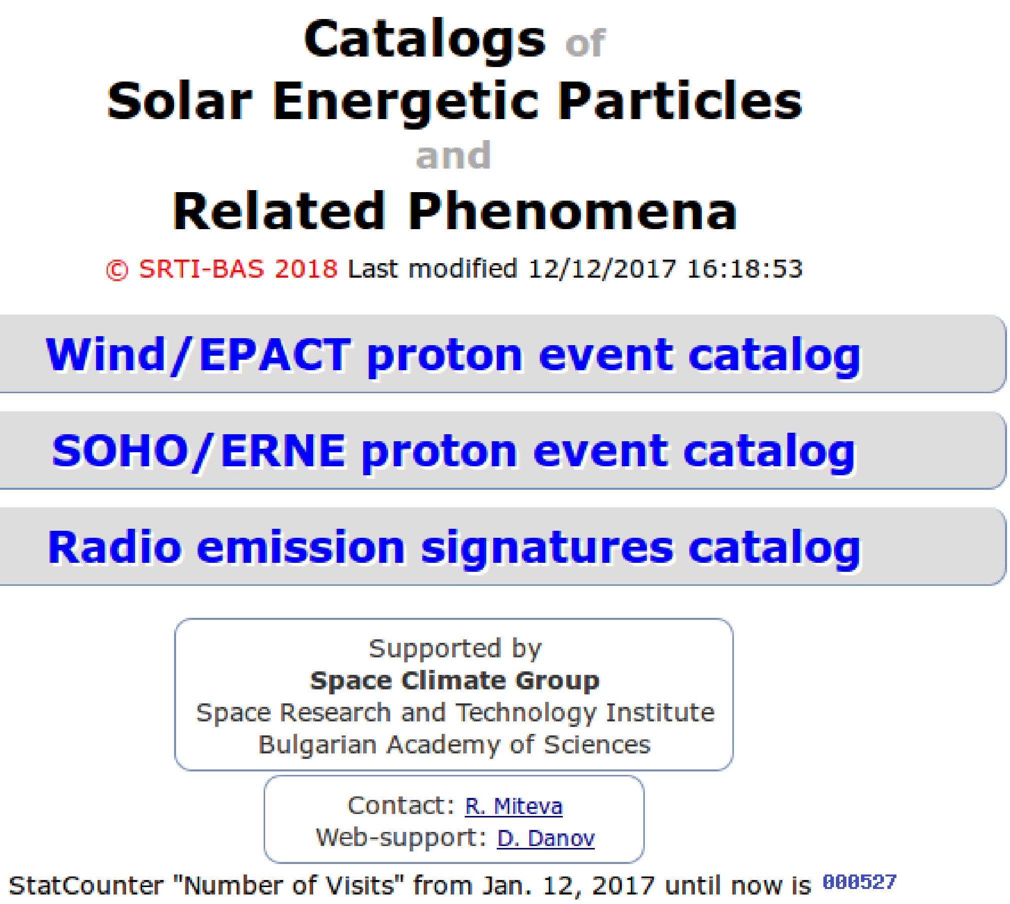

Fig. 1 Home page of the dedicated website hosting three different catalogs: http://newserver.stil.bas.bg/SEPcatalog.

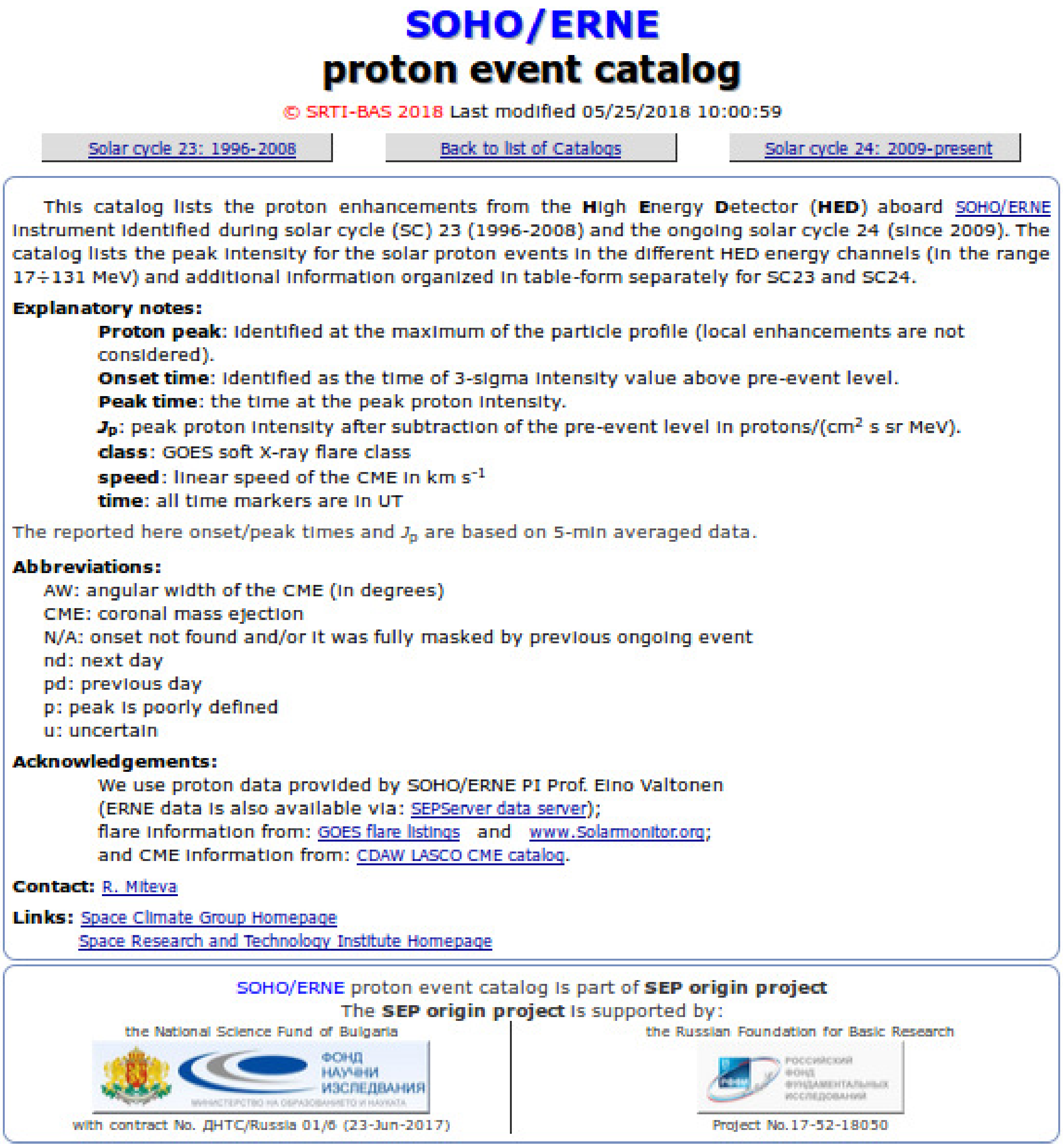

SOHO/ERNE
proton event catalog

© SRTI-BAS 2018 Last modified 05/25/2018 10:00:59

Solar cycle 23: 1996-2008 | Back to list of Catalogs | Solar cycle 24: 2009-present

This catalog lists the proton enhancements from the **H**igh **E**nergy **D**etector (**HED**) aboard SOHO/ERNE instrument identified during solar cycle (SC) 23 (1996-2008) and the ongoing solar cycle 24 (since 2009). The catalog lists the peak intensity for the solar proton events in the different HED energy channels (in the range 17÷131 MeV) and additional information organized in table-form separately for SC23 and SC24.

Explanatory notes:

Proton peak: identified at the maximum of the particle profile (local enhancements are not considered).
Onset time: identified as the time of 3-sigma intensity value above pre-event level.
Peak time: the time at the peak proton intensity.
J_p: peak proton intensity after subtraction of the pre-event level in protons/(cm^2 s sr MeV).
class: GOES soft X-ray flare class
speed: linear speed of the CME in km s^{-1}
time: all time markers are in UT

The reported here onset/peak times and J_p are based on 5-min averaged data.

Abbreviations:

AW: angular width of the CME (in degrees)
CME: coronal mass ejection
N/A: onset not found and/or it was fully masked by previous ongoing event
nd: next day
pd: previous day
p: peak is poorly defined
u: uncertain

Acknowledgements:

We use proton data provided by SOHO/ERNE PI Prof. Eino Valtonen
(ERNE data is also available via: SEPServer data server);
flare information from: GOES flare listings and www.Solarmonitor.org;
and CME information from: CDAW LASCO CME catalog.

Contact: R. Miteva

Links: Space Climate Group Homepage
Space Research and Technology Institute Homepage

SOHO/ERNE proton event catalog is part of **SEP origin project**
The **SEP origin project** is supported by:
the National Science Fund of Bulgaria | the Russian Foundation for Basic Research
ФОНД НАУЧНИ ИЗСЛЕДВАНИЯ
with contract No. ДНТС/Russia 01/6 (23-Jun-2017) | Project No.17-52-18050

Fig. 2 Description of the SOHO/ERNE proton event catalog.

The final web-level is accessed via the two buttons at the top of the page designed to contain the information separately on solar cycle (SC) 23 and 24. Each of these new pages (see Fig. 3) is structured as a table containing information about the proton events and their solar origin. Complete information (onset, peak time and peak proton intensity, J_p) is planned to be provided only for the reference energy channel. There, the value for J_p will be linked to an overview plot over two-day period (see Fig. 1 in Miteva 2017b), where two different symbols will depict the onset time (with a cross) and the peak intensity and time (with a diamond). The remaining columns will contain only the evaluated peak proton intensity for each proton enhancement in the specific energy. In many of the energy channels, no particle enhancement is identified (denoted by '-' for no event). Flare and CME information is provided in separate columns.

SOHO/ERNE
proton event catalog
Solar cycle 23: 1996-2008
© SRTI-BAS 2018 Last modified 03/26/2018 16:52:12

Back to list of Catalogs | Back to SOHO/ERNE | Solar cycle 24: 2009-present

Event date	14-17 MeV	17-22 MeV			21-28 MeV	26-32 MeV	32-40 MeV	40-51 MeV	51-67 MeV	64-80 MeV	80-101 MeV	101-131 MeV	Flare	
yyyy-mm-dd	J_p	onset time	peak time	J_p	J_p	J_p	J_p	J_p	J_p	J_p	J_p	J_p	class/onset/location	tim
1996-07-09		10:03	10:50	0.0016		0.0004		-		-		-	X2.6/09:05/S10W30	
1996-08-13		17:53	22:05	0.0038		0.0012		0.0005		-		-	uncertain	16:
1996-11-27		00:18	02:37	0.0004		-		-		-		-	B9.0/20:48^{pd}/u	21:
1996-11-27		14:22	15:20	0.0005		-		-		-		-	uncertain	
1996-11-28		19:53	22:09	0.0034		0.0007		-		-		-	C1.3/15:35/u	16:
1996-11-29		04:43	13:49	0.0015		0.0003		-		-		-	uncertain	
1996-11-30		06:23	07:14	0.0101		0.0022		0.0002		-		-	uncertain	
1996-12-01		22:05	01:33nd	0.0005		-		-		-		-	M1.0/20:16/S06W47	
1996-12-24		14:59	18:21	0.0050		0.0014		0.0003		-		-	C2.1/13:03/N05W95	13
1997														
1998														
1999														
2000														
2001														

Back to list of Catalogs | Back to SOHO/ERNE | Solar cycle 24: 2009-present

SOHO/ERNE
proton event catalog
Solar cycle 24: 2009-present
© SRTI-BAS 2018 Last modified 03/20/2018 19:49:11

Back to list of Catalogs | Back to SOHO/ERNE | Solar cycle 23: 1996-2008

Event date	14-17 MeV	17-22 MeV			21-28 MeV	26-32 MeV	32-40 MeV	40-51 MeV	51-67 MeV	64-80 MeV	80-101 MeV	101-131 MeV	Flare	
yyyy-mm-dd	J_p	onset time	peak time	J_p	J_p	J_p	J_p	J_p	J_p	J_p	J_p	J_p	class/onset/location	tim
2009-12-22		07:33	13:18	0.0011		0.0004		0.00022		-		-	C7.2/04:50/S26W46	
2010-02-12		17:20	22:19	0.0007		0.0003		-		-		-	M8.3/11:19/N23E11	
2010-04-04		10:23	11:06	0.0002		-		-		-		-	uncertain	
2010-06-12		02:32	07:02	0.0207		0.0061		0.0023		-		-	M2.0/00:30/N43W23	01:
2010-08-03		N/A	23:06^{u}	0.0326		0.0025		-		-		-	uncertain	
2010-08-07		20:09	01:33nd	0.0042		0.0042		0.0011		-		-	M1.0/17:55/N11E34	18:
2010-08-14		10:53	12:48	0.6267		0.1852		0.0512		-		-	C4.4/09:38/N17W52	10:
2010-08-18		07:18	11:52	0.1170		0.0190		0.0037		-		-	C4.5/04:45/N18W88	05:
2010-08-31		23:28	04:20nd	0.0191		0.0046		0.0010		-		-	uncertain	21:
2010-09-09		01:02	04:38	0.0135		0.0024		0.0006		-		-	C3.3/23:05/N21W87	23:
2010-12-31		05:58	06:57	0.0004		-		-		-		-	C1.3/04:18/N12W57	05
2011														
2012														
2013														

Back to list of Catalogs | Back to SOHO/ERNE | Solar cycle 23: 1996-2008

Fig. 3 Contents of the SOHO/ERNE proton event catalog (status end July 2018) for solar cycle 23 (upper) and solar cycle 24 (lower plot).

Preliminary results of the multi-energy analysis

The yearly distribution (1996-2016) of the proton event in two energy channels (~20 and ~116 MeV) is shown in Fig. 4. The solar cyclicity is evident, as well as the weaker, also in proton number, SC24.

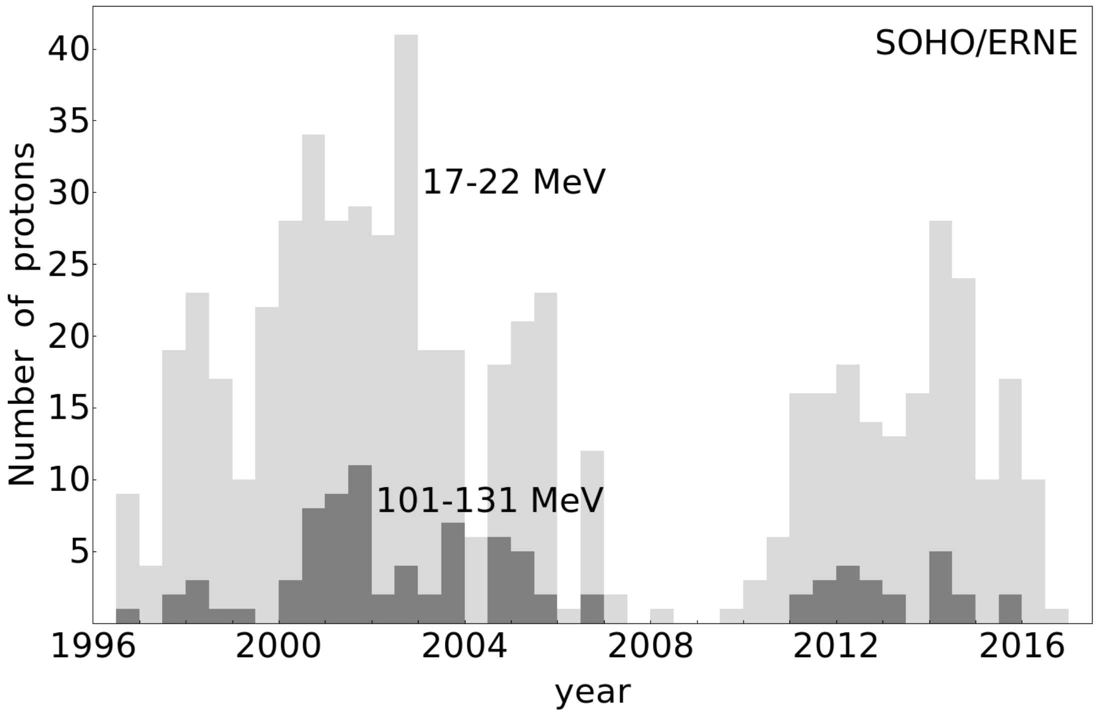

Fig. 4 The yearly distribution of proton events in the reference ~20 MeV and the highest, ~116 MeV, HED energy channel.

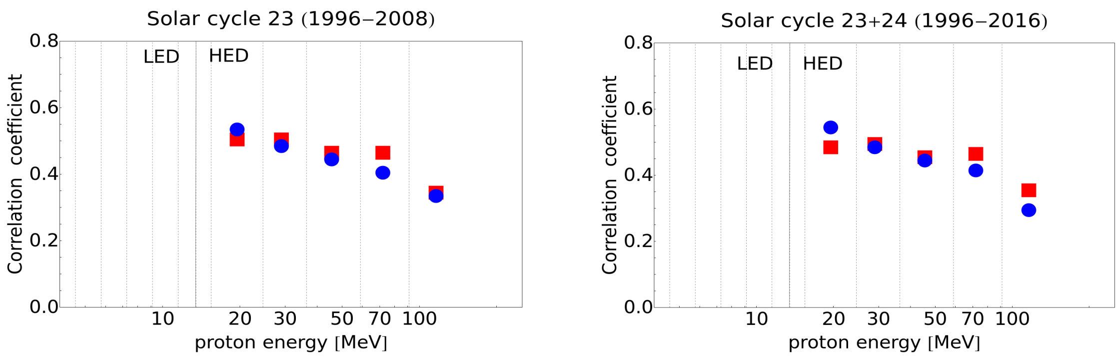

Fig. 5 The $\log_{10}$–$\log_{10}$ Pearson correlation coefficient with flare class (red squares) and CME speed (blue circles) for two time periods, as denoted at the top of the plot. LED and HED energy coverage is separated by solid vertical line.

The aim of the analysis over the available energy channels is to investigate the correlation behavior as a function of energy. Once the proton peak intensity in each energy channel is evaluated, the Pearson correlation coefficients with flare class and CME speed can be calculated. At present, the preliminary results over five energy channels is shown in Fig. 5, namely for HED channels (2), (4), (6), (8) and (10). The dotted vertical lines denote the channels under completion. Five LED energy channels are considered at present for further evaluation, namely for a better energy coverage over the entire range, namely (6)-(10). The range can be further extended at lower energies (down to 1.6 MeV) if necessary.

The first energy dependent statistical results are shown in Fig. 5, separately for data in SC23 (1996-2008) and for the entire evaluated period SC23+24 (1996-2016). There are no statistical differences between the results in the two period of interest.

The preliminary results show a steady declining trend of the correlation coefficients between the peak proton intensity and, both, flare class (opposite to the results in Dierckxsens et al. 2015 over SC23) and CME speed (confirming the results there). When the finalized evaluation of the proton intensity is completed, these calculations will be repeated in order to avoid differenced due to erroneous particle identifications.

Nevertheless, SOHO/ERNE instrument is subject to saturation when the proton flux surpasses certain intensity threshold (of about 10 flux units, as shown in Fig. 2 in Miteva (2017b), by comparing ~20 MeV SOHO/ERNE and ~25 MeV Wind/EPACT protons). This effect needs to be investigated at the different energy channels. Without suitable correction factor, the flux level of large proton events is underestimated. This effect could be responsible for a drop in the correlation trend, however such possibility needs to be carefully verified.

The complete catalog and energy dependent statistical results will be reported elsewhere. Finally, the catalog contents will be released on-line, covering the last two solar cycles (1996-2018) and beyond if SOHO/ERNE data is also been provided.

Acknowledgement

This work is supported by the National Science Fund of Bulgaria with Contract No. DNTS/Russia 01/6 (23-Jun-2017).

References

Cane H. V., Richardson, I. G., von Rosenvinge, T. T. (2010) A study of solar energetic particle events of 1997-2006: Their composition and associations, Journal of Geophysical Research, Vol. 115: A8, CiteID A08101

Kühl, P., Dresing N., Heber B., Klassen A. (2017) Energetic particle events with protons above 500 MeV between 1995 and 2015 measured with SOHO/EPHIN, Sol. Phys, Vol. 292: 10, 13pp.

Dierckxsens, M., Tziotziou, K., Dalla, S., Patsou, I., Marsh, M. S., Crosby, N. B. Malandraki, O., Tsiropoula, G. (2013) Relationship between Solar Energetic Particles and Properties of Flares and CMEs: Statistical Analysis of Solar Cycle 23 Events, Sol. Phys., Vol. 290: 3, pp. 841-874

Paassilta M., Raukunen O., Vainio R., Valtonen E., Papaioannou A., Siipola R., Riihonen E., Dierckxsens M., Crosby N., Malandraki O, Heber B., Klein K.-L. (2017), Catalogue of 55–80 MeV solar proton events extending through solar cycles 23 and 24, JSWSC, Vol. 7, A14, 19pp.

Papaioannou, A., Sandberg, I., Anastasiadis, A., Kouloumvakos, A., Georgoulis, M. K., Tziotziou, K., Tsiropoula, G., Jiggens, P., Hilgers, A. (2016) Solar flares, coronal mass ejections and solar energetic particle event characteristics, JSWSC, Vol. 6, A42, 29 pp.

Miteva, R., Klein, K.-L., Malandraki, O., Dorrian, G. (2013) Solar Energetic Particle Events in the 23rd Solar Cycle: Interplanetary Magnetic Field Configuration and Statistical Relationship with Flares and CMEs, Sol. Phys., Vol. 282: 2, pp. 579-613

Miteva R., Danov D. (2017a) On-line catalogs of solar energetic protons at SRTI-BAS, Proceeding of Ninth Workshop “Solar Influences on the Magentosphere, Ionosphere and Atmosphere”, Sunny Beach, Bulgaria, edited by K. Georgieva, B. Kirov and D. Danov. ISSN: 2367-7570, pp. 66-69

Miteva, R. (2017b) SOHO/ERNE proton event catalog: Description and first results, Proceedings Thirteenth International Scientific conference "Space, Ecology, Safety – SES2017", Sofia, Bulgaria, edited by G. Mardirossian, Ts. Srebrova and G. Jelev. ISSN: 1313-3888, pp. 52-56

Miteva R., Samwel S.W., Costa-Duarte M.V. (2018) The Wind/EPACT proton event catalog (1996–2016), Sol. Phys: 293: 2, article id. 27, 44pp.

Torsti, J., Valtonen, E., Lumme, M., Peltonen, P., Eronen, T., Louhola, M., Riihonen, E., Schultz, G., Teittinen, M., Ahola, K., Holmlund, C., Kelhä, V., Leppälä, K., Ruuska, P., Strömmer, E. (1995) Energetic Particle Experiment ERNE, Sol. Phys., Vol. 162: 1-2, pp. 505-531

Proceedings of
Tenth Workshop "Solar Influences on the Magnetosphere, Ionosphere and Atmosphere"
Primorsko, Bulgaria, June 4÷8, 2018

Results of comparative analysis of the SEP events and the microwave bursts observed by 2-24 GHz and 4-8 GHz spectropolarimeters in 2010-2016

Zhdanov D.A. [1], *Kashapova L.K.* [1], *Miteva R.* [2]

[1] Institute of Solar-Terrestrial Physics, SB RAS, Irkutsk, Russia
[2] Space Research and Technology Institute, Bulgarian Academy of Sciences, Sofia, Bulgaria
E-mail: zhdanov@iszf.irk.ru

Abstract.

We present a relationship analysis between the solar energetic particle (SEP) events and the microwave (MW) spectral observations of the solar bursts detected in 2010–2016. The information about the SEP events is taken from the Wind/EPACT catalog based on data in the period 1996÷2016. We use MW data from the archive of MW observations in the range 2÷24 GHz. Observations were made by spectropolarimeters of the SSRT observatory (Russia). We found that 40 events are present in both catalogs. We tested the relationships between the proton spectral index of SEP events and the peak frequency of the MW bursts and presence of circular polarization in MW emission of selected events. The results are finally discussed.

Introduction

Solar energetic particles (SEPs), i.e., temporal increases of charged particles flux in interplanetary (IP) space, together with their solar origins are keeping the interest of the Space Weather community during several dozen years [e.g. *Reames*, 2015]. There are several questions that have not been clarified yet. Where is the acceleration site of the particles, in the solar atmosphere during the flare or in the IP space on shock waves of coronal mass ejection (CME)? The comparison of solar event characteristics with the characteristics of the SEP events is one way to advance in solving these problems. The best tracers of acceleration processes are accelerated electrons. They move from the location of the primary energy release in two opposite directions and thus precipitate in two different conditions of plasma. The dense plasma provides generation of hard X-ray emission. The other part of electron flux occurs in conditions that are favorable for generating the gyrosynchrotron emission. It is assumed that the microwave (MW) emission at frequencies above 2 GHz is usually incoherent gyrosynchrotron emission from relativistic electrons. The flux maximum separates the MW spectrum into two parts. Accelerated electrons only generate the emission at frequencies above the peak frequency. The previous studies used 35 GHz frequency for testing of acceleration process during the flares produced the SEP events [e.g. *Grechnev, et al.,* 2017]. It is possible that this approach restricts the number of considered events that could result to a loss of important information as only the strongest flares can have flux at 35 GHz. The aim of this work is studying MW spectral signatures of the solar origins of SEP events with high proton flux in wide frequency region (2–24 GHz). We present the results of the first stage including the event selection and preliminary analysis.

Data

We used the microwave data of the 2–24 GHz Spectropolarimeter and 4–8 GHz Spectropolarimeter (BBMS) located in Radio Astrophysical Observatory of the Institute of Solar-Terrestrial Physics, Russia [*Zhdanov, et al.*, 2011]. The microwave data are the temporal profiles of the flux for right-hand circular polarization (RCP) and the left-hand of circular polarization (LCP) at 26 frequencies for the BBMS and at 16 frequencies for the 2–24 GHz Spectropolarimeter.

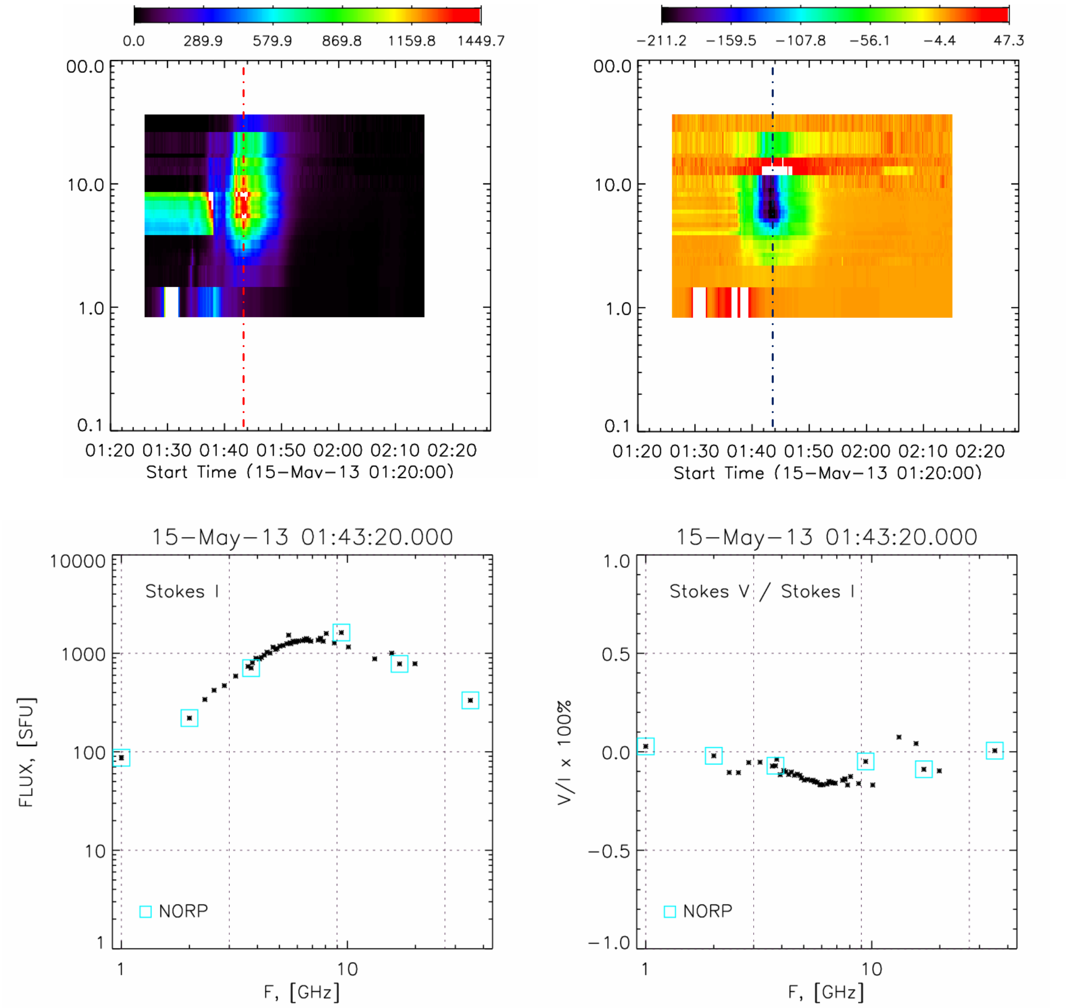

Fig. 1 Example of data processing for SOL2013-May-15 event: top row – dynamic spectra for both intensity (left plot) and the degree of polarization (right plot); bottom row – the spectrum at the time marked by the dash-dot lines for intensity (left plot) and the degree of polarization (right plot); the data points marked by squares denote data adopted from the Nobeyama Radio Polarimeters.

We used the catalog of SEP events detected by the Wind/EPACT instrument over the period 1996–2016 [*Miteva, et al.* 2018]. They are proton events. The catalog shows the times of SEP event onset, the peak times, the intensity of peak proton flux and the onset-to-peak proton fluences for proton fluxes detected in the two energy channels (above 25 and 50 MeV). Most of the events are associated with both solar flares and CME.

Results

We compared the data of the microwave burst catalog obtained by BBMS with the SEP event catalog obtained by Wind/EPACT. Microwave observations are available only from 2010, and it is limited by the local day time (00–10 UT). There are 172 SEP events that occurred from 2010 to 2016. Only 39 events from the 172 events took place between 0 and 10 UT that potentially could be observed by the spectropolarimeters. We carried out an analysis of these 39 events and found that 18 events are typical microwave bursts. Three events were related with very weak flares (B8.1, C1.2, C4.6) and 7 events had no microwave features. We did not reveal the solar flares for other 7 events. In the remaining 4 events, microwave observations finished earlier than 10 UT.

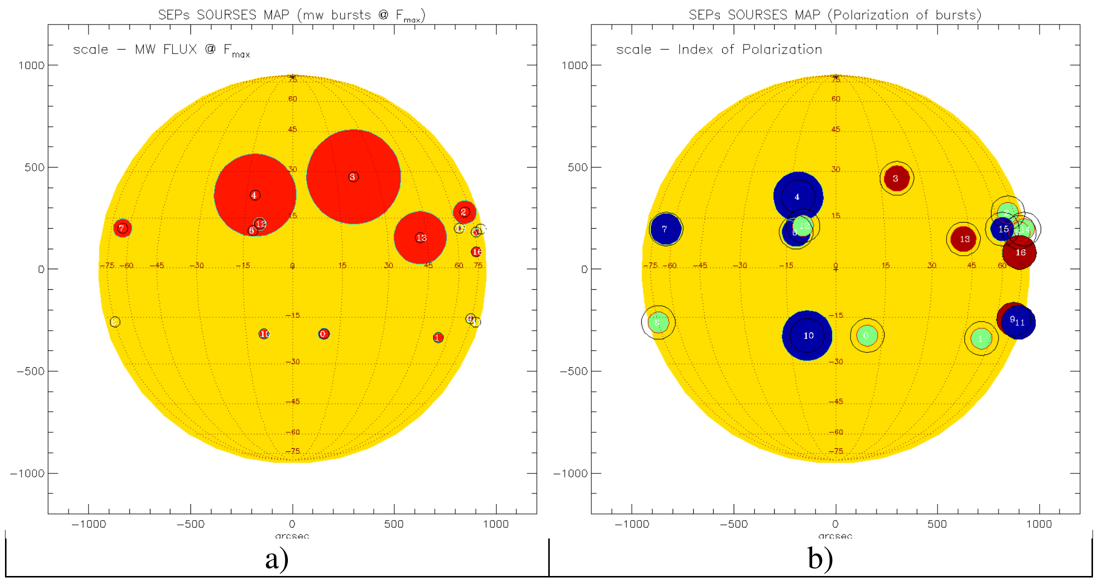

Fig. 2 SEP sources mapping; circles are positions of microwave bursts; sizes of circles depend on both strength of the microwave flux and values of the degree of polarization. a) microwave bursts; b) degree of polarization, blue color – LCP, red color – RCP, green color – no polarization

We focused further on the 18 events associated with microwave bursts. We processed the data, plotted the microwave spectrum and determined the following parameters for each event: the flux value at maximum; the frequency of spectral maximum; presence and sign of the polarization and the frequency of the maximum polarization value. Table 1 shows the obtained results.

Figure 1 shows the example of data processing for SOL2013-May-15 event. The top panel of the figure shows the dynamic spectra for both intensity (left plot) and the degree of polarization (right plot). The bottom panel shows the spectrum at the time marked by the dash-dot lines for intensity (left plot) and the degree of polarization (right plot). The squares denote the data of the Nobeyama Radio Polarimeters.

Figure 2 shows the location of radio sources on the solar disk according to the position of the solar origins in the SEP catalog. The left plot (a) shows the distribution of the strength of the microwave flux of the events. The right plot (b) shows the distribution of the values of the degree of polarization of the events. The circle color indicates the sign of polarization.

Summary

We carried out a selection and preliminary analysis of the microwave data for SEP events from the Wind/EPACT catalog. The studied events occurred from 0 to 10 UT in the years from 2010 to 2016. For information about microwave observations, we used data obtained by the 2–24 GHz spectropolarimeter and the 4–8 GHz spectropolarimeter.

We found that 39 events are present in both catalogs. But only 18 out of the 39 events were accompanied by typical MW bursts. The spatial distribution of MW bursts indicates to the more active northern hemisphere. The peak frequencies of the MW bursts vary within 2 GHz and 10 GHz. The circular polarization in MW emission was found in 10 events of the selected events. We did not reveal any dependence between the position of the solar origin of SEP event and the sign of circular polarization. The further analysis of the selected and processed data will allow getting new information about the properties of MW emission of SEP event origins.

Table 1. The characteristics of the 18 proton events associated with typical microwave bursts.

№	Date (yyyy-mm-dd)	Time (UT)	GOES class	$Flux_{max}$ (sfu)	F_{max} (GHz)	V/I (%)	F_{max} V (GHz)
1	2011-02-15	01:44	X2.2	1000	8	no	no
2	2011-06-07	06:16	M2.5	800	6.5	no	no
3	2011-08-09	07:48	X6.9	2000	10	no	no
4	2012-01-23	03:38	M8.7	8000	4	+10	4
5	2012-03-07	01:05	X1.3	7000	9.4	-30	3.7
6	2012-05-17	01:25	M5.1	600	5	no	no
7	2013-03-15	05:46	M1.1	120	1.5	-15	7.5
8	2013-05-15	01:25	X1.2	1600	7	-18	6.5
9	2013-06-21	02:30	M2.9	-	-	-	-
10	2013-11-02	04:40	C8.2	-	-	-	-
11	2014-02-20	07:26	M3.0	500	6	+20	6
12	2014-12-17	04:25	M8.7	800	7	-30	13
13	2015-06-18	00:33	M1.2	60	2	-20	2
14	2015-06-21	02:06	M2.6	1100	7.5	no	no
15	2015-06-25	08:02	M7.9	4500	9	+10	17
16	2016-03-16	06:34	C2.2	8	3.5	no	no
17	2016-04-18	00:14	M6.7	400	6	-8	9
18	2016-07-23	05:00	M7.6	850	2.5	+20	10

Acknowledgment

This study is supported by the project 'The origin on solar energetic particles: solar flares vs. coronal mass ejections', co-funded by the Russian Foundation for Basic Research with project No. 17-52-18050 and the National Science Fund of Bulgaria under contract No. DNTS/Russia 01/6 (23-Jun-2017). The results were obtained using the equipment of Center for Common Use «Angara» http://ckp-rf.ru/ckp/3056/. DZ and LK thank the budgetary funding of Basic Research program II.16 for partial support.

References

Grechnev, V., Kiselev, V., Meshalkina, N., Chertok, I. (2017), Correlation of near-Earth proton enhancements >100 MeV with parameters of solar microwave bursts, Solar-Terrestrial Physics, 3, no. 3, 3-12.

Miteva R., Samwel S. W., C-D Marcus V. (2018), The Wind/EPACT Proton Event Catalog (1996 - 2016), Solar Physics, 293, no. 2, article id. 27, 44.

Reames D. V. (2015), What Are the Sources of Solar Energetic Particles? Element Abundances and Source Plasma Temperatures, Space Science Reviews, 194, no. 1-4, 303-327

Zhdanov D.A., Zandanov V.G. (2011), Broadband microwave spectropolarimeters, Central European Astrophysical Bulletin, 35, 223-227.

Proceedings of
Tenth Workshop "Solar Influences on the Magnetosphere, Ionosphere and Atmosphere"
Primorsko, Bulgaria, June 4÷8, 2018

Comparison of Kinematics of the Solar Eruptive Prominence and a Spatial Distribution of the Magnetic Decay Index

I. Myshiakov [1], *Ts. Tsvetkov* [2], *N. Petrov* [2]

[1] Institute of Solar-Terrestrial Physics, SB RAS
[2] Institute of Astronomy and National Astronomical Observatory, BAS
E-mail: ivan_m@iszf.irk.ru

Abstract.

Theoretical studies of magnetic flux rope instabilities, designed to explain filament eruptions, indicate that the loss of equilibrium may develop when the surrounding magnetic field decreases sufficiently rapid with height. The decay index, a parameter that reflects the decrease of magnetic field, is a useful instrument for predicting the behavior of filaments. In our study, we perform potential extrapolation to obtain spatial distribution of the decay index in the coronal space, identified with an eruptive prominence. Analysis of time dependent height profile of the prominence revealed, that its speed increased when the prominence reached height with certain values of the computed decay index.

Introduction

Solar prominences are extended concentrations of coronal matter that is much denser and cooler than its surroundings and are clearly distinguishable when they are seeing above the solar limb. Because of the same reason they manifested as darker formations while observed in projection on the disk. In the latter case they are called filaments. Solar prominences may exist in a stable state for many days and then suddenly start to accelerate in an upward direction. If new state of equilibrium cannot be achieved at higher altitudes and rapid upward motion continues, they may produce a coronal mass ejection (CME).

Coronal magnetic field dominates over gas pressure, so motions of highly conductive plasma are allowed along force lines of the magnetic field. Thus, gradual formation of dense concentrations of coronal plasma, suspended in a stable state on magnetic force lines, is possible in regions, where magnetic lines has curvature which vector is directed upward. In the study [Kuperus M. and M.A. Raadu, 1974] was introduced a model of a prominence in which magnetic configuration, able to confine plasma, was created by linear horizontal electric current in the coronal space and its mirror reflection with opposite sign below the photosphere. In this model gravitational force, acting on dense matter in the prominence, is counterbalanced by the repulsive Lorentz force between currents with opposite directions. This is in agreement with the observations revealing that plasma inside prominences often takes twisted orientation, thus resembling magnetic flux ropes and indicating the presence of electric currents.

In the study [Van Tend W. and M. Kuperus, 1978] the model of [Kuperus M. and M.A. Raadu, 1974] was enhanced by introducing background coronal magnetic field. The authors investigated state of equilibrium of electric current, influenced by ambient magnetic field, and found that instability against small vertical displacements will develop when magnetic field decreases sufficiently rapidly with height. The rate of the magnetic field decrease may be represented by a parameter that is called magnetic decay index. Theoretical model for prominence eruption was further addressed in the paper [Kliem B. and T Torok, 2005], where authors investigated state of equilibrium of ring current anchored on the photosphere surface. The authors termed the loss of equilibrium for such configuration of the current as torus instability. In the studies [Filippov B.P. and O.G. Den, 2001], [Fillipov B.P. et.al., 2014] authors considered real observational data and by applying potential extrapolation showed that prominences exist in a stable state below the altitude at which instability of linear current may develop.

In our study, we consider a prominence that erupted above the solar limb. We use observational data, provided by Atmospheric Imaging Assembly (AIA) and Heliospheric and Magnetic Imager (HMI) instruments onboard Solar Dynamics Observatory (SDO) spacecraft [Pesnell W.D., B.J. Thompson, P.C. Chamberlin, 2012]. We compare kinematics of the eruptive prominence and spatial distribution of the magnetic decay index in the coronal space, obtained with use of potential extrapolation.

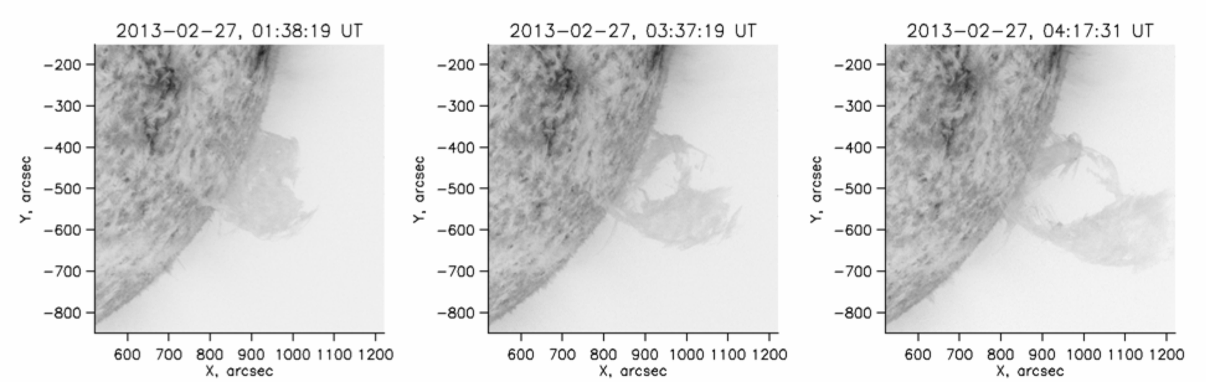

Fig. 1 SDO\AIA 304 Å images of the eruptive prominence.

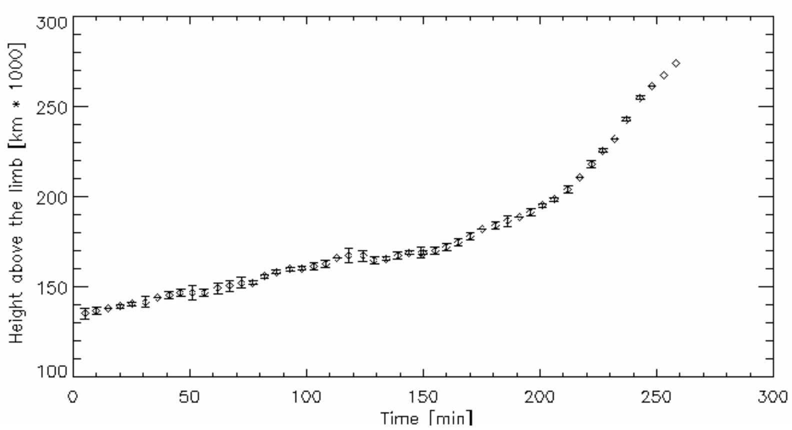

Fig. 2 Time-dependent height profile of the prominence's apex above the limb. The beginning of the timeline corresponds to February 27, year 2013, 0:00 UT.

Eruptive prominence

As an object for our study we chose a prominence outside active region that erupted on February 27, year 2013 when it was located above the South-Western solar limb (Fig. 1) According to catalog [Gopalswamy N. et al., 2009], the eruption was followed by a CME with average speed equal to 622 km/s. The position of the eruptive prominence allowed to track its apex by analyzing complete sequence of the SDO/AIA 304 Å images with ~5-min cadence, while prominence stayed in the instrument's field of view, and to build time-dependent height profile of the apex above the limb. Comprehensive explanation of this procedure is presented in the study [Tsvetkov Ts. and N. Petrov, 2018] and here we used some of the results from this paper (Fig. 2). By inspecting the obtained profile, we determined that the prominence had lost the equilibrium when its apex reached height of 180-190 Mm.

Magnetic field reconstruction

Coronal magnetic field is reconstructed using Green's function based potential extrapolation. The extrapolation code was developed by the authors of the present study and is designed to work in spherical geometry. As input boundary conditions SDO/HMI vector magnetograms with resolved pi-ambiguity is used, that allowed to calculate radial component of the magnetic field. Extrapolation is performed using magnetogram obtained on February 25, 0:00 UT. We used data, obtained several days before the eruption, because magnetograms that are too close to limb, obviously, have inappropriate quality due to projection effect. We assume, that large-scale magnetic structures outside the active region are rather stable and probably will have similar configuration after several days. Our extrapolation code works with predefined areas of the photosphere surface. For the case under consideration computational domain on the photosphere level is about 700 by 500 Mm, its height is 300 Mm and spatial resolution is 3 Mm. Outside the computational domain photosphere radial magnetic field considered equal to zero.

Magnetic decay index

Following [Kuperus M. and M.A. Raadu, 1974], to predict the prominence eruption it is necessary to know how fast coronal magnetic field decreases with height. This can be evaluated by using a parameter that is called magnetic decay index:

$$n = -\frac{\partial \ln(B_t)}{\partial \ln(h)} \tag{1}$$

here B_t – is transversal component of the ambient magnetic field, h – is the height above the photosphere. For a straight linear electric current estimated critical threshold is n=1. In the regions where magnetic decay index is greater than unity electric current of such configuration cannot be confined by magnetic field and start to ascend leading to the prominence eruption. In the study [Kliem B. and T. Torok, 2005] was determined that critical value of magnetic decay index for ring current is n=1.5.

Comparative analysis

Electric current in a stable state tend to be oriented along neutral line of the external magnetic field at each particular height, due to horizontal Lorentz forces vanishes there. Fig. 3 demonstrates that outside nearby active regions 11673, 11676 and 11677 neutral line of the extrapolated potential magnetic field corresponds to the prominence quite well. According to the extrapolation results different parts of the prominence located at different altitudes. Based on the obtained results we assume that the prominence ascended along the surface, formed by neutral lines, to the height where instability developed. Thus, regions of interest where spatial distribution of the magnetic decay index must be considered are in close proximity to the reconstructed neutral line.

Information on 3D structure of the extrapolated magnetic field allows one to calculate magnetic decay index everywhere inside the computational domain, using equation (1). Fig. 4 represents spatial distribution of the magnetic decay index at several particular heights. To avoid projection effects, the observer's position was relocated to the point above the center of the computational domain. According to the obtained results magnetic decay index increased monotonically in the region around the neutral line, identified with the eruptive prominence. From SDO/AIA 304 Å images we estimate that transverse size of the prominence by the onset of the eruption was up to 100 Mm. Assuming the electric current to be located near prominence's axis, we can subtract half of transverse size from previously estimated height of the apex of the prominence equal to 180-190 Mm. Obtained value is close to the height where magnetic decay index exceed critical value of 1.5, that is characteristic for the torus instability, over a considerable length of the neutral line.

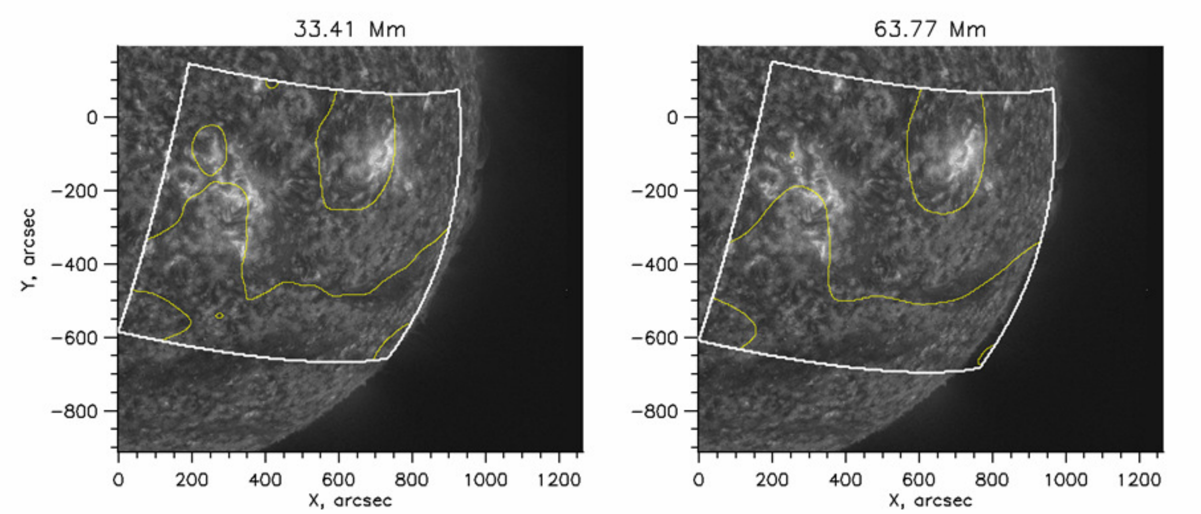

Fig. 3 Neutral line of the extrapolated magnetic field over HMI/AIA 304 Å image on February 25, year 2013, 0:00 UT. Yellow contours – neutral line. Thick white contour marks boundary of the computational domain. Neutral line is shown for two spherical layers above the photosphere surface. Heights of the layers are given in titles.

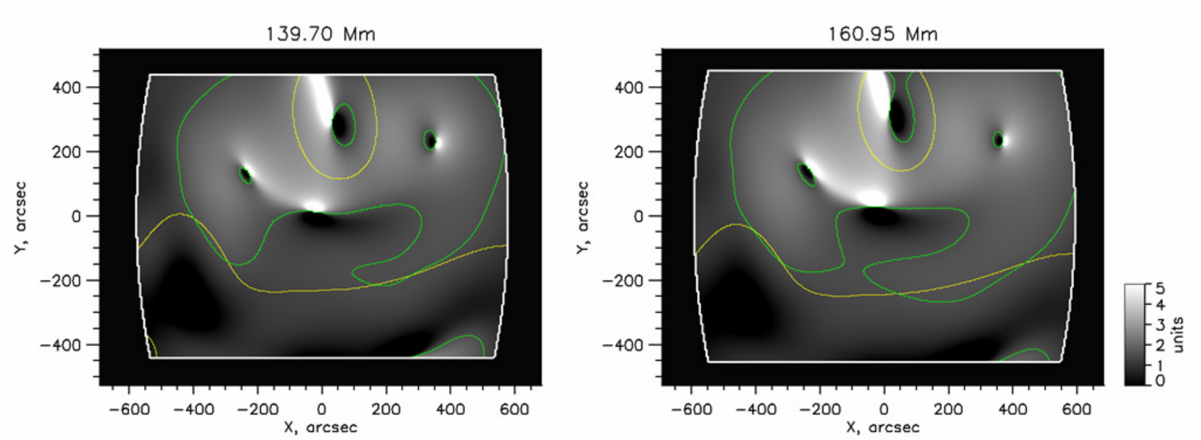

Fig. 4 Spatial distribution of the computed magnetic decay index at two heights above the photosphere, given in titles. Green contours correspond to decay index value equal to 1.5. Yellow contours – neutral line. Thick white contour marks boundary of the computational domain. Minimal and maximal values of the magnetic decay index are limited to 0 and 5.

Conclusions

The eruption of a solar prominence located above the solar limb is considered. Comparative analysis of kinematics of the prominence and spatial distribution of the magnetic decay index revealed that the prominence had lost its equilibrium when electric current, identified with approximate prominence's axis, reached height with critical values of the magnetic decay index equal to 1.5. That indicates the torus instability as possible mechanism of the prominence eruption.

Acknowledgment

This study was supported by RFBR research projects 17-52-18050 & the National Science Fund of Bulgaria under contract No. DNTS/Russia 01/6 (23-Jun-2017) (IM, TsTs, NP) and 18-32-00540 mol_a (IM); by Program No. 28 of the RAS Presidium (IM); by budgetary funding of Basic Research program II.16 (IM).

References

Kuperus, M. and M.A. Raadu (1974). The Support of Prominences Formed in Neutral Sheets. Astron&Astrophys., 31: 1189-193.

Van Tend W. and M. Kuperus (1978). The Development of Coronal Electric Current Systems in Active Regions and Their Relation to Filaments and Flares. Solar Phys., 59: 115-127.

Kliem B. and T Torok (2005). Torus Instability. Physical Review Letters, 96:255002-1 - 255002-4.

Filippov B.P. and O.G. Den (2001). A Critical Height of Quiescent Prominences before Eruption. Journal of Geophysical Research, 106: 25177-25184.

Filippov B.P., O.V. Martsenyuk, O.E. Den, Yu.V. Platov (2014). The Critical Decay Indices for the Magnetic Fields Observed in Solar Eruptive Phenomena. Astronomy Reports, 58: 928-935.

Gopalswamy N., S. Yashiro, G. Michalek, G. Stenborg, A. Vourlidas, S. Freeland, R. Howard (2009). The SOHO/LASCO CME Catalog. Earth Moon Planet, 104: 295-313.

Tsvetkov Ts. and N. Petrov (2018). Kinematics of prominence eruptions. Astronomical and Astrophysical Transactions (AApTr), Vol. 30: 3-4, pp 1-1, ISSN 1055-6796.

Pesnell W.D., B.J. Thompson, P.C. Chamberlin (2012). The Solar Dynamics Observatory (SDO). Solar Physics, 275: 3-15.

The Efficiency of Solar Energetic Particle Generation: CORONAS-F Mission Data Analysis

Myagkova I.N. [1], *Miteva R.* [2], *Kashapova L.* [3,5], *Bogomolov A.V.* [1], *Petrov N.* [4], *Tsvetkov Ts.* [4], *Meshalkina N.* [3], *Myshyakov I.* [3]

[1] Skobeltsyn Institute of Nuclear Physics, MSU, Moscow, Russia
[2] Space Research and Technology Institute, Bulgarian Academy of Sciences, Sofia, Bulgaria
[3] Institute of Solar-Terrestrial Physics SB RAS, Irkutsk, Russia
[4] Institute of Astronomy and NAO, Bulgarian Academy of Sciences, Sofia, Bulgaria
[5] Irkutsk State University, Physical Department, Irkutsk, Russia
E-mail: irina@srd.sinp.msu.ru

Abstract.

We present the results of a comparative analysis on the efficiency of the solar energetic particle events (SEP) and related solar flares. Both SEP events and solar flares were detected by the CORONAS-F solar mission. We selected the SEP events based on the presence of simultaneous observations from the hard X-ray (HXR) instrument SONG (CORONAS-F satellite) with radio emission ranging from microwaves to the meter-range, as evidence of accelerated particles generated during the events and solar proton and electron data measured by MKL instrument on board CORONAS-F satellite in polar caps. The results are discussed from point of using solar flare emission features as the criteria of generation of SEP event with high proton abundance.

Introduction

Solar energetic particles (SEPs) are the observed in situ electrons, protons and heavy nuclei at energies from the keV up to the GeV range (e.g. [Desai and Giacalone, 2016]). SEPs, together with the effects caused by their solar origin, flares and coronal mass ejections (CMEs) are important space weather agents and topic of ongoing research [Jiggens et al., 2014]. While in space, humans and technological devices are exposed to different radiation effects caused by energetic particles namely ones of solar origin, cosmic rays and particles of the radiation belt of the Earth [Baker, 2000].

The main goal of this work is the comparison of the efficiency of solar energetic particle (SEP) generation in solar flare observed by CORONAS-F solar mission. In this experiment, it was possible to register simultaneously a hard neutral emission of solar flares -X-rays, gamma quanta, neutrons, and SEP particles (in polar caps), which simplified multi-wavelength observations in near-Earth space. The target of this analysis was to reveal that both, powerful and weak, SEP events are associated with the solar flares observed by SONG with high temporal resolution.

Experiments

The CORONAS-F Russian solar space observatory was launched on July 31, 2001, and operated until the end of 2005. At the beginning of its flight CORONAS-F had a quasi-circular orbit, with initial parameters: altitude 507±21 km, inclination 82.5 degrees, and period of revolution 94.5 min. The primary goal of the CORONAS-F experiment was to investigate nonstationary processes on the Sun and their impact on the interplanetary medium and the Earth’s magnetosphere [Kuznetsov et al., 2014].

The development of a complex program of the studies of solar activity and its influence on the near-Earth space began in the USSR in the middle of 80s years of the 20th century. It resulted in a development of a number of satellites of CORONAS series. A set of scientific instruments Solar Cosmic Rays (SCR) was developed in order to study the relations between the radiation conditions in the near-Earth space and solar activity. This instrument was installed onboard the satellites CORONAS-I and CORONAS-F launched to orbit on March 2, 1994 and July 30, 2001, respectively. It consisted of three instruments (in this study we used two of them – SONG and MKL).

In such an orbit, the detection of neutral radiation from solar flares is possible only at low and middle latitudes outside the Earth's radiation belts, and also at the polar caps, in the absence of SEP particle flux in near-Earth space. In this case, the detector background counts are due to secondary local gamma-ray radiation produced by the interaction of primary cosmic rays with the material of the Earth's atmosphere, the spacecraft, and the detector itself. The duty cycle for the detection of solar flares on board CORONAS-F satellite was about 35% as a result of its orbit parameters, so many flares were missed. Solar energetic particles were measured by MKL in polar caps.

We used data of hard neutral radiation from solar flares obtained by the SONG (SOlar Neutrons and Gamma-rays) - multichannel gamma-ray spectrometer operated on board CORONAS-F solar space low-altitude observatory from the middle of 2001 until the end of 2005. Hard X-ray (HXR) and gamma-ray radiation are detected by the SONG instrument with the time resolution of the device was 2-4 s. SONG instrument is intended for detection of X-rays and gamma-emission within the energy range of 30 keV - 200 MeV, and neutrons with energies over 20 MeV.

MKL (Russian abbreviation for Monitor of Cosmic Rays) instrument is intended for detection of charged particles within the following energy ranges: spectra and fluxes of protons within the energy range of 1–90 MeV; spectra and fluxes of electrons within the energy range of 0.5–12 MeV; alpha-particles flux with energies of 100–140 MeV. Detector part of the instrument consists of two telescopic systems. The first scintillation detector D1 is

Table 1. Solar HXR- and gamma-ray flares detected by SONG (CORONAS-F). For abbreviations and further explanations see text.

№	dd/mm/yy	UT start-max-end of SXR, hh:mm	SXR class	AR	Coordi-nates	UT, HXR (SONG), hh:mm	Emax SONG, MeV	Jp , p/ (cm^2-s-sr)	Je, e/ (cm^2-s-sr)
1	20/08/02	08:22-08:26-08:30	M3.4	0069	S10W38	08:24-08:26	4.8-8.4	0.135	0.597
2	24/08/02	00:49-01:12-01:31	X3.4	0069	S12W51	00:58-01:07	4.8-8.4	44	6.67
3	17/03/03	18:50-19:05-19:16	X1.5	0314	S14W39	18:57-19:01	5.2-9.1	0.022	0.043
4	11/04/04	03:54-04:19-04:35	C9.6	0588	S16W46	04:13-04.18	0.18-0.7	0.51	0.243
5	17/01/05	09:59-09:52-10:07	X3.8	0720	N15W25	09:52-10:00	2-6	142.5	100
6	20/01/05	06:36-07:01-07:26	X7.1	0720	N14W61	09:44-09:56	90-150	233.5	1018

a part of spherical layer of plastic scintillator based on polystyrene inside the area enclosing a cone with a peak in the sphere's center and span angle of 140◦. Semiconductor detector D2 12 mm in diameter and 2 mm thick is located in the center of the sphere. Specific ionization of the particles for their movement in the considered system is used for particles' identification and determination of their energy. Amplitude of impulse produced by the charged particle is measured by scintillator detector, for the further analysis the particles with energy release in "n-p" detector exceeding double ionization of a relativistic single-charged particle are selected. The detailed description of SONG and MKL instruments is given in [Kuznetsov et al., 2014].

In addition, data from the Radio Solar Telescope Network (RSTN) is used for investigating the behavior of the temporal profiles of the radio emission. Single frequency radio records (in eight discrete frequencies from 245 MHz to 15.4 GHz) covering heights from low corona to upper chromosphere are available. Besides that, data obtained with the Nobeyama Radioheliograph (NoRH) (http://solar.nro.nao.ac.jp/norh) and radio polarimeter, NoRP, (http://solar.nro.nao.ac.jp/norp) were also used.

Data

We analyzed the SEP events associated with the solar flares that occurred on August 20 and 24, 2002, March 17, 2003, April 11, 2004, January 17 and 20, 2005. Table 1 presents data on six solar flares detected by SONG instrument on board CORONAS-F satellite. There, the following information is listed: the date of the flares, the time of start-maximum-end, the GOES class, the number of the active region (AR) in which the flare occurred, its coordinates on the solar disk, the time of HXR emission according to SONG data, the maximum energy, Emax, of gamma-ray which were detected by SONG, proton intensity, Jp (50–90 MeV) and electron intensity Je (1.5–3 MeV) detected by MKL SONG instrument on board CORONAS-F in polar caps. All times are in UT. The energy channels of proton and electron fluxes are selected in accordance with the channels of the MKL instrument. Both for protons and for electrons we used data observed in the highest-energy channels as available for all six events.

From Table 1 it can be seen that the class of studied flares varied in a wide range, from C9 to X7, and that all of them occurred in the central or western part of the solar disk. It is also seen from the table that the fluxes of SEP (both protons and electrons) are neither proportional to the class of flares in the SXR according GOES nor to the maximum HXR energy measured by the SONG instrument.

Figure 1 shows the time profiles of all six flares in the HXR-emission according to the SONG data (solid line) and ones in the microwave according to the data of the RSTN and the NORP (dashed line).

It can be seen from Fig. 1 that for all six flares the profiles in HXR and radio emission are similar, but one can lag behind the other and the correlation of the profiles of different flares is different. It is also easy to see that the ratio of the fluxes of in situ protons and electrons is substantially different. These differences were analyzed.

Results

Figure 2 shows the dependence of the ratio of the flux of solar protons with energy of 50–90 MeV to the flux of solar electrons with an energy of 1.5–3 MeV measured by the MKL instrument in polar caps, from the coefficient of correlation of HXR and microwave emission (left panel, blue diamonds) and from the delay time of the wave radiation relative to HXR-emission (right panel, red triangles).

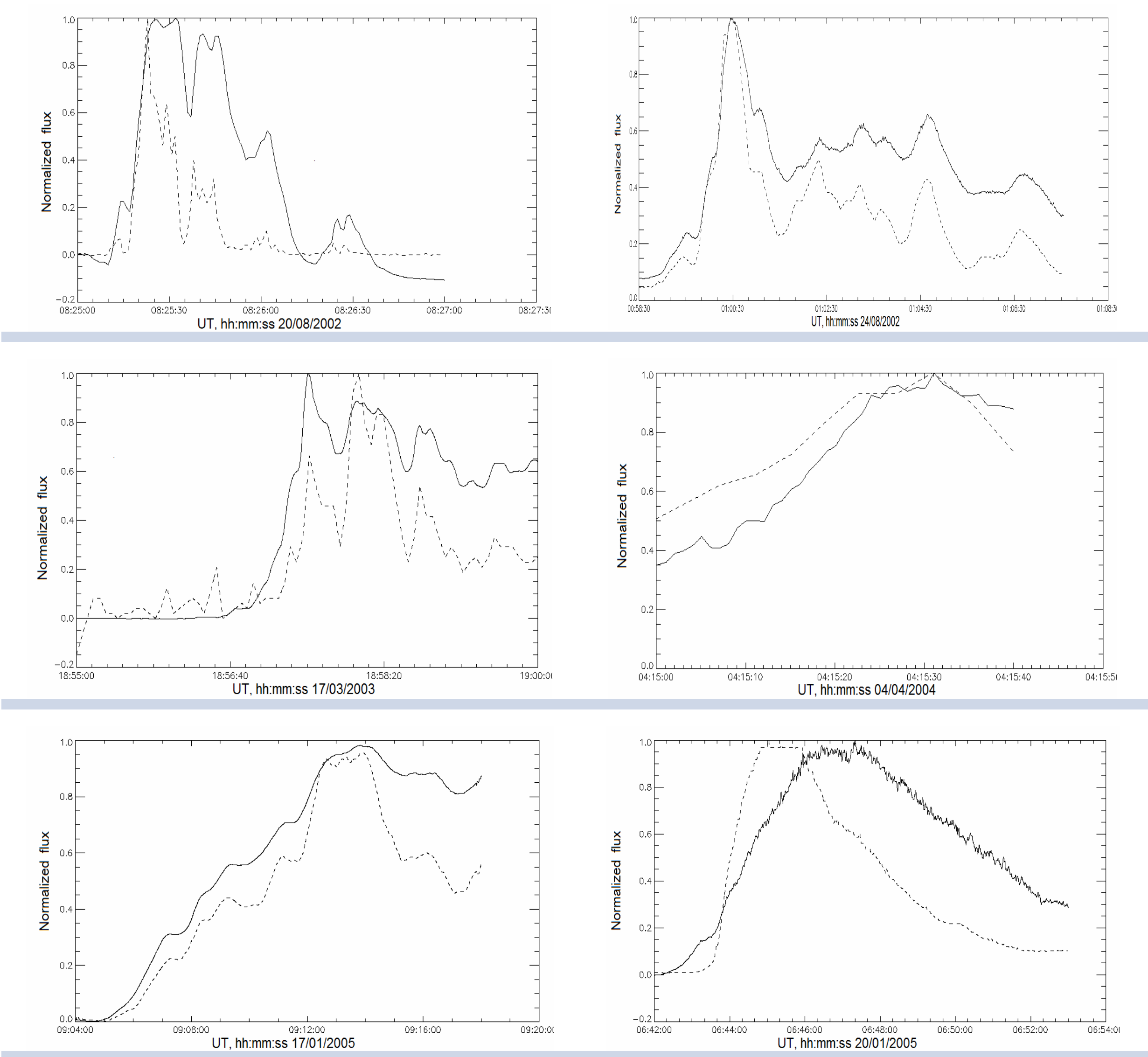

Fig. 1. The time profiles of HXR-rays (SONG), plotted in solid line, and radio (microwaves) emission, plotted in dotted line, of all six flares from Table 1. Time profiles were normalized to the maximum..

Three of the six events (August 20 2002, January 17, 2005 and January 20, 2005) have zero delays, and two of them, August 20 2002 and January 20, 2005, are characterized by a close ratio of the solar proton fluxes to the electron, so the exact dependencies of the obtained values are difficult to build. Nevertheless, both panels of Fig. 2 show a tendency to increase this ratio both with an increase in the coefficient of correlation, and with an increase in the delay time of microwave emission relative to HXR one.

The relationship of the proton to electron ratio to the correlation coefficient shows the clear dependence. Only the SOL2004-Aug-24 flare is not in good agreement with this dependence. This fact could be related with features of active regions (ARs) which were not taken into account in this study. In the paper of Bogomolov et al. [2018] to the analysis of SEP fluxes and flare plasma parameters were added also studies of the magnetic topology of the AR and its evolution before and during the solar flares. The presented results indicate that an arcade of high loops covering the AR could prevent escaping of the accelerated particles and generates a less proton-rich SEP event as it is expected by flare properties alone.

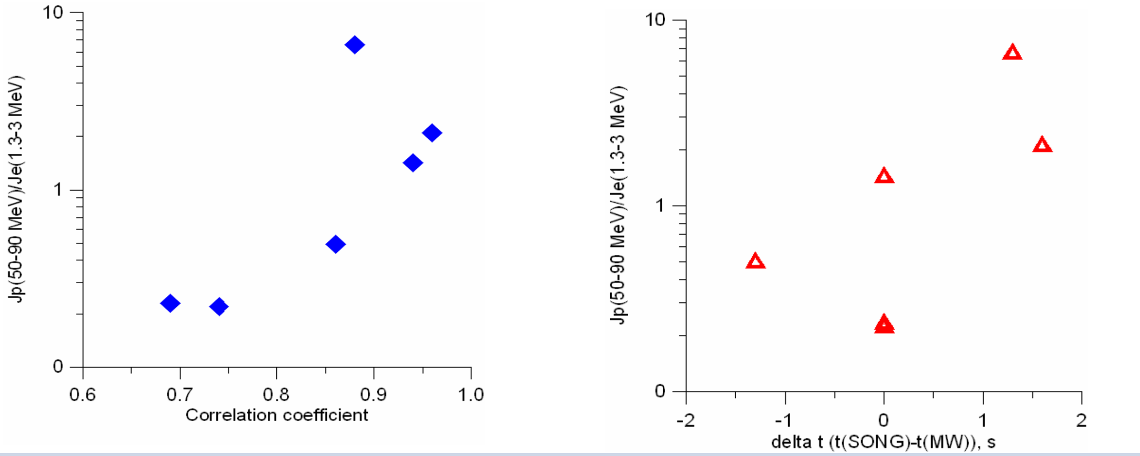

Fig. 2. The dependence of the ratio of the solar proton flux (50–90 MeV) to the solar electron one (1.5–3 MeV) on the coefficient of correlation of hard X-rays and microwave radiation (left panel) and on the delay time of the wave radiation relative to HXR-emission (right panel).

Alternatively, the flare associated with the proton-rich SEP event could occur in an AR where a fan of high loops is associated with open magnetic field lines.

Conclusions

We analyzed the SEP events detected on board the Russian solar observatory CORONAS-F simultaneously with the hard X-ray emission of flares that caused these events. The main feature of our study is that we used both HXR flare emission observations and SEP flux measurements obtained at the same spacecraft. We revealed the clear tendency of increasing the ratio of the flux of solar protons to the flux of solar electrons with rising of the correlation coefficient between HXR and microwave radiation. However, analysis of AR magnetic topology should be completed before the final conclusions. We think that these results show that the detection of energetic neutral and charged radiation on the same spacecraft could be important for the study of the relationship between the X-ray characteristics of flares and SEP events.

Acknowledgment

This study is supported by the project 'The origin on solar energetic particles: solar flares vs. coronal mass ejections', co-funded by the Russian Foundation for Basic Research with project No. 17-52-18050 and the National Science Fund of Bulgaria under contract No. DNTS/Russia 01/6 (23-Jun-2017). LK and NM thank the budgetary funding of Basic Research program II.16 for partial support.

References

Baker, D. (2000) The occurrence of operational anomalies in spacecraft and their relationship to space weather, IEEE Trans. Plasma Sci., 28, no6, 2007–2016.

Bogomolov A.V., Myagkova I.N., Myshyakov , Tsvetkov Ts., Kashapova L., Miteva R. (2018) Comparative analysis of the proton generation effciency during 17 March 2003 and 11 April 2004 solar flares. Journal of Atmospheric and Solar-Terrestrial Physics ((under review).

Desai,M., Giacalone, J. (2016). Large gradual solar energetic particle events. Living Reviews in Solar Physics 13, 3. doi:10.1007/s41116-016-0002-5

Jiggens, P., Chavy-Macdonald, M.A., Santin, G., Menicucci, A., Evans, H., Hilgers, A. (2014) The magnitude and effects of extreme solar particle events. Journal of Space Weather and Space Climate 4, A20. doi:10.1051/swsc/2014017.

Kuznetsov, S.N., Bogomolov, A.V., Galkin, V.I., Denisov, Y.I., Podorolsky, A.N., Ryumin, S.P., Kudela, K., Rojko, J. (2014) Scientific Set of Instruments "Solar Cosmic Rays", in: Kuznetsov, V. (Ed.), The Coronas-F Space Mission, p. 289. doi:10.1007/978-3-642-39268-9_9.

Analysing of the SEP origins based on microwave emission of solar flares

L. Kashapova [1,4], N. Meshalkina [1], R .Miteva [2], I. Myagkova [3], A. Bogomolov [3]

[1] Institute of Solar-Terrestrial Physics, SB RAS, Irkutsk, Russia
[2] Space Research and Technology Institute – Bulgarian Academy of Sciences, Sofia, Bulgaria
[3] Skobeltsyn Institute of Nuclear Physics, Moscow State University, Moscow, Russia
[4] Irkutsk State University, Itkutsk, Russia
E-mail: lkk@iszf.irk.ru

Abstract.

We present the results on the analysis of microwave emission in solar flares related to strong solar energetic particle (SEP) events observed during the previous solar cycle. The target of the work is to find criteria based on the solar flare features that would allow us to separate the SEP events into groups with more homogeneous physical/topological properties. In the current study, we compared peak frequency of microwave spectra and spectral index with spectral characteristics of SEP proton fluxes. The two groups of events related to the value of the peak frequency are found. We discuss revealed tendencies and physical reasons of the two population appearances.

Introduction

Magnetic reconnection in solar flares and the shock waves driven by coronal mass ejections (CMEs) are two main models for particle acceleration in the solar corona suggesting the explanation of solar energetic particle (SEP) event properties. All arguments pro et contra are based on correlation analysis between selected parameters of the SEP origin (flares and CMEs) and the in situ particles. The microwave (MW) emission is a sensitive indicator of particle acceleration and energy release processes in solar flares. Earlier studies of solar sources of SEP events used different spectral parameters of this kind of emission as indicators, see for example, [Daibog et al., 1993]. However, MW emission is sensitive to several parameters simultaneously. For example, the flux at a maximum of the spectrum could be a result of the electron flux or magnetic field strength (see Stähli et al., [1989], for example). If we compare this parameter with the properties of SEP particles, then we may face with the mixture of two populations. Thus the dependence related to the acceleration process is blurred.

The aim of this work is the comparison of spectral properties of the SEP events related to solar flares with MW spectral parameter and separation the events to groups with more close physical features. We chose the peak frequency of the microwave spectrum as the parameter characterizing the properties of MW emission. It is the frequency where flux is maximal in the MW spectrum. This parameter is mainly sensitive to the magnetic field strength. It is less affected by the angle of view and electron flux.

Data

We based our analysis of radio spectra on observations of the Radio Solar Telescope Network (RSTN). RSTN [Guidice et al. 1981] is providing radio data with 1 s temporal resolution at eight selected frequencies (245, 410, 610, 1415, 2695, 4995, 8800, 15400 MHz). The four worldwide stations (the Learmonth, (Australia), San Vito (Italy), Sagamore Hill and Palehua (USA)) allow having quasi-similar data 24 hours per day. For some events, we complemented our analysis by data of Nobeyama RadioPolarimeters (NoRP). The spectropolarimeter [Torii et al., 1979; Nakajima et al., 1985]. provides the intensity and circular polarization at six frequencies (1, 2, 3.75, 9.4, 17, & 35 GHz) and the intensity only at 80 GHz .The time resolution is 0.1 sec in the flare mode, and 1 sec in the background mode (no 80 GHz data). We used the catalog of strong energetic proton events by [Papaioannou et al,. 2016] for selection of the events that occurred within 2001–2005. The catalogue presents the fluxes of SEP events for the energies above 10 MeV, 30 MeV, 60 MeV and 100 MeV.

Data processing

There are 61 events with data about SEP (onset time) and associated flare (class, begin and end time, location at the solar disk) according to the catalog. Based on this information we selected the solar flares with radio bursts according to RSTN data. There are 26 events in total. We reconstructed the spectrum for the temporal maximum of the radio burst using data of all available frequency range. For the events jointly observed by the NoRP, we combined the data from these instruments into one composite dynamic spectrum. The flux of gyrosynchrotron microwave emission monotonously increases with increasing frequency until peak frequency. After this frequency, the microwave flux starts to decrease. The shape of the radio spectra of all selected events was typical for gyrosynchrotron emission [Dulk, 1985].

We obtained the spectrum parameters by fitting using the procedure tp_fit, part of the OVSA Explorer software (see [Nita et al., 2004], for more detail) and added linear interpolation for low-frequency and high-frequency parts of the spectra. In order to choose the better parameters, we calculated the standard deviation for the fitted curves obtained by the different methods. For the next step of the analysis, we used the parameter (spectral indices and peak frequency) corresponding to the fit with a minimum deviation value.

For comparison, we used the ratio of the proton peak integral flux for energies above 10, 30, 60 MeV (the catalog presented in the paper [Papaioannou et al., 2016]). Namely, there are the ratio parameters for channels 10 MeV to 30 MeV and 10 MeV to 60 MeV.

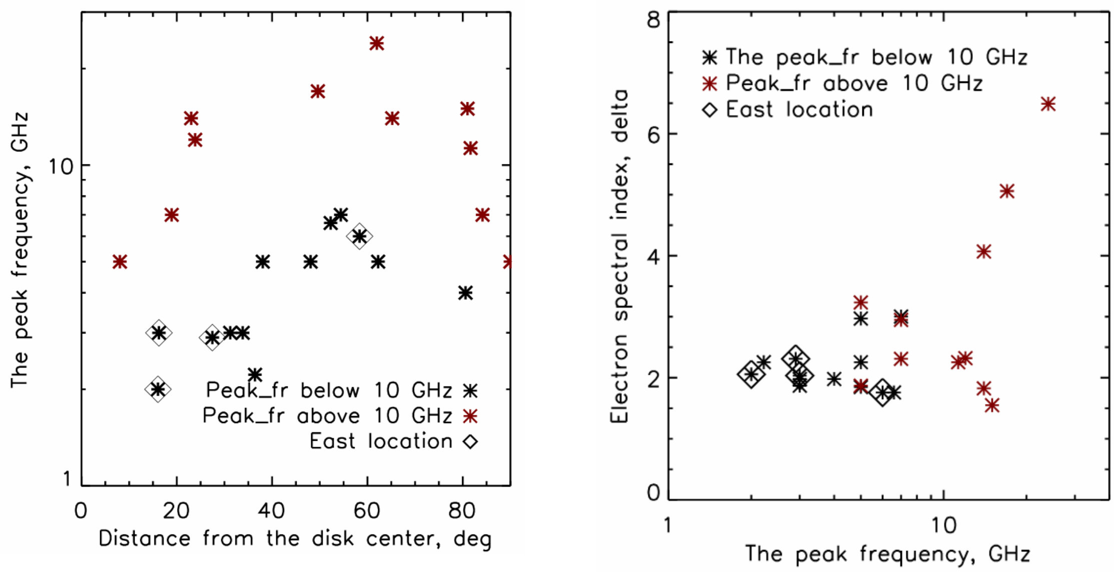

Fig. 1 The left panel: The peak frequency of the solar flares vs distance from the disk center. The black asterisks show the events with peak frequencies below 10 GHz and the red asterisk shows the events with peak frequencies above 10 GHz and the events related with them. The diamonds show the event located in the eastern part of the solar disk. The right panel: The electron spectral index relative to the peak frequency of the events.

Results

At first, we should check if there is any dependence between the peak frequency and location of the event on the solar disk. The left panel of Figure 1 presents the plot that shows the relationship between the peak frequency and position of the solar flare

.One can see two groups of events defined by the peak frequency value. The peak frequency of the first one is less than 10 GHz. It means that the magnetic field nearby the source of MW emission was not strong. The relationship between the peak frequency and distance from the solar disk center demonstrates the slow rise that reaches the maximum at about 60 degrees. We also revealed the other group of the events. For this group, the dependence of the peak frequency value relative to the event position looks similar to the first group. But the most of the frequency values are above 10 GHz. Both populations look like the branches located higher and lower in the plane of the peak frequency–distance. Such separation could mean that one group of events occurs in active regions with weak magnetic fields. The position of the other event group with the high value of the peak frequency was related with the large magnetic fields. We note that events located in the Eastern hemisphere all have peak frequencies below 10 GHz and blends with the corresponding dependence.

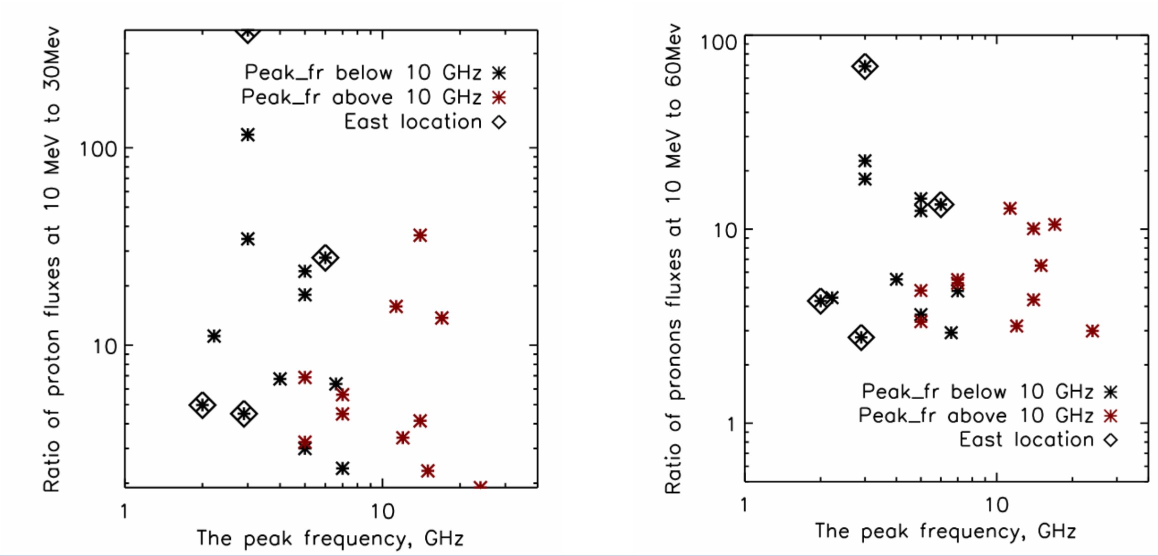

Fig. 2 The left panel: The ratio of the proton fluxes above 10 MeV to the proton fluxes above 30 MeV relative to the peak frequencies of MW spectra. The black asterisks show the events with peak frequencies below 10 GHz. The symbols as in Figure. 1The right panel: The ratio of the proton fluxes above 10 MeV to the proton fluxes above 60 MeV relative to the peak frequencies of MW spectra.

We marked the two groups by symbols of the different colors and tested if any other common properties are present for each group or not. The right panel of Figure 1 presents the relationship of the electron spectral index from the peak frequency. The electron spectral index δ is derived from the photon spectral index α by the formula δ=1.11α+1.36 [Dulk, 1985]. One can see that events with low peak frequencies are grouping nearby the electron spectral index about 2. This index is hard and assumes a large number of accelerated relativistic electrons with high energies and/or high level of processes of acceleration. The other group splits into two subsets with the opposite tendencies: of index hardening and of index softening. Most possibly these tendencies are related to the feature of magnetic field topology and they should be analyzed in details.

Figure 2 presents the proton flux ratio in two energy channels relative to the value of the peak frequencies of MW bursts corresponding to the events. The ratio is characteristic of spectral properties of the SEP proton flux. The higher values mean softer proton fluxes. We can see that both graphs look like the combination of the two distributions related to the peak frequencies above 10 GHz and below this value. Both distributions look like the normal distribution and have the maximum about 3 GHz and 15 GHz. We cannot claim anything definitive about the relation between the spectral properties of proton fluxes in SEP events and the peak frequency of the MW burst. But we propose that the peak frequency as a parameter splits SEP events into two populations. The properties and acceleration mechanisms of these populations should be different because of the same spectral characteristics of protons in SEPs achieved based on the different properties of the magnetic field in solar flares.

Summary

We carried out the comparative analysis of the spectral characteristics of SEP proton fluxes and the peak frequency of solar flare microwave spectra. We did the preliminary analysis dependence of the peak frequency from the distance from the center of the solar disk. The results show the existence of two populations of events related to high and low values of the peak frequency. We defined the border value as 10 GHz. These groups show the different properties as for electron spectral index and spectral properties of proton flux of SEPs.

Acknowledgment

This study is supported by the project 'The origin on solar energetic particles: solar flares vs. coronal mass ejections', co-funded by the Russian Foundation for Basic Research with project No. 17-52-18050 and the National Science Fund of Bulgaria under contract No. DNTS/Russia 01/6 (23-Jun-2017). LK and NM thank the budgetary funding of Basic Research program II.16 for partial support.

References

Dulk G. A. (1985), Radio emission from the sun and stars. Annual review of astronomy and astrophysics, 23, 169-224.

Guidice D. A., Cliver E. W., Barron W. R., Kahler S. (1981), The Air Force RSTN System. Bulletin of the American Astronomical Society, 13, 553.

Daibog E. I.;, Melnikov V. F., Stolpovskii V. G. (1993), Solar energetic particle events from solar flares with weak impulsive phases of microwave emission. Solar Physics, 144, 361-372

Nakajima, H.; Sekiguchi, H.; Sawa, M.; Kai, K.; Kawashima, S. (1985), The radiometer and polarimeters at 80, 35, and 17 GHz for solar observations at Nobeyama. Astronomical Society of Japan, Publications, 37, 163-170.

Nita G. M., Gary D.E., Lee, J. (2004), Statistical Study of Two Years of Solar Flare Radio Spectra Obtained with the Owens Valley Solar Array. The Astrophysical Journal, 605, 528-545.

Papaioannou A.; Sandberg I., Anastasiadis A, Kouloumvakos A., Georgoulis M.K., Tziotziou K., Tsiropoula G., Jiggens P., Hilgers A. (2016), Solar flares, coronal mass ejections and solar energetic particle event characteristics. Journal of Space Weather and Space Climate, 6, 29.

Stähli M., Gary D.E., Hurford G.J. (1989), High-resolution microwave spectra of solar burst. Solar Physics, 120, 351-368.

Torii C., Tsukiji, Y., Kobayashi S., Yoshimi N., Tanaka H., Enome S. (1979), Full-automatic radiopolarimeters for solar patrol at microwave frequencies. Nagoya University, Research Institute of Atmospherics, Proceedings, 26, 129-132.

Monitoring of space radiation and other hazards in multi-satellite project `Universat-SOCRAT`

Sadovnichii V.A. [1], *Panasyuk M.I.* [1], *Lipunov V.M.* [1], *Bogomolov A.V.* [1], *Bogomolov V.V.* [1], *Garipov G.K.* [1], *Gorbovskoii E.S.* [1], *Iyudin A.F.* [1], *Kalegaev V.V.* [1], *Klimov P.A.* [1], *Kornilov V.G.* [1], *Osedlo V.I.* [1], *Petrov V.L.* [1], *Podsolko M.V.* [1], *Popova E.P.* [1], *Rubinstein I.A.* [1], *Svertilov S.I.* [1], *Tulupov V.I.* [1], *Yashin I.V.* [1], *Grafodatskii O.S.* [2], *Lemeshevskii S.A.* [2]

[1] M. V. Lomonosov Moscow State University, Russia
[2] S. A. Lavochkin Space Corporation, Russia
E-mail: aabboogg@sinp.msu.ru

Abstract.

D.V. Skobeltsyn Institute of Nuclear Physics of M.V. Lomonosov Moscow State University is developing a project `Universat-SOCRAT` of a system of small satellites for monitoring of the space threats: ionizing radiation, potentially dangerous objects of natural (asteroids, meteoroids) and artificial (space debris) origin, and electromagnetic transients of Earth`s and space origin.

One of the primary tasks for this satellite system is operational (close to `real time`) monitoring of the fluxes of energetic charged particles in the wide range of Earth`s radiation belts. For this purpose at least two satellites with a mass <50-100 kg will be launched. One of them will have an orbit close to circular with a height of about 1500 km and an inclination of ~80°. The second one will be launched to an elliptical orbit with height of perigee and apogee ~700 and 8000 km and inclination 63.4°, which crosses wide range of magnetic drift shells at different altitudes. Satellites will be equipped with multidirectional spectrometers of energetic protons and electrons.

Another satellite will be launched to Sun-synchronous low Earth orbit. It provides the payload mass about 100 kg and its aims besides the radiation monitoring also should be observation of other space hazards, such as space debris and asteroids and electromagnetic transients. Space debris and asteroids should be observed by several wide-field cameras and robotic telescopes of MASTER type. Satellite may also carry number of detectors for study of electromagnetic transients in different wavelength ranges - from infrared to gamma. This means observation of such phenomena, as transient luminous events (TLE) in the atmosphere, terrestrial gamma ray flashes (TGF), cosmic gamma ray bursts (GRB) and solar flares in hard X-rays and gamma rays.

Introduction

The natural and technogenic space environment causes serious risks for the implementation of space missions, both automatic and human. The risk is determined by the specifics of the planned missions, i.e. their duration, localization in outer space and orbital parameters.

The specific of natural conditions in outer space such as the variety of radiation field physical parameters, the features of ballistic trajectories of natural space objects, as well as the consequences of human activities in space, i.e. pollution of space with man-made debris cause, as a rule, real difficulties for environment modeling and for calculating of risks.

Monitoring in real time of space natural and man-made objects which can be assumed as potential threats is an optimal and effective way to reduce risks. In this way the project "Universat-SOCRAT"[1] is proposed for implementation. Under this project we plan to create a grouping of small satellites for real time monitoring in the near-Earth space of potentially dangerous hazards, i.e. the radiation environment; dangerous objects of the natural (asteroids,

[1] English abbreviation "Universat" means University Satellites. "SOCRAT" is the Russian abbreviation "The System of Alerting the Cosmic Radiation, Asteroid and Technogenic hazards"

meteors) and technogenic origin (space debris), as well as electromagnetic transients (cosmic gamma-ray bursts, optical, ultraviolet and gamma ray flashes from the Earth's atmosphere.

The program of the new project Universat-SOCRAT is based on the results of experiments on the satellite Lomonosov and other satellites of Moscow State University intended on the study of extreme phenomena in the Earth's atmosphere and outer space (see, for example, [*Sadovnichiy V.A., et.al.*, 2013, *Panasyuk M.I., et.al.*, 2016a, 2016b]) including the results of observations of high-altitude electromagnetic discharges, precipitation of magnetospheric electrons, gamma-ray bursts of astrophysical and solar origin, as well as observations of space debris by wide-field optical cameras first installed on a spacecraft [*Lipunov V.M., et.al.*, 2018]

Potentially dangerous factors in the near-Earth space

a) Ionization radiation

One of the main goals of the elaborated multi satellite system is a real time monitoring of near-Earth radiation, which is dangerous for the satellite on-board systems and manned spacecraft crews. Mainly, there are energetic electron and protons fluxes of the Earth's radiation belts, as well as energetic particles of solar cosmic rays.

The necessity of such monitoring is caused by the fact that these fluxes even in geo-magnetically quiet conditions undergo by significant medium-term and long-term variations, which can not be described by existing quasi-static models of the Earth's radiation belts. On the other hand, modern satellite measurements are carried out only for a limited number of orbits and range of pitch angles, i.e. the angle between the particle velocity vector and the magnetic field line and can not give a global picture of the spatial and temporal variations of radiation in the near-Earth space.

Thus, the main goal of radiation monitoring and radiation environment forecasting in the near-Earth space is:

– operative estimation of radiation conditions for rating the radiation risks of space missions implementation and generating alert signals for decision-making on mission control;

– verification of modern calculation models of radiation fields.

b) Space debris, asteroids and large meteoroids

As of 2015, August 31, the total number of cosmic objects of technogenic origin that are located in outer space and cataloged in the databases "Warning System on dangerous situations in near-Earth space" amounted to 17 250 space objects. Of these, 1 362 space objects are operating spacecraft, and the remaining 15 888 space objects are space debris [*Harris A.,* 2015].

At extrapolating the existing rate of low Earth orbit (LEO) clogging, even taking into account various efforts to reduce it, a "cascade effect" of the mutual collision of space debris objects and particles can arise in the medium term. In the long term it may lead to a catastrophic increase in the number of space debris objects on the LEO and, as a consequence, to the practical impossibility of further space exploration.

The problem of asteroid danger is also actual. A celestial body is considered as potentially dangerous if it crosses the Earth's orbit at a distance <0.05 AU (about 19.5 distances from the Earth to the Moon), and its diameter exceeds 100–150 m. Objects of this size are large enough to cause unprecedented destruction on the Earth land, or a huge tsunami if it fall into the ocean. Events of this magnitude occur about once every 10 000 years. Based on information received from the WISE Space Telescope, experts estimate the presence of 4700±1500 potentially dangerous objects with a diameter of more than 100 meters [*Mainzer A., et.al.*, 2014].

c) Electromagnetic transients

Another goal of our project is monitoring and studying of electromagnetic transient phenomena in the upper atmosphere, which are observed in different wavelengths, from radio to gamma ray ranges. These phenomena are global in nature and associated with electric discharges, occurring at altitudes of tens of kilometers in the upper atmosphere. The energy released in them is large enough to have a significant impact on radio communications, modify the physical parameters of the mesosphere, and also have a direct impact on the onboard systems of stratospheric suborbital aircrafts.

Multisatellite space environment for space hazards monitoring

Within the framework of the Universat-SOCRAT project several small spacecrafts should be launched on specially selected orbits. In the minimal version, the group of satellites should consist of three spacecrafts [*Panasyuk M.I., et.al.*, 2015]. One spacecraft of medium mass (small satellite) should be launched on a low solar-synchronous orbit with a height of about 500–650 km and an inclination of 97–98°. Two other satellites of lower mass (micro satellites) should be launched on an orbit close to circular with a height of about 1500 km and an inclination of ~80° and on an elliptical orbit with an apogee of about 8000 km, a perigee of 600–700 km, inclination 63.4° and argument of perigee ~310°. The mutual arrangement of the orbits is shown in Figure 1.

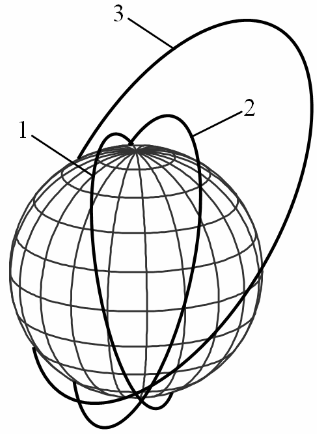

Fig. 1 The mutual arrangement of multi-satellite group orbits.

The small satellite payload should include instruments for monitoring of space radiation, a set of instruments for optical monitoring of hazardous objects, a set of instruments for studying of atmospheric phenomena in the optical range, a set of instruments for monitoring in gamma- range, and special unit for data collection. The payload should also include three-component magnetometer. The payload of each micro satellite should include instruments for space radiation monitoring, a compact gamma spectrometer, a wide field of view optical camera, an ultraviolet detector and an electronics unit for data collection. Payload of all three satellites also should include the special electronic unit for data collection from detector units, its transmission to the board systems and feeding to the instruments power supply and commands.

The main is on duty mode when all the instruments are switched-on and operate continuously. Instrument switching between the operational modes is carried out by commands from the Earth or by the internal cyclograms of the electronic unit. To optimize the payload energy consumption, the data exchange between the electronic unit and satellite board should be foreseen, including information on changing the parameters of the spacecraft power system and payload switching into energy-saving modes (changes in the instrument operating modes or their partial switching-off).

During the space experiment the ground control station should be elaborated. It also should be used for operative data reception and processing. Existing ground station, which is used in Lomonosov mission can be applied in future project. System of operative analysis and forecasting of radiation conditions in the near-Earth space also exists at the Moscow State University. It is based on the space monitoring data analysis with the use of operational models of space environment affecting factors [*Panasyuk M.I., et.al.*, 2017]. Their use will increase the effectiveness of the created space system "Universal-SOCRAT".

Radiation monitoring in the Universat-SOCRAT project

Instruments for radiation monitoring should include spectrometer of protons with energies from 2 up to >160 MeV and electrons with energies 0.15–10 MeV. Its main element is assembly as telescope including a few semiconductor (silicon) detectors with different thickness and scintillator detector, which are placed coaxially one under the other (see Figure 2, right panel). To measure pitch-angle distribution and omnidirectional fluxes several telescopes with differently directed axes will be used. One of the instrument layouts is shown in fig. 2, left panel. It is also discussed the instrument arrangement, in which axes of four telescopes are laying in the magnetic meridian plane and axis of one other telescope is normal to this plane. In the case of polar orbit it means that axis of 4 telescopes should lie in the orbital plane. The payload should also include three-component magnetometer.

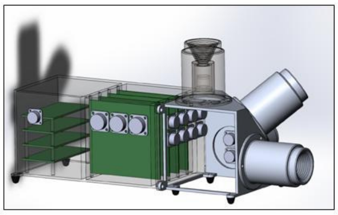

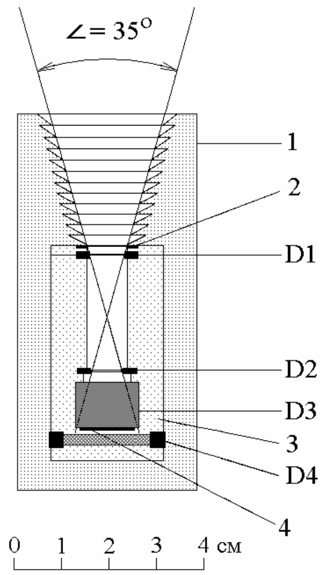

Fig. 2. Left panel: the detector unit of spectrometer of protons and electrons with differently directed telescopes (left) and its general view. Right panel: the structural scheme of telescope: 1 – box, 2 – foil of thickness ~10 µm Si, 3 – isolator, D1, D2, D4 – semiconductor (Si) detectors, D3 – scintillator (CsI(Tl)) detector, 4 – photodiode.rbits.

Thus, in the frame of Universat-SOCRAT mission several spectrometers of protons and electrons installed on the satellites launched on the special orbits should measure fluxes that allow prediction of current energetic charge particle distribution in the large volume of radiation belts up to geostationary orbit. As a sequence current values of radiation loads can be operatively estimated for a wide range of satellite orbits.

Electromagnnetic transient monitoring

Instruments for study transient luminous events (TLEs) in UV and optical bands should include position sensitive spectrometer, i.e. small lens telescope with high time resolution for spectral measurements of TLE and lightning and UV and infra-red (IR) detector-photometer DUFIK, which is similar to that used in Tatiana-2 and Vernov missions. This instrument will be added by channels in far UV range. It allows comparison with data of previous experiments on study UV flashes in the atmosphere. Spectral measurements are necessary to determine the type and altitude of TLE generation as well as to reveal lightning discharges by typical 777 nm line and by the absence of signal in the range of oxygen absorption lines about 762 nm.

The MLT instrument should consist of lens wide-field objective and such position sensitive detector as multi-anode photomultiplier (PMT) tube and number of PMTs for measuring of long time sets of TLE signals with high sensitivity and time resolution. It is necessary to foresee up to 16 spectral channels in the instrument construction (see Figure 4, left panel). Axes of MLT and DUFIK instruments should be directed toward Nadir with open angles about 90°.

The DUFIK instrument should consist of three photomultipliers with input widows closed by light filters providing sensitivity in different spectral bands, i.e. red-infrared (600–800 nm), near UV (240–400 nm) and sunny-blind (100–300 nm). Besides, the instrument also includes optical detector from micro-channel plate providing emission detection in the range from far UF to soft X-ray. The general view of the instrument from the input widow side is presented in Figure 4 (right panel).

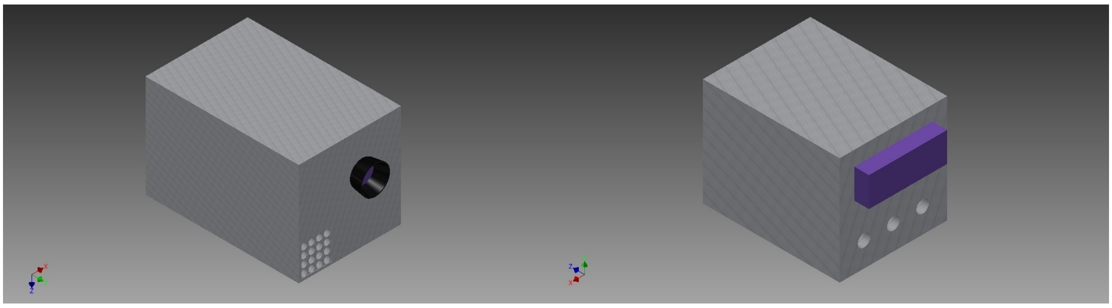

Figure 4. The general view of MLT (left panel) and DUFIK (right panel) instruments.

The instruments intended for monitoring in gamma rays include three wide-field scintillator detectors of BDRG type [*Svertilov S.I., et.al.*, 2018] for observations of upper atmosphere in the range 10–3000 keV and track gamma spectrometer of high resolution and sensitivity. Each BDRG detector unit is NaI(Tl)/CsI(Tl) phoswich with ∅13×0.3 cm NaI(Tl) and ∅13×1.7 cm CsI(Tl) scintillator crystals viewed by one PMT (see Figure 5, right panel). The BDRG detector axes should be normal to each other and directed along the mutually normal edges of the cube, as if forming a Cartesian coordinate system (see Figure 5, left panel). In this case, the main diagonal of the cube should be directed to the Nadir.

Track gamma spectrometer of high resolution and sensitivity is based on the combination of position sensitive detector and coding mask. It also includes hodoscope unit from scintillator fibers. The detector axis should be directed to the Zenith from the side of coding mask and to the Nadir from the side of hodoscope. The effective area of gamma spectrometer is ~250 cm2, energy range is 0.02–10 MeV (0.02–1.0 MeV in the mode of full coding), angular resolution is ~2°; field of full coding is ±25°. Due to possibility of imaging this instrument also can operate as a gamma telescope. It allows checking of point-like source appearance on the sky, that makes it possible to identify gamma ray bursts on the background of electron precipitation. The instrument also includes electronic unit, which provides data recording with high time resolution ~10 μs, image operative analysis and gamma ray burst trigger elaboration.

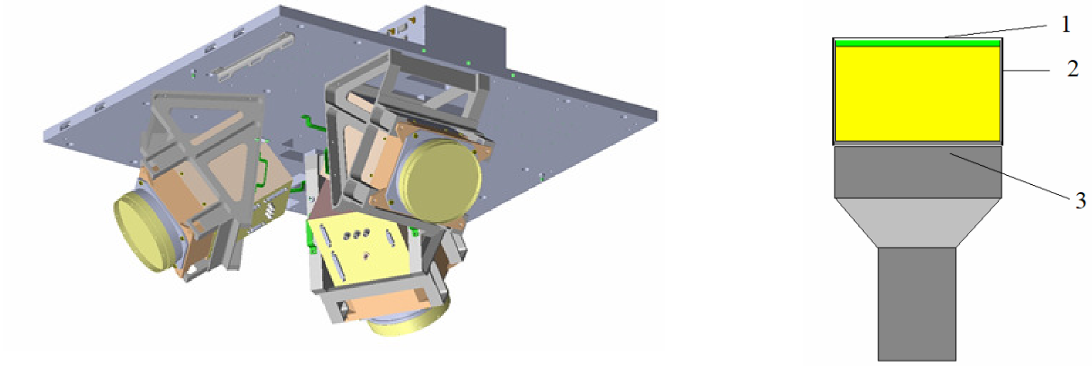

Figure 5. The general view of BDRG detector unit arrangement on the stellite board (left panel); the detector unit composition (right panel), 1 – NaI(Tl) crystal, 2 – CsI(Tl) crystal, 3 – PMT.

Conclusions

The successful realization of the project will make it possible for the first time in the world to create a prototype of a space system for monitoring and helping to prevent space hazards for both ongoing and planned space missions, including high-altitude atmospheric aircraft.

During the project realization, the following tasks should be solved:

– real-time estimation of radiation environment in near-Earth space for evaluation of the radiation risks of space missions and producing of the alert signals for decision accept on their control;

– verification of modern computational models of radiation fields in the near-Earth space;

– real-time control of potentially dangerous objects of natural and technogenic origin in the near-Earth space;

– control of electromagnetic transients in the upper Earth atmosphere and space (GRBs, Solar flares).

Acknowledgment

Financial support for this work was provided by the Ministry of Education and Science of Russian Federation, Project № RFMEFI60717X0175.

References

Harris A., The population of near-Earth asteroids, Icarus, v. 257, p. 302–312, 2015.

Lipunov V.M., Gorbovskoy E.S., Kornilov V.G. et al., SHOK – the first Russian wide-field optical camera in space, Space Science Review, 214(1):6, 2018.

Mainzer A., Bauer J., Grav T., Masiero J., The population of tiny near-Earth objects observed by NEOWISE, The Astrophysical Journal, v. 784, No. 2, p. 110, 2014.

Panasyuk M.I., Podzolko M.V., Kovtyukh A.S. et al., Operational radiation monitoring in near-Earth space based on the system of multiple small satellites, Cosmic Research, v. 53, No. 6, p. 423–429, 2015.

Panasyuk M.I., Svertilov S.I., Bogomolov V.V. et al., Experiment on the Vernov satellite: transient energetic processes in the Earth's atmosphere and magnetosphere. Part I: description of the experiment, Cosmic Research, v. 54, No. 4, p. 261–269, 2016a.

Panasyuk M.I., Svertilov S.I., Bogomolov V.V. et al., Experiment on the Vernov satellite: transient energetic processes in the Earth's atmosphere and magnetosphere. Part II: first results, Cosmic Research, v. 54, No. 5, p. 343–350, 2016b.

Panasyuk M.I., Podzolko M.V., Kovtyukh A.S. et al., Optimization of measurements of the Earth's radiation belt particle fluxes, Cosmic Research, v. 55, No. 2, p. 79–87, 2017

Sadovnichiy V.A., Amelushkin A.M., Angelopulos V. et al., Space experiments on board MSU satellite "Lomonosov", Cosmic Research, v. 51, No. 6, p. 427–433, 2013.

Svertilov S.I., Panasyuk M.I., Bogomolov V.V. et al., Wide-field gamma-spectrometer BDRG: GRB monitor on-board the Lomonosov Mission, Space Science Reviews, 214(1):8, 2018

Proceedings of
Tenth Workshop "Solar Influences on the Magnetosphere, Ionosphere and Atmosphere"
Primorsko, Bulgaria, June 4÷8, 2018

Small-sized radio telescopes for monitoring and studies of solar radio emission at meter and decameter wavelengths

S. Yerin [1,2], *A. Stanislavsky* [1,2], *I. Bubnov* [1], *A. Konovalenko* [1], *P. Tokarsky* [1], *V. Zakharenko* [1]

[1] Institute of Radio Astronomy of the NASU, Ukraine;
[2] V.N. Karazin Kharkiv National University, Ukraine
E-mail: yerin.serge@gmail.com

Abstract.

The paper shows development prospects of solar studies with small-sized sensitive radio telescopes such as the GURT active antenna which is an element of the phased array of the GURT radio telescope. Starting with GURT active antenna sensitivity calculations for solar observations, we compare our solar radio emission observations with the records of other radio telescopes. We discuss the potential of using this single antenna as an instrument for studying the active Sun manifestations from the lunar surface and suggest its possible adjustment to observe poor studied solar bursts under the terrestrial ionosphere cutoff.

Introduction

Low-frequency radio astronomy deals with many sporadic cosmic signals [Konovalenko et al., 2016]. One of the strongest cosmic signal types received on Earth is the solar sporadic radio emission. The emission at low frequencies is generated at 3-5 solar radii height and helps to examine properties of the upper solar corona. Solar radio emission is classified into many types which still have not been studied and interpreted thoroughly. Some types of the emission were explained by several different models and yet none of them fully explains all features of these emissions spectra.

Over all the history of radio astronomy the scientists tried to build larger telescopes to achieve higher sensitivity and spatial selectivity of their instruments. This process has led to construction of large instruments and considering experimental radio astronomy as a highly cost-consuming science. At the same time, the flux of solar radio emission at frequencies below 100 MHz as well as their sporadic nature and specific features in time-frequency domain allow one to distinguish it from other emission sources, register and study with sensitive wideband small-sized antennas. Unfortunately, in this case, we do not have a good spatial resolution of antenna, but the dynamic spectra obtained in this way still carry much "footprints" due to physical processes taking place in the solar corona. In addition, the almost omnidirectional antenna is easier to operate and allows observing solar emission from dusk to dawn [Tokarsky et al., 2015].

Antenna design and characteristics

A small antenna, matched to a receiving system in terms of its parameters, can be sufficiently sensitive for recording sporadic manifestations of solar emission on the Earth. In case of small-sized antenna with poor spatial selectivity the RFI signals from all directions, especially the ones near horizon, become an urgent problem. That is why heightened dynamic range of the whole system is an obligatory requirement.

Modern low-frequency radio telescopes use active antenna arrays as sensors of cosmic radio emission [Konovalenko et al., 2016]. Each element of the array is an active antenna that should satisfy all the requirements for small-sized solar radio telescope listed above. Giant Ukrainian Radio Telescope (GURT) is a project of new-generation low-frequency radio telescope developed in Ukraine by Institute of Radio Astronomy of National Academy of Sciences of Ukraine (IRA NASU) based on the experience of UTR-2 radio telescope maintenance and upgrading [Ryabov et al., 2010; Konovalenko et al., 2016]. GURT operates in 8-80 MHz range and consists of separate subarrays of 25 active antenna elements. Each subarray has discrete phase shifting based on true time-delay lines switching principle which allows beam pointing to 213 directions on celestial hemisphere. A two-channel ADR receiver was specially developed for receiving signals from each subarray to provide means of real-time digitization of the signal and waveform recording or on-the-fly spectra calculation and storing [Zakharenko et al., 2016]. The GURT active antenna element is developed to ensure high sensitivity in the whole operation range, and its characteristics are well studied by means of EM modeling and measurements. On the basis of these studies the sensitivity of single antenna element was calculated for ordinary observation parameters (100 ms integration time and 9.7 kHz frequency resolution, typical for solar observations with the ADR receiver). The results of calculations are shown in Fig. 1 and demonstrate that the sensitivity of the GURT active antenna is sufficient for registration of solar emission in the wide range of flux densities.

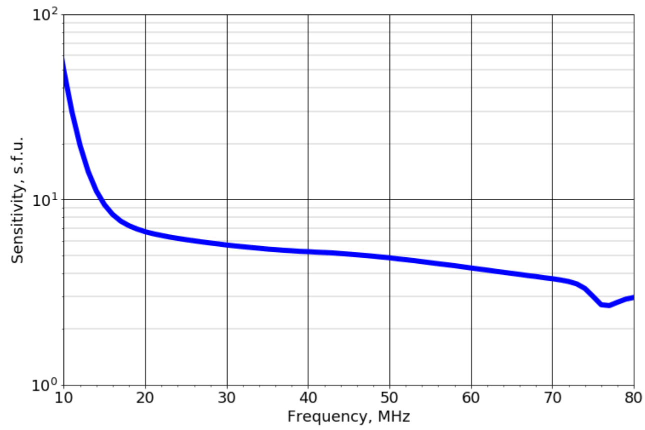

Fig.1. Sensitivity of the GURT active antenna for integration intervals in time and frequency of 100 ms and 4.9 kHz, respectively, as it follows from calculations in the paper [Tokarsky et al., 2017].

Test measurements and comparison with observations by other instruments

The best evidence of small-sized radio telescope performance is real observations of different type of emissions. During 2017-2018, we have conducted several sessions of such observations when together with the GURT subarrays a single active antenna was used. The results of observations show a great variety of solar radio bursts available for studies in detail: II, III, IIIb and IV types as well as drifting pairs [Stanislavsky et al., 2017] are distinctly seen on dynamic spectra obtained (see records in Fig. 2). The calculated sensitivity of the GURT active antenna is quite high to prove the quality of the instrument. We have compared several spectra with ones received by the well-known Nançay Decametric Array (NDA) radio telescope. NDA has 144 passive antennas of two circular polarizations (72 antennas of right-hand and 72 of left-hand). Fig. 3 shows a type II solar burst received with a single GURT active antenna and 72 passive antennas of NDA. The quality of the data is pretty much comparable, due to the high sensitivity of antenna systems developed at IRA NASU.

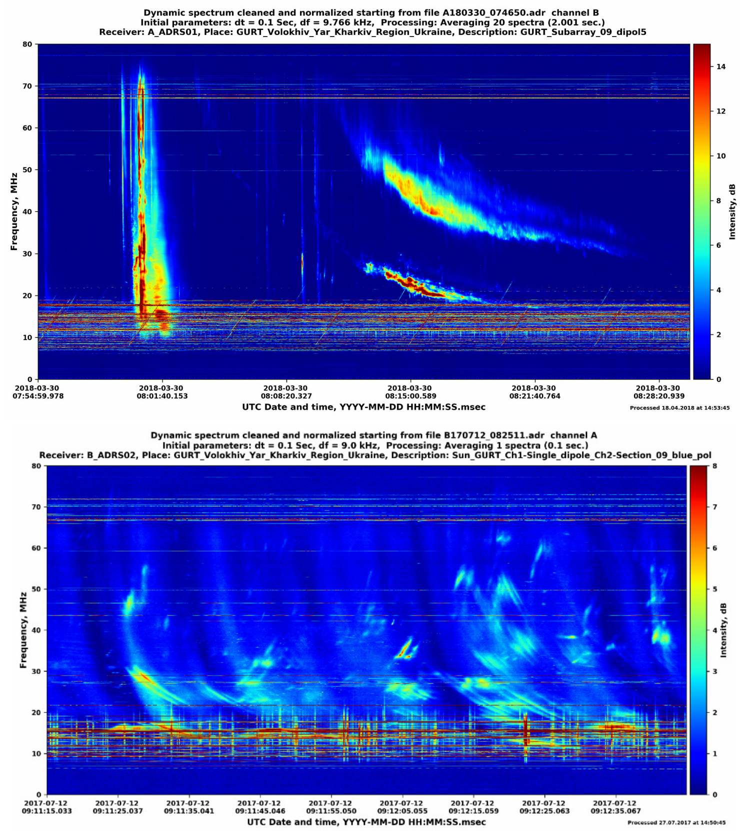

Fig.2. Examples of various bursts types in dynamic spectra recorded with the GURT active antenna.

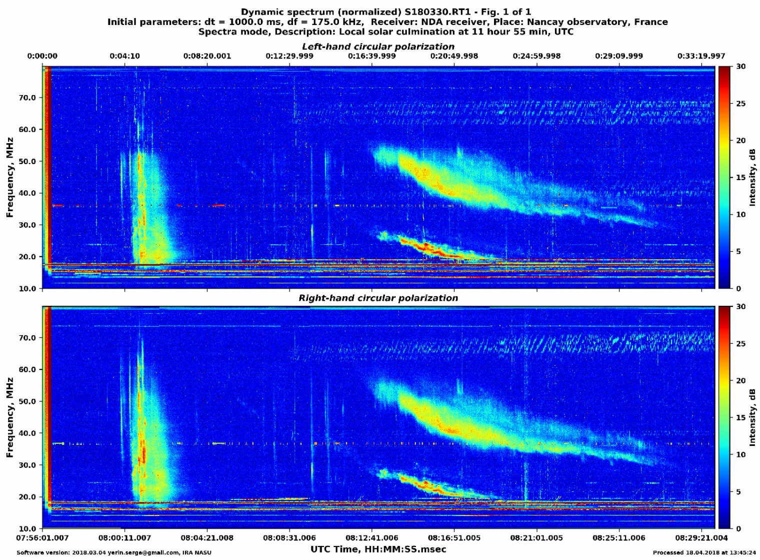

Fig.3. Dynamic spectrum of type III and II bursts obtained from the NDA observations on 30 March of 2018 simultaneously with GURT observations shown in Fig. 2.

Possible applications of small radio telescopes

Small-sized radio telescopes were of use at the beginning of radio astronomy but afterwards migrated to large-scale ones. Therefore, the question is natural: why do we need small-sized instruments nowadays? First of all, it should be noted that small-sized radio telescope can be a source of the immediate information on solar corona events, especially the coronal mass ejections (CME) and their velocities, affordable for many research centers, universities and colleges. Usually the data from well-known telescopes become available online in a several day gap, which can be critical for some applications. Such telescopes can also serve as triggers, signalizing for dedicated advanced telescopes to switch attention in solar observations from one event to another in case of strong, diverse or interesting events. To spread all over the world, a network of small-sized radio telescopes can conduct solar observations round the clock, providing reliability of results and higher RFI stability due to observations in different RFI and ionosphere conditions. There is also a chance for arranging VLBI system of many antennas that spread over globe to perform hi-res imaging of solar corona active regions, but the perspective needs substantial hardware and network resources. At the same time, the system of solar VLBI at lower frequencies could expand capabilities of such highly-demanded instruments as LOFAR, LWA, UTR-2 and SKA.

The main advantage of sensitive wideband small-sized radio telescopes is their size, which is critical in some applications, particularly in space missions. The high cost needed to launch big and heavy instruments to space limits the possibilities of space explorations. Small sized antenna like GURT active antenna is a perfect instrument to build a space- or lunar-based radio telescope [Shkuratov et al., 2018]. The shape of the antenna allows one to build antenna arrays from them and to transport it in a folded state. As the Moon has a much weaker ionosphere, which is a main hindering factor for observations at low frequencies from the Earth, the frequency range of the active antenna can be shifted down to lower frequencies. As the higher-to-lower operational frequency ratio is a constant which limits the operational band, it is possible to shift the operational range to 4-40 MHz range with changing the dimensions of dipole itself and matching circuits in the antenna amplifier. Such modification would allow observing solar radio emission under terrestrial ionosphere cutoff. This feature is especially useful for studies of solar drift pairs [Stanislavsky et al., 2017a and 2017b], which are known to be emitted at lower frequencies, and collect statistics of their appearance. Another advantage could be achieved by placing the radio telescope on the far side of the Moon, where manmade RFI are screened by the Moon itself [Mimoun et al., 2012].

The calculated values of GURT active antenna sensitivity were marked on the plot showing the levels of cosmic radio sources flux densities as seen from the Moon and are presented in Fig. 4. The figure clearly shows the prospect of solar emission studies with GURT active antenna on the far-side of the Moon.

Conclusions

New antenna systems in low frequency radio astronomy become more sensitive in wide frequency range, which means they can be used as small but sensitive instruments for particular observational tasks. On the example of the GURT active antenna we show the possibilities of single antennas to receive solar bursts of various types for their study at meter and decameter wavelengths. Also we discuss the possibility of using such antennas out of the terrestrial ionosphere to observe solar bursts under ionosphere cutoff. One of the most convenient places to install such a radio telescope could be the far-side of the Moon.

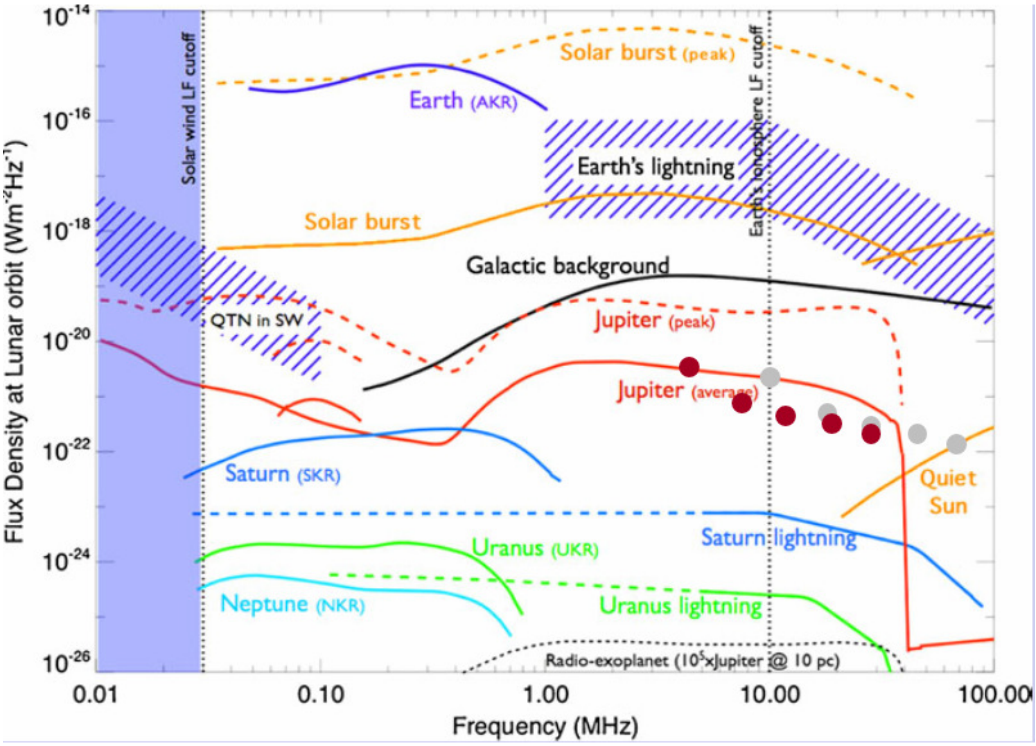

Fig.4.The levels of radio emission from different cosmic sources at the far-side of the Moon (courtesy of Mimoun et al., 2012). This figure shows estimated sensitivity of the GURT active antenna as it is (gray dots) and after frequency range shifting (red dots).

Acknowledgment

We would like to thank the NDA team for developing and operating the instrument and we are grateful for their open data policy. This research was partially supported by Research Grant 0118U000564 from the National Academy of Sciences of Ukraine.

References

Konovalenko A., L. Sodin, V. Zakharenko, et al. (2016). The modern radio astronomy network in Ukraine: UTR-2, URAN and GURT. Exp. Astron., 41, 1-38.

Mimoun D., M. Wieczorek, L. Alkalai, et al. (2012). Farside explorer: unique science from a mission to the farside of the moon. Exp. Astron., 33, 529-585

Ryabov V.B., D.M. Vavriv, P. Zarka, B.P. Ryabov, R. Kozhin, V.V. Vinogradov, L. Denis (2010). A low-noise, high dynamic range digital receiver for radio astronomy applications: an efficient solution for observing radio-bursts from Jupiter, the Sun, pulsars and other astrophysical plasmas below 30 MHz. Astron. Astrophys., 510, id. A16.

Shkuratov Y. G., A. A. Konovalenko, V. V. Zakharenko, A. A. et al. (2018). A twofold mission to the moon: objectives and payloads. Acta Astronautica, in press, available online.

Stanislavsky, A. A., A. A. Konovalenko, Ya. S. Volvach (2017a). Frequency drift rate of solar decameter "drift pair" bursts. Res. Astron. Astrophys. 17, no. 9, 97.

Stanislavsky, A.A., Ya. S. Volvach, A. A. Konovalenko, A. A. Koval (2017b). Solar drift-pair bursts. Sun and Geosphere, 12, no. 2, 99-103.

Tokarsky P. L., A. A. Konovalenko, I. S. Falkovich, S. N.Yerin (2015). SNR in active receiving antenna used as an element of phased antenna array for GURT radio telescope. In Proc. of the 45th European Microwave Conference (EuMC 2015), 7-10 September 2015. Paris, France. p. 1594-1597.

Tokarsky P. L., A. A. Konovalenko, S. N. Yerin (2017). Sensitivity of an active antenna array element for the low-frequency radio telescope GURT. IEEE Trans. on Antennas and Propagation. 65, no. 9, 4636-4644.

Zakharenko V., A.Konovalenko, P. Zarka, et al. (2016). Digital receivers for low-frequency radio telescopes UTR-2, URAN, GURT. J. Astron. Instrum. 5, is. 4. id. 1641010.

Proceedings of
Tenth Workshop "Solar Influences on the Magnetosphere, Ionosphere and Atmosphere"
Primorsko, Bulgaria, June 4÷8, 2018

Solar wind by IPS observations at decameter wavelengths

M.M. Kalinichenko [1], *O.O. Konovalenko* [1], *A.I. Brazhenko* [2], *N.V. Kuhai* [1,3], *O.I. Romanchuk* [1], *O.O. Lytvynenko* [1]

[1] Institute of Radio Astronomy of NASU, Kharkiv, Ukraine;
[2] Gravimetrical observatory of Geophysical institute of NASU, Poltava, Ukraine;
[3] Hlukhiv national pedagogical university, Hlukhiv, Ukraine
E-mail: kalinich@rian.kharkov.ua

Abstract.

This paper is devoted to the investigations of the solar wind by IPS observations at decameter wavelengths. IPS observations were carried out with the radio telescope URAN-2 (Ukraine, Poltava). Experiments include one observational session (January 2016). Two radio sources (3C274 and 3C144) were observed. The radio galaxy 3C274 scintillates only on the plasma irregularities of Earth's ionosphere while the radio source 3C144 shows both interplanetary and ionospheric scintillations. It was found that the power spectra of the interplanetary and ionospheric scintillations at decameter wavelengths were different. We obtained the solar wind parameters by fitting model IPS power spectra to the experimental one. The obtained parameters of the solar wind were in good agreement with those obtained by spacecraft.

Introduction

The solar wind is one of the most powerful factors that affect the state of space weather. There are several methods that allow conclusions to be made on solar wind parameters. One of the most effective is observations of interplanetary scintillations (IPS) (Hewish A. et al, 1964). IPS arises when the radiation from compact cosmic radio sources such as quasars, galaxies and pulsars is scattered due to the density irregularities in the solar wind. IPS strongly depends on observational frequency. IPS observations at decameter wavelengths allow the parameters and dynamic of the solar wind at different distances from the Sun (up to several a. u.) to be determined (Falkovich I.S. et al., 2010, Kalinichenko M.M., 2012).

Observations

We carry out IPS observations with the radio telescope URAN-2 ($8 \div 32$ MHz) (Konovalenko A.A. et. al, 2010) from January 11 to January 17, 2016 (during 7 days). Two radio sources (3C274 and 3C144) were observed at hour angles ±2 hr near the upper culmination with scans lasting 4 min. For processing, we customarily used the middle 30 s of a scan. We carried out the observations at night (elongation $\varepsilon \approx 150^0$). Records were obtained by using digital wideband receivers DSP-z (Zakharenko V.V. et al., 2016) with parameters of registration: the frequency range - 20.63 to 28.88 MHz and the time constant - 20 ms. In DSP-z the radio source signal $x(\tau)$is converted into a two-dimensional spectrogram $I(t, f)$ (otherwise called a dynamic spectrum).

$$I(t,f)=\left|X(t,f)\right|^2, \quad X(t,f)=\frac{1}{T}\int_{t-T/2}^{t+T/2} x(\tau)\,g(\tau-t)\,\mathbf{exp}(-i\pi f\tau)\,d\tau$$

where $g(t-\tau)$ is the "window function". $T = N_W \Delta t_S$. N_W is the window size, $\Delta t_s = 1/f_s$ is the sampling time, f_s is the sampling clock rate. In our observations $N_W = 2^{14} = 16384$, $f_s = 66$ MHz and we have 2048 FFT frequency channels in a dynamic spectrum.

Figure 1 (a, b) shows an examples of dynamic spectra

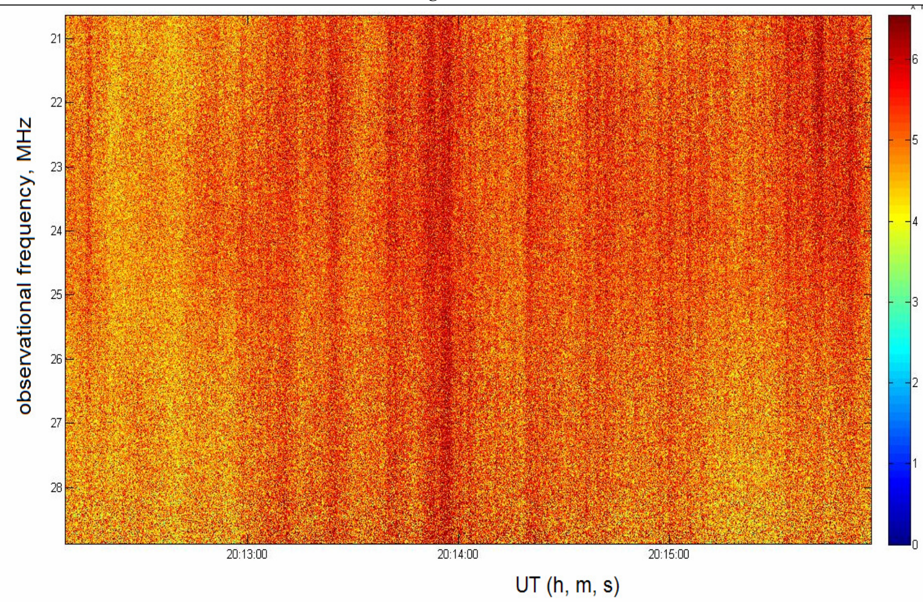

a)

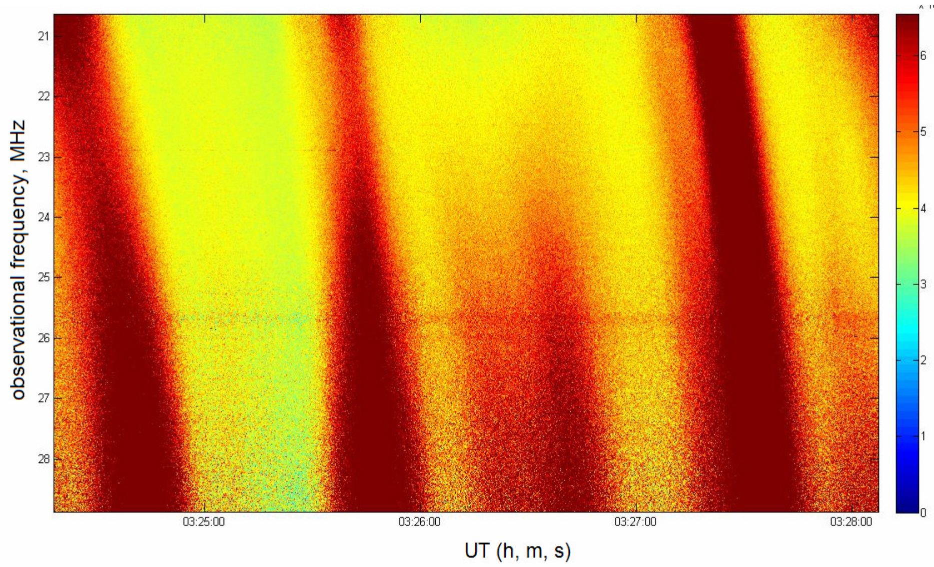

b)

Fig. 1 The dynamic spectra of scintillations of the radio sources 3C144 (a) and 3C274 (b)

Data processing

To obtain the solar wind parameters, the initial raw data that is received by the radio telescope URAN-2 needs to undergo several stages of processing. Firstly, as scintillations can originate in Earth's ionosphere too (Figure 1b), observations that exhibit ionospheric contribution to the IPS measurements have been discarded. To find such data we use spectral criterion. This criterion says that the interplanetary scintillations at decameter wavelengths have wider power spectrum then ionospheric ones (Kalinichenko et al., 2013). Secondly, FFT frequency channels, which are corrupted by interference, are removed from the data. The remaining ones are averaged to obtain the higher signal-to-noise ratio. Here we use the fact that the interplanetary scintillations are highly correlated in the frequency range from 20 to 30 MHz (Falkovich et al., 2004). Then experimental scintillation index and power spectra are estimated. The experimental scintillation power spectrum is usually corrected for noise by subtracting a constant which is estimated from the average of the spectrum between 5 and 10 Hz.

Figure 2 shows the scintillation index for the radio sources 3C144 and 3C274.

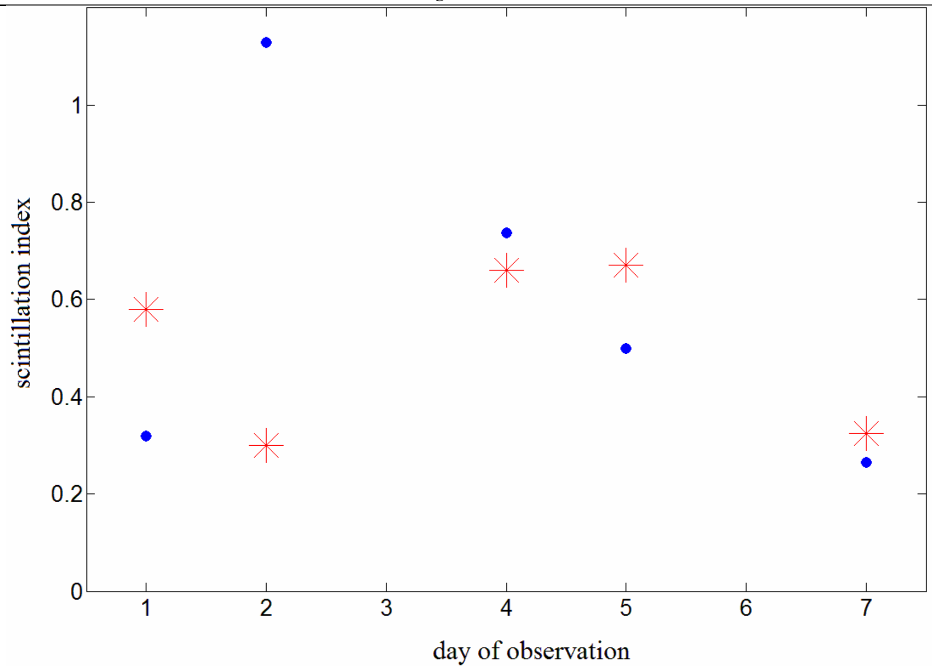

Fig. 2 The scintillation indexes of scintillations of the radio sources 3C144 (red) and 3C274 (blue)

It is seen that scintillation indexes of the interplanetary and ionospheric scintillations are close in the days of observations. The exception is January 12 when the scintillation index of the ionospheric scintillations was essentially higher. Except this day for the ionospheric scintillations both types of scintillations are moderate.

Power spectra estimated for one day of observations are shown in Figure 3 (red – 3C274, blue – 3C144).

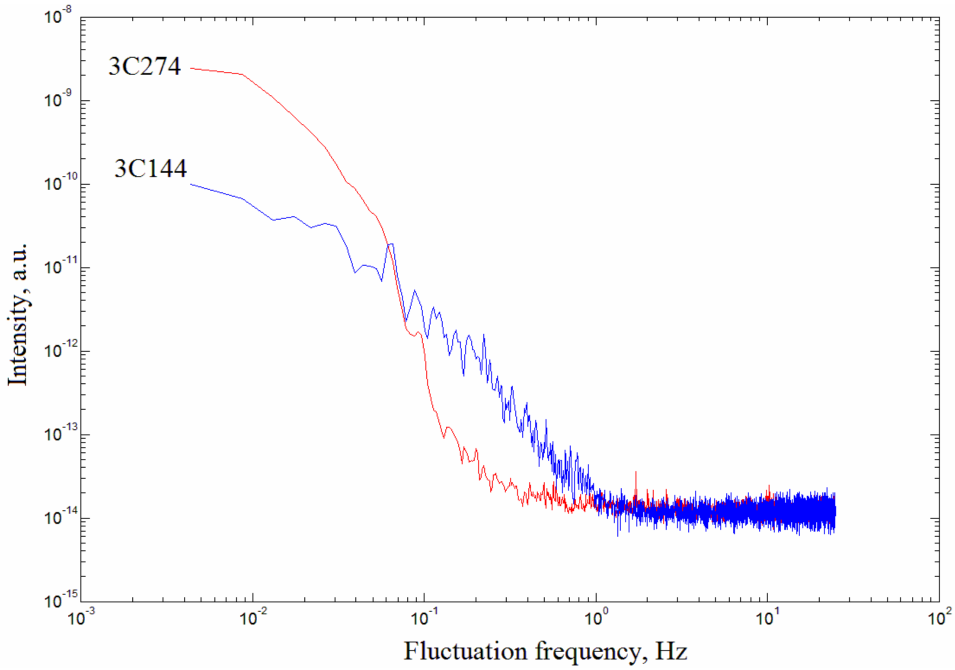

Fig. 3 The power spectra of scintillations of the radio sources 3C144 (blue) and 3C274 (red)

It is seen that the power spectrum of the interplanetary scintillations is wider then ionospheric ones. This difference was used for the separation of two types of scintillations.

Model fitting

To derive the solar wind parameters, the theoretical power spectra of the interplanetary scintillations (Figure 3, blue) are fitted to the observed one. Fitting the calculated curves for different models to the experimental characteristics is often used to define the solar wind parameters (e.g. Manoharan and Ananthakrishnan, 1990). In our case the theoretical power spectra are calculated by using phase screen model:

$$P(\nu)=2\pi(\lambda_{re})^2\int_0^\infty \frac{dz}{|V_\perp(z)|}\int_{-\infty}^{\infty} dk_y \times \Phi_{Ne}(k_x,k_y,k_z=0,z)\times F_{Fr}(k_x,k_y,z)\times F_{Source}(k_x,k_y,z)$$

where λ is the wavelength, r_e is the electron radius, x and y are the coordinates, z is the coordinate along the line of sight; $k=(k_x^2+k_y^2+k_z^2)^{1/2}$ is the spatial frequency; $\Phi_{Ne}(k_x,k_y,k_z=0,z)$ is the spatial spectrum of the turbulence, where n is the spectral index $n \approx 3 \div 4$; $F_{Fr}(k_x, k_y, z) = 4\sin^2(k^2 z\lambda / 4\pi)$ is Fresnel filter; $F_{\text{Source}}(k_x, k_y, z)$ is the source contribution for Gaussian distribution of brightness; $\theta_0 \approx \theta_S /2.25$ where θ_S is the angular size of the radio source; $V_\perp$ is the transversal component of the velocity.

The estimated solar wind parameters are shown in Figure 4 and Figure 5.

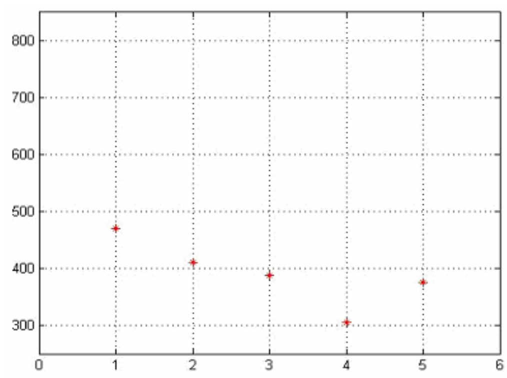

Fig. 4 The solar wind speed

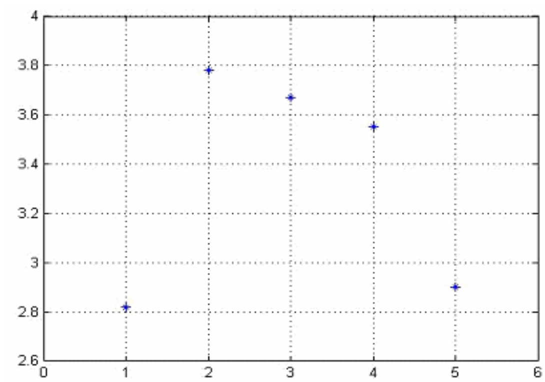

Fig. 5 The spectral index of spatial spectrum of electron density fluctuations

Conclusions

The observations of the interplanetary scintillations at decameter wavelengths allow conclusions to be made on the solar wind parameters (speed, spectral index of the interplanetary plasma spectrum) and to reconstruct the solar wind parameters at distances up to several a.u., 3 - 4 a.u.). The obtained parameters of the solar wind were in good agreement with those obtained by spacecraft.

Acknowledgment

This study was supported by Target Complex Program of the NAS of Ukraine for Scientific Space Studies for 2018-2022 "Kronos-2018" , 0118U000563.

References

Falkovich I.S., N.N. Kalinichenko, A.A. Gridin, I.N. Bubnov (2004). Possibility of wide-band IPS observations at decameter waves. Radio Physics and Radio Astronomy, 2,121-129.

Falkovich I.S., A.A. Konovalenko, N.N. Kalinichenko, M.R. Olyak, A.A. Gridin, I.N. Bubnov, A.I. Brazhenko, A. Lecacheux, H. Rucker (2010), Dispersion Analysis of Interplanetary Scintillations at Decameter Wavelengths: First Results. Radio Physics and Radio Astronomy, 1, no. 1, 3-9.

Hewish A., P.F. Scott, D. Wills (1964), Interplanetary Scintillation of Small Diameter Radio Sources. Nature, 203, no. 4951, 1214-1217.

Kalinichenko N.N. (2012), Scintillations of Radio Source 4C21.53 at decameter wavelengths and elongations 43o-138o. Radio Physics and Radio Astronomy, 3, no. 2, 131-138.

Kalinichenko N.N., I.S. Falkovich, A.A. Konovalenko, A.I. Brazhenko, A.I. (2013). Separation of interplanetary and ionospheric scintillations of cosmic sources in the decameter range of radio waves. Radio Physics and Radio Astronomy, 3, 210-219.

Konovalenko A.A., L.G. Sodin, V.V. Zakharenko, Ph. Zarka, O.M. Ulyanov, M.A. Sidorchuk, S.V. Stepkin,

P.L. Tokarsky, V.N. Melnik, N.N. Kalinichenko, et al. (2016). The modern radio astronomy network in Ukraine: UTR-2, URAN and GURT. Experimental Astronomy, 42, no. 1, 11 - 48.

Manoharan P.K., S. Ananthakrishnan (1990). Determination of solar-wind velocities using single - station measurements of interplanetary scintillations. MNRAS, 244, 691 - 695.

Zakharenko V.V., A.A. Konovalenko, P. Zarka, O.M. Ulyanov, M.A. Sidorchuk, S.V. Stepkin, V.L. Koliadin, N.N. Kalinichenko (2016). Digital receivers for low-frequency radio telescopes UTR-2, URAN, GURT. Journal of Astronomical Instrumentation, 4, 738-749.

Bulgarian Space Instrumentation

R. Miteva, T. Belichenova, M. Zaharinova, G. Mardirossian, P. Getsov

Space Research and Technology Institute, Bulgarian Academy of Sciences, Sofia, Bulgaria
E-mail: rmiteva@space.bas.bg

Abstract.
We outline the main idea and the current progress done concerning the gathering into a comprehensive list and the organization in a consistent way of all available information on space payloads, instruments and systems developed by Bulgarian scientists and engineers. Such database is designed to act as a catalog of Bulgarian space instrumentation, and to host a brief description of the scientific purpose, team, photo materials, references, etc. for each instrument. The main architecture of dedicated website is also presented here.

Background

The initiative to create a platform presenting all Bulgarian space efforts has been circulating the scientific community in Bulgaria for a number of decades. Nevertheless, to present day, no concise catalog of all space instrumentation is knows to us. The information is scattered in numerous books (many only available in Bulgarian and/or Russian), dissemination flyers, newspapers articles, web-sites, personal presentations/posters, private archives, etc. With the natural passage of time and the multiple restructuring of scientific institutes in Bulgaria, we are faced with the danger to lose vital (details of the) historical knowledge of the space efforts of Bulgarian scientists, engineers and technicians. Preserving the achievements of these people is our main motivation.

The idea towards the compilation of such catalog was put forth in March 2018 by R. Miteva and T. Belichenova, by formally requesting an official appointment and cooperation from their host institute, primarily involved in the past with building of space instruments – currently known as Space Research and Technology Institute – Bulgarian Academy of Sciences (SRTI-BAS). The idea was supported by SRTI-BAS and at present this project has a long-term plan that is put forth for implementation. This historical archive, named *Bulgarian Space Instrumentation*, is planned to be built as a freely accessible web-site supporting English and Bulgarian language versions. The initial list of team members primarily involved in collecting and structuring of the information as well as developing of the web-platform is: R. Miteva (project leader, writing of the catalog contents), T. Belichenova (librarian, archive materials search, verification), M. Zaharinova (web-design, development and support of the dedicated web-site), G. Mardirossian (photo-materials, instrument description) and P. Getsov, where all members are also involved in editing.

During the first stage of the work, the team members have contacted known specialists involved in space instrument design and building for providing assistance and support with materials and information. Thus several of the descriptions of instruments are expected to be prepared in collaboration. The web-site is planned:

- to present a short technical and scientific description on each of the Bulgarian space instruments (and for completeness also on their carrier, usually a Russian satellite);
- to provide the complete list the constructors and developers where reliable sources are found;
- to provide references for further reading (books, e.g., Serafimov (1979), Mishev (2004), Ivanova and Stoyanov (2002), research (Chapkunov et al. 1977, Dachev et al. 2015) and popular articles, etc.);

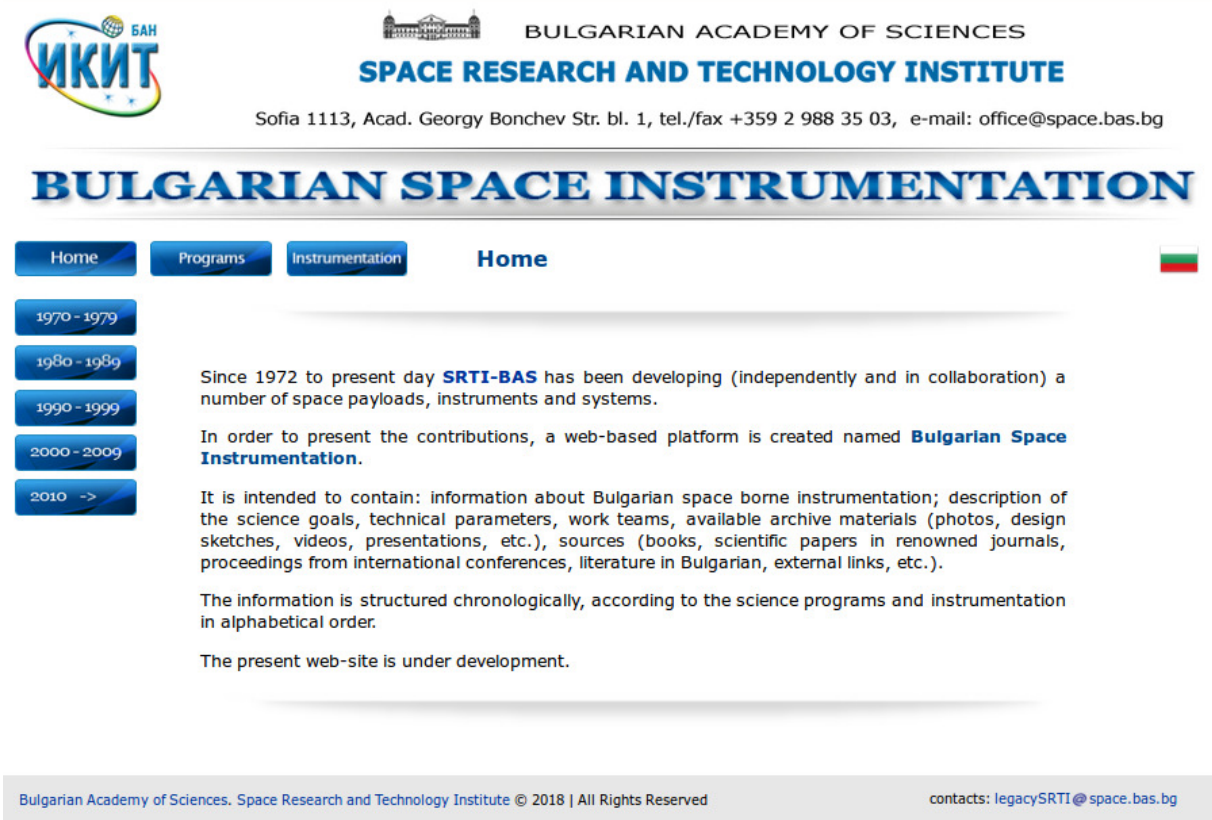

Fig. 1 Overview of the home page of the dedicated web-site (status July 2018) describing the Bulgarian Space Instrumentation project: www.space.bas.bg/legacy.

- to give links to other web-sites providing relevant information (NASA, RSRS, etc.);
- to host a rich photo and video album.

The direct access to the web-site is possible via: www.space.bas.bg/legacy. Such long-term web-site based project for gathering information, cross-referencing and editing is finally targeted to reach different communities, both specialists and the general public.

Web-site

The overall structure of the dedicated web-site is shown in Fig. 1 with the initial version of the preface.

a) Chronological ordering

The chronology of the instrumentation is ordered in decades, starting from 1970 (see Fig. 2) to present day. The first payload (P-1) was completed and launched on 01.12.1972, as part of the instrumentation aboard the Intercosmos 8 spacecraft. With the successful launch and operation of this payload Bulgaria became number 18 among the space countries, according to the UN agreement from 1965.

Each instrument is presented by describing first the carrier – satellite, space probe, station, rocket, etc., then adding a list of all instruments aboard. Note that the web-site describes in detail only those instruments created by Bulgarian specialists from different science institutes in Bulgaria.

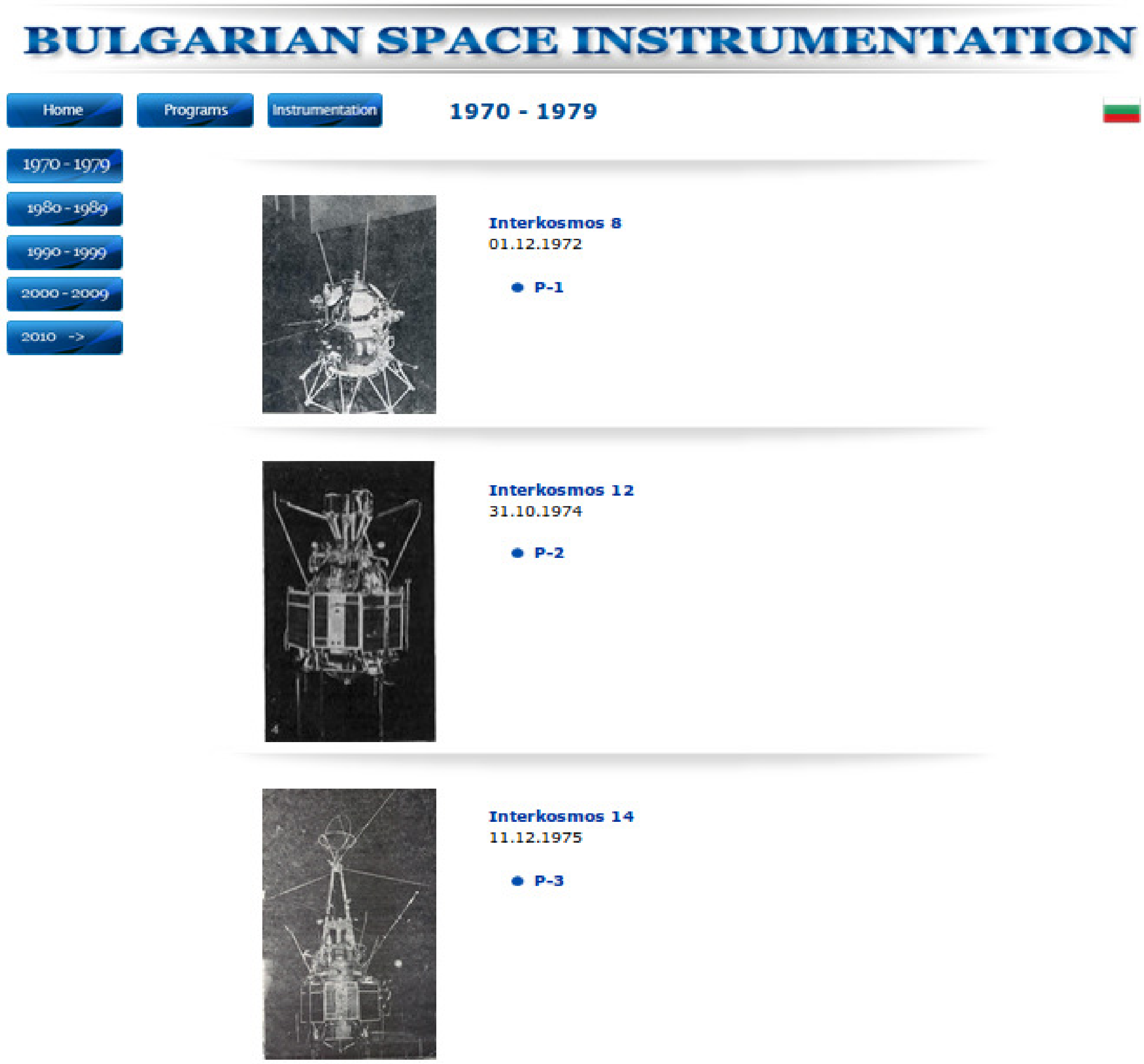

Fig. 2 Example snap-shot from the web-site (status July 2018) describing the chronological structure of the web-site: here only for the first three payloads and their satellite carrier in 1970s.

The *preliminary list of the instrumentation* for the respective decade is given below as: name of the respective satellite and in brackets are the name or abbreviation of the instrument(s):

70s: 1970-1979

Interkosmos 8 (P-1); Interkosmos 12 (P-2); Interkosmos 14 (P-3); Vertical 3 (P-1R); Vertical 4 (P-2R); Vertical 6 (P-3R, EMO-2R); Vertical 7 (P-3R, EMO-2R, 4ELI); Centaure-II (RIKI, EMO-1R); Interkosmos 19 (P-4, EMO-1); Flight of the first Bulgarian cosmonaut Georgy Ivanov (Spectrum 15, Duga, Sredets, Vital).

80s: 1980-1989

Bulgaria 1300-II (SMP-32, RM-1, BU); Bulgaria1300-I (P6-IL, ID-1, P7-3L, DIET, AMEI, ANEPE, PROTON-1, IESP, IMAP, PHOTON-1, EMO-5, OLCC); Vertical 10 (ID-1R, ZOND-R); Vega 1 (TKS); Vega 2 (TKS); Flight of the second Bulgarian cosmonaut Alexander Alexandrov (Rozhen, Terma, Paralaks-Zagorka, Spectrum 256, Pleven 87, Son-3, Liulin, Doza-B, Zora); Granat (Sunflower); PHOBOS-1 (FREGAT, LIMA-D); PHOBOS-2 (FREGAT, LIMA-D); OS MIR (Liulin); Interkosmos 24 (HBK/OHK); Magion-2 (KEM-1).

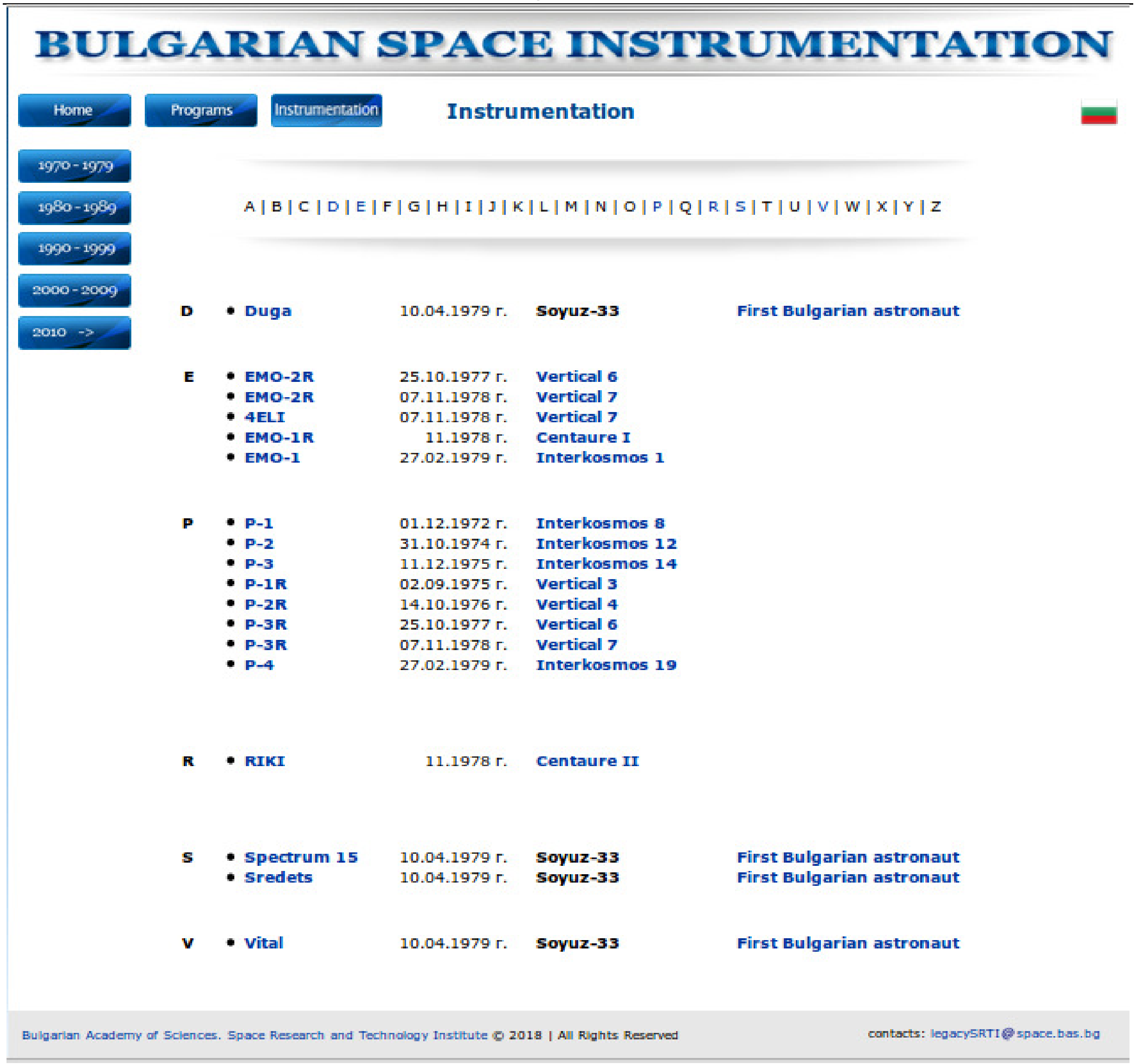

BULGARIAN SPACE INSTRUMENTATION

Home | Programs | Instrumentation

Instrumentation

1970 - 1979
1980 - 1989
1990 - 1999
2000 - 2009
2010 ->

A | B | C | D | E | F | G | H | I | J | K | L | M | N | O | P | Q | R | S | T | U | V | W | X | Y | Z

D	• Duga	10.04.1979 г.	Soyuz-33	First Bulgarian astronaut
E	• EMO-2R	25.10.1977 г.	Vertical 6	
	• EMO-2R	07.11.1978 г.	Vertical 7	
	• 4ELI	07.11.1978 г.	Vertical 7	
	• EMO-1R	11.1978 г.	Centaure I	
	• EMO-1	27.02.1979 г.	Interkosmos 1	
P	• P-1	01.12.1972 г.	Interkosmos 8	
	• P-2	31.10.1974 г.	Interkosmos 12	
	• P-3	11.12.1975 г.	Interkosmos 14	
	• P-1R	02.09.1975 г.	Vertical 3	
	• P-2R	14.10.1976 г.	Vertical 4	
	• P-3R	25.10.1977 г.	Vertical 6	
	• P-3R	07.11.1978 г.	Vertical 7	
	• P-4	27.02.1979 г.	Interkosmos 19	
R	• RIKI	11.1978 г.	Centaure II	
S	• Spectrum 15	10.04.1979 г.	Soyuz-33	First Bulgarian astronaut
	• Sredets	10.04.1979 г.	Soyuz-33	First Bulgarian astronaut
V	• Vital	10.04.1979 г.	Soyuz-33	First Bulgarian astronaut

Bulgarian Academy of Sciences. Space Research and Technology Institute © 2018 | All Rights Reserved

contacts: legacySRTI@space.bas.bg

Fig. 3 Snap-shot from the web-site (status July 2018) describing the instrumentation ordered alphabetically.

90s: 1990-1999

OS MIR-Kvant (SVET, SVET-2); Interkosmos 25 (DEP-2E); Magion-3 (KEM-2); INTERBALL-1 (AMEI-2); Magion-4 (KEM-3, FM-3I); INTERBALL-2 (IMAP-3, UFSIPS, IESP-2M); Magion-5 (KEM-4).

2000s: 2000-2009

ISS (Liulin-E094); Foton M2 (R3D-B2); ISS (Liulin MKS); ISS (Liulin 5); Foton M3 (R3D-B3, Liulin-Photo); ISS (R3DE); Chandrayan-1 (RADOM); ISS-Zvezda (R3DR).

2010s: 2010-2019

Phobos-Grunt (Liulin-Fobos); BION-M No.1 (RD3-B3); ISS-Zvesdza (DP-2, ZL-2); Foton-M No. 4 (RD3-B3); ExoMars Trace Gas Orbiter (FREND/Liulin-MO).

b) Alphabetical ordering by the scientific program

Each instrument is part of a scientific program that can either include a number of satellites and experiments or is specifically designed with a single scientific purpose and unique (or dual) launch.

The *preliminary list of science programs* included in the project is as follows:

- Intercosmos (IK): series of IK satellites 1-25, rockets Vertical and manned space flights
- AKTIVEN: series of Magion 1-5 satellites
- PHOBOS: two-probe mission to the Martian moons
- VEGA: two-part mission to Venus with Halley comet flyby
- Shipka: a dedicated scientific program for the second Bulgarian cosmonaut
- Shuttle-Mir (1994-1998), https://history.nasa.gov/SP-4225.pdf
- Mir-NASA: continuation of the greenhouse in space experiments
- ExoMars, http://exploration.esa.int/mars/

c) Alphabetical ordering by the instrumentation name

In addition, in order to facilitate a searching according to the name or abbreviation of the instrument, a different section of the web-site is developed. There, all the instrumentation is ordered alphabetically. The current status of this web-site module (as of end July 2018) is shown in Fig. 3.

Future development

The list of provided here instruments will be enriched or entire sections could be modified when new sources of information are found or been provided to the project team. Commentaries and first account information from Bulgarian participants in the different programs are also planned to be included in the web-site. Contact and suggestions are collected via the project e-mail: legacySRTI@space.bas.bg

Acknowledgement

The web-site www.space.bas.bg/legacy is supported by the Space Research and Technology Institute – Bulgarian Academy of Sciences.

References

Chapkunov, S., Ivanova T., Petrunova, M. (1977) Bulgarian space instruments for near Earth plasma investigation. Radio, television and electronics, Vol. 11, pp. 12-13 (in Bulgarian)
Serafimov K. (1979) Space research in Bulgaria, Bulgarian Academy of science Publ. Sofia, 447pp. (in Russian)
Mished, D. (2004) Space research in Bulgaria, Academic Publisher 'Marin Drinov', Sofia, 247pp. (in Bulgarian)
Ivanova, I. and Stoyanov, V. (2002) Greenhouse under the sky, VST, Sofia (in Bulgarian)
Dachev, T. P., Semkova, J. V.; Tomov, B. T.; Matviichuk, Yu. N.; Dimitrov, P. G.; Koleva, R. T. et al. (2015), Life sciences in space research, Vol. 4, pp. 92-114
NASA Space Science Data Coordinated Archive: https://nssdc.gsfc.nasa.gov/nmc/SpacecraftQuery.jsp
RSRS Russian scientific/research satellites: http://rammb.cira.colostate.edu/dev/hillger/Russian.htm

SEVAN particle detector at Zagreb Astronomical Observatory: 10 years of operation

F. Šterc [1], D. Roša [1], D. Maričić [1], D. Hržina [1], I. Romštajn [1], A. Chilingarian [2], T. Karapetyan [2], D. Cafuta [3] and M. Horvat [3]

[1] Zagreb Astronomical Observatory, Zagreb, Croatia
[2] Alikhanyan Physics Institute, Yerevan, Armenia
[3] Zagreb University of Applied Sciences, Zagreb, Croatia
E-mail: fsterc@gmail.com

Abstract.

At the "Regional IHY (International Heliophysical Year) Planning Meeting for the Balkan and Black Sea Region", organized by Solar Terrestrial Influences Laboratory in Bulgaria 2005, the possibilities of new network of the Space Weather particle detectors designed by Armenian scientists were presented. Network is known today as SEVAN (Space Environment Viewing and Analysis Network). In December 2008 the installation of the SEVAN particle detector at Zagreb Astronomical Observatory was finished. It is the first instrument for detecting cosmic rays in Croatia and its installation greatly promotes solar physics research in our country. Here we present some results obtained from data collected by SEVAN particle detector at Zagreb Astronomical Observatory during first 10 years of operation. We calculated the barometric coefficients using two statistical methods (least square method and least absolute deviation method. Pressure corrected data is available on web page of the Zagreb observatory. Examples of solar modulation effects (Forbush decrease) and first evidence of registration of TGEs (Thunderstorm Ground Enhancements) are also given.

Introduction

In December of 2008th Zagreb Astronomical Observatory was included in the SEVAN network (Space Environmental Viewing and Analysis Network) and SEVAN CRO unit it is the first cosmic ray particle detector that was installed in Croatia thanks to the cooperation with Aragat's Space Environmental Centre (ASEC) of the Alikhanyan Physics Institute (Armenia) who provided all the logistics. The SEVAN network is a ground based worldwide network of instruments on different geographic locations and altitudes. The main scientific goal is to improve research in solar and atmospheric physics, space weather conditions, and thunder forming events. SEVAN measures the flux intensity of secondary cosmic rays formed in cascades in the Earth’s atmosphere from the primary cosmic rays. The basic SEVAN unit consists of two identical plastic scintillator slab sizes (4 standard slabs) of 50 ... 50 ... 5 cm^3 in the upper layer and lower layer and 5 thick scintillator slabs sizes of 50 ... 50 ... 25 cm^3 in the middle of the instrument. The upper and lower layers are separated by two lead absorbers which are the size of 100 ... 100 ... 5 cm^3. All scintillator layers are light protected in iron shielding with a photomultiplier tube. This construction allows the detection of low energy particles, neutral particles and high energy muons fluxes, depending on the registration of signal or the absence of a signal (*Roša et.al.*, 2010, *Chilingarian et.al.*, 2018). In this paper we present the most important data and research during the 10 year operational period of SEVAN CRO cosmic ray detector.

Data & Analysis

The count rate intensity of the incoming cosmic ray particle flux on ground based instruments is affected by local atmospheric pressure. The barometric coefficient has to be calculated for the correction of the data because the barometric effect affects the variations of the measured count rate (*Dorman*, 1974). The measurements at SEVAN CRO were performed during the solar minimum at the end of the 24th Solar cycle, with no disturbances of the IMF (interplanetary magnetic field) and magnetosphere and in the period of significant atmospheric pressure variations. The dataset of a four day minute count rate from SEVAN CRO particle detector during 25. – 28. December 2017 was used for calculating the barometric coefficient during the biggest oscillations pressure period (~30 mbar difference between the lowest and the highest pressure rates) and during a period with no geomagnetic storms where the Dst Index was < -30 nT (*Loewe and Prolss*, 1997), Dst values were obtained from Kyoto University given at http://wdc.kugi.kyoto-u.ac.jp/dstdir/index.html.. Real pressure data was taken from DHMZ (Croatian Meteorological and Hydrological Service) which was calibrated with the SEVAN CRO pressure data using linear regression, with the correlation coefficient being 0.9986.

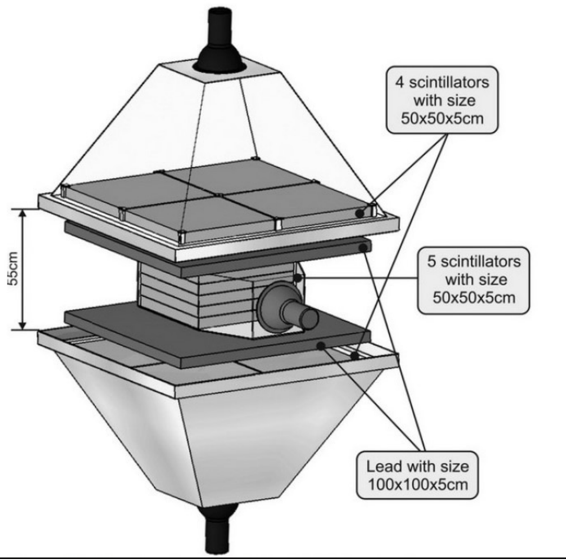

Fig. 1 SEVAN particle detector module schematic. The corresponding signals: 100 – traversal of the low energy charged particle. 010 – traversal of the neutral particles, 111 , 101 – traversal of the high energy muons (> 250 MeV). SEVAN CRO is located on latitude 45.82 N; longitude 15.97 E; altitude 170 m; vertical cut-off rigidity ≈ 4.9 GV

When the incoming flux of secondary cosmic rays is constant, the measured intensity *I* depends on the local atmospheric pressure which is shown in the following equation (*Dorman*, 1974, *Chilingarian et.al.*, 2009):

$$dI = -\beta dP \tag{1}$$

Where dI is the change in intensity because of the change in pressure dP and β is the barometric coefficient. If β is constant the expression (1) gives:

$$I = I_0 e^{-\beta(P-P_0)} \tag{2}$$

Where I are the counting rates at pressure P and I_0 and P_0 are the average counting rate and pressure for the measuring interval. By performing the transformation, we can apply the expression for linear regression:

$$ln\,(I / I_0) = -\beta(P - P_0) \tag{3}$$

In figure 2 the left side of the graphs show the relation between intensity and atmospheric pressure. We calculated the barometric coefficient during the period of 25 – 28 December 2017 for high energy muons, neutral particles and low energy particles. The corresponding barometric coefficients are -0.169 %/mbar for muons with largest correlation coefficient of analyzed dana -0.775; -0.282 %/mbar for neutrons with a relative lower correlation coefficient of -0.368 and -0.254 %/mbar for low energy particles with a correlation coefficient of -0.765.

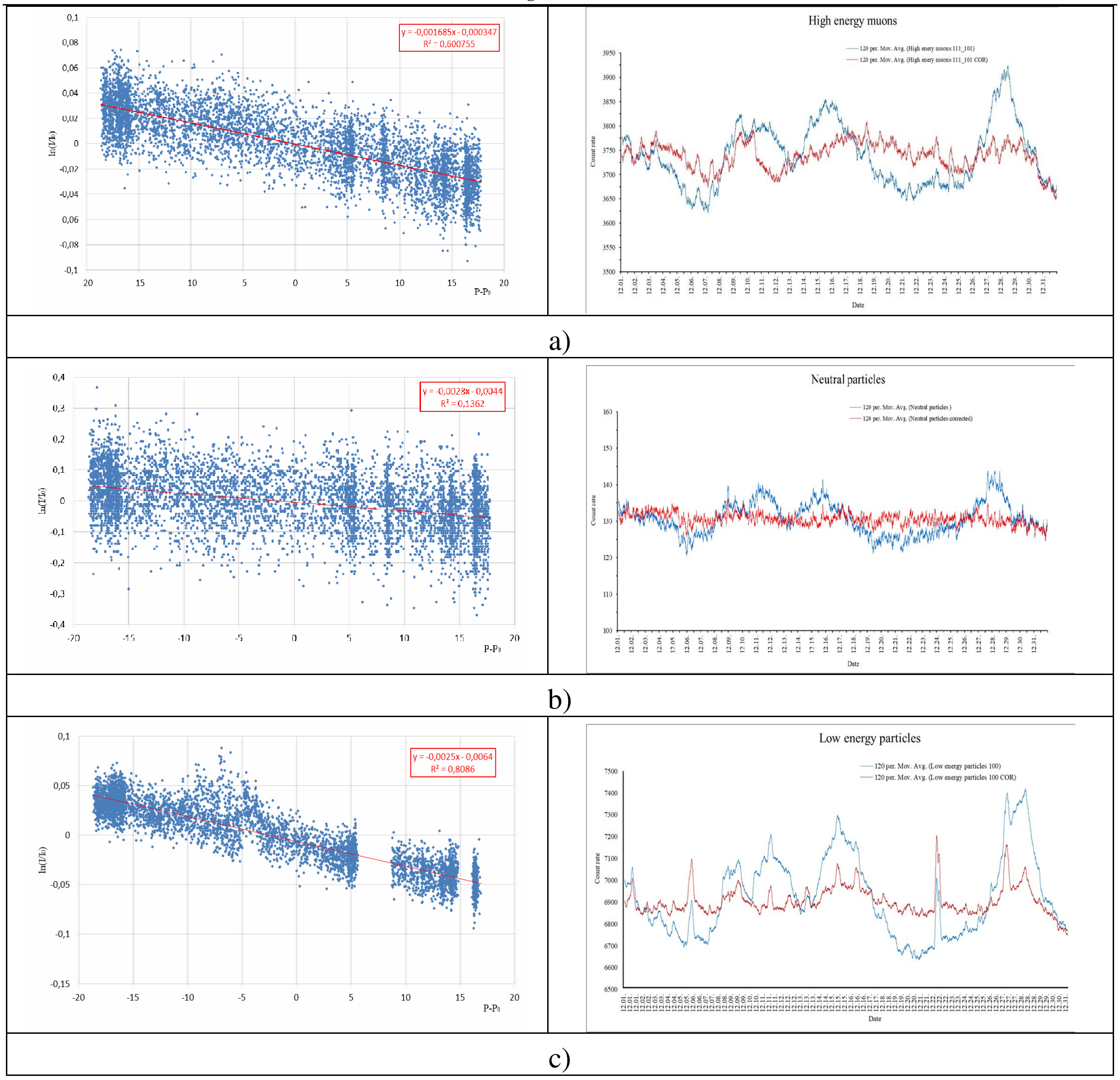

Fig. 2 Graphs for barometric coefficient are on the left side, from top to bottom; a) high energy muons, b) neural particles and c) lower energy particles (with excluded data, see Tab. 1.). On the right side are the monthly smoothed graphs with moving average which show corrected data using the barometric coefficient.

Absolute values of barometric coefficients are lower in total because of the location of detector is on a lower altitude, also the barometric coefficient for neutral particles and low energy particles are higher then for muons, which is expected as lower altitudes are less sensitive to lower energies, register less cascade particles showers and are less sensitive to primary lower energies beacuse of lower cut off rigidity (*Chilingarian*, 2009). For lower energy particles some data had to be excluded because of an appearant consistant fault in instruments during some periods. These events need to be investigated further. Excluded events are shown on *Tab. 1*. We also calculated the barometric ceofficent with another statistical analysis, the least absolute deviaton method (LAD). LAD method is similiar to least square method LSM, it minimizes the sum of absolute errors and is more robust which extends its application to studies where outliers dont need to be emphasized. We developed a special algorithm for this method. In figure 2 on the right side a 30 day minute count for December 2017 is shown with a moving average. The curves show measuring (uncorrected) counting rate (blue line) and pressure corrected data (red line).

Tab. 1 Compiled data for all the channels where β is the barometric coefficient using LSM and LAD with their appropriate error; r is the correlation coefficient, σ is the standard deviation and N is the number of events.

Monitor	β(%/mbar) LSM	β(%/mbar) LAD	r	σ LSM	σ LAD	N
High Energy Muons	-0.169±0.0018	-0.169±0.00022	-0.775	0.01693	0.01693	5760
Neutrons	-0.282±0.0093	-0.274±0.00115	-0.368	0.08747	0.0875	5760
Low Energy Charged Particles	-0.202±0.0022	-0.224±0.00028	-0.765	0.02091	0.02137	5760
Upper Detector	-0.190±0.0018	-0.202±0.00020	-0.838	0.01521	0.01543	5760
Middle Detector	-0.147±0.0026	-0.144±0.00033	-0.584	0.02519	0.02521	5760
Lower Detector	-0.179±0.0016	-0.188±0.00021	-0.817	0.01559	0.01572	5760
Low Energy Charged Particles*	-0.251		-0.894			4799*
Lower Detector*	-0.209		-0.888			4799*

* *shows the excluded data for lower energy particles and the lower detector.*

The database for uncorrected and corrected pressure on SEVAN CRO unit can be accessed on a online tool on the web page of Zagreb Astronomical Observatory https://zvjezdarnica.hr/obrazovni/znanost/sevan-podaci/.

Forbush decreases are rapid short decreases in the galactic cosmic ray intensity which are induced by short term changes in solar wind and the interplanetary magnetic field which are related to interplanetary coronal mass ejections and corotating interaction regions (*Maričić et.al.*, 2013). We present an example of a Forbush decrease which was registered with our SEVAN CRO instrument. In the period of 17 - 18 February 2011 there is a rapid decrease in secondary cosmic ray particle count rate. The data shows modulation of the flux for low energy particles, high energy muons and neutral particles.

Diurnal cosmic ray variations depend on the geographic location of the cosmic ray detector, magnetospheric and heliospheric magnetic field conditions. Diurnal variations are characterized by phase and amplitude and are important data for measuring and research of the Sun – Earth interaction and the analysis of the cosmic ray fluxes (*Mailyan and Chilingarian*, 2010). For the period of 1 - 20 November 2010, we calculated the average values of count rate for the same minute of each day. The data is smoothed with the moving average of two hours. For high energy muons the peak is ~ 13:00 UT, low energy particles have two peaks ~ 6:30 UT and ~ 10:00 UT and neutral particles also show two peaks at ~ 9:00 UT and ~ 11:00 UT.

Thunderstorm Ground Enhancements (TGE) are sudden changes of secondary cosmic ray particle fluxes (enhancing fluxes of electrons, gamma rays and neutrons) during thunderstorms which are connected to high energy events in Earth's atmosphere. They consist of a few minutes high-energy emission (up to 30 - 40 MeV) and a few hours duration of low energy emission (< 3 MeV). TGEs occur mainly during deep negative electric field periods. The flux enhancement is well correlated with the electric field disturbances (*Chilingarian et.al.*, 2015). Here we present the first evidence of TGEs at Zagreb Observatory by SEVAN detector. We show the disturbances of the electric field measured on a station located 1.5 km from the Zagreb Astronomical Observatory on 14 May 2017 during lightning activity .

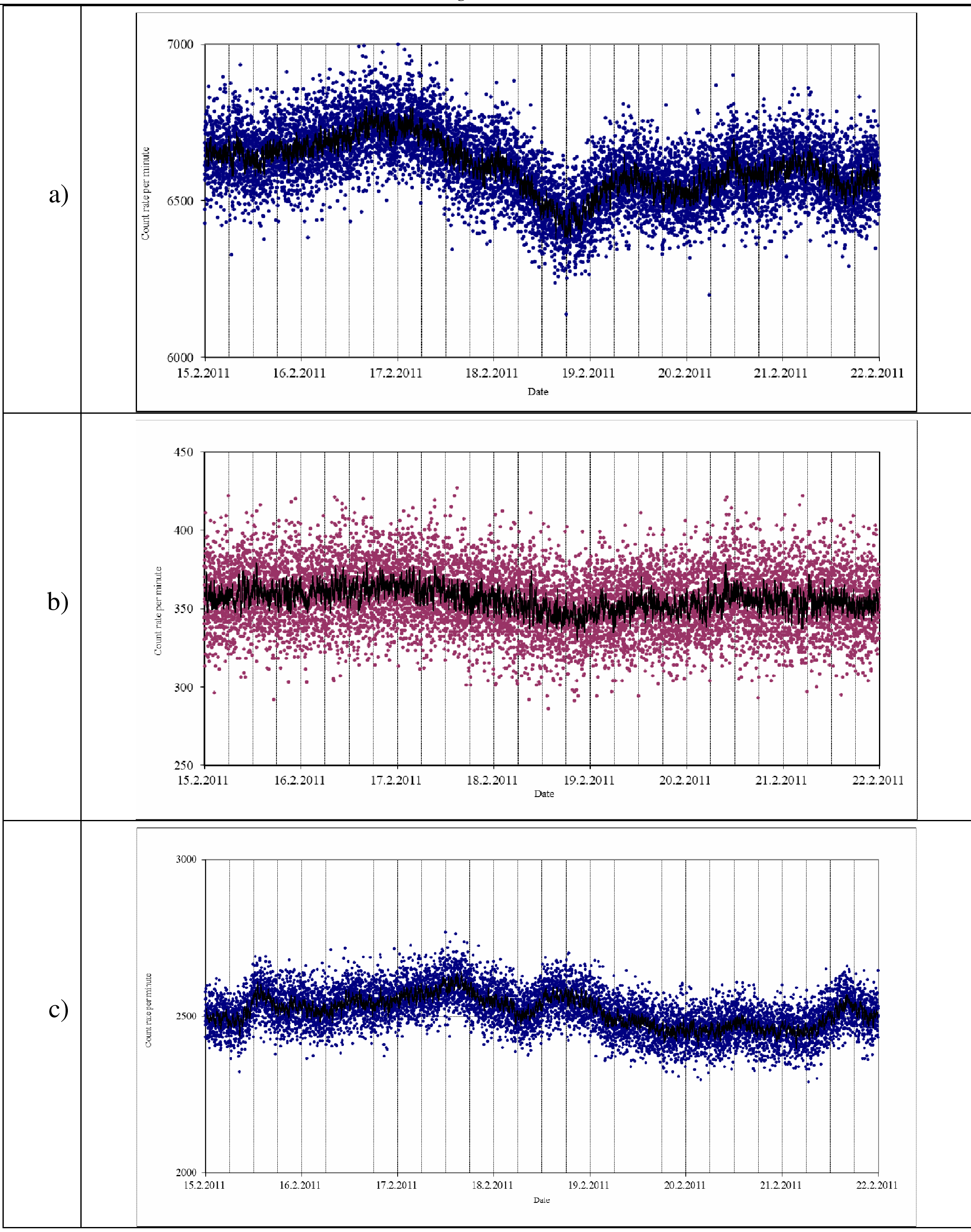

Fig. 3 Forbush decrease detected on SEVAN CRO instrument showing from top to bottom: a) low energy particles, b) neural particles, c) high energy muons

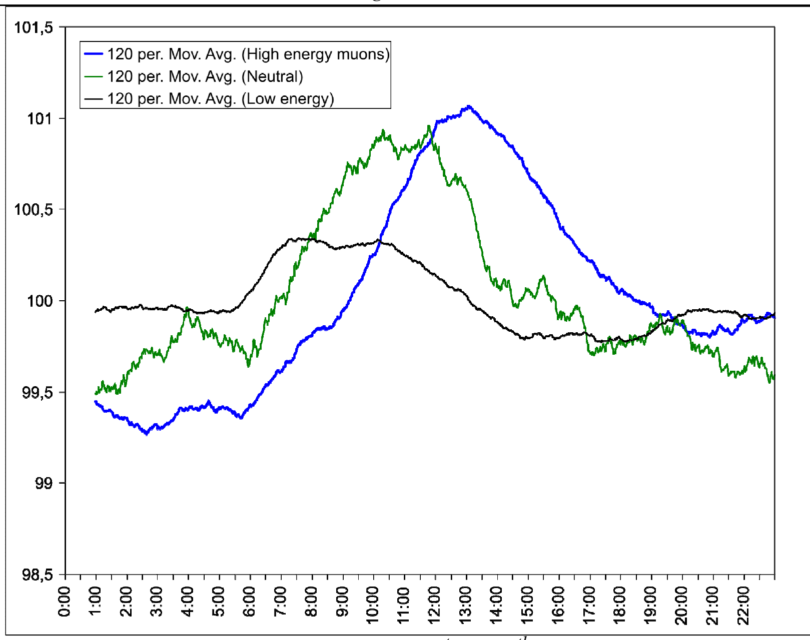

Fig. 4 Diurnal cosmic ray variation of 20 days from 1st to 20th November 2010

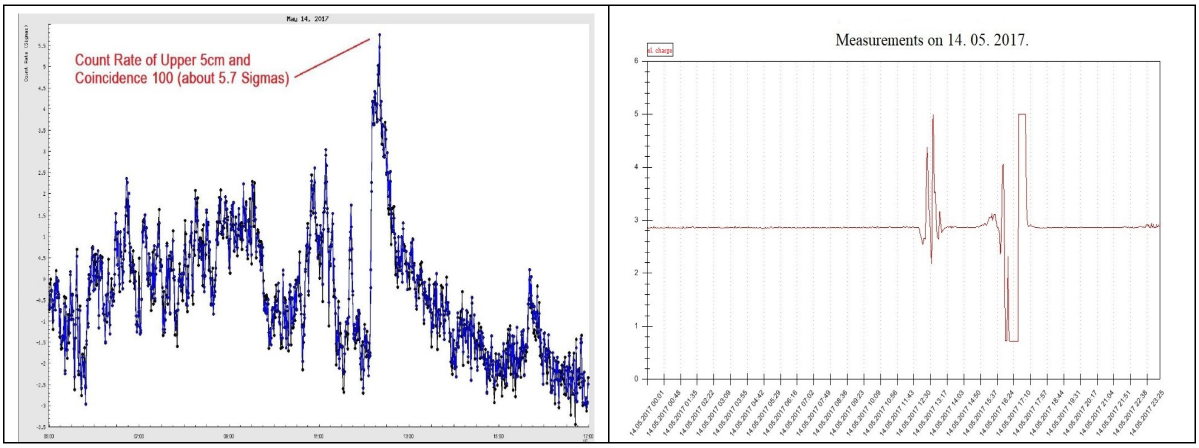

Fig. 5 On the right side is the measurement of disturbance in electric field, the measurements are relative and the instrument is not calibrated during the lightning event. On the left side is the TGE enhancement in upper 5cm plastic scintillator and coincidence of "100" (mostly low energy electrons and gamma rays) where we can see an increase in count rate during a lightning.

Conclusions

In this paper we presented some results obtained by SEVAN CRO detector during its 10 operational years, such as the values of barometric coefficients, diurnal variation, example of a Forbush decrease and the flux enhancements related to TGE events. The ability of detection of different particle fluxes (e.g. neutrons, high and low energy muons) is suitable for monitoring space weather conditions, especially solar modulation of cosmic ray flux. But also SEVAN data can be very useful for analysis of high energy phenomena in Earths atmosphere, such as the physics of the thunderstorms which still remain unsolved.

Acknowledgment

We would like to thank DHMZ (Croatian Meteorological and Hydrological Service) for the atmospheric pressure data, Kyoto university teams for they open policy and database regarding Dst index and colleagues from Ruđer Bošković Institute led by Ivan Kontušić regarding the atmospheric electric field data.

References

Chilingarian, A.; Karapetyan T.;Mailyan, B.; (2009). Calculation of the barometric coefficients for the particle detectors belonging to the world-wide networks at the start of the 24th Solar Activity cycle, Proceedings of FORGES-2008 conference

Chilingarian, A.; Chilingarian, S.;Reymers, A. (2015). Atmospheric discharges and particle fluxes, Journal of Geophysical Research: *Space Physics* 120 (7), 5845-5853

Chilingarian, A ; Babayan, V,; Karapetyan, T,; & Mailyan, B.; Sargsyan, B.; Zazyan, M. (2018). The SEVAN Worldwide network of particle detectors: 10 years of operation. Advances in Space Research. 10.1016/j.asr.2018.02.030.

Dorman, L.I., (1974). Cosmic Rays, Variations and Space Exploration.North-Holland, Amsterdam

Loewe A., Prölss C & W., G. ; (1997). Classification and mean behavior of magnetic storms. Journal of Geophysical Research. 102. 14209-14214. 10.1029/96JA04020.

Maričić, D.; Vršnak, B.; Dumbović, M.; Žic, T.; Roša, D.; Hržina, D; Lulić, S.; Romštajn, I.; Bušić, I.; Salamon, K.; Temmer, M.; Rollett, T.; Veronig, A.; Bostanjyan, N.; Chilingarian, A.; Mailyan, B.; Arakelyan, K.; Hovhannisyan, A.; Mujić, N.; (2013). Kinematics of Interacting ICMEs and Related Forbush Decrease: Case Study, *Solar Physics*, 286

Mailyan, B., Chilingarian, A.; (2010). Investigation of diurnal variations of cosmic ray fluxes measured with using ASEC and NMDB monitors. *Advances in Space Research*. 45. 1380-1387. 10.1016/j.asr.2010.01.027.

Roša, D.; Angelov, Ch.; Arakelyan, K.; Arsov, T.; Avakyan, K.; Chilingarian, A.; Chilingaryan, S.; Hovhanissyan, A.; Hovhannisyan, T.; Hovsepyan, G. et al.; (2010). SEVAN CRO Particle Detector for Solar Physics and Space Weather research *// Central European astrophysical* bulletin*,* 34, 115-122

.

Results from Langmuir Probe Measurements Aboard the International Space Station

B. Kirov, S. Asenovski

Space Research and Technology Institute, Bulgarian Academy of Sciences, Sofia, Bulgaria
E-mail: bkirov@space.bas.bg

Abstract.

In this paper, the Langmuir probes are described included in "Obstanovka“ experiment aboard the International Space Station which has been operating since April 2013. One of the main goals of this experiment is to study the surface charging of super-big objects like the International Space Station.

Introduction

Langmuir probe is a classical instrument for plasma diagnostics, and among the first ones for in situ measurements of thermal plasma in the near-Earth environment. In the last decades, the Langmuir probe is one of the classical instruments for plasma diagnostics [*Mott-Smith and Langmuir*, 1926] and among the first space-borne instruments. Langmuir probes have been successfully used aboard a number of rockets and satellites for in situ measurements of thermal plasma parameters in the terrestrial ionosphere [*Klimov et al.*, 1995], at other planets [*Bogges et al.*, 1959] and comets [*Krehbiel et al.*, 1980; *Grard et al.*, 1989] – e.g. in satellite mission such as Tiros, Explorer, Alouette, ISIS, DMSP, Atmosphere Explorer, Interkosmos, Dynamics Explorer, Kosmos, Interball, Demeter, Astrid, Freja, Kyushu, CHAMP, CRRES, SCATHA, KOREASAT and many others, including several stratosphere rocket launches of the Vertical series, and planetary exploration missions such as Viking (Mars), Cassini (Saturn), Pioneer Venus (Venus), VEGA (Venus and the Comet Halley), etc.

The parameters measured by Langmuir probes are the electron and ion concentrations Ne and Ni, the electron temperature Te, and the satellite body potential Us.

In this paper, the Langmuir probes are described included in "Obstanovka“ experiment aboard the International Space Station which has been operating since April 2013. One of the main goals of this experiment is to study the surface charging of super-big objects like the International Space Station. All earlier studies have been conducted for relatively small and homogenous spacecraft, while with the launch and gradual build-up of the International Space Station we face the problems of the interaction of a super-large structure at a low orbit with its environment. For the first time, we have a structure which is not only that large but also so much energy consuming and emitting. Here we demonstrate how the various factors in the near-Earth space affect the surface charging of the International Space Station.

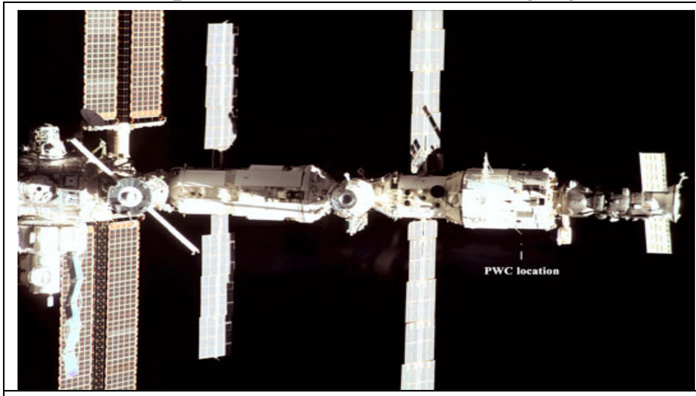

b

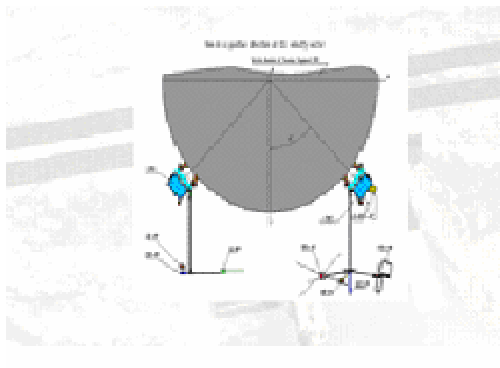

a

Fig. 1 (a) location of the PWC modules placed on the outer surface of ISS; (b) cross section of the position of LP1 and LP2on the body of ISS, in the direction of the positive ISS speed vector.

“Obstanovka” Hardware

The PWC hardware of 'Obstanovka' consists of several modules, combined in three blocks (Fig.1). Two of them are placed in open space location outside of ISS and the third block (BSTM) is located inside the station. The following physical parameters are being measured by the system: - electron and ion temperatures T_e and T_i; electron and ion concentrations Ne, Ni; DC and AC electrostatic and magnetic fields and currents; plasma and ISS potentials; electron spectra in the range 0.01-10keV; spectra of the VLF electromagnetic waves. To study the plasma discharge effects in space, PWC includes as well a separate discharge generator.

There are two cylindrical LP probe setups (LP-1, 2),

LP1 and LP2 are used to characterize

- thermal plasma parameters in two locations outside ISS;
- plasma electron temperature Te in the range 1000-6000 Kelvin;
- electron and ion concentration Ne, Ni in the range $1.10^9 – 1.10^{13}$ m^{-3};
- ISS potential Up, (referenced to the surrounding plasma, in the range ±100 V;
- fast fluctuations in the plasma concentration.

The complete hardware setup of PWC “Obstanovka” is shown in Table 1. Several research teams from the UK, Poland, Russia, Ukraine, Hungary, Sweden and Bulgaria partnered in the full PWC implementation.

Table 1: Full hardware module list of the PWC setup

Device	Organization
Combined Wave Sensor - CWS-1, CWS-2	LC ISR
Magnetometer – DFM-1	IKI
Magnetometer – DFM-2	LC ISR
Langmuir probes - LP-1, LP-2	SRTI-BAS
ISS potential sensor - DP-1, DP-2	SRTI-BAS
Plasma discharge simulator – SPP	SKB
Correlating electronic specrometer (10eV – 10KeV) CORES	Sussex University
Radio frequency Analyzer – RFA (Scorpion)	SISP; SRC
Signal Analyser – SAS3	SRG, BLE
Data Acusion and Control Unit - DACU-1, DACU-1	KFKI RMKI; Sheffield Uni
Telemetry information storage module – BSTM (inside ISS)	KFKI RMKI; Sheffield Uni
Ground segment equipment – GSE	KFKI RMKI; SRC

Langmuir probe – LP

An important part of the “Obstanovka” experiment are the two Langmuir probes LP1 and LP2.

In principle, a Langmuir probe can be any conducting body introduced into the plasma. Voltage is applied to the probe, changing over a certain range, and the probe current is measured. The dependence of the probe current on the voltage is usually referred to as "probe characteristic" or "volt-ampere curve". Fig.2 presents a volt-ampere curved measured by the Langmuir probe aboard the Intercosmos Bulgaria-1300 satellite [*Georgieva et al.*, 1984]. The plasma parameters are derived from the form and amplitude of this volt-ampere curve. When the probe potential is negative enough to repel all the electrons, the probe current is due only to the ions which are accelerated towards the probe, and the current's amplitude is proportional to the ion concentration.

When the probe potential is less negative, the more energetic electrons overcome it, and produce an electron current, exponentially increasing when the voltage is further decreased. The electron temperature is derived from the slope of the volt-ampere curve in this electron retardation region. When the probe is positive with respect to the plasma, the ion current is negligible while the electrons are accelerated, and the amplitude of the current is a function of the electrons concentration.

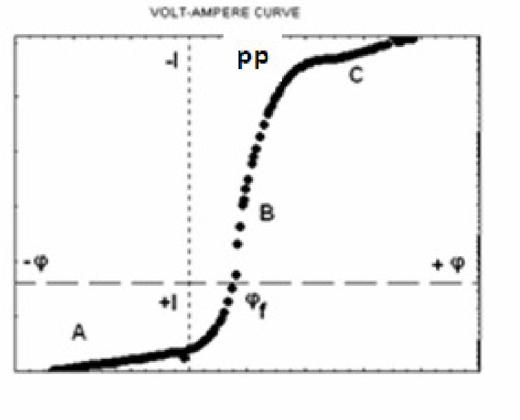

Fig. 2 A typical volt-ampere characteristic from the cylindrical Langmuir probe aboard Intercosmos Bulgaria-1300 satellite.

Regarding the problem of the satellite electrization, of special interest is the probe characteristic point at the potential at which the net current to the probe becomes zero – e.g., the electron and ion fluxes impinging on the probe are equal. This is the floating potential φ_f - the potential which the probe in plasma reaches if no voltage is applied to it from an external electric circuit. The point marked PP in Fig.5 is an inflection point in the volt-ampere curve. It corresponds to the plasma potential with respect to the spacecraft, or the spacecraft potential with respect to the plasma. The determination of this potential is equivalent to measuring the spacecraft charging.

Spacecraft charging

Since the seminal work by Mott-Smith and Langmuir [*Mott-Smith and Langmuir*, 1926] it is known that anybody immersed into plasma charges to a certain potential (called "floating potential") such that the current flowing between the body and the surrounding plasma is zero. The charging of the spacecraft is due to both the surrounding plasma and the solar electromagnetic radiation.

The net current J to the surface of the spacecraft can be written as:

$$J = J_{\mathrm{e}} - (J_{\mathrm{p}} + J_{\mathrm{se}} + J_{\mathrm{bse}} + J_{\mathrm{sp}} + J_{\Phi}),$$

where: J_e - plasma electron current; J_p - plasma proton current; J_{se} - secondary electron emission current; J_{bse} – backscattered electrons current; J_{sp} – secondary electron emission due to protons; J_{Φ} - photoelectron emission current.

The plasma electron current J_e brings negative charge to the spacecraft surface, the other currents remove the negative charge from the surface. The resulting floating potential is determined by the dynamical equilibrium on the surface when the net current $J = 0$. However, the various current components to or from the surface are not zero – that is, there is a continuous charge exchange between the spacecraft surface and the surrounding plasma. The change in any parameter influencing this charge exchange (e.g., the surface coefficient of secondary electron emission, or plasma particles energy) will lead to shifting in the equilibrium state: the net current will be zero at another value of the surface potential. In the equilibrium state, a potential difference is settled between the surface and the surrounding plasma, which regulates the flow of plasma particles to the surface, retarding particles of one sign and accelerating particles of the opposite sign. At the same energy, plasma electrons have a considerably higher velocity than ions because of the difference in masses. Therefore initially, while the body introduced into the plasma is not yet charged, the electron flux to the surface exceeds the positive ion flux, and the body charges negatively. The further flow of charged particles to the surface is determined by the electric field retarding the electrons and accelerating the positive ions, which eventually leads to the equilibrium of the electron and ion fluxes to the surface at equilibrium negative surface potential. This equilibrium potential depends on the average energy of the plasma particles (the higher the plasma temperature, the higher negative potential the surface can acquire), and on the secondary emission properties of the surface.

Based on general considerations when the station is in the dark, it should be charged negatively (Fig. 3).

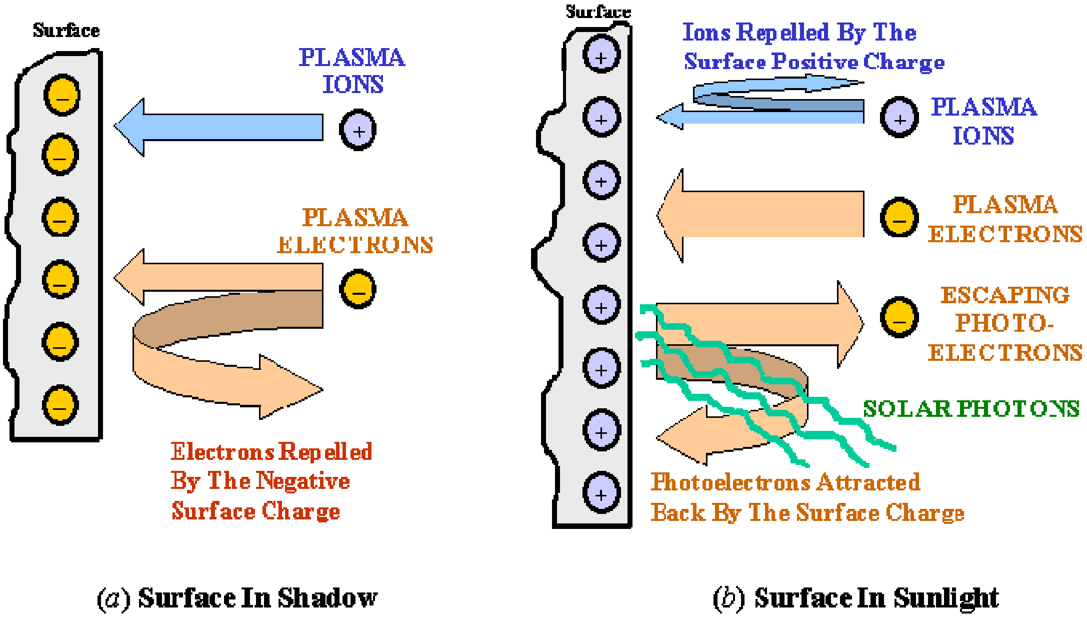

Fig 3. Surface charging of the station in shadow (a) and sunlight (b).

During the measurements, we have found that the plasma potential is positive, or with other words, the potential of the plasma is negative as it can be seen in Fig. 4.

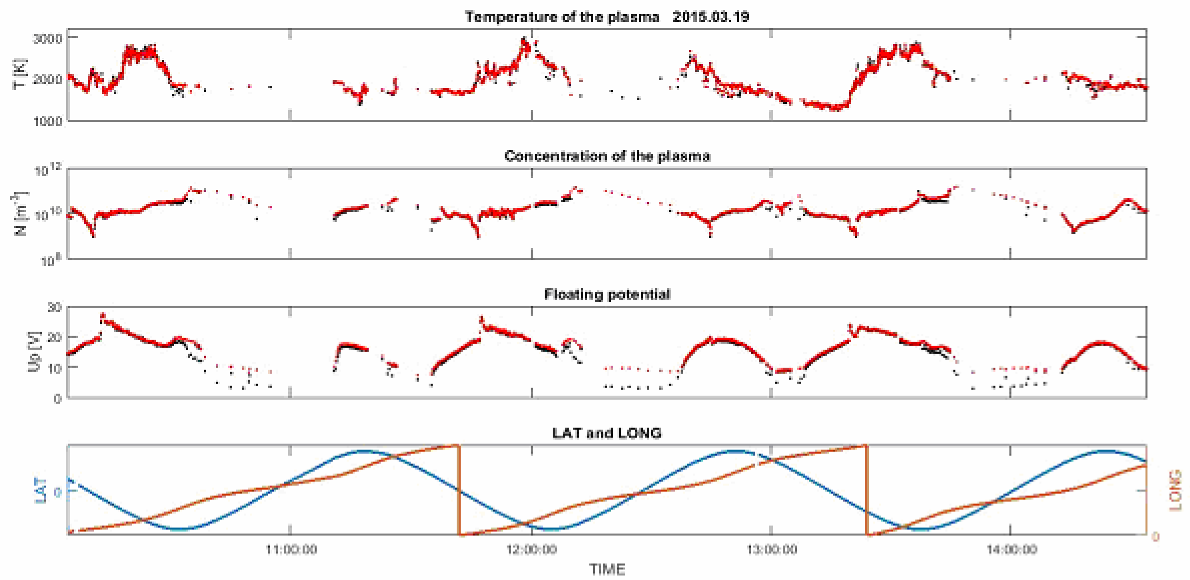

Fig 4.– Te (K) upper panel; Ne (m-3) second panel; Up (V) – third panel; orbital parameters – bottom panel.

Effect of the Equator crossing

Over the Equator area there are regions with low plasma concentration (equatorial anomaly). One example is shown in Fig. 4. Here the station crosses the Equator at 10:15. The station enters a region of low concentration and local temperature maximum which leads to increase in the Up.

Effect of terminator crossing

When the ISS crosses the terminator, the observations show a jump of the floating potential. In the case shown in Fig. 5 the potential Up(V) (third panel) suddenly changed from 10 to 25V (i.e. the floating potential of the station became -25V). According to our American colleges [*Barjatya et al.*, 2009] such a jump is caused by "charging due to additional electron collection on the exposed edges of solar cells".

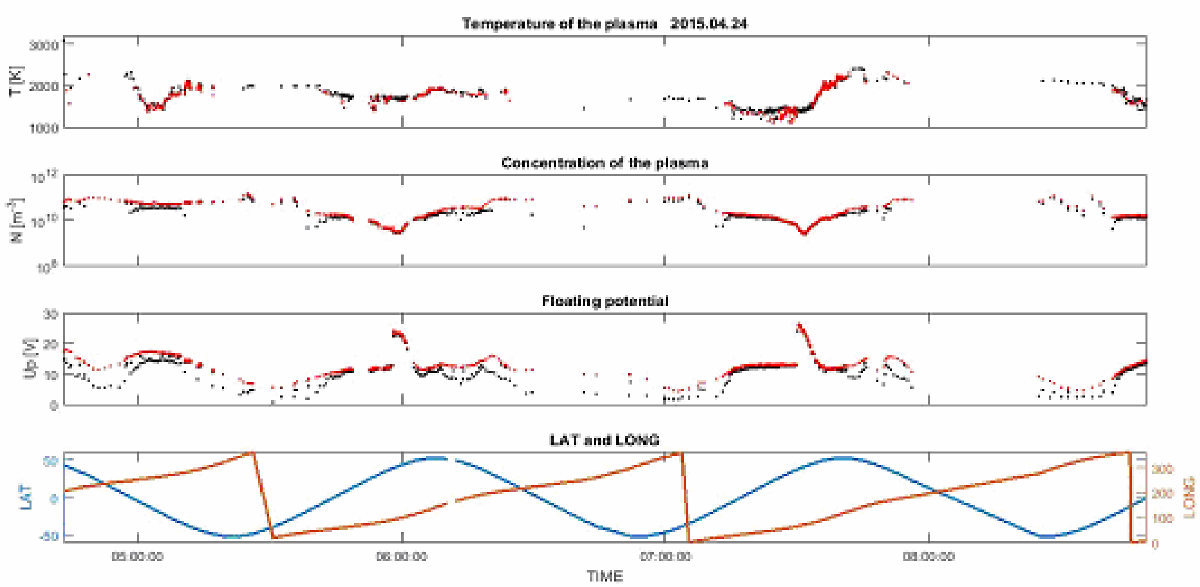

Fig 5.– Te (K) upper panel; Ne (m^{-3}) second panel; Up (V) – third panel; orbital parameters – bottom panel.

Conclusions

The spacecraft potential is always negative with respect to the plasma and varies between 0 and -30 V.

The spacecraft potential can change sharply during passages of the terminator and the equatorial anomaly.

References

Mott-Smith H.M., Langmuir I. (1926), The Theory of Collectors in Gaseous Discharges, Phys. Rev., 28, 727.

Klimov S.I., Agafonov, Yu.N., Skalsky A.A., Rodin V.G. (1995), The electromagnetic clean sub-satellite SPELIS for studies on plasma-wave phenomena caused by operations of the electrodynamics tethered systems (EDTS) in space plasmas. Proceedings of the Fourth International Conference on Tethers in Space, Smithsonian Institution, Washington, D.C., 10-14 April, p.1643-1652.

Bogges R.L., Brace L.H.,Spencer N.W. (1959), Langmuir probe measurements in the ionosphere, J. Geophys. Res., 64, 1627.

Krehbiel J.P., Brace L.H., Theis R.F., et al. (1980), Pioneer Venus Orbiter Electron Temperature Probe, J.Geophys. Res., GE-18, 1980, 49-54.

Grard R., Laakso H., Pedersen A., Trotignon J.G., Mikhailov Y. (1989), Observations of the plasma environment of Comet Halley during the VEGA flybys, Annales Geophysicae 7, 141-149.

Georgieva K., Kirov B., Kraleva L. (1984), BAN Doklady, 37 (2), 157 (In Russian).

Barjatya A., Swenson C.M.,. Thompson D.C, Wright K.H. (2009), Jr., Rev. Sci. Instrum, 80, 041301(1-11).

Time dependent physicochemical model of the auroral ionosphere.

Dashkevich Zh.V. [1], *Ivanov V.E.* [1], *Sergienko T.I.* [2], *Kozelov B.V.* [1]

[1] Polar Geophisical Institute, Apatity, Russia
[2] Swedish Institute of Space Physics, Kiruna, Sweden
E-mail: mailto:zhanna@pgia.ru

Abstract

The time dependent physicochemical model of the auroral ionosphere is presented. The model allows us to compute the altitude density profiles of both the excited and the neutral components of the ionosphere during electron precipitation. These are: O_2^+, N_2^+, $O^+(^4S)$, $O^+(^2D)$, $O^+(^2P)$, $O(^1D)$, $O(^1S)$, $N(^4S)$, $N(^2D)$, $N(^2P)$, NO, NO^+, N^+, $N_2(A^3\Sigma_u^+)$, $N_2(B^3\Pi_g)$, $N_2(W^3\Delta_u)$, $N_2(B'^3\Sigma_u^-)$ and electrons. The input model parameters are the auroral electron energy spectrum in the upper boundary of the ionosphere , densities of neutral components N_2, O_2, O and the temperature. The model is composed of 56 physicochemical reactions characterizing the redistribution of electron energy and effecting on the components densities mentioned above. The model is tested on the coordinated rocket and satellite measurements of the auroral event. The best, at present, fit between modeling and experimental data is achieved.

Introduction

The modeling of ionosphere processes occurring during high-energy particle precipitation, is important when investigating and understanding the physics of the disturbed polar ionosphere. These models should characterize both the processes of excitation of electronically vibrational state of ionosphere components by direct electron impact and the subsequent redistribution of the revealed electron energy due to initiated chemical reactions.

Model

a) Production rate

The auroral electrons, precipitated into the polar ionosphere, loose their energy in collision with atoms and molecules of the atmosphere. Thereby they initiate the complex of physicochemical processes such as excitation and ionization of the atmospheric gases, which determine disturbed ionosphere composition.

For the *E*- and F_1-region of the high- latitude ionosphere, where the transport processes of low-energy ionosphere components may be neglected, modeling includes the solution of the system of non-stationary continuity equations:

$$\frac{dN_{Yk}(h,t)}{dt} = Q_{Yk}(h,t) + Q^*_{Yk}(h,t) - L_{Yk}(h,t),$$

where: $N_{Yk}(h,t)$ is the concentration of the exited k state of the atmosphere gas Y, $Q_{Yk}(h,t)$ is the production rate of the exited k state of the atmosphere gas Y by direct impact, $Q^*_{Yk}(h,t)$ is the production rate of the exited k state of the atmosphere gas Y as results chemical reaction, $L_{Yk}(h,t)$ is the quenching rate of *Yk*-state component , *h* is the altitude, *t* is the precipitation duration.

In the aurora a significant contribution to excitation of many ionosphere components is made by direct impact. The calculation of the direct impact production rate is an important feature, which distinguishes this model from the others. For the model, the production rate of the atmosphere gases have been calculated using the energy coast method.The basis of this method is that the energy coast ε_{Yk} weakly depends on both the parameters and the penetration depth of an precipitating electron flux:

$$\varepsilon_{Yk} = \frac{W^Y}{Q_{Yk}},$$

where W^Y - the auroral electron energy spent for both excitation and ionization of atmosphere gas Y. The value W^Y can be calculate using the dissipation function of an electron flux in the Earth's atmosphere [Sergienko and Ivanov, 1993]

For a time-stationary electron flux, the relation between the altitude profiles of the production rate of atmosphere component and the initial electron spectrum $F(E)$ is as follows:

$$Q_{Yk}(h) = P_Y(h)\rho(h)\frac{1}{\varepsilon_{Yk}}\int_E \frac{E\,F(E)\left[1 - T_E(E)\right]}{R(E)}\lambda(E,\chi)dE$$

where: $P_Y(h)$ is a part of the electron energy spent for excitation of the atmosphere gas Y, $\rho(h)$ is atmospheric gas density, ε_{Yk} is the energy coast for the exited k state of the atmosphere gas Y, $T_E(E)$ is the albedo-flux that is the part of initial energy of the electron flux reflected by the atmosphere, $R(E)$ is the average range of electron in atmosphere, $\lambda(E,\chi)$ is the normalized energy dissipation function, χ is dimensionless parameter which is equal to distance from electron source to the altitude h .In calculations there were used the $T_E(E)$, $R(E)$, $\lambda(E,\chi)$ dependencies obtained in [Sergienko and Ivanov, 1993].

The production rate of the k state of the atmosphere gas Y by collisional reactions is

$$Q^*_{Yk}(h,t) = \sum_X \sum_Z N_X(h,t) N_Z(h,t) k_{XZ},$$

where $N_X(h,t)$ and $N_Z(h,t)$ are X- and Z- gas number densities, k_{XZ} is the rate coefficient of collision reaction between X and Z gases .

The quenching of Yk-state originates from both collision reactions and radiative transitions. The quenching rate is

$$L_{Yk}(h,t) = \sum_X N_{Yk}(h,t) N_X(h,t) k_{YX} + \sum_i A^{Yk}_{Yi} N_{Yk}(h,t)$$

where $N_{Yk}(h,t)$ is the Yk-state density, $N_X(h,t)$ is the X- gas number density, k_{YX} – is the rate coefficient of collision reaction between X and Y gases, A^{Yk}_{Yi} is the Einstein transition probability from the Yk level to the Yi level.

Thus the density of 14 ionosphere component N_2^+, O_2^+, $O^+(^4S)$, $O^+(^2D)$, $O^+(^2P)$, $O(^1D)$, $O(^1S)$, $N(^4S)$, $N(^2D)$, $N(^2P)$, NO, NO^+, N^+, $N_2(A^3)$ and electrons concentration are connected by 56 chemical reactions in the model. The reactions and the corresponding reaction rates are presented in Table.

b)The electro-vibrational kinetics of the N_2 triplet states

The collisional reaction between molecular nitrogen triplet state $N_2(A^3\Sigma_u^+)$ and the monatomic oxygen results the excitation of the $O(^1S)$ (in Table- reaction 56) which is the origin of the auroral green line. The $O(^1S)$ production rate depends on $N_2(A^3\Sigma_u^+)$ vibrational quantum number, so a correct estimation of the $N_2(A^3\Sigma_u^+)$ vibrational population is nessesary.

Table 1. The model physico-chemical reactions for aurora.

$\mathrm{N_2^+}$	$\mathrm{O^+(^2P)}$	$\mathrm{N(^4S)}$
$\mathrm{N_2^+ + O_2 \rightarrow N_2 + O_2^+}$	$\mathrm{O^+(^2P) + N_2 \rightarrow O^+(^4S) + N_2}$	$\mathrm{N(^4S) + O_2 \rightarrow NO + O}$
$\mathrm{N_2^+ + O \rightarrow N_2 + O^+(^4S)}$	$\mathrm{O^+(^2P) + N_2 \rightarrow N_2^+ + O}$	$\mathrm{N(^4S) + NO \rightarrow N_2 + O}$
$\mathrm{N_2^+ + O \rightarrow NO^+ + N(^2D)}$	$\mathrm{O^+(^2P) + O \rightarrow O^+(^4S) + O}$	$\mathrm{N(^2D)}$
$\mathrm{N_2^+ + NO \rightarrow N_2 + NO^+}$	$\mathrm{O^+(^2P) + O_2 \rightarrow O_2^+ + O}$	$\mathrm{N(^2D) + O_2 \rightarrow NO + O(^3P,^1D)}$
$\mathrm{N_2^+ + e \rightarrow N(^4S) + N(^2D)}$	$\mathrm{O^+(^2P) \rightarrow O^+(^2D) + h\nu}$	$\mathrm{N(^2D) + O \rightarrow N(^4S) + O(^3P,^1D)}$
$\mathrm{O_2^+}$	$\mathrm{O^+(^2P) \rightarrow O^+(^4S) + h\nu}$	$\mathrm{N(^2D) + NO \rightarrow N_2 + O}$
$\mathrm{O_2^+ + e \rightarrow O(^1S) + O(^1D)}$	$\mathrm{O^+(^2P) + e \rightarrow O^+(^2D) + e}$	$\mathrm{N(^2D) + NO \rightarrow N(^4S) + NO}$
$\mathrm{O_2^+ + N(^4S) \rightarrow NO^+ + O(^1S)}$	$\mathrm{O^+(^2P) + e \rightarrow O^+(^4S) + e}$	$\mathrm{N(^2D) + e \rightarrow N(^4S) + e}$
$\mathrm{O_2^+ + NO \rightarrow NO^+ + O_2}$	$\mathrm{O(^1D)}$	$\mathrm{N(^2D) \rightarrow N(^4S) + h\nu}$
$\mathrm{O_2^+ + N(^2D) \rightarrow NO^+ + O}$	$\mathrm{O(^1D) + N_2 \rightarrow O + N_2}$	$\mathrm{N(^2P)}$
$\mathrm{O^+(^4S)}$	$\mathrm{O(^1D) + O_2 \rightarrow O + O_2}$	$\mathrm{N(^2P) + O_2 \rightarrow NO + O(^1S,^1D,^3P)}$
$\mathrm{O^+(^4S) + N_2 \rightarrow NO^+ + N(^4S)}$	$\mathrm{O(^1D) + O \rightarrow O + O}$	$\mathrm{N(^2P) + O \rightarrow N(^2D) + O}$
$\mathrm{O^+(^4S) + O_2 \rightarrow O_2^+ + O}$	$\mathrm{O(^1D) \rightarrow O + h\nu}$	$\mathrm{N(^2P) \rightarrow N(^2D) + h\nu}$
$\mathrm{O^+(^4S) + NO \rightarrow NO^+ + O}$	$\mathrm{O(^1D) + e \rightarrow O + e}$	$\mathrm{N(^2P) \rightarrow N(^4S) + h\nu}$
$\mathrm{O^+(^2D)}$	$\mathrm{O(^1S)}$	$\mathrm{N(^2P) + NO \rightarrow N_2 + O}$
$\mathrm{O^+(^2D) + N_2 \rightarrow N_2^+ + O}$	$\mathrm{O(^1S) + O \rightarrow O + O}$	$\mathrm{N^+}$
$\mathrm{O^+(^2D) + N_2 \rightarrow NO^+ + N(^4S)}$	$\mathrm{O(^1S) \rightarrow O(^1D) + h\nu}$	$\mathrm{N^+ + O_2 \rightarrow O_2^+ + N(^4S,^2D)}$
$\mathrm{O^+(^2D) + O_2 \rightarrow O_2^+ + O}$	$\mathrm{O(^1S) \rightarrow O + h\nu}$	$\mathrm{N^+ + O_2 \rightarrow NO^+ + O(^1D,^1S)}$
$\mathrm{O^+(^2D) + O_2 \rightarrow O^+(^4S) + O_2}$	$\mathrm{O(^1S) + O_2 \rightarrow O + O_2}$	$\mathrm{N^+ + O_2 \rightarrow O^+(^4S) + NO}$
$\mathrm{O^+(^2D) + O \rightarrow O^+(^4S) + O}$	$\mathrm{O(^1S) + NO \rightarrow O + NO}$	$\mathrm{N^+ + O \rightarrow O^+(^4S) + N(^4S)}$
$\mathrm{O^+(^2D) + e \rightarrow O^+(^4S) + e}$		
$\mathrm{O^+(^2D) \rightarrow O^+(^4S) + h\nu}$	$\mathrm{N_2(A^3\Sigma_u^+) + O \rightarrow N_2 + O(^1S)}$	$\mathrm{NO^+ + e \rightarrow O + N(^4S,^2D)}$

The electro-vibrational kinetics of the N_2 triplet states is based on the following processes:

- the excitation by a direct electron impact: $N_2(X^1\Sigma_g^+, v') + e^* \rightarrow N_2(L_i, v'') + e$
- spontaneous transitions between N2 triplet states (radiative cascade and intersystem cascade): $N_2(L_i, v) \leftrightarrow N_2(L_j, v'') + h\nu$

energy transfer between triplet states by collisional reaction (intersystem collisional transfer): $N_2(L_i, v) + N_2(X^1\Sigma_g^+, v''=0) \rightarrow N_2(L_j, v') + N_2(X^1\Sigma_g^+, v'' \geq 0)$

energy redistribution between vibrational levels of N_2 triplet states(vibrational redistribition): $N_2(L_i, v) + N_2(X^1\Sigma_g^+, v''=0) \rightarrow N_2(L_i, v') + N_2(X^1\Sigma_g^+, v'' \geq 0)$

- radiative transitions: $N_2(L_i, v) \rightarrow N_2(X^1\Sigma_g^+ \vee L_j) + h\nu$
- inelastic collisions with O, N2, O2 atmosphere gases : $N_2(L_i, v) + Z \rightarrow N_2(X^1\Sigma_g^+) + Z^*$

Here L_i and L_j are triplet states, v- the vibrational quantum number.

The vibrational kinetics described above is based on the model from paper [Morill and Benesch, 1996]. In addition in this study the energy redistribution between the triplet states is taken into account.

The computation of the production rate for every vibrational level of the triplet state is reduced to the balance equation system solution. The balance equation can be written under the photochemical equilibrium as

$$Q_{L_i} q_v^{L_i} + \sum_{v'} N_{v'}^{L_i} A_{v'v}^{L_j L_i} + \sum_{v', L_j} N_{v'}^{L_j} [N_2] k_{v'}^{L_j L_i} + \sum_{v'} N_{v'}^{L_i} [N_2] k_{v'v}^{L_i L_i} =$$
$$\sum_{v'} N_{v'}^{L_i} A_{vv'}^{L_i L_j} + \sum_{v', L_i} N_{v'}^{L_i} A_{vv'}^{L_j L_i} + \sum_{v} N_{v'}^{L_i} [N_2] k_{v'v}^{L_i L_i} + \sum_{v'} N_{v'}^{L_i} [N_2] k_{v'v}^{L_i L_i} + + \sum_{Z} N_v^{L_i} [Z] k_v^{L_i Z}$$

where: $N_v^{L_i}$ is the population of vibrational level v of L_i triplet state, Q_{L_i} is the L_i triplet state production rate, $q_v^{L_i}$ is the Frank-Condon factor, $A_{vv'}^{L_i L_j}$ is the Einstein transition probability $L_i, v \rightarrow L_j, v'$, $k_{vv'}^{L_i L_j}$ is rate coefficients of collisional reaction with energy transfer from level L_i, v to level L_j, v', $k_v^{L_i Z}$ is the quenching rate coefficient of L_i, v level by atmosphere gas Z, $[Z]$ – density of atmosphere gas Z.

In order to determine the N_2 triplet state vibrational populations the linean system of 73 balance equations was made for 22 vibrational levels of $A^3\Sigma_u^+$state, 13 vibrational levels of $B^3\Pi_g$ state (this term predissociates beginning from 13 vibrational levels), 19 vibrational level of $W^3\Delta_u$ state, 14 vibrational levels of $B'^3\Sigma_u^-$state and 5 vibrational levels of $C^3\Pi_u$ state.

The triplet state production rates were computed similar to equation. The Frank-Condon factors and Einstein coefficients was taken from [Gilmore et al., 1992], energy costs –from [Ivanov and Kozelov, 2001], the rate coefficients of collisional reactions are from [Morill and Benesch, 1996; Kirillov, 2008; Tomas and Kaufman,1985]. For example, the vibrational populations of the triplet state for different altitudes. A comparison of the calculated population with the theoretical results from [Gilmore et al., 1992] and experimental estimated from [Vallance Jones A. and Gattinger, 1976; Eastes and Sharp, 1987] show a satisfactory agreement.

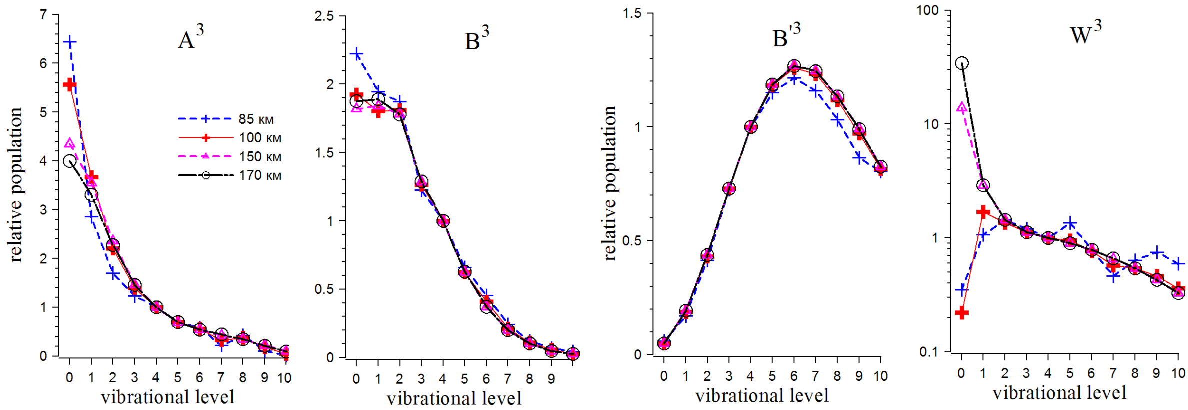

Fig1. The vibrational populations of the triplet state for different altitudes

Modeling results

The results of the coordinated rocket-satellite experiment were used to test the model [Ress et al., 1977; Sharp ey al., 1979] Measured in experiment were the auroral electron energy spectra, the N_2, O_2 and O densities within the height range 160-240 km, the density altitude profiles of N_2^+, O_2^+, O^+ and NO^+ ions, the altitude profiles of intensity of 5577 Å and 6300 Å of atomic oxygen, 3914 Å of the First negative system N_2^+, 3371 Å of the Second positive system N_2 and 3200 Å of the Vegard-Kaplan system. It should be noted that , according to the data of ground-based photometer measurements, during the rocket flight, there were no significant variations in the 3914 Å emission intensity for 20 minutes. This fact makes it possible to take the precipitation electron flux to be constant in the period when rocket measurements were made.

Based on the experimental conditions, calculations were performed with the assumption that electron precipitation lasted 20 minutes. The neutral atmosphere model (MSIS 90) was adapted to the observation conditions. At altitudes of more 160 km, the N_2, O_2 and O densities were adjusted to the densities measured in the experiment. Below 160 km, the densities of molecular and monatomic oxygen were corrected to obtain the best agreement between the calculated and experimental densities of the corresponding ions.

Figures 2 show the altitude profiles of the N_2^+, O_2^+, O^+, NO^+ ions and electrons densities, and the altitude profiles of 5577 Å, 6300 Å, 3914 Å ,3371 Å and 3200 Å emission intensities calculated by the model and measured in experiment.The horizontal lines show the measurement errors. It is seen, good fit between modeling and experimental data is achieved.

Thus, the model presented characterizes correctly the processes in the Earth upper atmosphere in aurora.

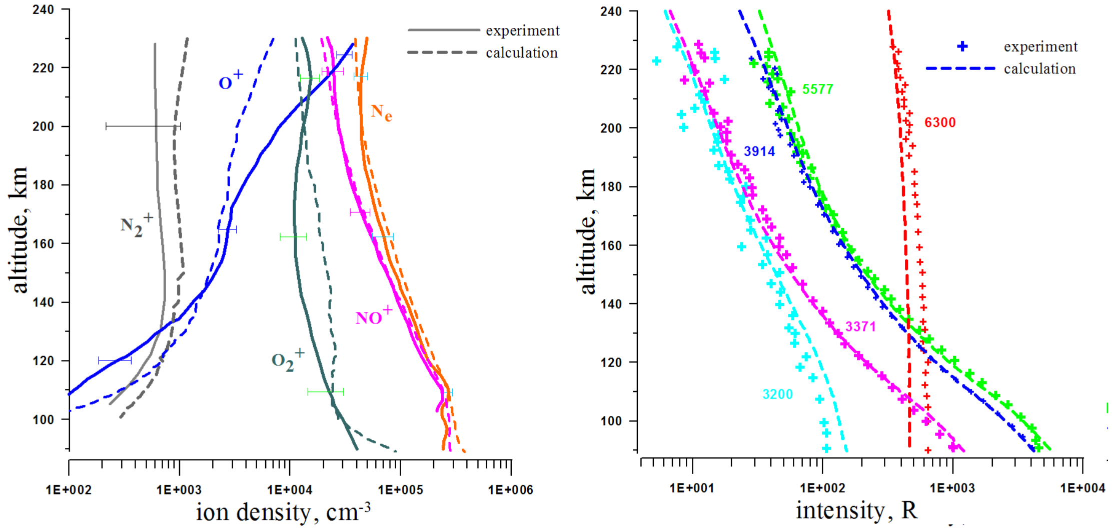

Fig. 2 The altitude profiles of the N_2^+, O_2^+, O^+, NO^+ ions and the electrons, and altitude profiles of 5577A, 6300A, 3914A, 3371A, 3200A emission intensities calculated by model and experimental measured.

Conclution

The time-depend model characterizing the processes of interaction between the main excited and ionized atmosphere components during auroral electron precipitations is presented. The model is based on the data available in scientific publications and contains 56 physicochemical reactions. The model is valid for *E* and *F1*-regions of the ionosphere because the effects of mass- transfer of excited ionosphere components are not taken account. Moreover, to correctly compute the intensities of N_2 band system emissions, physicochemical reaction characterized the energy redistribution between N_2 triplet state vibrational levels are included in the model.The model makes it possible to compute altitude density profiles of 14 ionosphere components and electrons concentration, time dynamics of the ionospheric component density and the altitude profiles of auroral emissions intensities including 5577Å, 6300A, 1NG system, 2PG system and Vegard-Kaplan system emissions.

References

Eastes R.W., Sharp W.E. Rocket-borne spectroscopic measurements in the ultraviolet aurora: The Lyman-Birge-Hopfield bands (1987). J. Geophys. Res., 92, no. A9, 10095-10100.

Gilmore F.R., Laher R.R., Espy P.J. Franck-Condon factors, r-centroids, electronic transition moments, and Einstein coefficients for many nitrogen and oxygen band systems (1992). J. Phys. Chem. Ref. Data., 21, no. 5, 1005.

Ivanov V.E., Kozelov B.V. Transport of electron and proton-hydrogen atom fluxes in the Earth atmosphere (2001). Apatity: Publ. Kola Science Center of RAS.

Kirillov A.S. The study of intermolecular energy transfers in electronic energy quenching for molecular collisions N2-N2, N2-O2, O2-O2 (2008). Ann. Geophys., 26, 1149-1157.

Morrill J.S., Benesch W.M. Auroral N2 emissions and effect of collisional processes on N2 state vibrational populations (1996). J. Geophys. Res., 101, no. A1, 261-274.

Rees M.H., Vallance Jones A. Time dependent studies of the aurora – II. Spectroscopic morphology (1973). Planet. Space. Sci., 21, no. 7, 1213-1235.

Rees M.H., Stewart A.I., Sharp W.E. et al. Coordinated rocket and satellite measurements of an auroral event. 1. Satellite observation and analysis (1977). J. Geophys. Res., 82, no.16, 2250-2261.

Sergienko T.I., Ivanov V.E. A new approach to calculate the excitation of atmospheric gases by auroral electron impact (1993). Ann.Geophys., 11, no. 8, 717–727.

Thomas J.M., Kaufman F. Rate constants of the reactions of metastable $N_2(A^3\Sigma_u^+)$ in v=0,1,2, and 3 with ground state O_2 and O (1985). J. Chem. Phys., 83, no. 6, 2900-2903.

Vallance Jones A., Gattinger R.L. Quenching of the N_2 Vegard-Kaplan system in aurora (1976). J. Geophys. Res.,81, no. 4, 497-450.

The effect of auroral electron precipitation on the effective recombination coefficient.

Dashkevich Zh.D., Ivanov V.E.

Polar Geophysical Institute, Apatity, Russia
E-mail: zhanna@pgia.ru

Abstract

The analysis of expected effect of the precipitated electron flux parameters on the effective recombination coefficient of electron α_{eff} is presented. It is demonstrate, that in the ionosphere *E*-region the α_{eff} value is related to thephysicochemical properties of environment. However, in the ionosphere *F1*-region the effective recombination coefficient becomes responsive from both the energy flux and the average energy of the precipitated electrons.

Introduction

Many researchers use the notion of the effective recombination coefficient when solving problems of modeling, interpretation and analysis of experimental data characterizing the structure of the ionosphere disturbed. The effective recombination coefficient determines a simple relation between the ionization rate and the electron density. It is considered that in the *E*-region and the *F1*-layer of the ionosphere the effective recombination coefficient is a parameter that is mainly determined by the neutral atmosphere composition and the rates of chemical reactions. Given in [Vickrey et al.,1982] and [Gledhill ,1986] are the recombination coefficient altitude profile approximations averaged over different experimental data:

$$\alpha_{\mathrm{eff}} = 2.5\times10^{-6}\,exp(-h/51.2) \quad \text{for } h > 85 \text{ km}$$

and

$$\alpha_{\mathrm{eff}} = 4.3\times10^{-6}\,exp\left(-2.42\times10^{-2}h\right) + 8.16\times10^{12}\,exp(-0.524h) \quad \text{for } h = 50\text{–}150 \text{ km} .$$

It is obvious that these approximations suggest that α_{eff} depends only on the physical-chemical properties of the medium.

Under the auroral conditions, the energy emitted by the precipitating high energy particles affects atmospheric processes. Therefore, the parameters of the initial electron flux can influence the altitude profile of the effective recombination coefficient.

Modelling

In the night high-latitude ionosphere, at an altitude of the *E*-region $h \approx 90 \div 140$ km) and the F1-layer ($h \approx 140 \div 200$ km), secondary electrons are generated via the O_2, N_2 molecules and O atom ionization produced by the precipitating high –energy electrons flux, while their loss occurs in the reactions of dissociative recombination of the O_2^+, N_2^+ and NO^+ ions:

$$N_2^+ + e \rightarrow N(^4S) + N(^2D)$$

$$O_2^+ + e \rightarrow O(^1S) + O(^1D)$$

$$NO^+ + e \rightarrow O + N(^4S,^2D)$$

The equation of the electrons continuity in photochemical approximation, i.e., disregarding the transfer members is:

$$\frac{dn_e}{dt} = Q_e - L_e ,$$

where n_e, Q_e, L_e are the concentration, the rate of electron generation and the rate of electron loss, respectively.

This approximation is valid for the altitudes of the E and F1 ionosphere, where the electron concentration change caused by physical-chemical processes, occurs faster than that caused by transfer processes.

In the case of a three–component model of the neutral atmosphere:

$$Q_e = q_{O_2} + q_{N_2} + q_O,$$

where q_O , q_{N_2} and q_O are the rates of O_2, N_2 and O ionization, respectively.

The rate of electron loss in dissociative recombination reactions is:

$$L_e = n_e(k_{O_2^+}[O_2^+] + k_{N_2^+}[N_2^+] + k_{NO^+}[NO^+]),$$

where $k_{O_2^+}, k_{N_2^+}, k_{NO^+}$ are the rate coefficients , $[O_2^+],[N_2^+],[NO^+]$ are the ion concentrations.

If the effective recombination coefficient (Brunelli and Namgaladze, 1988) is introduced:

$$\alpha_{eff} = \frac{k_{O_2^+}[O_2^+] + k_{N_2^+}[N_2^+] + k_{NO^+}[NO^+]}{n_e}.$$

the continuity equation can be written as:

$$\frac{dn_e}{dt} = Q_e - \alpha_{эф} n_e^2$$

In the stationary case:

$$\alpha_{eff} = \frac{Q_e}{n_e^2}$$

The characteristics of the of α_{eff} behaviour at different altitudes in the polar aurora region were studied on a time-dependent physico-chemical model presented in detail in [Dashkevich et al, 2017]. The model includes 56 phycico-chemical reactions characterizing the redistribution of the energy released during the electron flux precipitation in the ionosphere, of which 32 describe the processes of ionosphere ions generation and destruction. These reactions are presented in Table. The calculations were made using the MSIS-90 neutral atmosphere model and the Maxwell initial electron spectrum:

$$N(E) = N_0 E \exp(-E/E_0)/E_0^2,$$

where N_0 and E_0 are the initial electron flux and the characteristic energy, respectively.
The initial energy flux for this distribution is expressed as $F_0=2N_0E_0$. The characteristic energy E_0 varied within 0.5-20 keV; the energy flux varied within 1-15 erg cm^{-2}s^{-1}. These ranges of the initial parameters of precipitating electrons correspond to aurora whose green line intensity is in the interval of 0.5 to 20 kR.

Figure 1 shows the calculated dependence of the recombination coefficient on the ionization rate for altitudes ranging from 90 km to 200 km. It is obvious from the figure that within the altitude interval of 90-140 km, the effective recombination coefficient is practically independent of the ionization rate Q_e and, thus, of the electron flux energy released at this altitude.

However, as the altitude increases, α_{eff} decreases as the ionization rate increases. At altitudes of >140 km, the effective recombination coefficient calculated by formula, is no more a “universal” parameter indicating the physico-chemical properties of the medium.
It becomes dependent on the energy released at this altitude and, thus, on the type of the energy spectrum of the precipitating electrons.

Table. The physico-chemical reactions for ionosphere ions.

N_2^+	$O^+(^2P)$	N^+
$N_2^+ + O_2 \rightarrow N_2 + O_2^+$	$O^+(^2P) + N_2 \rightarrow O^+(^4S) + N_2$	$N^+ + O_2 \rightarrow O_2{}^+ + N(^4S,^2D)$
$N_2^+ + O \rightarrow N_2 + O^+(^4S)$	$O^+(^2P) + N_2 \rightarrow N_2^+ + O$	$N^+ + O_2 \rightarrow NO^+ + O(^1D,^1S)$
$N_2^+ + O \rightarrow NO^+ + N(^2D)$	$O^+(^2P) + O \rightarrow O^+(^4S) + O$	$N^+ + O_2 \rightarrow O^+(^4S) + NO$
$N_2^+ + NO \rightarrow N_2 + NO^+$	$O^+(^2P) + O_2 \rightarrow O_2^+ + O$	$N^+ + O \rightarrow O^+(^4S) + N(^4S)$
$N_2^+ + e \rightarrow N(^4S) + N(^2D)$	$O^+(^2P) \rightarrow O^+(^2D) + h\nu$	**$O^+(^2D)$**
	$O^+(^2P) \rightarrow O^+(^4S) + h\nu$	$O^+(^2D) + N_2 \rightarrow N_2^+ + O$
O_2^+	$O^+(^2P) + e \rightarrow O^+(^2D) + e$	$O^+(^2D) + N_2 \rightarrow NO^+ + N(^4S)$
$O_2^+ + e \rightarrow O(^1S) + O(^1D)$	$O^+(^2P) + e \rightarrow O^+(^4S) + e$	$O^+(^2D) + O_2 \rightarrow O_2^+ + O$
$O_2^+ + N(^4S) \rightarrow NO^+ + O(^1S)$	**NO^+**	$O^+(^2D) + O_2 \rightarrow O^+(^4S) + O_2$
$O_2^+ + NO \rightarrow NO^+ + O_2$	$NO^+ + e \rightarrow O + N(^4S,^2D)$	$O^+(^2D) + O \rightarrow O^+(^4S) + O$
$O_2^+ + N(^2D) \rightarrow NO^+ + O$	**$O^+(^4S)$**	$O^+(^2D) + e \rightarrow O^+(^4S) + e$
	$O^+(^4S) + N_2 \rightarrow NO^+ + N(^4S)$	$O^+(^2D) \rightarrow O^+(^4S) + h\nu$
	$O^+(^4S) + O_2 \rightarrow O_2^+ + O$	
	$O^+(^4S) + NO \rightarrow NO^+ + O$	

- reaction rate coefficients are given in paper [Dashkevich et al, 2017]

The altitude profile α_{eff}

The flux parameters effect on the effective recombination coefficient is demonstrated in Figure 2. The left panel presents the altitudinal dependences of α_{eff} ,calculated for different energy spectra (3) with the characteristic energy E_0 within the interval of 1-15 keV, and the energy flux of precipitating electrons F_0 =1 erg cm^{-2}s^{-1}.

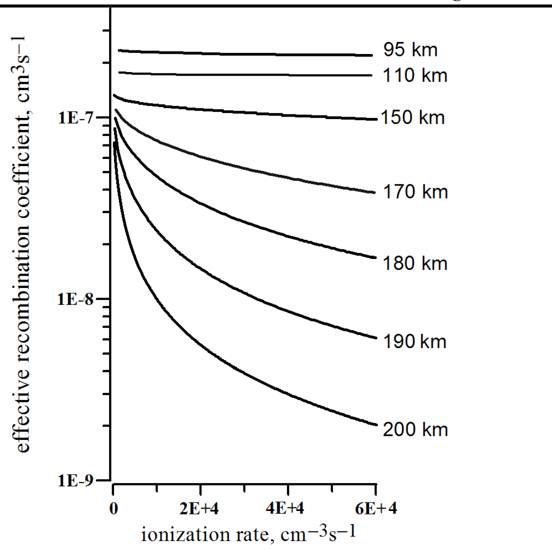

Fig. 1 The dependence of the dissociative recombination coefficient on the ionization rate for various altitudes

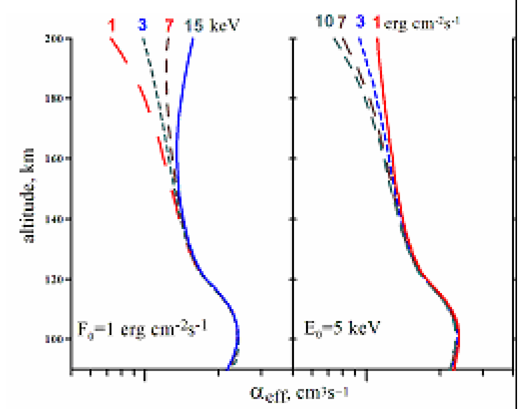

Fig. 2 The dependence of the dissociative recombination coefficient on electron flux parameters

The right panel shows the altitudinal dependences of α_{eff} , calculated for the initial energy spectrum of precipitating electrons with E_0= 5 keV and the energy fluxes within the interval of 1-10 erg cm^{-2}s^{-1}. The figure shows that at the ionosphere altitudes of over than 140 km, the influence of both E_0 and F_0 on the effective recombination coefficient value becomes more pronounced.For instance, at an altitude of 200 km, at the change of the characteristic energy E_0 from 1 to 15 keV, the relative variation of the effective recombination coefficient is as great as ~200% , and at the change of the flux value F_0 from 1 to 10 erg cm^{-2}s^{-1}, it is ~ 70% .

Interpretation

It is generally known that under thermodynamic equilibrium, the electron concentration is equal to the sum of the ion concentrations. In the E-region, the prevailing ions are O_2^+ and NO^+, while the O^+ and N_2^+ ions concentration is small. The recombination coefficient is approximately equal to the rate of O_2^+ and NO^+ ions deactivation.As the altitude increases in the F1-layer, the atomic oxygen prevails in the atmosphere composition and the propotion of O^+ ions in the ion composition increases. In this case the quantity of O^+ ions should be taken into account when estimating the electron concentration.Since the atomic oxygen ions are not subject to the deactivation reaction, greater the O^+ concentration in the F1-layer the lesser α_{eff} is. Since the number of ions in the aurora atmosphere depends on the amount of energy released, we expect the effective recombination coefficient to depend on the precipitating electron flux parameters.As the average energy of the electron flux increases, the maximum of the energy released is shifted to lower altitudes, and, as a result of it, the amount of ions generated at higher altitudes, decreases.At the same time, as the electron flux increases, the amount of the ions generated at a certain altitude increases. Hence, the effective recombination coefficient will decrease as the average electron energy increases.

Conclusions

The effect of the precipitating electron flux on the effective recombination coefficient value in the E-region and the F-layer of the ionosphere is studied.

The model calculations have shown that the effective recombination coefficient in the e-region of the ionosphere does not depend on the precipitating electron flux parameters and is mainly specified by the neutral atmosphere composition and rate coefficients of chemical reactions. However in the F-layer of the ionosphere, atomic oxygen prevails and a large number of O^+ ions generate. Since the O^+ ions do not take part in the process of the dissociative recombination, the effective recombination coefficient is no longer the parameter determined by the ionosphere composition. It depends on both the energy flux and the average energy of the precipitating electrons.

References

Dashkevich Zh.V., Ivanov V.E., Sergienko T.I., Kozelov B.V. Physicochemical model of the auroral ionosphere (2017). Cosmic research, 55, no. 2, 88−100..

Gledhill J.A. The effective recombination coefficient of electrons in the ionosphere between 50-150 km (1986). Radio. Sci., 21, no. A3, 399−408.

Vickrey J.F., Vondrak R.R., Matthews S.J. Energy deposition by precipitating particles and Joule dissipation in the auroral ionosphere (1982). J. Geophys. Res., 87, no. A7, 5184−5196.

Data on Solar Activity and Interplanetary Medium in WDC for STP

Sergeyeva N. [1], *Ishkov V.* [2], *Zabarinskaya L.* [1], *Nisilevich M.* [1]

[1] Geophysical Center RAS, Moscow, Russia
[2] Pushkov Institute of Terrestrial Magnetism, Ionosphere and Radio Wave Propagation RAS, Moscow, Troitsk, Russia
E-mail: n.sergeyeva@gcras.ru

Abstract.

Solar energy is the main cause of a variety of physical phenomena and processes in the Earth's atmosphere and magnetosphere. In recent years, experimental data on solar activity are widely used in the field of basic and applied scientific research. The long-term observations are the most valuable data. The World Data Center for Solar-Terrestrial Physics in Moscow, Russia has a representative collection of results of solar observations obtained by the world network of solar and astronomical observatories and devices installed on spacecrafts. The article describes the data on solar activity and interplanetary space which stored in the repository and is available on the website of the Center in free access.

Introduction

The latest research is based on a comprehensive analysis of large amounts of data from different fields of science and on the use of modern computer methods for processing, analyzing and interpreting data. The World Data Center for Solar-Terrestrial Physics (WDC for STP) in Moscow, Russia provides free access to a vast amount of data, to long series of observations, to a unique and representative collection of domestic and foreign data on solar-terrestrial and space physics.

WDC for STP in Moscow exists since 1956 when the World Data Center System of the International Council for Sciences (ICSU) was established with the purpose to collect data obtained as a result of implementation of the observational programs of the International Geophysical Year (IGY), held in 1957-1958. The WDCs ensured the accumulation of data, their long-term guaranteed storage and free access to data of scientists and researchers in accordance with specially developed rules [*CSAGI Guide* …, 1959].

WDC System was retained after the end of IGY. The results of various international and national geophysical projects and programs, the results of observations at stations and observatories, ships, drifting stations, aircrafts, satellites, etc. were collected and stored in WDCs for more than 50 years [*Kharin E.P, Sergeyeva N.A.,* 2007]. After the International Polar Year (2007–2008) it became clear that the old system was not able to respond fully to modern data needs. Since 2009 according to the decision of the ICSU a new structure - World Data System (WDS), is formed in order to consolidate all the accumulated multidisciplinary data in a single structure, to develop methods and technologies of data storage that will ensure the safety of information and access to data for use now and in the future. WDC for STP became a regular member of the ICSU-WDS in 2012. It is guided by principles of the WDS Constitution and fully supports the WDS Data Policy [*World* …, 2015].

WDC for STP has a website in English and Russian with a brief description of the Center's activities, catalogues of data availability, information for users and access to data on all disciplines (fig.1). The repository of the Center contains historical and current results of global observations that include data on the Earth's magnetic field (records of magnetic field variations, one minute and hourly mean values of magnetic field elements and geomagnetic activity indices, data on magnetic storms and pulsations), ionospheric phenomena (results of radio sounding of the ionosphere from the Earth's surface and from satellites, data on the absorption of radio waves by the ionosphere and its structural characteristics, the results of measurements of radio noise) and cosmic rays (data on solar and galactic protons, neutrons,

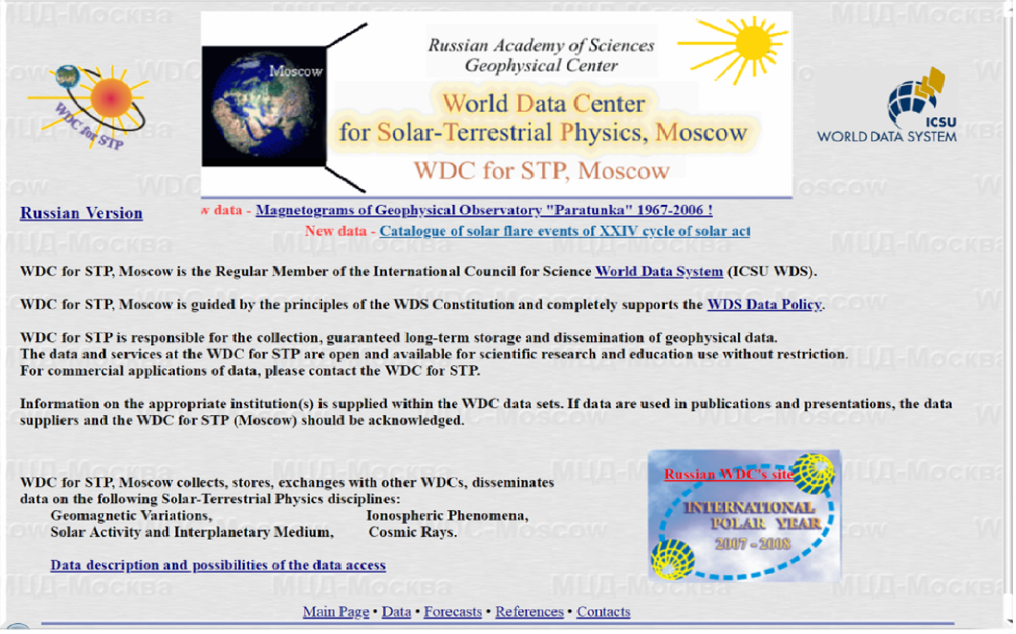

Fig.1 The Main Page of the World Data Center for Solar-Terrestrial Physics website http://www.wdcb.ru/stp/index.en.html

mesons, data from neutron monitors, meson telescopes and ion chambers). The data on solar activity and interplanetary magnetic field are given at the separate section.

Data on Solar Activity

The main data repository of the WDC for STP contains offline historical data (hardcopy documents: tables, solar maps and so on) on phenomena that occur on the Sun. These data were obtained at the world network of 117 solar and astronomical observatories and cover the period from 1957 to the beginning of the 1990s. The data include a wide range of routine solar measurements and events such as sunspot numbers and sunspot groups, their positions and areas, calcium plages, solar magnetic fields, mass ejection from the Sun, prominences and filaments from observations in the Hα-line (656.3nm). Additionally, synoptic and photographic charts of the Sun, the results of optical observations of the corona, observations of flares in the line Hα and patrol observations of solar activity, measurements of the total flux of radio emission from the Sun, observations at fixed frequencies of outstanding phenomena on the Sun and radio bursts, radio east-west scans of solar disk, radio spectrograms of solar events are available.

Simultaneously with the exchange of observational data, the World Data Centers exchanged publications containing special data compilations and information of interest to researchers. Such publications included the "Solar Geophysical Data" distributed monthly by the National Geophysical Data Center of the USA from 1955 to 2009 and UAG (Upper Atmosphere Geophysics) data reports distributed on an irregular basis from 1968 to 1996 by the same center. The WDC for STP also published series entitled "Materials of the World Data Center B" with data sets on various manifestations of solar activity.

Since the emergence of devices with a computer registration, the WDCs began to exchange data in the form of data files accompanied by a format description and explanatory text, recorded in all the communication media such as magnetic tapes, floppy disks, CD-disks. In the 1980s the unified international formats for data in machine-readable form were adopted to facilitate the exchange and use of information within the scientific community. A large body of historical data stored in the WDC for STP consists of data sets in machine-readable form (electronic form). All of them are available on the Center's website.

New data on solar activity were obtained from instruments that were mounted on satellites: observations of solar radiation fluxes in the Lyman-alpha line from the satellite Explorer during the period 1982-1989, observations in the ultraviolet band from the satellite Explorer-E in 1977-1980, observations in the soft X-ray band (1÷8 Å) from the satellite Solrad (1968-1974) and geostationary satellite GOES. The measurement of the Earth's radiation above the Earth's atmosphere by a cavity pyrheliometer mounted on the Nimbus-7 satellite (1978-1989) and measurements of the radio emission from the Sun aboard of the orbital station Solar Maximum Mission (1980-1987) are kept by the WDC for STP. A significant datasets of hourly mean solar wind parameters and interplanetary magnetic field values were gathered from several satellites by Dr. J.H King at the NASA's Goddard Space Flight Center and were provided to the WDC for STP.

In parallel, the ground-based observations in machine-readable form have appeared which were stored in the Center and currently available for use. This is other information collection:

The values of the coronal solar activity index, which characterizes the total radiation energy of the outermost atmospheric layer of the Sun (corona) at 530.3 nm, obtained from the photometric patrol observations at 8 ground stations in 1964-1986.

Data on the relative numbers of sunspots in the international (Zurich) system: maxima and minima, daily, monthly, annual and smoothed values for the entire time of observations. Daily reports on the number of spots from the Greenwich Observatory (1874-1982), astronomical observatories Rome (1958-1990) and Taipei observatory (1964-1992). Summaries of sunspot groups from the astronomical observatories of Mount Wilson (1967-1989), Rome (1978-1990), Greenwich (1875-2018), Catania (1978-1987) and the US Sun Service (1981-2018).

Data on solar flares from observatories in the strongest hydrogen spectral line H-alpha (1938-1994), a complete list of solar flares from patrol observations (1955-1994) and a compilation flare index calculated for all major flares over the period 1955-1980.

Measurements of radio noise at ground stations (1960-1989) and spectral radio noise (1967-1989).

The results of calcium flocculi observations (chromospheric brightenings) obtained at solar observatories Hale (1979-1981), Big Bear (1981-1987) and McMath (1942-1979).

Measurements of the solar magnetic field (Sun as a Star), summed over the solar disk (the intensity of the magnetic field in μT); each value is the weighted average of all measurements during the day. This is data of the Crimean Astrophysical Observatory from 1968 to 1976 and the Stanford Solar Observatory from 1975 to 1989.

The density of solar radiation recorded at a frequency of 2,800 MHz by a radio telescope near Ottawa (1947-2018) in the form of tables containing observed, corrected and absolute flux values averaged over day, month and year intervals. These data were prepared by Herzberg Institute of Astrophysics, Canada.

Most of the data collections included in the modern funds of WDC for STP are being completed with new information; new digital collections are being created. Currently, the most frequently-used data are freely available at the "Solar Activity and Interplanetary Medium" section (fig.2) of the WDC for STP website.

One of the most popular parameters (indices) of solar activity is the relative sunspot number (the Wolf number). The website WDC for STP contains the old version of data on sunspot numbers such as daily total number of sunspots from 1818, the average monthly number of sunspots from 1749 and the average annual number of sunspots from 1700. Since July 1st 2015, the original sunspot number data (version 1.0) have been replaced by a new entirely revised data series (version 2.0) and can be freely downloaded from the website of the Royal Observatory of Belgium (WDC- SILSO) http://sidc.oma.be/silso/newdataset. On this

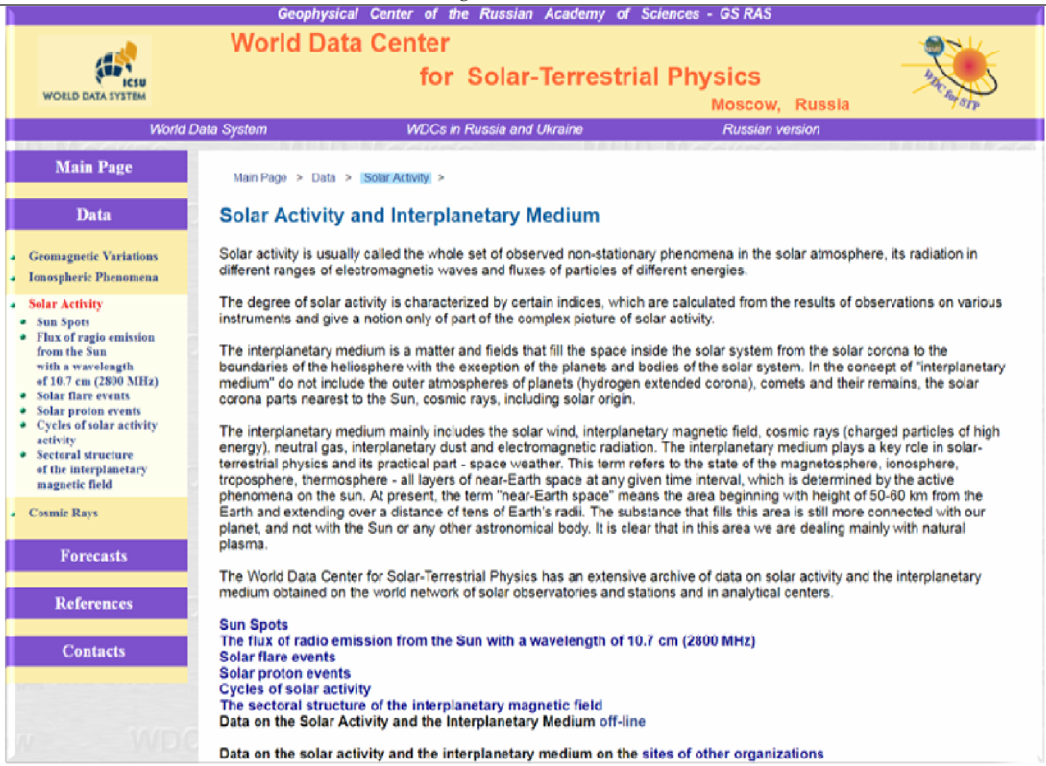

Fig.2 Section “Solar Activity and Interplanetary Medium” on the WDC for STP website *http://www.wdcb.ru/stp/solar/solar_activity.html*

occasion, the data are presented in a new array of files, containing additional values that were not present in the original series.

Another important index of solar activity for many studies is the radio emission of the Sun with a wavelength of 10.7 cm (2800 MHz), which correlates well with the change in solar activity on the entire visible disk of the Sun. The website provides access to series of daily, monthly and yearly values of the radio emission flux measured by the solar radio telescope in three ways: observed, corrected for changing the Earth-Sun distance and reduced to the mean distance and absolute values. These data are published by the Dominion Radio Astrophysical Observatory (British Columbia, Canada).

Website visitors are able to easily access the table of solar activity cycles which includes the year of the beginning, maximum and minimum of each cycle, the relative sunspot numbers smoothed over 13 months, the cycle duration and the duration of the rise and fall brunches, as well as the description of the character features of the 24th solar cycle. It has also published the catalogues of solar flare events for the XXIII and XXIV solar cycles with an X-ray class greater M1. The solar flares show the power of the corresponding magnetic fields, and the behavior of the flare parameters in the 11-year cycle is of considerable interest. The catalogue contains the time parameters for each flare, X-ray class and optical importance of the flare event (observed in the Hα line), integrated X-ray flux from the start, coordinates (heliographic latitude, central meridian, Carrington longitude), solar active region number, peak radio flux at selected frequencies, dynamic radio bursts, the coronal emission of matter, the time and maximum energy of hard X-ray radiation, the maximum flux of solar protons, and the accompanying dynamic phenomena in the optical range.

The website contains electronic versions of six catalogues for solar proton events (SPE) and their energy spectra. The catalogues were prepared by professionals in the field of solar-terrestrial physics, edited by Yu.I. Logachev. The catalogues include unified data about events with proton generation, for which the maximum proton flux with energy $Ep > 10$ MeV exceeded the value 1 $cm^{-2}\cdot s^{-1}\cdot ster^{-1}$ (pfu), and contain information about the sources of particles and the electromagnetic radiation associated with this event over the available observation range. The catalogues cover the entire period from 1970 to 2008. The integrated energy spectrum, tables and charts of the proton fluxes (for SPE from 1996 to 2008) at the maximum of the temporal intensity profile are given for each event. Measurements of proton fluxes have been taken from various spacecrafts.

The sectoral structure data of the interplanetary magnetic field include tables containing daily determinations of the polarity direction for the interplanetary magnetic field - from the Sun or to the Sun (sector sign), according to Stanford University (1947-1975), and measurements at the Vostok and Thule observatories (1974-2010); the table compiled by L. Svalgaard, of the most probable times of passage of the sectoral boundary, when the polarity of the interplanetary magnetic field reverses, and the table and the corresponding charts containing the azimuthal angles of the interplanetary magnetic field calculated on the basis of the daily average hourly values of the components X and Y according to the Goddard Space Flight Center.

Development of data management system in the WDC for STP

The WDC for STP constantly works to improve the methods of storage, systematization and distribution of large arrays of geophysical data and information, providing them with free network access. The Center's website (http://www.wdcb.ru/stp/index.html) existing since 1995 is a part of the global distributed system of information resources on geophysics. The "links" system provides the flexibility to anywhere access to data and information available in other data centers, institutions, scientific organizations and researchers.

In 2014 the project "Preservation of old data" started in the WDC for STP with the aim to transfer data from paper medium to electronic form, to increase data sets in electronic form, to prevent the loss of valuable historical data, and, lastly, to provide free on-line access to them for more efficient use.

The second important project entitled "Earth Science DataBase" (ESDB) is carried out in the Center with the purpose of creating a modern system for registering, publishing and citing geophysical data with the assignment of the digital object identifier (DOI) [*Ishkov V. et al.*, 2017]. The attitude of the international community towards the data, their distribution, citation and documentation has changed significantly. Maintaining and constantly updating data is seen as a full-fledged result of scientific research to be disseminated and cited in the same way as other research information resources: journals, articles, books. Each data set with the assigned DOI index becomes more accessible for searching, identifying and citing.

Data registration and publication with the assignment of DOI takes place through the Crossref agency. The central repository of the ESDB was created. It contains the metadata collections of all registered databases and datasets, including complete data descriptions, information about authors and producers, providers and data publishers and other information that may be useful to users. For each registered object, a landing page with complete information on the database/dataset including the URL for downloading data and the citation pattern was created.

For example, an individual digital object identifier was assigned to the entire database of 6 catalogues for solar proton events and to each catalogue separately. The landing pages were created for the database and each catalogue (fig.3). These solar database and datasets published on the WDC website for STP are available at the address for "download" the data on the corresponding landing page.

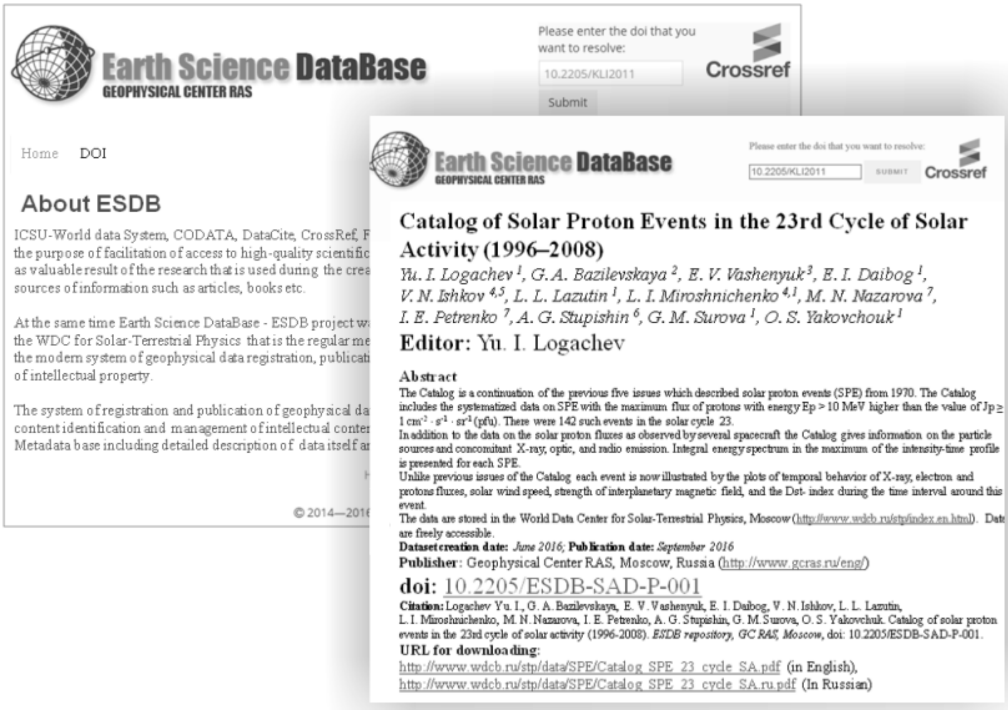

Fig. 3 Main page of the ESDB project central repository and landing page for the Catalog of Solar Proton Events [Logachev Yu., et al., 2016] to which DOI was assigned.

Conclusions

The World Data Center for Solar-Terrestrial Physics preserving historical data sets, supplementing them with new observational results, improving data management system, is working to ensure that scientists have simple and convenient access to updated historical and modern datasets. The Center believes it can raise the value of scientific data and create conditions for more efficient utilization of them.

Acknowledgment

This work was carried out within the framework of scientific research 0145-2016-0005 of the state task for the Geophysical Center RAS.

References

Constitution of the International Council for Science World Data System (ICSU-WDS) (pdf) http://www.icsu-wds.org/organization/constitution_and_bylaws/constitution.

CSAGI Guide to World Data Centers (1959). Annals of the International Geophysical Year, vol. 7, 139̃374. New York: Pergamon Press.

Ishkov V.N., L.P. Zabarinskaya, N.A. Sergeyeva (2017). Modern representation of databases on the example of the Catalog of solar proton events 23 cycle of Solar activity, Geomagnetism and Aeronomy, 57, no. 6, 684–690, DOI: 10.1134/S0016793217060044.

Kharin E.P., N.A. Sergeyeva (2007). The Golden fund of the Earth sciences. Earth and Universe, 4. 66÷71, (in Russian).

Logachev Yu.I., G.A. Bazilevskaya, V.N. Ishkov et al. (2016). Catalogue of Solar Proton Events in the 23rd Cycle of Solar Activity (1996÷2008), DOI: 10.2205/ESDB-SAD-P-001-RU.

World Data System (WDS) Data Sharing Principles (2015). WDS Scientific Commitee. DOI: http://dx.doi.org/10.5281/zenodo.34354.

Efficiency Study of Electron Resonance Acceleration by a Wave Packet In Space Plasma

Shkevov R. [1], *Erokhin N.S.* [2], *Loznikov V.M.* [2], *Zolnikova N.N.* [2], *Mikhailovskaya L.A.* [2]

[1] Space Research and Technology Institute, Bulgarian Academy of Sciences, Sofia, Bulgaria
[2] Space Research Institute, Russian Academy of Sciences, Moscow, Russia
E-mail: shkevov@space.bas.bg, nerokhin@mx.iki.rssi.ru

Abstract

The study of strong surfatron acceleration of electrons by an electromagnetic wave packet in space plasma is conducted by means of numerical analyses. The second order nonlinear, nonstationary differential equation for the wave phase on the accelerated electron trajectory is numerically solved. The electron initial energy and wave packet propagation speed are assumed as low relativistic. The efficiency of the surfatron acceleration mechanism is evaluated on the basis of the calculated energy growth throughout the whole resonance acceleration process. In this case the final energy of a low relativistic electron at resonance acceleration increases by minimum of three orders of magnitude. The momentum dynamics for the time interval of numerical calculations is shown. Some interesting cases of the charged particle strong surfatron acceleration are analyzed. Conclusions about the electron surfatron acceleration mechanism's efficiency and the particle's energy rise are drawn.

Introduction

The present work is a research focused on the charged particles' resonant acceleration processes studied in the natural conditions of space plasmas. Streams formation mechanisms of relativistic and ultra-relativistic particles are one of the actual tasks of space plasma physics. One effective mechanism of generation of ultra-relativistic particles flow is the surfatron acceleration of charged particles by electromagnetic waves, described earlier in [*Bulanov and Sakharov,* 1986, *Chernikov, et al.,* 1992, *Dieckmann and Shukla*, 2006, *Erokhin, et al.,* 1987, 1989, 2007*, 2010, Gribov, et al.,* 1985, *Itin, et al.,* 2000*, Joshi,* 1984; *Katsouleas and Dawson,* 1983; *Kichigin,* 1995; 2001, *Loznikov and Erokhin,* 2010, *Neishtadt, et al.,* 2009, *Sitnov,* 1988, *Takeuchi et al.,* 1987, *Vasiliev et al.,* 2012]. An efficiency of the surfatron acceleration of electrons with low relativistic initial energy in the presence of a weak constant magnetic field is analyzed. For the problems of cosmic rays generation in astrophysics, the occurrence of variations of cosmic rays fluxes, their dependence on space weather, as well as the correct interpretation of the observation data are of great interest. The correct estimations of the accelerated particles' parameters, their energy spectra, and acceleration region typical scales require a detailed analysis of the charged particles' capture conditions in the surfatron acceleration mode. The analysis of favorable conditions for the charged particle captures by electromagnetic waves as well as the investigation of particle acceleration efficiency under the influence of finite amplitude spatially localized waves packet is a difficult enough task. The task is multiparametric and revealing the main features of the charged particles surfing on the waves packets in space plasma, a very large volume of numerical calculations is needed. This kind of analyses significantly improves the understanding on energy transfer from the wave packet to the charged particle under resonance interactions.

Theoretical background and basic equations

The problem discussed considers resonance wave-particle interactions of the electromagnetic wave packet, which propagates across a weak constant magnetic field in quiet space plasma. The wave packet possesses a smooth Lorentz envelope, low relativistic phase speed and the electrons also have low-relativistic initial energies. The surfatron acceleration of charged particles due to the realization of Cherenkov resonance in magnetoactive space plasma is possible when the electromagnetic wave is of p-polarization and the wave phase speed is below the speed of light in vacuum. It is assumed that the electron energy and the waves packet speed are low relativistic and the wave amplitude is above a certain threshold value. Once the electron is captured by the wave, the cyclotron rotation of charged particles is suppressed, and the particle in average is moving in an accelerating wave field an occurrence due to the effective potential well for the trapped particle. For the discussed cases, suitable electromagnetic fluctuations are waves with frequencies close to the plasma upper hybrid resonance. In the case of transverse propagation of electromagnetic wave with p-polarization [*Erokhin, et al.,* 1987, 1989] for the square of plasma refractive index $N^2 = (c\ k/\omega)^2$ on the upper hybrid resonance frequency we have:

$$N^2 = 1 - [v\,(1 - v)] / (1 - u^2 - v) \equiv \varepsilon_f$$

where $u = \omega_{He}/\omega$, $v = (\omega_{pe}/\omega)^2$, ε_f is determined by the plasma dielectric permittivity components, $\omega_{He} = eH_0/m_e\,c$ - gyro frequency of the non-relativistic electrons in the plasma, $\omega_{pe} = (4\pi e^2 n_0/m_e)^{1/2}$ – electron Langmuir frequency, n_o – plasma density. The external magnetic field is directed along the z axis: $H_0 = H_0\,.e_z$.

In this paper, we consider the case $u^2 << 1$. Then the phase velocity of the electromagnetic wave is less than the velocity of light in vacuum for the next area of the parameter v: $1 - u^2 < v < 1$. The capture in surfing mode occurs when the wave field is above a critical value σ_c, i.e.:

$$\sigma \equiv e\,E_0 / m_e\,c\omega > \sigma_c = u\,\gamma_p = u / (1 - \beta_p^2)^{1/2},\ \beta_p = \omega / c\,k. \tag{1}$$

According to the calculations performed previously, vortex components of wave fields E_y, H_z can be safely ignored. Nonlinear effects from the interaction of the accelerating wave with the plasma are insignificant, if the wave amplitude E_0 is significantly lower than the field of relativistic nonlinearity, i.e. on the condition $\sigma^2 << 1$ [*Erokhin, et al.,* 1987*,* 1989*,* 2007, 2010, *Shkevov, et al.,* 2013, 2016, 2017].

Let us consider the relativistic equations of motion of electrons with mass m_e in the field of an electromagnetic wave $E_x = E_0 \cos\Psi$, $\Psi = \omega t - kx$. It is supposed that $\boldsymbol{\beta} = \mathbf{v}/c$, $\tau = \omega t$ dimensionless time, $\xi = \omega x\ /c$. Then $\boldsymbol{\beta} = \mathbf{v}/c$, $\beta_x = \beta_p\ (1 - d\Psi/d\tau\ )$. For the electrons with $J = \gamma\cdot\beta_y - u\cdot\beta_p\cdot(\tau - \Psi\ )$, transverse momentum is $\gamma\,\beta_y = J + u\,\beta_p\ (\ \tau - \Psi\ ) \equiv g$. The relativistic factor of the electron is equal to:

$$\gamma = (\ 1 + h^2 + g^2\ )^{1/2} / (1 - \beta_x^2)^{1/2}. \tag{2}$$

The electric field of a spatially localized wave packet with Lorentz envelope has the form:

$$Ex\ (x, t) = \{\ E0 / [\ 1 + \zeta 2 / L2\ ]\ \}\cos(\omega 0\ t - k0\ x), \tag{3}$$

where $\zeta = x - v_g\,(k_0)\ t$, $L = 1/k_p$, v_g – group velocity, L – full width at half maximum of the wave packet. The propagating group velocity of the wave packet is $2k_p$. The typical packet size in k-space is $\beta_g = v_g / c << 1$, β_g – dimensionless wave packet group speed.

For the wave phase on the particle trajectory, using (1), (2) and (3) we have the equation [*Katsouleas and Dawson,* 1983, *Erokhin, et al.,* 1987, 1989, *Kichigin,* 1995, *Shkevov, et al.,* 2013, 2017]:

$$\gamma\,\beta p\ d2\ \Psi / d\tau 2 - \{\ \sigma / [\ 1 + (\ \tau - \Psi\ )2/\ \rho 2\ ]\ \}\ (1 - \beta x2\ )\cdot\cos\Psi - u\ \beta y = 0, \tag{4}$$

where $\rho = \omega L / c >> 1$, $E_x\,(x, t)$ is given above, $\beta_{p0} = \omega_0 / c\ k_0$, $r_0 = \gamma\,\beta_y$ is the initial particle momentum component along wave front and the integral of motion $J = \gamma\,\beta_y + u_0\,\beta_{p0}(\Psi_0 - \tau)$ is taken into account. There exists second integral of motion $\gamma\,\beta_z = const \equiv h$. The electron velocity component β_x in (4) is given by the expression $\beta_x = \beta_{p0}\ [1 - (\ d\Psi_0 / d\tau\ )\ ]$.

Numerical calculations and discussion

The numerical experiment on surfatron acceleration of low relativistic electrons is completed using one set of initial parameters. The calculations are performed for an initial position of the particle chosen in the center of the wave packet structure. This position corresponds to $\Psi_0 = \Psi(0) = 0$ where the wave packet electric field amplitude has the maximum value. The calculation maximum value. The calculations length is τ max = 70k (where 70k τ = 7.104 τ). For the different values for the wave packet phase in range of -3.1 to +3.1. Thus 70 calculations tasks were formed, where in each case the trapping possibility is assessed.

In this paper calculations are presented with the following set of initial parameters of the charged particle: u = 0.20; β = 0.25; h = 0.20; g = 0.21; a = 0; ρ = 70000; $\sigma = u\,\gamma_p = 1.65\,\sigma_c$; $\Psi_0 = \Psi(0) = 0$. Such parameters set corresponds to a low relativistic initial energy of the electron with initial relativistic factor of γ (0) = 1.075 and the electron initial energy is $E_{ini} \cong$ 0.55 MeV.

The calculations results are presented in Table 1, where τ_c is the moment of the particle's capturing, and the number in the cell indicates the time periods. The $\delta\Psi_0$ is the value of the wave packet phase and the first point ($\delta\Psi_0 = \Psi$ (0) = 0) corresponds to the particle position centered in the wave packet, as was mentioned above. The wave packet electric field amplitude has to be above σ_c - $\sigma \geq \sigma_c$, (the surfatron acceleration below the line $\sigma < \sigma_c$ is impossible).

Table 1. Numerical calculations results for Ψ(0) = 0 and the set of initial parameters corresponds to the low relativistic initial energy of the electron with γ(0) = 1.075 and $E_{INI} \cong$ 0.55 MeV, $E_{ini} \cong$ 0.55 MeV.

$\delta\Psi_0$	-3.1	-3.0	-2.9	-2.8	-2.7	-2.6	-2.5	-2.4	-2.3	-2.2
τ_c	0	0	0	19741	15732	6181	9417	27895	3535	16573
$\delta\Psi_0$	-2.1	-2.0	-1.9	-1.8	-1.7	-1.6	-1.5	-1.4	-1.3	-1.2
τ_c	3003	11578	17924	33662	3221	10447	13343	27706	19198	3403
$\delta\Psi_0$	-1.1	-1.0	-0.9	-0.8	-0.7	-0.6	-0.5	-0.4	-0.3	-0.2
τ_c	5011	8693	20675	20212	21529	3653	11614	> 70k	23938	10238
$\delta\Psi_0$	-0.1	-0.05	-0.02	-0.01	0	0.01	0.02	0.03	0.05	0.1
τ_c	1058	2836	10684	25605	3451	21183	1491	> 70k	20636	12235
$\delta\Psi_0$	0.2	0.3	0.4	0.5	0.6	0.7	0.8	0.9	1.0	1.1
τ_c	0	0	0	0	0	0	0	0	0	0
$\delta\Psi_0$	1.2	1.3	1.4	1.5	1.6	1.7	1.8	1.9	2.0	2.1
τ_c	0	0	0	0	0	0	0	0	0	0
$\delta\Psi_0$	2.2	2.3	2.4	2.5	2.6	2.7	2.8	2.9	3.0	3.1
τc	0	0	0	0	0	0	0	0	0	0

According to the results presented in the Table 1, the 70 different calculations cases are completed. Analysis of the Table 1 shows that in two cases no particle trapping (marked with > 70k), in thirty-five cases electron initially performs cyclotron rotation with subsequent strong acceleration (the number points capturing periods moment) and in thirty-three cases charged particle is trapped immediately (marked with 0). The approximate value of total particle capturing probability is 97 %. Further analysis of Table 1 showed that two cases when there is no electrons trapping and marked with (> 70k) ≈ 3 % (in grey); thirty two cases when electrons are immediately trapped ≈ 47 % of calculated cases (dark blue) and thirty six cases (light blue) with initial particle cyclotron rotation and subsequent strong surfatron acceleration ≈ 50 %.

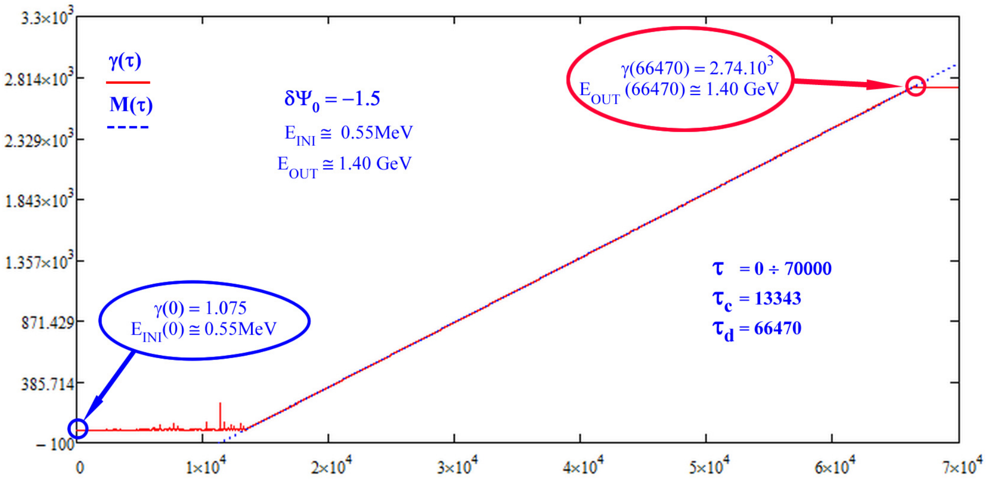

Fig.1 Charged particle relativistic factor $\gamma(\tau)$ and its analytical approximation $M(\tau)$ for $\delta\Psi_0 = -1.5$. Particle is accelerated from $\gamma(0) = 1.075$ up to $\gamma(66470) = 2.74.10^3$ and $E_{OUT} \cong 1.40$ GeV.

In earlier works [*Erokhin, et al.,* 1987, 1991*, Loznikov, et al.,* 2010*, Shkevov, et al.* 2013*, 2016,* 2017] was shown that the most effective particle acceleration takes place in the case when particle capture occurs on the left side of the wave packet, but from the other hand, the particle capture probability is higher when the charged particle is situated in the center of the wave packet structure, similar to the problem discussed in current paper.

For the correct estimation of the particle energy growth, it is needed to calculate the relativistic factor value before and after surfatron acceleration period. As it was mentioned above, electron initial relativistic factor is $\gamma(0) = 1.075$ from where is received $E_{INI} \cong 0.55$ MeV resulting electron initial energy. Dynamics of the relativistic factor $\gamma(\tau)$ analysis of all cases showed that for the case $\delta\Psi_0 = -1.5$ particle is accelerated and energy growth is $\gamma(66470) = 2.74.10^3$, $E_{OUT} \cong 1.40$ GeV. The higher efficiency occurs in case with $\delta\Psi_0 = +1.4$; $\gamma(57280) = 2.957.10^4$ and E_{OUT} max $\cong 1.51$ GeV.

Fig.1 illustrates the particle relativistic factors dynamics and his analytical approximation for $\delta\Psi_0 = -1.5$. In this case the capture moment is $\tau_c = 13343$ and charged particle is accelerated up to fly out from the potential well moment $\tau_d = 66470$. For this acceleration period the electron reach the value of the relativistic factor $\gamma(66470) = 2.739.10^3$, $E_{OUT} \cong 1.40$ GeV and the coincidence between proposed function of analytical approximation $M(\tau)$ is accurate up to the third sign $M(66470) = 2.742.10^3$ at the acceleration period.

The most effective acceleration case is presented on the Fig. 2. The higher calculated value for the $\gamma(\tau)$ is received at $\delta\Psi_0 = +1.4$. The particle is trapped immediately $\tau_c = 0$ and at satisfied Cherenkov resonance conditions and the strong acceleration is applied to the electron up to detrapping moment at $\tau_d = 56280$. At this acceleration period, electron relativistic factor from $\gamma(0) = 1.075$ and $E_{INI} = 0.55$MeV reach value of $\gamma(56280) = 2.98.10^3$, corresponding to $E_{OUT} \cong 1.51$ GeV. The resulting electron energy growth in the second discussed case estimated to $E_{RES} \cong (E_{OUT} - E_{INI})$ eV $\cong (1.51.\ 10^9 - 0.55.10^6)$ eV $= 1.50945.10^9$ eV $\cong 1.509$ GeV.

The carried out numerical analysis showed the extremely high efficiency of the resonance processes in accelerating the charged particles in cosmic plasma. The calculations showed that, even both are with very low-relativistic particle energy and electromagnetic wave packet propagation velocity, the electron energy growth is more than three orders of magnitude.

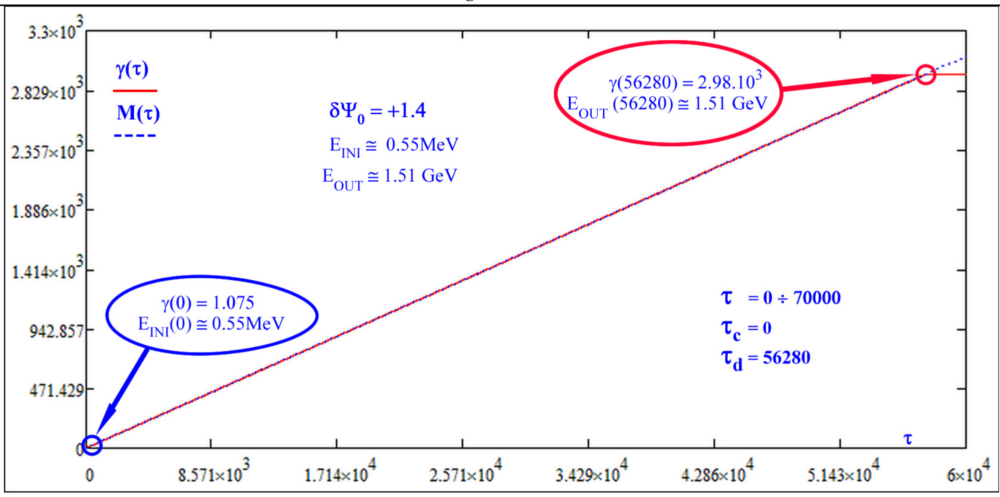

Fig.2. Plot of charged particle relativistic factor $\gamma(\tau)$ and its analytical approximation $M(\tau)$ for $\delta\Psi_0 = +1.4$. Particle is accelerated from $\gamma(0) = 1.075$ ($E_{INI} = 0.55MeV$) up to $\gamma(56280) = 2.98.10^3$ and resulting acceleration energy is $E_{OUT} \cong 1.51$ GeV.

Conclusions

- Resonance wave-particle interactions of the electrons and electromagnetic wave packet with Lorenz envelope is studied by the numerical analysis.
- The initial energy of charged particle and wave packet both are assumed as low relativistic ($\gamma(0) = 1.08$, $E_{ini} \cong 0.55$ MeV) and the initial position of the particle is in the center of the wave packet structure $\Psi(0) = 0$.
- Based on the 70 different values for the wave packet phase around $\Psi(0) = 0$ in range from -3.1 to +3.1 70 calculation tasks are formed with maximal calculation length of $\tau_{max} = 7.104\ \tau$.
- According to the results presented in Table 1, cumulative particle capturing probability is ≈ 97%.
- In ≈ 47% of cases, the wave packet traps particle immediately $\delta\Psi_0 = 0$ and in another ≈ 50 % electron is trapped after periods with different length of cyclotron rotation.
- Estimations of the energy growth of chosen cases are made and presented.
- The particle energy growth at strong surfatron acceleration estimated to approximately three orders of magnitude in considered low-relativistic case.
- Electrons with an initial MeV energy thus acquire an energy in GeV range.The strong surfatron acceleration mechanism is one of the possible sources of the cosmic rays and very useful at interpretation of experimental data for relativistic particles fluxes registered in space conditions

Acknowledgment

This study is part of a joint Russian - Bulgarian Project "Surfatron" between IKI RAS and IKIT-BAS under the Fundamental Space Research Program between RAS and BAS.

References

Bulanov, S. V., A. S. Sakharov (1986). Acceleration of particles captured by a strong electrostatic wave with curved wave front in a magnetic field. JETP Letters, V. 44, No. 9, p. 543.

Chernikov, A. A., G. Schmidt, A. I. Neishtadt (1992). Unlimited Particle Acceleration by Waves in a Magnetic Field. Physical Review Letters, v. 68, № 10, pp. 1507-1510.

Dieckmann, M.E., P.K., Shukla (2006). Plasma Physics and Controlled Fusion. V. 48, p. 1515,

Erokhin, N.S., S.S. Moiseev, R.Z. Sagdeev (1987). The fascination and following acceleration of the charged particles by slow phase velocity wave in non-uniform plasma. Doklady RAS, Vol. 295, No.4, pp. 849-852.

Erokhin, N.S., S.S. Moiseev, R.Z. Sagdeev (1989). Relativistic surfing in non-uniform plasma and cosmic rays generation. Astronomy Letters, Vol.15, № 1, pp. 3-10.

Erokhin, N.S., N.N. Zolnikova, R. Shkevov, L.A. Mikhailovskaya, P. Trenchev (2007). On the charged particles surfatron acceleration in space plasmas. Proc. BAS (C. R. Acad. Bulg. Sci.) V. 60, pp. 967-972.

Erokhin, N.S., N.N. Zolnikova, E.A. Kuznetsov, L.A. Mikhailovskaya (2010). Dynamics of the relativistic acceleration of charged particles in space plasma at the surfing at packet of electromagnetic waves. Problems of atomic science and technology (PAST), Plasma El. and New Methods of Acceleration, V.4 (68), pp. 116-120.

Gribov, B.E., R.Z. Sagdeev, V.D. Shapiro, V.I. Shevchenko (1985). Damping of plasma waves and acceleration of resonant electrons in a transverse magnetic field. JETP Letters, V. 42, No. 2, p. 63.

Itin, A. P., A.I. Neishtadt, A.A. Vasiliev (2000). Captures into resonance and scattering on resonance in dynamics of a charged relativistic particle in magnetic field and electrostatic wave, Physica D: Nonlinear Phenomena, 141, 281-296, doi: 10.1016/S0167-2789(00)00039-7.

Joshi C. (1984). The surfatron laser-plasma accelerators. Prospects and limitations. Radiation in plasmas, v.1, No. 4, pp. 514-527.

Katsouleas, N. and J.M. Dawson (1983). Unlimited electron acceleration in laser-driven plasma wave. Physical Review Letters, v.51, № 5, pp. 392-395.

Kichigin, G.N. (1995). The features of electrons surfatron acceleration. JETP, Vol. 81, No. 4, p. 736.

Kichigin, G.N. (2001). The surfatron acceleration of cosmic rays in the galactic plasma. JETP, V.92, N.6, p.895.

Loznikov, V.M., N.S. Erokhin (2010). The variable source of space electrons excess in the heliosphere. Problems of atomic science and technology (PAST), Plasma El. and New Methods of Acceleration, V.4 (68), pp. 121-124.

Neishtadt, A.I., A.V. Artemyev, L.M. Zelenyi, D.L. Vainshtein (2009). Surfatron acceleration in electro-magnetic waves with a low phase velocity, JETP Letters, 89, 441-447, doi: 10.1134/S0021364009090045.

Shkevov, R., N. S. Erokhin, L. A. Mikhailovskaya, N. N. Zolnikova (2013). Numerical investigation of the surfatron acceleration efficiency of charged particles by wave packets in space plasma, Journal of Atmospheric and Solar-Terrestrial Physics, http://dx.doi.org/10.1016/j.jastp.2012.07.001, JASTP V.99 pp. 73–77.

Shkevov, R., N. Erokhin, N. Zolnikova, L. Mikhailovskaya (2016). Protons surfatron acceleration by electromagnetic wave in space plasma, C. R. Acad. Bulg. Sci.,Tome 69, No. 2, p.p.177-182.

Shkevov, R., N.S. Erokhin, V.M. Loznikov, N.N. Zolnikova, L.A. Mikhailovskaya (2017). Surfatron acceleration of weakly relativistic electrons by electromagnetic wave packet in space plasma. Journal of Atmospheric and Solar-Terrestrial Physics, JASTP, https://doi.org/10.1016/j.jastp.2017.11.001

Sitnov, M.I. (1988). Maximal particles energy in surfatron “unlimited” acceleration mode. Technical Physics Letters, Vol.14, No.1, pp. 89-92.

Takeuchi, S., K. Sakai, M. Matsumoto, R. Sugihara (1987). Unlimited acceleration of a charged particle by an electromagnetic wave with a purely transverse electric field, Physics Letters A, 122, 257-261, doi:10.1016/0375-9601(87)90818-8.

Vasiliev, A.A., Neishtadt, A.I., Artemyev, A.V. (2011). Nonlinear dynamics of charged particles in an oblique electromagnetic wave. Physics Letters A 375, 3075-3079.

Proceedings of
Tenth Workshop "Solar Influences on the Magnetosphere, Ionosphere and Atmosphere"
Primorsko, Bulgaria, June 4÷8, 2018

Long-term trends of magnetic bright points: The evolution of MBP size

D. Utz [1,2], T. Van Doorsselaere [3], E. Gagelmans [3], C.O' Rourke [3], A. Vuerinckx [3], R. Muller [4], A. Veronig [1]

[1] IGAM/Institute of Physics, Karl-Franzens University Graz, Austria
[2] Instituto de Astrofísica de Andalucía - IAA/CSIC, Granada, Spain
[3] Center for mathematical Plasma Astropyhsics CmPA, KU Leuven, Belgium
[4] Observatoire Pic du Midi, University of Toulouse, France
E-mail: dominik.utz@uni-graz.at

Abstract.

Magnetic Bright Points (MBPs) are small-scale, very strong, solar magnetic field concentrations visible in the lower solar atmosphere. While there is a large and ever-increasing knowledge base and understanding of large-scale solar magnetic fields, i.e., sunspots and active regions, and their involvement in the solar cycle, much less is known about small-scale fields such as MBPs. Thus, we aim on contributing to our understanding of these tiny, but, important solar features by investigating the size distribution and its variation over time.

For this purpose, we obtained the synoptic G-band data set of the Hinode mission which is now since nearly 12 years in space and operational (launched in October 2006). After careful image calibration and selection we analysed the G-band data set with an automated MBP identification algorithm to calculate in a next step the equivalent diameter of the MBPs.

The so gained size distribution follows a Gamma distribution with pronounced changes during the solar activity cycle. The MBP sizes appear to be somewhat smaller during the solar minimum and somewhat more extended during the solar maxima as expressed by the scale-parameter of the Gamma distribution.

Introduction

MBPs are small-scale, strong, solar, magnetic field features seen in the lower solar atmosphere. They represent practically the cross-section of kG strong vertical magnetic flux tubes (see Utz et al. 2013). As these flux tubes are possible guides for magneto-hydrodynamic waves, which can heat the upper solar atmosphere (see Mathioudakis et al. 2013, Grant et al. 2015), MBPs are of great interest for research.

But not only do they contribute to the solar atmospheric heating problem, they are also of interest for flux balance studies, i.e. how much magnetic flux is created, transported, submerged, reconnected, and recycled by time, dynamo theory, i.e. scientific insights into MBPs can and will contribute to the controversy of surface versus global dynamo theories, as well as the total solar irradiance variation (TSI variation) due to their different and higher spectral irradiance especially to smaller wavelengths.

In the current contribution we would like to have a look on the long-term behaviour of MBPs. Previous studies (see Utz et al. 2016, 2017) have already dealt with the number of MBPs at the solar disc centre versus time on time scales of the solar cycle. In this work we would now like to shed light on the characteristic MBP size and its evolution over time. This is important as it can tell us about fundamental magneto-convection properties in the Sun.

Data

Data are taken from the Hinode data archive. Hinode is a Japanese/US/European satellite mission launched in autumn 2006 and dedicated to the study of solar magnetic fields (see Kosugi et al. 2006). In our study we used the BFI synoptic G-band data set of Hinode comprising around 4000 single images taken at the solar disc centre with a cadence of roughly one image a day. In the beginning of the mission the images were taken with a higher cadence and with full pixel sampling of 4048 pixels by 2024 pixels corresponding to roughly 200 by 100 arcsec^2. After the failure of the main downlink antenna the images have been binned onboard to reduce the data load. For more details about the data see also Utz et al. 2016, 2017.

After downloading of the data and re-binning all the images to the same pixel sampling an automated image segmentation and MBP identification algorithm was applied to the data set (see Utz et al. 2009). These procedure gives us the raw data, identified MBPs at solar disc centre.

The next step consisted of a careful image selection procedure to avoid de-focused images or broken images. Sometimes problems occurred during the downlink of the data causing a part of the image to be missing – broken image, the other case of a de-focused image can happen due to rapid heat load changes when the satellite operators reposition the spacecraft, e.g., from the solar limb to the disc centre. In such a case the heat load and thus the optimum focal position changes strongly, causing sometimes the operators to miss the optimum set up.

The image selection procedure was as follows: First we calculated the image contrast and only selected those images in a narrow band around the best available image contrast. This practically eliminates out of focus images, broken images, as well as sunspot images (sunspots leading to high contrast values due to their extended dark appearance).

After eliminating these bad images, we calculate the median number of MBPs per month and select then the image of the month corresponding to this number as representative for the given month, i.e., the MBP size distribution is calculated from the MBPs detected in this selected image.

Results

a) Size distribution of MBPs

The used MBP algorithm obtains the size of identified MBPs in pixels which can then be easily re-calculated to an equivalently sized circular structure of which we can derive the diameter. The result is shown for two months of the observational period in Fig. 1.

The left panel (Fig. 1.a) shows the obtained size distribution for October 2011 (around MBP minimum activity) while the right panel (Fig. 1.b) shows the size distribution of MBPs more to the end of the observational period in February 2016, i.e. slightly posterior to the MBP number activity maximum (see Utz et al. 2017). In addition to the histogram itself we also plotted a line fit following a so-called Gamma distribution (see Eq. 1).

$$f(x;\alpha,\beta)=\frac{\beta^{\alpha}x^{\alpha-1}e^{-\beta x}}{\Gamma(\alpha)}\ for\ x>0\ and\ \alpha,\beta>0, \qquad \text{(Eq.1)}$$

where α and β are the fitting coefficients, with α representing a scale parameter and β representing a shape parameter. Immediately we can recognise a change in the shape as well as in the scale parameter for the two months under consideration.

b) Long-time trend of the size distribution of MBPs

Stimulated by this finding we have now a look on the whole data set for the month of December of all the observed years. The result is shown as a curve family plot (only giving the line fits according to Eq. 1) in Fig. 2. It becomes clear that there is a variation of the size of MBPs over time. With a decrease in likelihood of smaller elements versus an increased probability for larger elements later during the Hinode campaign.

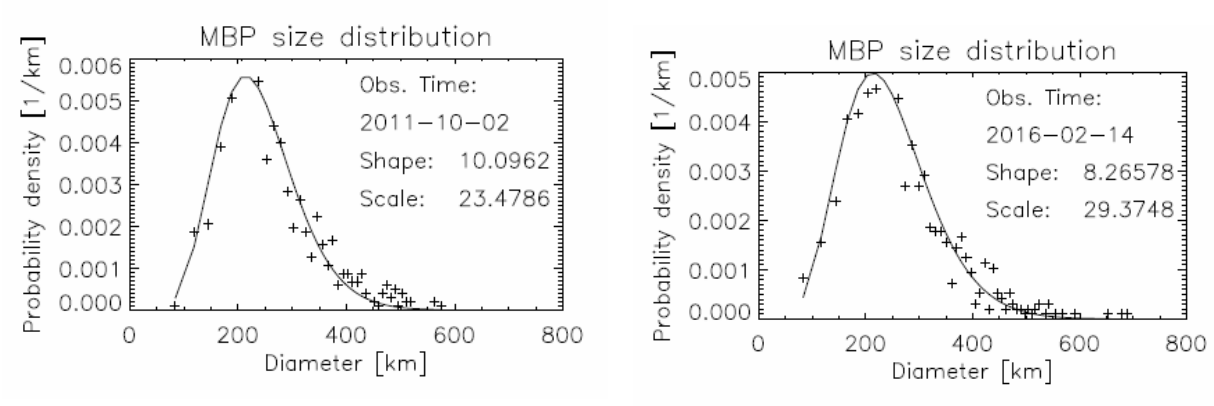

a) b)

Fig. 1 The MBP size distribution plotted in the form of equivalent diameter, i.e., assuming circularly shaped features. The solid line follows a Gamma distribution according to Eq. 1. Panel a) shows the size distribution for the month of October 2011 (exactly on the 2nd of October) while b) shows the same distribution for February 2016. The fitting parameters are stated in the panels.

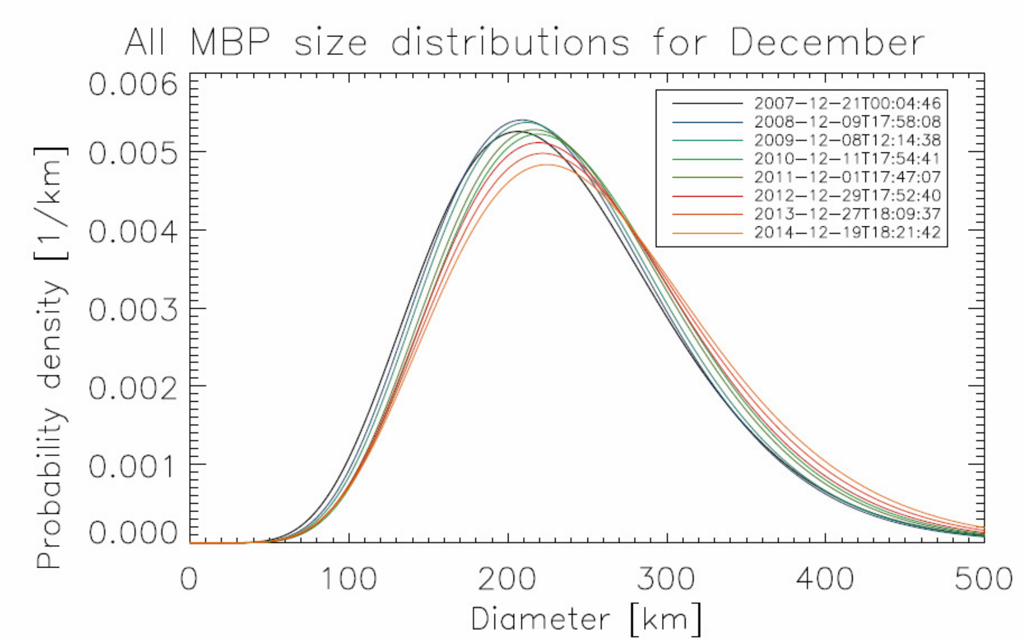

Fig. 2 The fitted size distributions of the MBPs for all the observed years for the month of December.

c) Size distribution of MBPs and relative sunspot number activity

To work out this behavior in a clearer way we like to show now the two parameters separately but over-plotted with the general used proxy for solar activity – the relative sunspot number. The result can be seen in Fig. 3. The depicted sunspot number was taken from SIDC (Solar Influence Data Centre; WDC-SILSO, Royal Observatory of Belgium, Brussels http://sidc.oma.be/). We see that the scale parameter (upper solid line) decreases in the beginning of the observed temporal frame until the period 2010 to 2012, when it shows a bulge like structure, before it starts a permanent increase after 2011. This is somewhat in line with the relative sunspot number which shows a pronounced minimum in the early years of the observational period until 2010. The shape parameter outlines an opposite trend with an early increase and later a steady decrease.

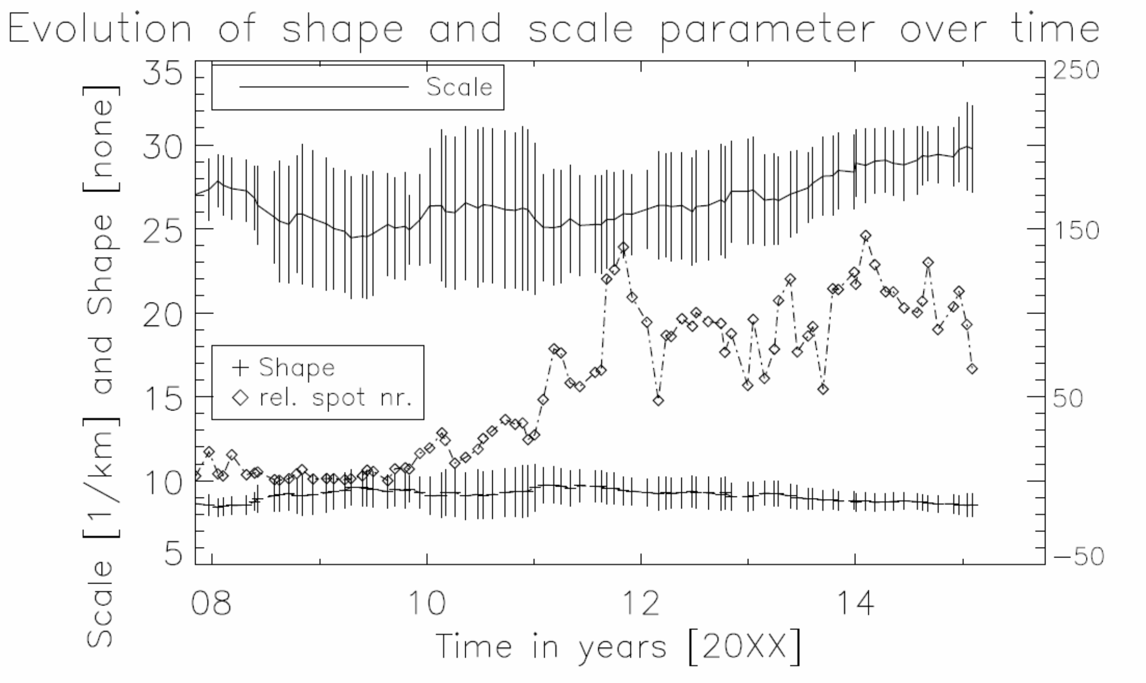

Fig. 3 Both fit parameters of the size distribution (see Fig. 1 & 2; Eq.1, respectively) are shown together with the relative sunspot number obtained from SILSO/SIDC. The upper solid line is the scale parameter while the bottom dashed line represents the shape parameter. The dash-dotted line in between corresponds to the relative sunspot number. The bar gives the standard deviation range of the parameters.

Discussion

a) Size distribution of MBPs

The proper size distribution of MBPs is still under discussion and debate as one can see in Abramenko et al. 2010, in which the authors compared recent findings of size distributions and re-measured the size distribution with the NST (New Solar Telescope at Big Bear Solar Observatory). Most recent studies indicated a log-normal distribution which is fundamentally linked to the merging and fragmentation process MBPs are undergoing (see Bogdan et al. 1988). However, a so-called Cullen and Frey graph (see Fig. 4), reproduced here for all of the monthly data sets, would tell us to use the Gamma distribution instead as the main cloud of scatter falls, except of a few outliers, closer to the Gamma distribution line than to any other indicated distribution.

For the Gamma distribution one can find a reasonable physical interpretation of the involved scale and shape parameter. Namely that the scale parameter describes a true "exponential" distribution implying that the size of MBPs is not restricted to a smallest cut-off size, neither would there be a "typical" standard size, rather the size distribution would continue to ever smaller sizes with ever more features. This would also imply that the smallest scales are of great importance as, due to the exponential increase in number, most magnetic flux could be probably found there. The shape parameter on the other hand would be given by the instrument and/or observation quality constraints. Practically the shape parameter models the "real" diffraction limit to small-scales in any real observation. Thus, even a theoretical exponential distribution must somehow start to decline to smaller scales as the smallest scales cannot be resolved. Exactly this behavior, this kind of transition, is modelled via the shape parameter. To test these ideas, the authors propose to use the same identification algorithm on

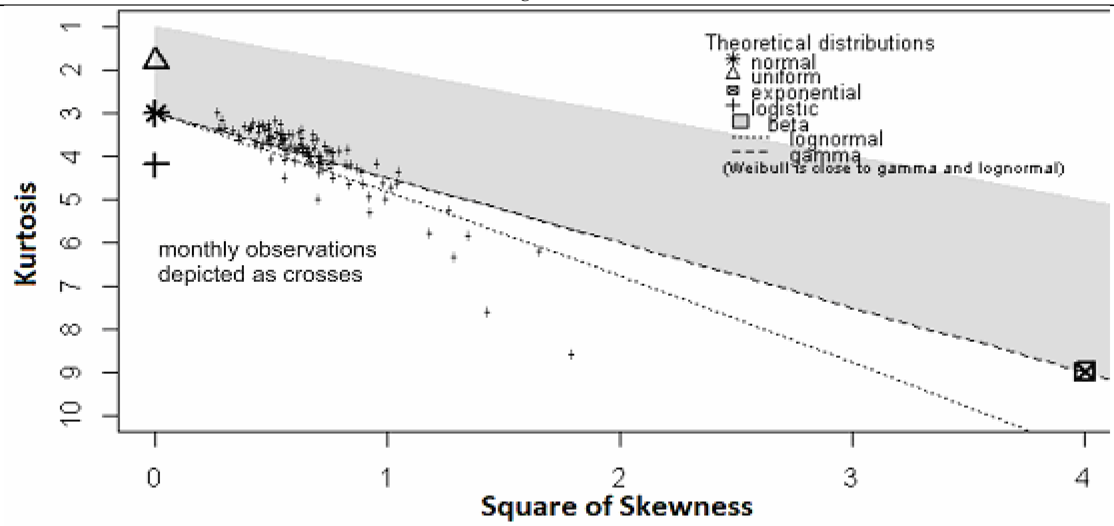

Fig. 4 Cullen and Frey graph for all of the monthly obtained size distributions calculated from the Hinode data set showing the possible region of the obtained data versus typical probability distributions in the 2-dimensional skewness/kurtosis space.

different telescopes and resolved data sets. The best data set for such an endeavor would be taken at the same position and time with different instruments. If the authors are right it would imply that one should always find the same scale parameter for the size distribution but different shape parameters according to the telescope.

b) Long-time variation of the Size distribution of MBPs

As we have seen in the various Figs. from Fig. 1 to 3 the size distribution of MBPs changes over time and seems to be correlated to the change of solar activity as expressed by the relative sunspot number. A similar behaviour was found for the number of MBPs at disc centre, see Utz et al. (2016) and (2017). Here the authors observed a decrease in MBP number temporally shifted slightly (between at least half a year and 2 years; depending on the time epoch used for the correlation). They attributed this shift to the necessity of flux transport, i.e., from the sunspot belts to the solar disc centre.

In this contribution we see now a change of the size distribution, namely a shrinkage during the minimum and an increase afterwards during the rising phase of the current solar cycle. Additionally, both seem to be shifted in time, probably indicating that the flux is related to the sunspot cycle and shifted due to the fact that it needs to be transported. The other important conclusion, which can be drawn, is that if the size distribution for MBPs varies it might imply that the fundamental solar convection changes over the solar cycle as the varying size distribution might be due to a varying width of the intergranular lanes in which they are situated. However, this would have to be tested in the future by more careful analysis, e.g., calculating the semi-major axes instead of an equivalent diameter and having a look in the variation of these axes.

Conclusions

1. The size distribution of MBPs appears to follow a Gamma distribution.
2. The interpretation of the Gamma distribution parameters is as follows: The scale parameter is related to the true physics and describes an exponential scaling of the sizes of MBPs. This means that there are no "minimum" MBP sizes and according to this we should be able to see MBPs down to yet smaller scales when they become available by new generation telescopes. The shape parameter on the other hand is due to the used telescopes and mimics the diffraction limit of any telescope, i.e., the true size distribution gets folded by the telescope transfer function giving rise to a declining measured size distribution for small sizes. This decline is modelled by the shape parameter.
3. There is a long-term development and variation of MBPs with the solar cycle. Seemingly shifted to the sunspot cycle (as also seen by Utz et al. 2016/2017 for the number of MBPs at disc centre). The change and variation in the scale parameter might be interpreted as follows: MBPs get somewhat smaller during solar minimum and somewhat larger during solar maximum. This might be related to a change in width of the intergranular lanes and thus indicates a fundamental variation (however, a very small one) of the magneto-convective plasma transport.

Acknowledgment

This study received financial support under FWF grant P27800-N16 as well as through an Odysseus grant of the FWO Vlaanderen, the IAP P7/08 CHARM (Belspo), and GOA-2015014 (KU Leuven). Additionally, the study has received funding from the European Research Council (ERC) under the European Union's Horizon 2020 research and innovation programme (grant agreement No 724326). The authors wish to specially congratulate the Hinode team for their superb instruments and maintaining the high data quality over all the mission years. *Hinode* is a Japanese mission developed and launched by ISAS/JAXA, with NAOJ as domestic partner and NASA and STFC (UK) as international partners. It is operated by these agencies in co-operation with ESA and NSC (Norway). Moreover, we wish to acknowledge SILSO/SIDC for promoting, preparing, and distributing the international relative sunspot number. Source of the relative sunspot number: WDC-SILSO, Royal Observatory of Belgium, Brussels. D.U. wishes to express his gratitude to Aaron Hernandez for countless fruitful discussions over the one or other cup of coffee.

References

Abramenko V., V. Yurchyshyn, P. Goode, A. Kilcik (2010), Statistical Distribution of Size and Lifetime of Bright Points Observed with the New Solar Telescope, ApJ, 725, 101.

Bogdan T. J., P. A. Gilman, I. Lerche, R. Howard (1988), Distribution of sunspot umbral areas - 1917-1982, ApJ, 327, 451.

Grant S. D. T., D. B. Jess, M. G. Moreels et al. (2015), Wave Damping Observed in Upwardly Propagating Sausage-mode Oscillations Contained within a Magnetic Pore, ApJ, 806, 132

Kosugi T., K. Matsuzaki, et al. (2007), The Hinode (Solar-B) Mission: An Overview, Solar Physics 243, 3-17.

Mathioudakis M., D. B. Jess, R. Erdélyi (2013), Alfvén Waves in the Solar Atmosphere. From Theory to Observations. SSR, 175, 1-27.

Utz D., A. Hanslmeier, C. Möstl, R. Muller, A. Veronig (2009), The size distribution of magnetic bright points derived from Hinode/SOT observations. A&A, 498, 289.

Utz D., J. Jurčák, A. Hanslmeier, R. Muller, A. Veronig, O. Kühner (2013), Magnetic field strength distribution of magnetic bright points inferred from filtergrams and spectro-polarimetric data. A&A, 554, 65.

Utz D., R. Muller, S. Thonhofer, A. Veronig, A. Hanslmeier, M. Bodnáová, M. Bárta, J. C. del Toro Iniesta (2016), Long-term trends of magnetic bright points. I. Number of magnetic bright points at disc centre. A&A, 585, 39.

Utz D., R. Muller, T. Van Doorsselaere (2017), Temporal relations between magnetic bright points and the solar sunspot cycle. PASJ, 69, 98.

Proceedings of
Tenth Workshop "Solar Influences on the Magnetosphere, Ionosphere and Atmosphere"
Primorsko, Bulgaria, June 4÷8, 2018

Electrical coupling of auroral ionosphere with lower atmospheric regions during SEP

Tonev P.T.

Space Research and Technology Institute BAS, Sofia, Bulgaria
E-mail: ptonev@bas.bg

Abstract.

The behavior of the atmospheric electric current *Jz* flowing from the ionosphere to ground at auroral latitudes during solar energetic particle events (SEP) is under consideration. Hypothetically, the current *Jz* is factor of weather formation. Experimental data demonstrate peculiar variations of *Jz* at high latitudes during strong SEP. To explain these, we consider such variations as caused by dynamic changes of atmospheric conductivity profile due to SEP which lead to enhanced electrical coupling between auroral ionosphere and atmosphere. To estimate the effect of this factor on electric current *Jz*, we study by modeling the contribution in *Jz* of currents of ionospheric origin which possibly penetrate below as tiny remaining of field-aligned currents (FAC). While the closure of FAC becomes principally in the ionosphere, it is shown that a tiny (as small as 10^{-6}) portion of FAC can penetrate during SEP events down to the stratosphere where it can significantly contribute to the global atmospheric electrical circuit.

Introduction

The aim of this work is to explain the peculiar large and long-time variations of the ionosphere-to-ground electric current *Jz* which is a part of the global atmospheric electrical circuit (GEC). Such peculiar variations have been observed by balloon-borne measurements in the high-latitudinal stratosphere during a strong SEP event - the solar proton event SPE69 on 20 January 2005 [*Kokorowsky et al.,* 2006]. This SPE of very hard proton energy spectrum was accompanied also by ground-level enhancement (GLE) event. The typical value of the electrical current *Jz* is ~2 pA/m^2; usually it exhibits small (up to few tens of percent) and slow (diurnal) temporal variations which are related to diurnal changes of the global thunderstorm activity [*Rycroft et al*., 2012]. Nevertheless, unpredictable and actually unexplained rapid and large variations of the electric current *Jz* were observed in the considered case, as response to SPE69, discussed in this paper. Similar peculiar behavior of *Jz* in stratosphere was observed also in another two strong SPE accompanied by GLE, on 4 August 1982 and on .. [*Holzworth and Mozer,* 1979; *Holzworth et al.*, 1987]. The observed behavior of the current *Jz* can be an important phenomenon according to hypothesis by [*Tinsley,* 2000]: *Jz* and its variations at the cloud boundaries in the troposphere can be of key importance for weather formation.

The electric current *Jz* forms part of GEC which is principally driven by thunderstorms and electrified clouds acting in the earth's troposphere and generating upward currents (~2 kA totally) into the ionosphere. *Jz* is return current in GEC: it flows downwardly in regions of fair-weather conditions. GEC forms positive electrical potential of ~250 kV in the ionosphere (related to ground) which is equipotential at any time except of high altitudes. There dawn-to-dusk trans-polar potential difference of 20-100 kV (or even more) is created as result of the ionospheric convection and field-aligned currents (FAC).

To explain the peculiar behavior of the electric current *Jz* observed in the Antarctic stratosphere during SPE69, we suggest that strong SPE initiate more effective electrical coupling between ionosphere and middle atmosphere at high latitudes, so that a significant current of ionospheric origin is superposed to *Jz*. Here we show that by means of modeling.

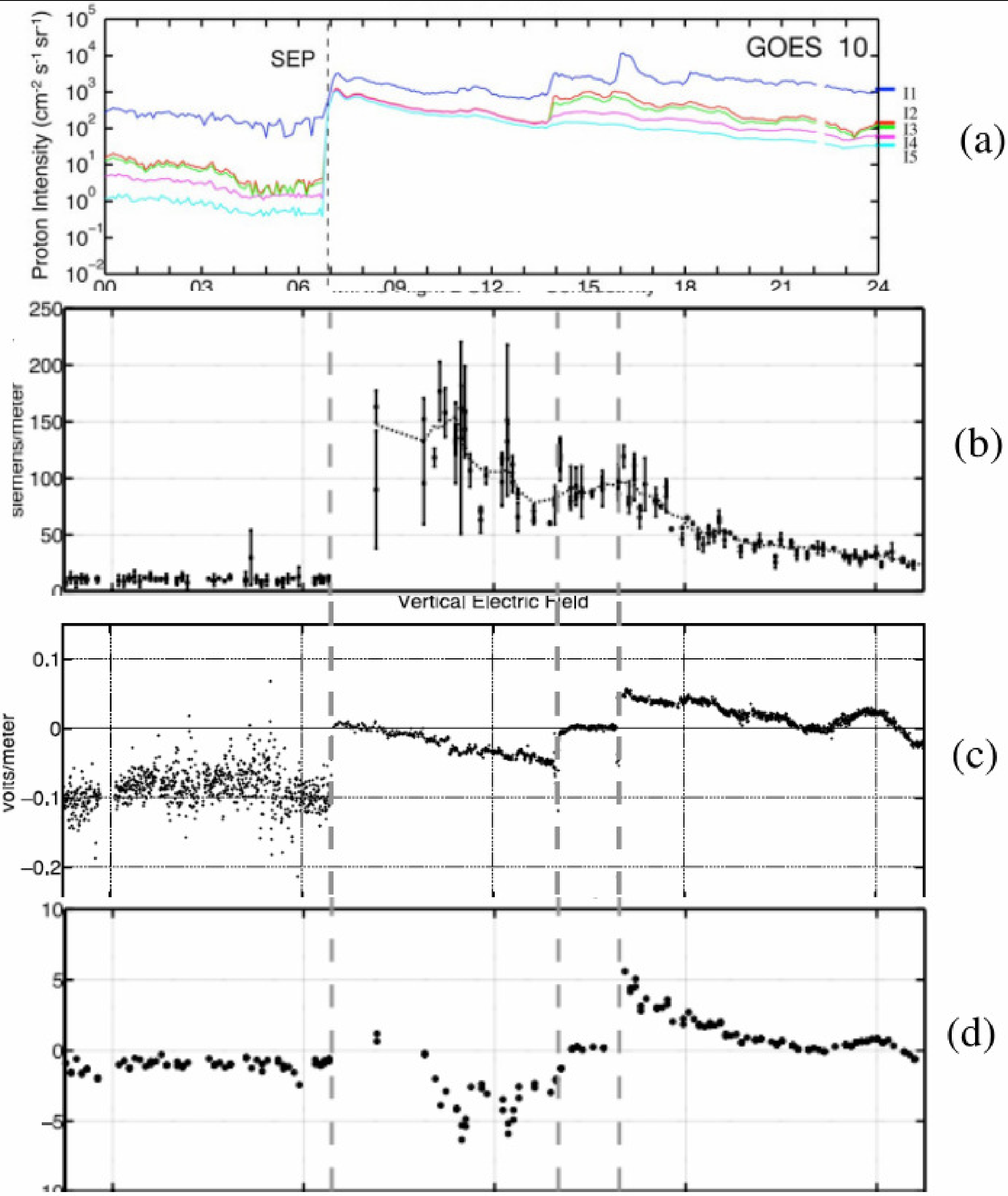

Fig.1.(a) Data from GOES-10 for the integral proton intensity energies for channels 1-5 for > 1, 10, 30, and 50 MeV; (b-d) Electric conductivity σ; vertical electric field Ez; and current Jz from simultaneous balloon-borne measurements in Antarctic stratosphere.

Electric characteristics in Antarctic stratosphere during SPE69

a) Experimental results

SPE69 on 20 January 2005 was the strongest solar proton event for the last six decades, characterized by very hard energetic spectrum. Data from GOES-10 for solar proton flux are demonstrated in Fig.1a [*Kokorowski et al.*, 2012]. Simultaneous balloon-borne measurements in Antarctic stratosphere are represented for conductivity σ (Fig.1b), the vertical electric field *Ez* (Fig1c) and the related current *Jz* (Fig.1d). The balloon drift is from (70.9°S, 10.9°W) to (71.4°S, 21.5°W) at altitudes 30.9 - 33.2 km [*Kokorowski et al.,* 2006].

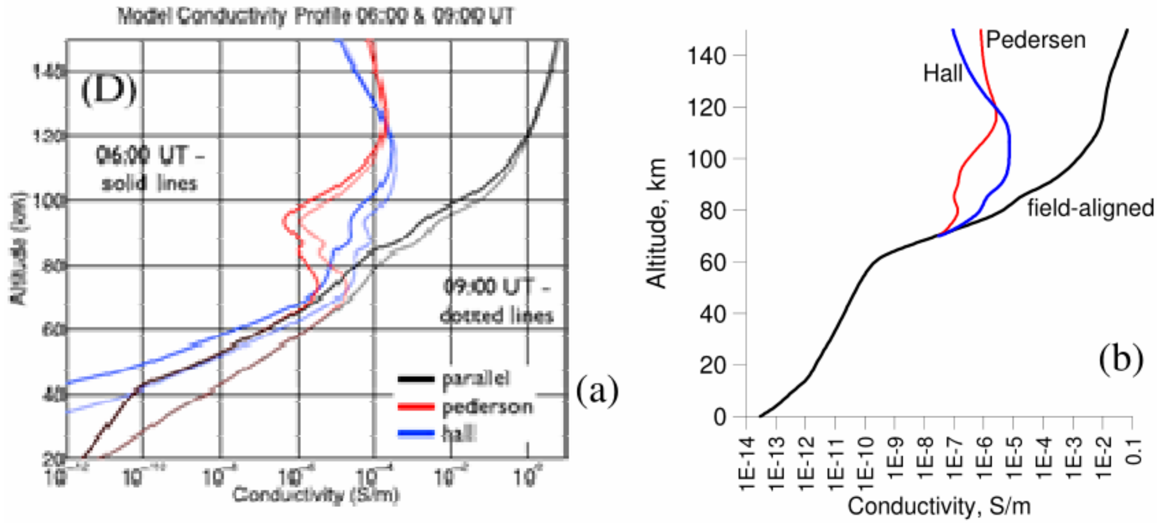

Fig.2. Conductivity profiles adopted for high latitudes (a) and for lower latitudes (b)

Before the onset of SPE69 σ, *Ez* and *Jz* (computed from σ and *Ez*) have typical values: σ is few $\times 10^{-10}$ S/m; *Ez* and *Jz* have downward direction and *Jz* ~2 pA/m^2 (in average). After the SPE arrival at time t_0 = 06:51 UT conductivity increased rapidly by at least one order of magnitude (due to ionization by protons with energies ~100 MeV). The most peculiar is the response of *Ez* and *Jz* to SPE69 after 13:48 UT. Between 13:48 UT and 15:58 UT *Ez* and *Jz* close to zero for the whole period. After 15:58 UT *Ez* and *Jz* suddenly changed their behavior - they paradoxically altered their direction from downward to upward. Besides, current *Jz* exceeded more than twice (yet in opposite direction) its typical value for hours. These peculiarities remain actually unexplained. Our goal is to propose such explanation.

b) Atmospheric effects of SPE69

According to model data [*Usoskin et al.,* 2011] SPE69 caused strong ionization in the middle atmosphere at hih latitudes whose rate *q* was ~1300 and ~1600 ions cm^{-3} s^{-1} at altitudes z = 30 and 40 km, respectively. As result of the strong ionization, conductivity σ also increases. The model results [*Kokorowski et al*., 2012] in Fig.2a demonstrate the conductivity profile at the balloon coordinates before (at 06:00 UT) and after (at 09:00 UT) arrival of SPE.

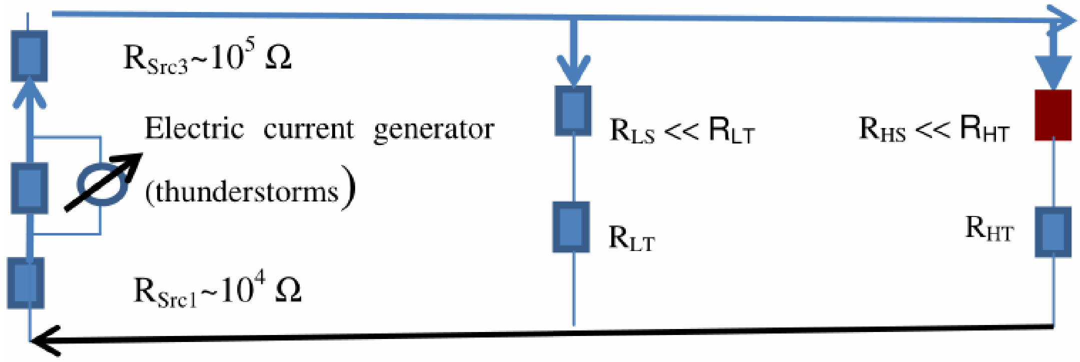

Fig.3. Equivalent electrical circuit.

c) Interpretation of discrepancy between data and former theoretical predictions

First, we estimate the maximum variations of the vertical electric current *Jz* in GEC during SPE69 just as result of conductivity modifications. GEC is represented in Fig.3 by an equivalent electric circuit. The vertical links represent: *i*) the generalized tropospheric electric source of thunderstorms and electrified clouds (left link); *ii*) the downward current *Jz* under fair-weather conditions at high (right) and at lower (central link) latitudes. The columnar resistances of links *ii*) are presented as sum of resistances R_T for troposphere and R_S for higher altitudes. The only resistance significantly affected by SPE is R_{HS} above the troposphere at high latitudes. But since the part of R_{HS} in the total columnar resistance is few percent, its modifications by SPE can lead only to insignificant (<5%) variations of the current Jz.

To explain the discrepancy with the measured large variations of Jz we consider possible coupling of GEC with electrical currents in the auroral ionosphere by the system of field-aligned currents (FAC) caused by the solar wind interaction with magnetosphere. In the auroral ionosphere FAC flow downwardly in the dawn sector and upwardly in the dusk sector in region 1 closer to magnetic pole (inner), and vice-versa in the outer region 2. The closure of FAC is effectively completed in the E-region by Hall and Pedersen current systems. We assume that a tiny part J_{IS} of FAC penetrate into the middle atmosphere during SPE due to enhancement of conductivity at high latitudes. While FAC density in the ionosphere is of the order of 1 μV/m, the current J_{IS} in the stratosphere can be few pA/m^2 or less; nevertheless, it can affect significantly the ionosphere-to-ground current Jz - effective electrical coupling of auroral ionosphere with GEC would occur. We thus represent the electric current Jz in the middle atmosphere at high latitudes by the following sum:

$$J_z = J_{TS} + J_{IS} \qquad (1)$$

where J_{TS} is the ionosphere-ground current due to the tropospheric electrical sources, and J_{IS} results from ionosphere-GEC coupling. During strong enough SPE this coupling becomes more effective so that J_{IS} can become comparable or larger than J_{TS}, so that the behavior of J_z is dictated by variations of J_{IS}. This suggestion is supported by results of [*D'Angelo et al.* (1982] and [*Park and Dejnakarintra*, 1977]. Long balloon data obtained by D'Angelo et al. (1982) show that moderately increased geomagnetic activity (by Kp>2) leads to enhanced contribution of the electric current J_{IS} in J_z at ~30 km, auroral latitudes.

To estimate the contribution of the electric current J_{IS} in J_z (according to Eq.1) in the stratosphere at high latitudes during SPE69, we estimate here J_{IS} by modeling.

Model estimations of electric current J_{IS} below auroral ionosphere

a) Model description

The continuity equation is solved for the electric current density **j** in the region between ground and Z=150 km altitude under DC conditions:

$$\nabla \cdot \mathbf{j} = 0 \qquad (2)$$

The source of the current **j** are FAC at altitude Z=150 km which are assumed to flow vertically. The electric field related to **j** is **E**, $\mathbf{E} = -\nabla u$ where u is the potential. $\mathbf{j} = [\sigma]\mathbf{E}$ where $[\sigma]$ represents conductivity: it is a tensor above 65 km and a scalar below that height. The boundary conditions to Eq,(2) are: *i*) u = 0 at ground level; *ii*) the vertical component of **j** (i.e. J_{IS}) at Z=150 km altitude is determined by FAC, $J_{IS}=j_{FAC}$. It is assumed that at geomagnetic latitudes below 50° j_{FAC}= 0.

To explain the most striking peculiarity, i.e. the reversal of direction of jz and Ez after time t_2=15:58 UT, we solve Eq.(2) with boundary conditions *i*) and *ii*) to estimate **j** and its vertical current J_{IS} in the model domain. Three events occurred in the period of interest:

1) It is marked by geomagnetic storm (Kp= 4o and 5- from 12:00 to 18:00 UT) and a strong substorm (AE~1200 nT) ~15:00-18:00 UT, unlike during the period before. The distribution of FAC is derived from the model of [Weimer, 1994] (presented in Fig.4).
2) The balloon position changed from one below downward FAC to one of upward FAC.
3) The solar proton flux with energies ~1-2 MeV has jump at ~16:00 UT.

The distribution of FAC at Z=150 km is represented here as superposition of m elementary sources of sample distribution. Two types of sample distribution are used: *a*) $j_{FAC}(r) = j_{FAC}(r{=}0)\exp(-r/r_s)$; *b*) $j_{FAC}(r) = j_{FAC}(r{=}0)$ by $r \le r_s$, $j_{FAC}(r)$=0 by $r>r_s$. r is the horizontal distance from the elementary source centre; r_s characterizes the source dimension. The integrated current j_{FAC} at z=150 km should be zero (condition for balanced system of FAC).

b) Horizontal scale of electric current J_{IS} from single elementary source of FAC

For first estimations, the current J_{IS} is obtained from Eq.(1) by assumption for flat ground and laterally unlimited model domain. FAC is represented as a single elementary source of type *a*). The actual distribution of FAC at 150 km is superposition of *m* elementary sources. Cylindrical coordinates (r,φ,z) are used: *r* is distance from the source center, φ is azimuth, *z* is altitude. Axial symmetry is assumed. Solution is obtained analytically with step-wise approximation of conductivity profiles (σ=const within each of *n* layers [z_i, z_{i+1}), 0.5 km thick (n=300). The conductivity profile in Fig.2a at 09:00 UT is used; no dependence on *r* is assumed. The following results are obtained for J_{IS} as function of *r* and *z*:

z, km	*r*, km	0	10^1	10^2	10^3	10^4
30	J_{IS}, pA/m^2	0.036	0.032	0.028	0.019	0.0012
40	J_{IS}, pA/m^2	0.053	0.045	0.034	0.020	0.0012
50	J_{IS}, pA/m^2	0.43	0.33	0.095	0.021	0.0012

According to this oversimplified formulation, the current J_{IS} exhibits extremely large horizontal dissipation in the mesosphere and stratosphere: the horizontal scale of J_{IS} exceeds the earth's dimension (which is unphysical result). Because of that and since no dependence of conductivity profiles on latitude is taken into account, the results for $J_{IS}=j_z$ in the stratosphere by small r<~100 km are significantly below the actual values, i.e. the relevant values of J_{IS} must be much bigger. Another factor for the increase of actual J_{IS} values is difference between conductivity profiles at high and lower latitudes during SPE69: this last is much smaller (Fig.2a,b). From the results we conclude that: *A*) The current J_{IS} is highly dissipated horizontally so that in stratosphere it is distributed over the whole globe; *B*) More adequate model is needed with account to the earth's shape and dimensions, and with differentiation of conductivity profiles at high and lower latitudes.

c) Corrected model results

To obtain more adequate results, Eq,(2) should be solved in spherical coordinates (r,θ,φ) where *r* is the distance from the earth's center, and θ and φ are geomagnetic co-latitude and longitude, with account to different conductivity profiles depending on coordinates and time. This model is not yet fully implemented: due to difficulties in reaching good computational accuracy. Correction of results is achieved here with the account to *A*) and *B*). I) The developed model allows the use of two different conductivity profiles by $r \le r_1$ and $r > r_1$, respectively; II) Solutions are still obtained in cylindrical coordinates, but with re-scaling by requirement u=0 for $r > \pi R_E$ where R_E = 6371 km is the earth radius. First, a single elementary source of FAC of type *b*) is used with parameters relevant to represent local structures of FAC in Fig.4: $j_{FAC}(r=0)$=1 μAm^{-2}, r_S= km. Conductivity profile is adopted from Fig.2a (at 09:00 UT) for $\theta \le 20^0$ and from Fig.2b for θ>20°. At time 16:00 UT (when the balloon position is close below the maximum of upward FAC) we obtain that, depending on the parameters of the elementary source of FAC, the electric current J_{IS} at z=30 km can be of the order of several pA/m^2. Further J_{IS} is estimated at the same conditions as superposition of a .balanced set of m=3 elementary sources of

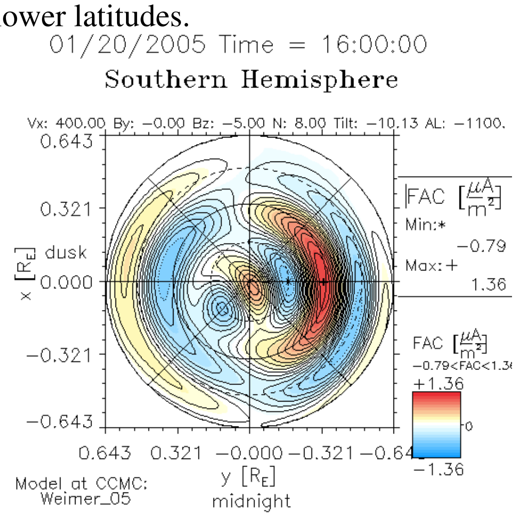

Fig.4. Distribution of FAC in Southern hemisphere on 20.01.2005 with index AL=1100 nT and relevant solar parameters parameters according to model of [Weimer, 1995].

downward and upward FAC Results are obtained at altitudes 30, 40, and 50 km when the balloon position is close below the maximum of the upward FAC in region 1:

z, km	30	40	50
J_{IS}, pA/m^2	6.1	9.5	80

In this case the term J_{IS} in Eq.(1) exceeds by module J_{TS} about 3 times at altitude z=30 km, and more than that at higher altitudes. Since J_{IS} has positive sign (the current direction is determined by that of the FAC of the closest structure) this leads to reversal of J_z in upward direction and J_z will be about twice as large as typical values of $|J_{TS}|$ values. This agrees with the data for Jz after 16:00 UT demonstrated in Fig.1d. At higher altitudes $|J_{IS}|>>|J_{TS}|$, i.e. the electric current J_{IS} totally determines the behavior of Jz.

Conclusions

1. Explanation is proposed of the observed effects of the solar proton event SPE69 (20 January 2005) on ionosphere-to-ground electric current Jz in stratosphere at high latitudes.
2. The observed peculiar behavior of the electrical current Jz is due to enforced during SPE electrical coupling between ionosphere and atmosphere at high latitudes.
3. A small part ($\sim 10^{-6}$) of ionospheric field-aligned currents can penetrate down to the stratoshere during SPE, due to the significant modification of conductivity, where it can significantly contribute to the electric current Jz.

References

D'Angelo, N., I.B. Iversen and M. Mohl Madsen (1982), Influence of the dawn-dusk potential drop across the polar cap on the high-latitude atmospheric vertical current. Geophys. Res. Lett., 9, 773-776

Holzworth R.H., F.S.Mozer (1979). Direct Evidence of Solar Flare Modification of Stratospheric Electric Fields. J. Geophys. Res.. 84(CI), 363-367.

Holzworth, R.H., K. W. Norville, P. R. Williamson (1987). Solar flare perturbations in stratospheric current systems. Geophys. Res. Lett., 14, 852-855.

Kokorovski, M., J. G. Sample, et al. (2006). Rapid fluctuations of stratospheric electric field following a solar energetic particle event, Geophys. Res. Lett., 33, L20105.

Kokorowski, M., A. Seppälä, et al. (2012). Atmosphere-ionosphere conductivity enhancements during a hard solar energetic particle event, J. Geophys. Res., 117, A05319.

Park C.G., M. Dejnakarintra (1977). The effects of magnetospheric convection on atmospheric electric fields in the polar cap, In: Electrical Processes in Atmospheres, Proc. 5th Int. Conf. on Atmospheric Electricity, Garmisch-Partenkirchen, 2-7 September 1974, ed. by H. Dolzelek and R. Reiter, 1977, pp. 536-543.

Rycroft, M.J., K.A.Nicoll, K.L. Aplin, R.G. Harrison (2012). Recent advances in global electric circuit coupling between the space environment and the troposphere. J. Atmos Solar-Terr. Phys., 90–91, 198–211.

Tinsley, B.A., (2000). Influence of solar wind on the global electric circuit, and inferred effects on cloud microphysics, temperature and dynamics in the troposphere. Space Sci. Rev., 94, 231-258.

Tinsley, B.A., Zhou, L. (2006). Initial results of a global circuit model with variable stratospheric and tropospheric aerosols. J.Geophys.Res., 111, D16205.

Usoskin, I.G., G.A. Kovaltsov, etc. (2011). Ionization effect of solar particle GLE events in low and middle atmosphere. Atmos. Chem. Phys., 11, 1979-1988.

Weimer, D. R. (1995). Models of high-latitude electric potentials derived with a least error fit of spherical harmonic coefficients, J. Geophys. Res., 100, 19,595-19,607.